

Design and Analysis of Inflatable Space Structures

Dr Manpreet Singh Puri

Department of Civil & Environmental Engineering,
University of Strathclyde

Presented as a thesis for the degree of Ph.D.
in the University of Strathclyde, 75 Montrose Street,
Glasgow G1 1XQ

© Dr. Manpreet S. Puri, 2016

Contents

Acknowledgements	xii
Acronyms	xiii
Preface	xv
Summary	1
1 Introduction	1
1.1 Background	2
1.2 Motivation	6
1.3 Organisation of this Thesis	11
2 Background Theory	13
2.1 Non-Linear Continuum Mechanics	13
2.1.1 Geometry Arrangement	14
2.1.2 Kinematics	18
2.1.3 Strain Measure	23
2.1.4 Stress Measure	26
2.1.5 Conservation Equations	27
2.1.6 Constitutive Equations	38
2.2 Mechanics of Membrane Structures	44
2.2.1 Membrane Theory	44
2.2.2 Membrane Wrinkling	46
2.2.3 Membrane Wrinkling Algorithm	49
2.3 Time Integration Methods	50
2.3.1 Explicit Time Integration Method	51
2.3.2 Implicit Time Integration Method	53

2.3.3	Explicit versus Implicit Integration Methods	56
2.4	Originality of the Current Work	59
2.4.1	A novel patent pending smart adaptive space structure to harness solar energy to be re-used as a potential source of green energy on the ground	61
2.4.2	Design of the new cell structures for the adaptive smart cell to be shaped to the user specification after deployment	61
2.4.3	The post-inflation of the deformed inflated membrane structure to restore it to its approximate initial configura- tion	62
2.4.4	Simulation design of the membrane elements used within Abaqus using the fluid cavity inflation and internal layer method	63
2.4.5	Abaqus simulation technique employed to meet conver- gence and run successfully	64
3	Rectangular Membrane Model	66
3.1	Literature Review of Rectangular Membrane Structures	67
3.2	Finite Element Analysis with Abaqus	72
3.3	Analysis Procedure	73
3.3.1	Initial Conditions	73
3.3.2	Pre-Buckling Eigenvalue Analysis	75
3.3.3	Post-Buckling Analysis	79
3.3.4	Material Model	80
3.3.5	Element Selection	82
3.3.6	Responsiveness to Stimuli	84
3.3.7	Stabilizing Factor	86
3.3.8	Finite Element Models	87
3.4	Axial Loading on the Membrane Structure	88
3.4.1	Simulation Methodology	88
3.4.2	Simulation Analysis	89
3.4.3	Wrinkling Analysis	92

3.4.4	Validation of the Axial Loading on the Membrane	95
3.5	Shear Loading on the Membrane Structure	97
3.5.1	Simulation Methodology	97
3.5.2	Simulation Analysis	100
3.5.3	Wrinkling Analysis	102
3.5.4	Validation of the Shear Loading on the Membrane	103
3.6	Discussions & Conclusions	105
4	Smart Adaptive Structures	108
4.1	Literature Review of Adaptive Smart Structures	109
4.2	Introduction	115
4.3	System Design	117
4.3.1	Ground Segment	118
4.3.2	Space Segment	118
4.4	Bio-Inspiration for the Structure	121
4.4.1	Heliotropism and Phototropism	121
4.4.2	The Principal	122
4.4.3	Residual Air Inflation	123
4.4.4	Cell Design	124
4.4.5	Cell Fabrication	126
4.5	Deployment Simulations	128
4.5.1	Smart Adaptive Single Cell Simulation	130
4.5.2	Double Smart Adaptive Cell Simulation	132
4.5.3	Adaptive Smart Cell Array Simulation	135
4.5.4	Multiple Cell Inflation from Packed Environment	137
4.6	Method of Shape Adaption	144
4.7	Potential Applications	146
4.8	Discussions & Conclusions	147
5	Inflated Beam Model	149
5.1	Literature Review of Inflatable Beam Models	150
5.2	Introduction	155
5.3	Deformation of the Inflated Cylinder	157
5.3.1	Simulation Method	158

5.3.2	Simulation Model	159
5.3.3	Simulation Analysis	162
5.4	Post-Inflation for Wrinkling Control	170
5.4.1	Simulation Method	170
5.4.2	Simulation Model	171
5.4.3	Simulation Analysis	172
5.5	Potential Applications	181
5.6	Discussions & Conclusions	182
6	Thesis Conclusions	184
6.1	Research Overview	185
6.2	Research Conclusions	187
6.2.1	Rectangular Membrane Model	187
6.2.2	Smart Adaptive Structure Model	189
6.2.3	Inflated Beam Model	190
6.3	Originality of Research	192
6.4	Relevance of the Abaqus Simulations	193
6.5	Discussion and Outlook	194
A	Appendix One	197
A.1	Axial Loading Input File	197
A.2	Shear Loading Input File	202
B	Appendix Two	207
B.1	Single Smart Cell Abaqus Input File	207
B.2	Double Smart Cell Abaqus Input File	215
B.3	Smart Cell Array Input File within Abaqus	226
C	Appendix Three	246
C.1	Bending and buckling of the inflated cylinder without the Fluid Activation Method	247
C.2	Bending and buckling of the inflated cylinder with the Fluid Activation Method	253
C.3	UMAT Fortran subroutine	264

C.4 Post-inflation of the bent and buckled cylinder with the UMAT subroutine	275
---	-----

Bibliography	293
---------------------	------------

List of Figures

1.1	<i>Simple illustrations of inflatable membranes: (A) Inflatable Wall for the Federation Square in Melbourne, (B) Eco-Friendly Blimp used by the Police in Florida, America, (C) Red Blood Cells within the Arterial Wall, (D) Mars Exploration Rover Protective Airbag, (E) Vehicle Airbag Crash Test, (F) Vehicle Airbag Full Deployment</i>	7
2.1	<i>Geometry Arrangement</i>	15
2.2	<i>Kinematic Body Arrangement</i>	18
2.3	<i>An Example of Wrinkling within a Square Membrane subjected to Tangential Displacement at Opposite Corners [20]</i>	47
2.4	<i>An Example of Wrinkling within a Square Membrane</i>	56
3.1	<i>Flowchart depicting the Abaqus Wrinkling Analysis</i>	74
3.2	<i>Shell Element Name representation within Abaqus</i>	83
3.3	<i>Contour Map depicting the Buckling Strain (critical) for 0.1mm thickness membranes [46]</i>	90
3.4	<i>Buckling analysis of the Kapton membrane under axial loading in five stages</i>	94
3.5	<i>Comparison of eigenvalues with different thickness and aspect ratios for the Abaqus FEA simulation and previously documented results</i>	96
3.6	<i>Wrinkling of the membrane under shear loading</i>	103

3.7	<i>Comparison of eigenvalues with different thickness for the Abaqus FEA simulation solution, S. Kumar solution [36]</i>	105
4.1	<i>Graphical Representation of the SPS-Alpha Structure</i>	117
4.2	<i>Representation of the Space Segment in Operation</i>	117
4.3	<i>Representation of the rigidized solar panel on top and the power transmission system at the bottom</i>	119
4.4	<i>Residual air inflated cell within a vacuum chamber</i>	123
4.5	<i>38 Cell array modelled in Abaqus simulation software</i>	125
4.6	<i>Prototype of the Myler array</i>	127
4.7	<i>Adopted triangular mass inflow for the control volume approach</i>	130
4.8	<i>Simulation of the inflation of a single cell in Abaqus</i>	131
4.9	<i>Abaqus inflation of the multi-smart cell structure to be used as visual comparison with experimental results</i>	135
4.10	<i>A finite element Abaqus comparison of the experimental inflated smart cell array</i>	141
4.11	<i>Inflation of a flat packed array of adaptive membrane</i>	142
4.12	<i>Cell radius monitored during the inflation process from initial to final state</i>	143
4.13	<i>Inflation of a membrane array (blue) from a deployment box (green)</i>	144
4.14	<i>Designed simplified schematic of the multi-body model</i>	146
5.1	<i>A summarized Abaqus model of the inflated cylinder deformation</i>	164
5.2	<i>Graphical representation of the buckling of the membrane model with and without the wrinkling subroutine</i>	165
5.3	<i>Correlation of the elastic modulus of the membrane model versus the beam deflection at a given displacement load</i>	166
5.4	<i>Impact of the membrane material thickness in regards to the beam deflection under the same given load</i>	167

5.5	<i>Depiction of the deflection load versus an altered internal pressure until membrane failure</i>	168
5.6	<i>Comparison of FEM dimensionless load-deflection relationships between current study and previous documented results [75] [80] [83] [91] [92]</i>	169
5.7	<i>Representation of the six phases at 0.05 second increments within the bending and buckling analysis</i>	174
5.8	<i>Representation of the final phases of the bending and buckling analysis while the last frame depicts the start of the post-inflation phase</i>	176
5.9	<i>Illustration of the post-inflation phase of the inflated cylinder subjected to bending and buckling. The final frame also depicts the over compensation of loading</i>	177
5.10	<i>Illustration of the post-inflation phase of the inflated cylinder subjected to bending and buckling. The final frame also depicts the over compensation of loading and the dispersion of the instability forces on the inflated cylinder</i>	178
5.11	<i>Displaying the magnitude of the cylindrical instability within the post-inflation analysis</i>	179
5.12	<i>Depiction of how the beams Young's Modulus effects the rate of post-inflation of the bent and buckled cylinder</i>	180
5.13	<i>Graph showing the correlation with varied membrane thickness against post-inflation pressure and deflection</i>	180
5.14	<i>Image of the CentiFloat being used by the Migrant Offshore Aid Station (image courtesy of the Huffington Post)</i>	182

List of Tables

2.1	<i>Wrinkling criterion to define the different membrane states . . .</i>	50
2.2	<i>Advantages and Disadvantages for Explicit and Implicit Methods</i>	55
3.1	<i>Effect of the Stabilizing Factor on the Post-buckling Analysis solution</i>	87
3.2	<i>Kapton Membrane parameters used within Abaqus</i>	88
3.3	<i>Material properties of the Kapton membrane used for the vali- dation simulation within Abaqus FEA</i>	95
3.4	<i>Effects of Imperfection Magnitudes</i>	101
3.5	<i>Comparison of Eigenvalue and Number of Wrinkles when the pre-stressed of 0.005m is applied to the membrane Kapton ma- terial subjected to shear loading</i>	104
5.1	<i>Membrane properties and geometric dimensions of the Kapton beam membrane</i>	160
6.1	Table representing the highest and lowest eigenvalue (<i>1st mode</i>) percentile differences between the derived Abaqus results and results published by Satish Kumar [36]	188

Acknowledgements

First and foremost I would like to thank my supervisor and advisor of studies, Dr. Yixiang Xu for his contributions. Yixiang has taught me how to manage myself independently. I would also like to thank Prof. Zoe Shipton for her external support, time and effort to make my Ph.D. experience enjoyable and productive. The members of the Advanced Space Concepts Laboratory and fellow colleagues at the Department of Civil & Environmental Engineering have also contributed to my personal and professional time at Strathclyde. They have been a good source of friendship, collaboration and consultation. From the stresses of understanding three different programming languages to installing each program to run effortlessly, without them, this Ph.D. would not have been completed. Due to the freedom received from Dr Yixiang, I have been able to successfully submit my Ph.D. thesis and complete a difficult Pg. Dip. in Geospatial and Mapping Sciences alongside my Ph.D. study to implement my ideas within the real world.

I am very thankful to my brother from another mother and, my friend for over 18 years, John Paterson, who represents the finer things in life. He has shown me what success can achieve and how to grasp the opportunity to achieve it. My best friend, Alasdair Taylor, who has been a constant push for me to stay stern with my Ph.D. study during times of hardship and moments of weakness. Eddy Hull for his presence and moral support. They have been able to show

different perspectives in complex problems which were the primary resultant in deriving simplistic solutions.

I gratefully acknowledge the funding source that made my Ph.D. possible. This Ph.D. in its entirety was funded by EPSRC *Engineering and Physical Sciences Research Council* for my first three and a half years. I was honoured to achieve the Faculty Excellence Award and the respected positions as an Assistant Lecturer with the Department of Civil & Environmental Engineering and Student Mentor with the Disability Services to help with my final year finances.

Lastly, I would like to thank my family for all their love, support and encouragement. For my parents, Gurdeep Singh Puri and Manjeet Kaur Puri, who let me choose my own path in my academic journey and supported me with all my pursuits. For the presence of my sisters, Amanpreet Puri and Puneet Puri at home. And most of all my loving, supportive, encouraging, and patient wife, Kirandeep Minas, whose faithful determination and support during the final phases of this Ph.D. is forever appreciated. Thank you all.

Manpreet Singh Puri
Doctorate Researcher
University of Strathclyde
March 2016

Acronyms

Acronym	Definition
FEA	Finite Element Analysis
FEM	Finite Element Method
IMP	Iterative Material Properties
VUMAT	User Defined Material Model
ODE	Ordinary Differential Equation
CAD	Computer Aided Design
NIAC	NASA's Innovative Advance Concepts
ESA	European Space Association
NASA	National Aeronautics and Space Administration
JAXA	Japan Aerospace Exploration Agency
PET	Polyethylene Terephthalate
REXUS	Rocket Experiments for University Students
DLR	German Aerospace Centre
SNSB	Swedish National Space Board
ULDB	Ultra Long Duration Balloon
LDB	Long Duration Balloon
S\$R\$	Small Strain Shell Elements
M\$R\$	Small Strain Membrane Elements

Preface

A description in clarity for the complete framework for the numerical formulation, implementation algorithms to deduce a finite element simulation solution within this thesis is given. As the subsequent models analysed our quite varied in their structural configuration, it is not possible to adopt the same formulation to analyse each model. A clean straightforward layout approach has been used, with this chapter dedicated to the motivation for this study to define the significant chapters taken into review during the numerical formulation and analysis process of the membrane structures. Then, successive chapters will characterize the problem at hand alongside the undetermined issues that have to be taken into consideration. A detailed overview outline will be presented at the end of this chapter for relevance. It should be noted that for the sake of brevity, only a broad overview is stated herewith. Comprehensive examinations and literature reviews are deferred to the relevant sections within the subsequent chapters.

Research Objectives and Overview

The objectives of this research are listed below:

1. This research study will be investigating new innovative wrinkling models for membrane materials, taking into account the model competency, accuracy, simulation expenditure and the rate of convergence. These derived wrinkling models should be able to be applied to a wide range of material models.
2. The second concern in this research is to take into account the effects of the pressure acting on the membrane surface in an analytical manner. This matter leads to additional stiffness terms within the constitutive equations caused either by the variation of the membrane surface normals, altering cavity pressure or the deformation of the membrane. This research focuses on a variety of membrane models; ranging from the displacement of rectangular membrane model to fully enclosed cavity membrane models filled with gas or fluid.
3. The third interest is to assimilate the user-defined material (VUMAT) subroutine into the membrane model. This subroutine will define the material dynamics and contact issues for inflatable membranes undergoing large deformation. The expected conclusion is an accurate, reliable and stable formula which depicts the benefits of the VUMAT subroutine integration. This derived formula appears to be much more realistic compared to conventional treatment of membrane material and contact problems.
4. The final goal will be to combine all the algorithms and methods mentioned above into one unique tool which is able to solve all these phenomena simultaneously.

Summary

This thesis gives the conceptualization of inflation of inflatable membrane space structures. Although there has been little study using software simulation and the majority of documented research is based on theoretical numerical calculations. This research advanced the prior understanding of wrinkling within inflated membranes by using complex structures subjected to deformation loads.

Within this thesis, a computational framework for the numerical analysis of the interaction between acting forces on the membrane and the membrane structure dynamics is presented. Moreover, in the case with thin membrane deformations, the synergy between the membrane wrinkling and structural forces has to be examined. This membrane structure-anatomical forces correlation results in a dynamic wrinkling problem, which can only be modelled easily and effectively by a simulation software that can integrate each assumption and attribute within the analysis.

In the structural simulation within Abaqus FEA software, key consideration has to be given in modelling the geometric non-linearity behaviour of the membrane. By using the existing continuum expression for the virtual internal work in curvilinear coordinates. This is used to derive the modified fundamental formulation in which all subsequent analysis is established on and the initial equilibrium shape of the membrane.

A critical feature of the new formulation is the prospect of adding pre-stressed forces to the membrane structure. The approach developed, established on an alteration of the material stiffness matrix to integrate the effects of wrinkling and deformation, can be utilized to calculate the behaviour of the membrane within a finite element simulation. In the wrinkling model, the state of the membrane element (*taut, wrinkled or slack*) is characterized by a mixed wrinkling criterion. Once it has been identified that the membrane element is wrinkled, an iterative scheme looks for the wrinkled orientation angle and the precise stress distribution, including only uni-axial tension in the wrinkle direction, is then derived.

The wrinkling model has been verified and validated by contrasting the simulated conclusions with documented results for the instance of a time-independent isotropic membrane subjected to shear and axial loading. Utilizing the time-integration method, a time-dependant pseudo-elastic stiffness matrix was represented and therefore, rather than calculating the convolution integral all through the Abaqus simulation, then we can calculate the behaviour of a membrane structure by superposition of a series of step by step increments in basic finite element software.

The theoretical computations from the Abaqus/Explicit analysis were compared with documented results for the shear and axial loading. The results agreed very well, assuming friction and any relativistic dynamic effects were excluded. The discrepancy between the shear loading solution is 7% while the discrepancy between the axial loading is only 5% between the Abaqus model and the documented model. This discrepancy could be the resultant of the source of energy dissipation from the visco-elastic behaviour during the loading and unloading of forces. It can be stated that for the Kapton HN membrane, this result falls within acceptable range but to increase accuracy, the load and

unloading will be carried out on a set steady amplitude to inhibit in shock effects within the model.

A three-dimensional finite element model which integrates wrinkling and frictionless contact has been developed to simulate the adaptive smart cell and cylindrical membrane structure. The loading of both structures is given by a non-uniform differential inflation pressure with a continual gradient adjacent to height. The resultant solutions are computed using Abaqus/Explicit software, with an integrated user-defined material subroutine to account for elastic wrinkling deformation that administers a combined stress-strain criterion. Frictionless contact within the membrane structure is prescribed for both complex structures (*Adaptive Smart Structures Model and Inflatable Beam Model*) in order to prohibit the penetration of the membrane structure through itself.

Both the complex inflatable membrane wrinkling models accomplish the purpose of exceptional subgrid scale performance in relation to accuracy, competency, computing hardware & software expense, complexity and the model convergence rate. The numerical algorithm is created in general context and is flexible for a large variety of material models. For a closed membrane structure, the skew symmetric constraint parameters vanish, while the existing symmetric domain variables mirror preservation of the system. This procedure does not demand the discretization of the fluid (gas) domain or the link between coupling of fluid (gas) and membrane. As a result of this basic fact, the computation is drastically simplified.

The adaptive structures model introduces a novel approach in harnessing solar power for reuse on the ground as a stable source of power. The simulations were based on the space part of the stiff structure created of hexagonal membrane cells. Simulations are carried out in Abaqus Finite Element Analysis software for simplicity & a comparison for validation purposes is tested against an

experimental inflatable cell within a vacuum chamber. It was showcased that the final configuration could be achieved regardless of the packaging shape of the inflatable cell array.

The inflatable beam model is comprised of two sections, the bending & buckling of the inflated beam and the post-inflation of the bent and buckled beam. Abaqus software was used to simulate the inflatable beam during each configuration utilizing the integration of a modified VUMAT subroutine. A comparison is showcased representing the importance of the integration of the VUMAT subroutine within our Abaqus model.

Chapter 1

Introduction

This thesis explores the detailed stress distribution in the membrane skin of an inflatable structure. By using numerical models based on the finite element method (FEM) alongside solution algorithms of structural and material performance to derive a detailed understanding for the inflatable structure behaviour. We will address three key non-linearities within the derived result to achieve an accurate solution: a user-defined material model subroutine to attain an efficient wrinkling model, additional stiffness terms to accurately define the pressure loads acting upon the material membrane surface and finally deduced discretized non-linear formulation to take into account the frictionless contact problems in case of infinitesimal deformations for inflatable membranes with regards to material dynamics, potency, efficiency and rate of convergence. This derived solution will be incorporated within an Abaqus simulation to model the relative inflated Kapton membrane structures. In this chapter, we will look into the background of inflatable membrane structures and the underlying motivation for this Doctorate research.

1.1 Background

The foundations of membrane design can be traced back to the Ice Age, approximately 40,000 years ago, where the findings have concluded simplistic shelters created and constructed of animal hide. This implies that this is the first human construction to be uncovered, where simplistic textiles were used for spatial division and shelters [1]. This simplistic method evolved into one of the dominant classes of fabric structural design, the freely woven black tent. The black tent concept spread quickly through the Arab conquests in the eighth century. The lightweight and portability characteristics of the membrane structure inevitably brought about great military interest. During the first century BC, Roman Legions used an abundance of leather tents from military use to recreational banquets. Moving through the fabric of time, during the 12th century, exquisite and extravagant tent structures became a fashion accessory in Western Europe for the prestige and elite members of society. These structures became increasingly larger and glamorous by the turn of the sixteenth century and matured into symbolic icons for wealth and fortune [2].

The first circus tent, a large linen structure was hoisted upright in 1770 at Westminster Bridge, UK. In essence, this paved the first steps to widespread commercialisation of fabric structures and by 1887, the first American Railway circus had begun its national excursions. In August 1783, the next evolution of membrane structures was initiated with the Montgolfier Brothers attempting the first mass advertised unmanned public launch of a large-scale hot-air balloon [3]. This was the foundation stone that allowed mankind to reach space in less than 200 years from this date. Even in this day in age we can use rockets and aeroplanes to carry out research, balloons still play an integral role as they require no energy to keep aloft.

After the Montgolfier brothers demonstration, a French scientist named Jacques Charles developed the first manned hydrogen filled balloon. Jacques Charles and his co-pilot Nicolas Louis Robert reached an altitude of approximately 1800 feet in December 1783. Their invention of hydrogen propulsion for engine throttle led to this class of balloon being named Charliere (as opposed to a Mongolfiere which used hot air) [4]. It was evident from the manned flight that the hydrogen balloon design was much superior to the hot air balloon design. During this era, hot air balloons were made from paper and could only be safely used for one flight while hydrogen balloons could be used more than once and had a higher lifting capacity. In order to have a successful launch mission, Jacques Charles based his hydrogen balloon on two different designs. The first was a hydrogen balloon with a super pressure design with an enclosed envelope. This prevailed to an increase in differential pressures while ascending and the envelope would eventually burst. In order to overcome this anatomical deterioration, the succeeding design had an aperture at the base of the balloon; therefore, the preceding stresses formed at the balloon envelope were acute in magnitude. This design was also more or less independent of the altitude the balloon reached. This design is still used in modern day balloons and is known as zero-super pressure designs.

In the nineteenth century, the majority of the manned scientific balloon flights investigated the properties of the atmosphere. In the 1890s, these manned missions however evolved once the balloon sondes became readily accessible, allowing unmanned missions to carry out the desired research. The balloon borne-sounding system (SONDE) gives sedentary evaluations (*vertical profiles*) including atmospheric wind speed, direction and its thermodynamic state [5]. Even though scientists were able to carry out ground breaking research, one main problem was that the balloon drifted considerably away from the launch point. This was very time consuming and, costly as there was no way to locate

the balloon once it drifted back to Earth or if it reached an altitude not visible clearly from the ground. This drifting dilemma was nonetheless resolved by Richard ABmann in 1892, who introduced super-pressure balloons that ruptured when they ascended a given altitude and descended back to the ground using a variety of different parachutes to ease the fall [3]. Another breakthrough was achieved by a Russian scientist called Pavel Molchanov in 1930. The super-pressure balloons were equipped with radio transmitters making it possible to attain accurate actual time information of the atmosphere [6].

Similar instruments are used in modern day research throughout the Globe for gathering information which is essential to accurately forecast the weather conditions and, secondly to initialise arithmetical calculations. In order to further our understanding of the solar system, manned balloons are utilized as a scientific podium in the early nineteenth century to study the intrinsic influences of the Sun and cosmic rays outside the intrusion of atmospheric instabilities. Nevertheless, the growing altitudes of balloon flights showcased a severe complication. Once an organic life form reaches above 12 km, the deficiency in air pressure leads to relative gases bubbling out of the blood. Therefore balloon structures are not equipped with the necessary pressure vessel and often prove lethal and the cause of an excruciating and painful death [3]. A number of test flights were taken by the US Army Air Corps in 1929 to an altitude of above 13 km. These flights were made to test clothing, oxygen systems and various scientific systems. But all were in vain as there wasn't a successful mission that allowed a manned craft to safely land back on ground after reaching this altitude. This prompted the American Space programme to carry out detailed investigation of spacesuits. This major problem was overcome in the 1930 by a Swiss physicist Auguste Piccard by developing a pressurized, spherical gondola for two men with an approximate diameter of two metres [4]. This gondola contained a scientific instrument that prevented

carbon dioxide from building up and also had a supply of bottled oxygen. Other small but crucial changes were also implemented by Auguste Piccard in his design. These utilize an envelope which is bigger by a magnitude of five when compared with the gas volume required to achieve ascension from the ground. Earlier envelopes were entirely inflated on the Earth and, most of the gas was lost due to considerable expansion during the ascent [7]. By using this change in design, there was minuscule gas lost during ascension and attained sufficient lift amid the night to arrive safely to the ground. Although with these radical envelope changes, this was not an optimal shape for the balloon design. Antecedently to the commencement of World War Two, supported by the National Geographic Society, U.S. Army Air Corps Captain Albert W. Stevens in 1933 made the first helium balloon flight. Albert W. Stevens along with Captain Orvil Anderson used a $10,000m^3$ balloon [8].

Helium replenished hydrogen balloons comprehensively during the subsequent decade established on safe usage as hydrogen gas was very flammable. During this time, it was obvious that the giant and weighty balloon envelopes, comprised of rubberised fabrics had arrived at their operational capacity. After World War Two ended, scientists had to come to a new design concept in regards to the structural material used. During this era, post World War Two, polyethylene had become widely attainable, which led to new design concepts for future balloons.

In the 1950s, large plastic-strato balloons constructed by Otto Winzen, were used in scientific unmanned and manned research projects to reach extreme heights into the stratosphere [9]. This was achieved by constructing innate-assembled zero super-pressure balloons from n-identical flat polyethylene gores by wielding adjacent lobes collectively and incorporating a stiff tendon along the joining boundary. Hence, the load tapes carry the differential pressure

with acute membrane stresses; so in essence, it is conceivable to carry bigger payloads to self-weight proportion. The longitudinal tendons also aid a focal connection point for cargo resulting in no extra consideration [10]. These balloons were a new era of super-pressure balloon design commenced in the 1960s. These balloons have been the scientific podium for a large selection of experiments.

The next stage of evolution was reached at the start of the twenty-first century. Inflatable structures have now evolved from these spherical enclosed habitats to complex structures engineered for specific mission parameters. A number of space missions have proposed and successfully delivered inflatable space structures for lightweight radars, space antennas, optical communications systems and telescopes, amongst other viable potential structures. These structures range from free deployment to semi- and controlled deployment to achieve mission requirements. The first fully inflatable antenna experiment was launched in 1996 and marked the first fully inflated space structure using free deployment from its host satellite. These experiments led to major scientific innovations and discoveries that changed the modern day of life.

1.2 Motivation

Inflatable space structures are being used in these missions, such that the negative impact, not only on human health but also on other animal and plant life, can be reduced drastically. Inflatable space structures are needed in a number of space fields from solar sails and potential inflatable rovers to the next generation of habitat modules for extra-terrestrial exploration. For these structures to be efficient and effective, the membrane surface has to be wrinkle free, the support booms have to be strong and rigid to support any and all external

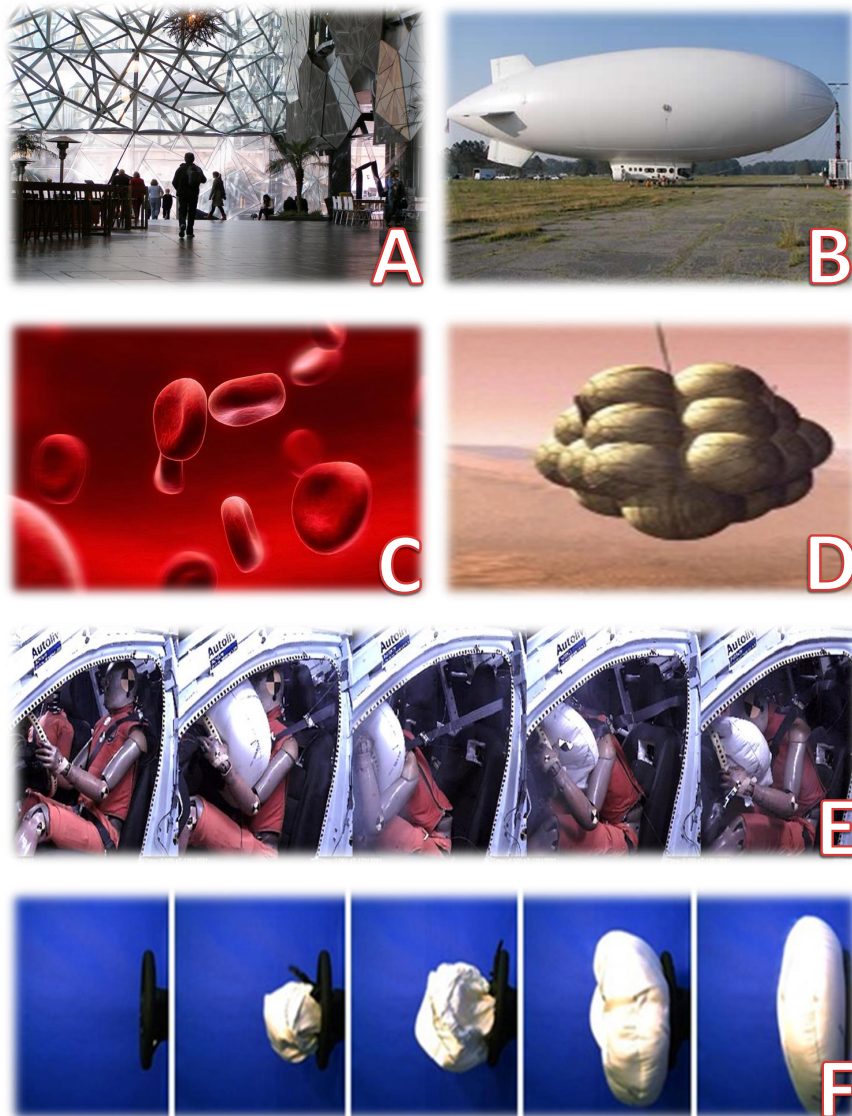


Figure 1.1: *Simple illustrations of inflatable membranes: (A) Inflatable Wall for the Federation Square in Melbourne, (B) Eco-Friendly Blimp used by the Police in Florida, America, (C) Red Blood Cells within the Arterial Wall, (D) Mars Exploration Rover Protective Airbag, (E) Vehicle Airbag Crash Test, (F) Vehicle Airbag Full Deployment*

loads while the structure has to reach a stable deployment configuration. The structure also has to be able to survive in a host environment different from Earth and deployment storage.

Albert Einstein once said, "Pretty good scientists can explain complex things in complex terms but excellent scientists can explain complex things in simplistic terms". In order to understand the complex problems presented within this thesis, we will divulge into a number of illustrations to act as simplified analogous.

In figure 1.1A, we can see a large-scale inflatable membrane structure, acting as a building wall and in figure 1.1B, we can notice an eco-friendly blimp composed from thin membrane fabric. This blimp can achieve flight due to the air pressure interactions from inside the membrane material and the outside atmosphere. This exchange in gases is inspired from continuum mechanics, notably, Archimedes Principle and has led to breakthroughs in air and marine technology. Collisions of red blood cells flowing through the blood plasma can be seen in figure 1.1C. Each cell is an membrane enclosed fluid cavity interacting with the fluid plasma and the impact interactions with other blood cells and the arterial wall. The Mars Exploration Rover used a protective cushion for impact control against the Mars surface. This protective cushion was formed from twenty-four inflated membrane lobes which when fully deployed look like a massive bunch of white grapes with the rover cradled inside and is visible in figure 1.1D. In figure 1.1E, we can observe the impact assessment for the collision of a driver against the deployed airbag. The airbag here is pressurized with a multiple mixture of gases and then undergoes large deformation upon contact with the driver. One can examine the propagating wrinkles through the airbag membrane surface area, where the compressive stresses are induced at the point of contact. The airbag deployment can also be seen in figure

1.1F, showcasing the deployment process achieving full equilibrium with the outside atmosphere. It is apparent that non-linearities arise between the actions and responses of an inflatable membrane undergoing large deformations. In this thesis, we will analyse three issues of these non-linearities: wrinkling of the membrane surfaces, the depiction of displacement loads acting on the membrane surfaces and the contact interactions of these membrane surfaces.

Membrane wrinkling is a local phenomenon, generally based on the elastic shell theory and is caused by the lack of resistance against compressive stresses. A membrane is usually assumed to have no bending stiffness, therefore, negating the existence of any compressive stresses, i.e. the formation of immediate wrinkling. A purely tensile stress state is said to be free from wrinkles when subjected on a membrane surface but, on occasion wrinkles can occur because of the in-plane loads acting in the structure.

Wrinkling can generically be categorised in two types, namely structural and material wrinkling. Material wrinkling is a permanent deformation and, can cause surface creases on the membrane surface. Material wrinkling results from manufacturing flaws and/or packaging imperfections caused by high localised strains. Structural wrinkling is a temporary deformation by reason of localised buckling of the membrane when undergoing compressive stress. The wrinkle characteristics (i.e. size, direction and wavelength) varies depending on the load paths and boundary conditions with the membrane structure. One of the key areas focussed on this thesis will be to research effective ways to eradicate structural wrinkles through design and analysis of the membrane structures.

The second key interest area is the investigation of dependant forces acting on the membrane structure. If the inflated membrane structure is modelled as an enclosed cavity, the acting loads can be affected by the interaction between the internal fluid and/or gas with the surrounding membrane. This interac-

tion is commonly a dynamic process and can potentially decrease the structural responses of the enclosed membrane to the applied action. The influences of the inertial forces will be assumed to be negligible due to the dynamic deformation process occurring at a relatively slow pace. With this presumption in mind, we can concur that there will be no inertial forces transmitted between the cavity membrane surface and the enclosed cavity fluid/gas.

The final subject of concern is the contact interactions of the inflatable membrane. The main problem in regards to the contact interaction would be to find an uncertain unknown contact area at any particular point of the simulation while penetration between the bodies and surfaces of the model are restricted. From which we can calculate the membrane contact pressure over the resulting contact area which can alter drastically depending on the connection between the constraints and the conforming contact pressure. This connection is very problematic in regards to the geometrical and material nonlinearities. In present day technology, numerical problem solving covering large deformation continuum mechanics, non-linear equations and constitutive response techniques are satisfactory but the material dynamics of the membrane have not been investigated thoroughly. By incorporating a user-defined material subroutine (VUMAT) to the model to characterize the material dynamics has shown great promise and has successfully depicted the material behaviour much more accurately. We will analyse this VUMAT against conventional finite element models and well documented theories, taking into account the membrane material dynamics at each incremental step within the model simulation.

1.3 Organisation of this Thesis

The introductory Chapter 1 presents the background and motivation for this work and a brief understanding of the key areas of interest within this thesis research. Due to the complexity of the membrane wrinkling problem and anisotropic deformation, a list of relevant publications describing the background, theoretical understanding and practical implementation is provided in the respective chapters.

The background of the evolution of membrane structures is presented, describing the importance of this thesis study and the potential applications of how this can be used in potential applications for the benefits of science.

Chapter 2 is where the main characteristics and attributes of membrane structures are discussed. These are the fundamental theories at which our methods and numerical simulations with the Finite Element Method are based. These models incorporate the non-linear continuum mechanics, mechanics of membrane structures and time integration methods. The culmination of all these attributes are utilized to setup a numerical model to act as the foundation, for all membrane structures used within this PhD research.

In Chapter 3, important components of membrane wrinkling are presented. The definition of each component is given alongside the relevance to our model is presented. Two model approaches, axial and shear loading, are used to analyze the theoretical assumptions and accuracy of our foundation model. These models have been documented numerous times and comparisons are made with the simulation results derived against documented results.

Chapter 4 investigates a novel green approach in harnessing solar energy to be used as a fuel source on the ground usage. The detailed bio-inspired concept is

presented of a smart membrane material which has the capability of changing size and shape to meet mission requirements.

In Chapter 5, a detailed study is given of an inflatable boom which is necessary for over 90% of inflatable space structures to act as a load bearing support. The chapter is divided into two parts, the bending and buckling of the inflatable beam and the post-inflation of the beam to restore it to its approximate initial configuration after deformation.

Finally, Chapter 6 gives a summary and discussion of the methods developed and the results obtained within this research. The thesis concludes with a discussion, how and to what extent, the simulation models and results can be used for the design and analysis of inflatable membrane structures.

Chapter 2

Background Theory

In this chapter, we will review the notational, conceptual and computational theoretical background of the relevant problems investigated within this Doctoral Research. Therefore, we will not be going into stringent depth of the theory but to provide a platform to define the global equations into which the subsequent chapters are incorporated. In case of interest, the reader can consult [11], [12], [13], and [14] for a comprehensive guide.

2.1 Non-Linear Continuum Mechanics

Continuum mechanics is defined as the study of the kinematic and mechanical behaviour of materials shaped on the continuum supposition. Continuum mechanics can be divided into two key themes; namely fundamental and constitutive equations. In the first theme, attention is given to the derivation of the fundamental equations which hold for all continuous media. These derived fundamental equations are established upon universal laws of physics, such as

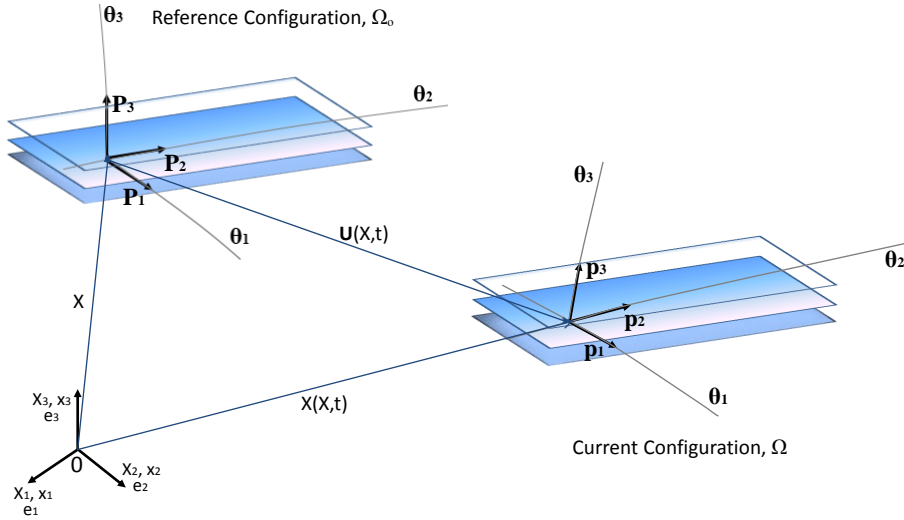
principle of energy and momentum, conservation of mass etc. In the subsequent theme, primary consideration is on the construction of the constitutive equations portraying the behaviour of specific rhapsodised materials. These equations define the vital points about which research in elasticity, plasticity, visco-elasticity and fluid mechanics proceed.

Non-linear and linear continuum mechanics act on similar topics such as kinematics, stress and constitutive behaviour. But there is a key difference between the two. In linear continuum mechanics, the assumption is stated that the deformation is relatively small to have any significant change in the geometrical arrangement of the solid, whereas in non-linear continuum mechanics, there is no constraint on the deformation magnitude. As we are only dealing with large deformations of membrane materials within this research, focus will solely be given to non-linear continuum mechanics.

2.1.1 Geometry Arrangement

Within this section, a generic arrangement geometry used within continuum mechanics of the interested problems within this research are presented. The characterization of differential geometry and kinematics utilise the quintessential tensor analysis that illustrates the operations taking place in three dimensional Euclidean space \mathbb{R} (as long as space and time is decoupled).

Spatial surfaces in \mathbb{R} are usually defined by either a Cartesian coordinate system x_i that is connected via orthonormal vectors $e_i = e^i$ or a curvilinear coordinate system θ^i . It should be noted that each material point P on the surface is designated by two autonomous surface coordinates or surface parameters θ^1 and θ^2 . In essence, the designated lines, i.e. coordinate lines, lines of constant surface coordinates, are curved lines in space. The position vector \mathbf{r}

Figure 2.1: *Geometry Arrangement*

of a material point P on the surface can be described in the notation:

$$\mathbf{r} = \mathbf{r}(\theta^1, \theta^2) \quad (2.1)$$

where θ^1 and θ^2 represent a specific location on the surface.

Using a similar notation arrangement, a position vector in a three dimensional body is defined as $\mathbf{x}(\theta^1, \theta^2, \theta^3)$, where θ^3 is the thickness-direction parameter needed to define the three dimensional body illustrated in figure 2.1. The body under examination is comprised of the aforesaid surface, its mid-surface, as a subset in the form

$$\mathbf{x}(\theta^1, \theta^2, 0) = \mathbf{x}|_{\theta^3=0} = \mathbf{r}(\theta^1, \theta^2), \quad \theta^3 \in \left[-\frac{t(\theta^1, \theta^2)}{2}, \frac{t(\theta^1, \theta^2)}{2}\right], \quad (2.2)$$

where $t(\theta^1, \theta^2)$ is the shell thickness. On the mid-surface, we can represent the *covariant base vectors* \mathbf{g}_1 and \mathbf{g}_2 by differentiation of the reciprocal position vectors \mathbf{x} with reference to the convective coordinate in either case.

$$\mathbf{g}_1 = \frac{\partial \mathbf{x}}{\partial \theta^1}; \quad \mathbf{g}_2 = \frac{\partial \mathbf{x}}{\partial \theta^2} \quad \Rightarrow \quad \mathbf{g}_i = \mathbf{x}_{,i}. \quad (2.3)$$

The covariant base vectors are tangential to the relevant surface coordinate lines, for example, \mathbf{g}_1 is tangential to the coordinate line θ^1 where an alternative coordinate θ^2 is constant. Covariant base vectors are generally not orthogonal or of unit length. The *surface normal vector* \mathbf{g}_3 is determined as,

$$\mathbf{g}_3 = \frac{\mathbf{g}_1 \times \mathbf{g}_2}{\|\mathbf{g}_1 \times \mathbf{g}_2\|}; \quad |\mathbf{g}_3| = 1. \quad (2.4)$$

Their scalar products g_{ij} , the factors of the covariant metric tensor \mathbf{I} (identity tensor) which mirrors the metric of the surface, i.e. the magnitude of the covariant base vectors and the angle amidst them, can be conveyed both in the co- and contra-variant basis in the form:

$$\begin{aligned} \mathbf{I} &= g_{ij} \cdot \mathbf{g}^i \otimes \mathbf{g}^j = g^{ij} \cdot \mathbf{g}_i \otimes \mathbf{g}_j = \mathbf{g}^i \otimes \mathbf{g}_i = \mathbf{g}_i \otimes \mathbf{g}^i; \\ &g_{ij} = \mathbf{g}_i \cdot \mathbf{g}_j \text{ and } g^{ij} = \mathbf{g}^i \cdot \mathbf{g}^j \end{aligned} \quad (2.5)$$

where \otimes represents the tensor product. The contra-variant tensor is regarded as the reversal of the co-variant metric tensor:

$$g^{ij} = (g_{ij})^{-1} \quad (2.6)$$

As a dual pair of the co-variant basis, the contra-variant basis \mathbf{g}^i are formalised by,

$$\mathbf{g}^i \cdot \mathbf{g}_j = \delta_j^i = \begin{cases} 1 & i = j, \\ 0 & \text{otherwise,} \end{cases} \quad (2.7)$$

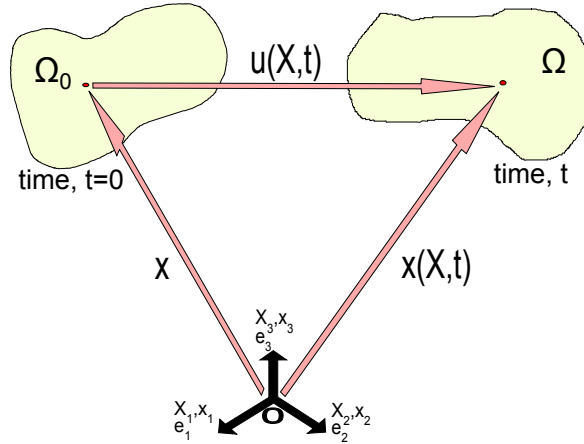
where δ_j^i symbolizes the *Kronecker delta*. It should be noted that Equation 2.7 advises the contra-variant basis \mathbf{g}^i is the dual basis of the covariant basis \mathbf{g}_j , on the presumption that both of them are orthogonal to each other. It can be stated that \mathbf{g}_3 is orthogonal to both \mathbf{g}^i and \mathbf{g}_j , hence, it can be said that $\mathbf{g}^3 = \mathbf{g}_3$ and $\|\mathbf{g}^3\| = 1$. Another way to describe the contra-variant basis is by partially deriving the relative convective coordinate with respect to the position vector \mathbf{x} , particularly,

$$\mathbf{g}_1 = \frac{\partial \theta^1}{\partial \mathbf{x}}; \quad \mathbf{g}_2 = \frac{\partial \theta^2}{\partial \mathbf{x}} \quad \Rightarrow \quad \mathbf{g}^i = \frac{\partial \theta^i}{\partial \mathbf{x}} \quad (2.8)$$

By incorporating the use of metric tensors, the co- and contra-variant components and base vectors are remodelled into:

$$A_i = g_{ij} \cdot A^j; \quad B^i = g^{ij} \cdot B_j; \quad \mathbf{g}_i = g_{ij} \cdot \mathbf{g}^j; \quad \mathbf{g}^i = g^{ij} \cdot \mathbf{g}_j. \quad (2.9)$$

The differential surface of area da is described by the vector parallelogram that can be postulated by the co-variant base vector \mathbf{g}_1 and \mathbf{g}_2 . An infinitesimal area content da is conferred by the total area a in regards to the surface coordinates by

Figure 2.2: *Kinematic Body Arrangement*

$$\begin{aligned}
 da &= \|\mathbf{g}_1 \times \mathbf{g}_2\| d\theta^1 d\theta^2 = j d\theta^1 d\theta^2 \\
 \Rightarrow a &= \int_{\theta^1} \int_{\theta^2} j d\theta^1 d\theta^2 = \int_{\theta^1} \int_{\theta^2} \|\mathbf{g}_1 \times \mathbf{g}_2\| d\theta^1 d\theta^2.
 \end{aligned} \tag{2.10}$$

2.1.2 Kinematics

Kinematics is the analysis of movement and distortion of continua disregarding the forces liable for the corresponding action. The precise definition is a necessity to accurately represent the motion of continua.

A deformable body \mathcal{B} can be described as the constituents of an array of material points residing in the domain of Euclidean space \mathbb{R}^3 (where the 3 represents three-dimensional Euclidean space). This relative body is in the primary mode of being at time, $t = 0$ as illustrated in figure 2.2. It should be noted that this body is bounded by the boundary defined by $d\mathcal{B}$. In this state, the body has a domain, Ω_0 occupying a region in Euclidean space, \mathbb{R}^3 , named the initial arrangement. To characterize the kinematics of this body, we need to define a secondary arrangement where mathematical solutions are designated to, and

we call this the reference/secondary arrangement. For simplicity, we assume the initial arrangement coincides with the reference arrangement, unless specified otherwise. As the body \mathcal{B} translates in space from one instance to another, it populates a sequence of regions named Ω_t for any subsequent time $t > 0$. During this period, the arrangement and state of the body is named the current arrangement or deformed arrangement. The stated dimension of any model is designated η_{dim} and represents the bodies associated sum of space ranges. Boundary of the domain in question is denoted by Γ_n , where n is the domain number.

Within the reference arrangement, a material point's positional vector can be stated as \bar{x} , where

$$\bar{x} = \mathbf{X}_i \mathbf{e}_i = \sum_{i=1}^{\eta_{dim}} \mathbf{X}_i \mathbf{e}_i \quad (2.11)$$

In the reference arrangement, \bar{x} is a constituent of \mathbf{X}_i and \mathbf{e}_i are the unit base vectors for a rectangular Cartesian coordinate system. The changeable vectors \bar{x} are termed material coordinates or Lagrangian coordinates. The movement of this body \mathcal{B} is stated as

$$\mathbf{x} = \Phi(\bar{x}, t) = \mathbf{x}(\bar{x}, t) \quad (2.12)$$

where

$$\mathbf{x} = x_i \mathbf{e}_i = \sum_{i=1}^{\eta_{dim}} x_i \mathbf{e}_i \quad (2.13)$$

is the positional location of the material point \bar{x} in the current arrangement.

The variable vectors \mathbf{x} are termed spatial coordinates or Euclidean coordinates, and the stated function $\Phi(\bar{x}, t)$ is needed to align and map the reference arrangement against the current arrangement.

The discrepancy for a material point from its current arrangement to its reference arrangement yields the displacement that can be stated (in material characterization) as

$$\mathbf{u}(\bar{x}, t) = x - \bar{x} \quad (2.14)$$

Incorporating the Equation 2.11 and Equation 2.12 into Equation 2.14 gives

$$\mathbf{u}(\bar{x}, t) = \Phi(\bar{x}, t) - \Phi(\bar{x}, 0) = \Phi(\bar{x}, t) - \bar{x} \quad (2.15)$$

We achieve this, by reason of taking $t = 0, x = \Phi(\bar{x}, 0) = \bar{x}$ and that implies $x = \bar{x}$. Utilizing (x, t) as the autonomous variables, the inverse mapping of the movement is characterized as

$$\bar{x} = \Phi^{-1}(x, t) = \bar{x}(x, t) \quad (2.16)$$

This implies that the material point \bar{x} is related with both the location x and the time t . The velocity is described as the derivative of the position vector, for a given material point. Assuming \bar{x} is taken to be a consistent value, then the derivative is described as the material time derivative. Utilising Equation 2.12 and Equation 2.15, the material velocity can be stated as

$$\mathbf{v}(\bar{x}, t) = \frac{\partial \mathbf{x}(\bar{x}, t)}{\partial t} = \frac{\partial \mathbf{u}(\bar{x}, t)}{\partial t} = \dot{\mathbf{u}}(\bar{x}, t) \quad (2.17)$$

As stated in general physics, the material acceleration can be calculated by the derivation of the material time velocity derivative and is expressed as

$$\mathbf{a}(\bar{x}, t) = \frac{\partial \mathbf{v}(\bar{x}, t)}{\partial t} = \dot{v}(\bar{x}, t) = \ddot{u}(\bar{x}, t) \quad (2.18)$$

For interpretations given in spatial description, i.e. the velocity $\mathbf{v}(\mathbf{x}, t) = \mathbf{v}(\mathbf{x}(\bar{x}, t), t)$. Assimilating this with Equation 2.12, we can determine the material time derivative by

$$\frac{Dv_i(\mathbf{x}, t)}{Dt} = \frac{\partial \mathbf{v}(\mathbf{x}, t)}{\partial t} + \frac{\partial \mathbf{v}(\mathbf{x}, t)}{\partial x_j} \cdot \frac{\partial x_j(\bar{x}, t)}{\partial t} = \frac{\partial v_i}{\partial t} + \frac{\partial v_i}{\partial x_j} v_j \quad (2.19)$$

where $\frac{\partial x_j(\bar{x}, t)}{\partial t}$ is the spatial time derivative and $\frac{\partial v_i}{\partial x_j}$ is the right gradient of the velocity vector field in regards to the spatial coordinates. This variable can be expressed as $v_{i,j}$ in its indicial form or $\nabla \mathbf{v}$ in its tensor representation.

Employing Equation 2.16 to present the velocity in spatial description, we can rewrite Equation 2.19 as,

$$\frac{D\mathbf{v}(\mathbf{x}, t)}{Dt} = \frac{\partial \mathbf{v}(\mathbf{x}, t)}{\partial t} + \mathbf{v}(\mathbf{x}, t) \cdot \nabla \mathbf{v}(\mathbf{x}, t) \quad (2.20)$$

where $\nabla \mathbf{v}$ is the left gradient of the velocity vector field in relation to the spatial coordinates, which can be stated as $\partial_j v_i$ in its indicial form.

Hence, one can come to the critical conclusion that

$$\frac{D\mathbf{v}(\mathbf{x}, t)}{Dt} = \frac{\partial \mathbf{v}(\bar{x}, t)}{\partial t} \quad (2.21)$$

Generically, we can acquire the material time derivative for any given function, vector or tensor in regards to its spatial variables \mathbf{x} and time t via

$$\frac{D(\bullet)}{Dt} = \frac{\partial(\bullet)}{\partial t} + \mathbf{v} \cdot \nabla \bullet \quad (2.22)$$

As the body translates from the reference arrangement Ω_0 to the current arrangement Ω , the extent and structural form alters due to its deformation. One key method of determining the deformation amount in non-linear mechanics is the material deformation gradient tensor given by,

$$\mathbf{F} = \frac{\partial \mathbf{x}}{\partial \bar{x}} \quad \text{or} \quad F_{ij} = \frac{\partial \phi_i}{\partial X_j} = \frac{\partial x_i}{\partial X_j} \quad (2.23)$$

which depicts a variable in the reference arrangement to its relating variable within the current arrangement. To help understand this better; let us examine a minuscule line segment $d\mathbf{x}$ within the reference arrangement, then incorporating Equation 2.23, the proceeding line segment within the current arrangement is given by,

$$d\mathbf{x} = \mathbf{F} \cdot d\bar{x} \quad \text{or} \quad dx_i = F_{ij} d\bar{x}_j \quad (2.24)$$

where \mathbf{F} is the deformation gradient, otherwise known as the Jacobian matrix. To conserve the consecutive structure in Ω at the same time as the deformation, the mapping Equation 2.16 has to be completed respectively, i.e. \mathbf{F} can never be singular which is comparable to the case,

$$J = \frac{dv}{dV} = \det(\mathbf{F}) \neq 0 \quad (2.25)$$

where J is the Jacobian determinant.

We have the Jacobian determinant $J > 0$ to exclude self penetration for the model. This positive scalar also illustrates the ratio between the current differential volume dv and the reference differential volume dV of the material. Integrating Equation 2.14 and Equation 2.23, we can rewrite the deformation gradient tensor as

$$F = \frac{\partial u_i}{\partial X_j} + \frac{\partial X_i}{\partial X_j} = \frac{\partial u_i}{\partial X_j} + \delta_{ij} \quad (2.26)$$

where $\frac{\partial u_i}{\partial X_j}$ is connoted the material displacement gradient tensor and δ_{ij} represents the Kronecker delta function which has the values

$$\delta_{ij} = \begin{cases} 1 & i = j, \\ 0 & \text{otherwise,} \end{cases} \quad (2.27)$$

2.1.3 Strain Measure

Structural components or continuum bodies will exhibit large strains when undergoing a geometrically non-linear deformation process. In terms of material behaviour, the geometrical distortion induced via the forces exercised on a continuum body \mathcal{B} is called the strain. The inherent difference amid the bodies undistorted initial composition and its deformed final composition. Hence, the strain conveys the movement and distortion/deformation of the body.

There are a number of methods of kinematically measuring the strain within continuum mechanics. The most widely used, symmetric and objective material for the Lagrangian description is the Green-Lagrange Strain tensor:

$$\mathbf{E} = \frac{1}{2}(\mathbf{F}^T \cdot \mathbf{F} - \mathbf{I}) \quad (2.28)$$

where \mathbf{E} is the material tensor and \mathbf{F} is the deformation gradient and \mathbf{I} is the identity matrix, as previously stated. This equation can be modified and represented as a function of the displacement gradient tensor giving,

$$E_{ij} = \frac{1}{2} \left(\frac{\partial U_i}{\partial X_j} + \frac{\partial U_j}{\partial X_i} + \frac{\partial U_k}{\partial X_i} \frac{\partial U_k}{\partial X_j} \right) \quad (2.29)$$

In regards to linear strain problems; we can determine the infinitesimal strain tensor from the above equation, by ignoring the non-linear variables, viz,

$$\varepsilon_{ij} = \frac{1}{2} \left(\frac{\partial U_i}{\partial X_j} + \frac{\partial U_j}{\partial X_i} \right) \quad (2.30)$$

We will now establish the spatial velocity gradient tensor by

$$\mathbf{l} = \frac{\partial \mathbf{v}}{\partial \mathbf{x}} \quad \text{or} \quad l_{ij} = \frac{\partial v_i}{\partial x_j} \quad (2.31)$$

This can be broken down into its symmetric and skew-symmetric segments via,

$$\mathbf{l} = \frac{1}{2} (\mathbf{l} + \mathbf{l}^T) + \frac{1}{2} (\mathbf{l} - \mathbf{l}^T) \quad (2.32)$$

Using the symmetric component of the velocity gradient tensor, we can determine \mathbf{d} , the spatial rate of deformation, commonly called the velocity strain tensor

$$\mathbf{d} = \frac{1}{2}(\mathbf{1} + \mathbf{1}^T) \quad \text{or} \quad d_{ij} = \frac{1}{2}\left(\frac{\partial v_i}{\partial x_j} + \frac{\partial v_j}{\partial x_i}\right) \quad (2.33)$$

Hence, vice-versa, we can use the skew-symmetric component to attain the spatial rate of rotation tensor $\boldsymbol{\omega}$, commonly called the spin tensor

$$\boldsymbol{\omega} = \frac{1}{2}(\mathbf{1} - \mathbf{1}^T) \quad \text{or} \quad \omega_{ij} = \frac{1}{2}\left(\frac{\partial v_i}{\partial x_j} - \frac{\partial v_j}{\partial x_i}\right) \quad (2.34)$$

Taking into account the material time derivative component of the deformation gradient tensor from the stated Equation 2.23, we can deduce,

$$\dot{\mathbf{F}} = \frac{\partial \mathbf{v}}{\partial \bar{\mathbf{x}}} \quad \text{or} \quad \dot{F}_{ij} = \frac{\partial v_i}{\partial X_j} \quad (2.35)$$

This can be used to rewrite Equation 2.31 as,

$$\mathbf{1} = \dot{\mathbf{F}} \cdot \mathbf{F}^{-1} \quad \text{or} \quad l_{ij} = \dot{F}_{ik} F_{kj}^{-1} \quad (2.36)$$

We can incorporate this into the spatial deformation gradient tensor to give

$$\mathbf{F}^{-1} = \frac{\partial \bar{\mathbf{x}}}{\partial \mathbf{x}} \quad \text{or} \quad F_{kj}^{-1} = \frac{\partial X_k}{\partial x_j} \quad (2.37)$$

Using the material time derivative from the Equation 2.28, we can derive,

$$\dot{\mathbf{E}} = \frac{1}{2}(\mathbf{F}^T \cdot \dot{\mathbf{F}} + \dot{\mathbf{F}}^T \cdot \mathbf{F}) = \mathbf{F}^T \cdot \mathbf{d} \cdot \mathbf{F} \quad (2.38)$$

2.1.4 Stress Measure

The stress measure portrays the magnitude of the force occurring in the interior parts of the body \mathcal{B} while it interacts with the neighbouring body and the environment during the deformation. Let us take point, P , of the body \mathcal{B} on the boundary Γ , \mathbf{n} the unit outward normal vector for P and $d\Gamma$, the bodies surface boundary constraint. Now, we can describe the surface traction \mathbf{t} on the surface at point P with unit normal \mathbf{n} as,

$$\mathbf{t} = \mathbf{t}(\mathbf{n}) = \lim_{d\Gamma \rightarrow 0} \frac{d\mathbf{f}_s}{d\Gamma} \quad (2.39)$$

where \mathbf{t} does not have to correspond with the unit normal vector \mathbf{n} direction. The units of the surface traction are *force/area(unit)* for the equation stated above. We will introduce a spatial tensor field $\boldsymbol{\sigma}$, commonly known as the Cauchy stress tensor,

$$\mathbf{t} = \mathbf{n} \cdot \boldsymbol{\sigma} = \boldsymbol{\sigma}^T \cdot \mathbf{n} \quad \text{or} \quad t_i = \sigma_{ji}n_j \quad (2.40)$$

The equation above postulates a relation between the Cauchy traction \mathbf{t} and the unit normal vector \mathbf{n} of an arbitrary surface, also known as the *Cauchy's Theorem*. The Cauchy traction tensor is a symmetric stress tensor defined in the current arrangement. While in the reference arrangement, the accompaniment to Equation 2.40 is,

$$\mathbf{t}_0 = \mathbf{n}_0 \cdot \mathbf{P} \quad \text{or} \quad t_i^0 = P_{ji}n_j^0 \quad (2.41)$$

where \mathbf{P} is the nominal stress tensor, \mathbf{n}_0 and \mathbf{t}_0 is the unit normal vector

and surface traction force with respect to the reference arrangement. Being the counterpart, it can be stated that the nominal stress tensor has a non-symmetric nature. If we were to transpose the nominal stress tensor matrix, we would attain the *first Piola-Kirchhoff stress tensor*,

$$\mathbf{P} = \det \mathbf{F} \boldsymbol{\sigma} \mathbf{F}^{-T} \quad (2.42)$$

With some manipulation, we can derive a symmetric tensor in the current arrangement called the *second Piola-Kirchhoff stress tensor* \mathbf{S} ,

$$\mathbf{F}^{-1} \cdot \mathbf{t}_0 = \mathbf{n}_0 \cdot \mathbf{S} \quad (2.43)$$

where the transmutation of the forces by \mathbf{F}^{-1} attributes to the stress tensor being symmetric. The transmutation betwixt these stresses can be stated via

$$\boldsymbol{\sigma} = J^{-1} \mathbf{F} \cdot \mathbf{P} = J^{-1} \mathbf{F} \cdot \mathbf{S} \cdot \mathbf{F}^T \quad (2.44)$$

$$\mathbf{P} = j \mathbf{F}^{-1} \cdot \boldsymbol{\sigma} = \mathbf{S} \cdot \mathbf{F}^T \quad (2.45)$$

$$\mathbf{S} = J \mathbf{F}^{-1} \cdot \boldsymbol{\sigma} \cdot \mathbf{F}^{-T} = \mathbf{P} \cdot \mathbf{F}^{-T} \quad (2.46)$$

2.1.5 Conservation Equations

Conservation equations mirror a physical quantity for a continuum body and as a prerequisite must be fulfilled and have no constraints in their utilization

to any material.

In this section, we derive an integral relation by applying the conservation equations to a domain Ω of a body \mathcal{B} . This derived integral relation has to maintain for all the \mathcal{B} sub-domains; this allows the conservation equations to be represented as partial differential equations.

Antecedent to representing the conservation equations, we must specify the material time derivative of an integral relation for any spatial property

$$\frac{D}{Dt} \int_{\Omega} (\bullet) = \int_{\Omega} \left(\frac{D(\bullet)}{Dt} + (\bullet) \nabla \cdot \mathbf{v} \right) d\Omega \quad (2.47)$$

Equation 2.47 is also known as *Reynold's Transport Theorem*. In brief, the *Reynold's Transport Theorem* is a three-dimensional postulation of the *Leibniz Integral Rule* which is also known as differentiation under the integral. It should be noted that the *divergence* $\nabla \cdot (\bullet)$ has been employed in regards to the current arrangement and can additionally be represented as *div*(\mathbf{v}) or in its incial configuration $v_{i,i}$.

Mass Conservation

Mass conservation is the principle that in any closed system subjected to no external forces, the mass is constant irrespective of its changes in form.

Let us examine the domain Ω of a body \mathcal{B} constrained by the surface Γ that is occupied by a fixed perpetual material density $\rho(\bar{x}, t)$. Then we can state the mass of the body as,

$$m = \int_{\Omega} \rho(\bar{x}, t) d\Omega = \int_{\Omega_0} \rho(\bar{x}, t) J d\Omega_0 = \int_{\Omega_0} \rho_0(\bar{x}) d\Omega_0 \quad (2.48)$$

where the Jacobian determinant is utilized to correlate the reference and current arrangement integrals. A fundamental requirement for the mass of conservation to hold is that the mass of any material domain must be fixed. Therefore, the material time derivative of the mass has to equate to zero, viz

$$\frac{Dm}{Dt} = \frac{D}{Dt} \int_{\Omega} \rho d\Omega = 0 \quad (2.49)$$

This brings us to the subsequent integral relation employing Equation 2.47,

$$\frac{D}{m} = \frac{D}{Dt} \int_{\Omega} \left(\frac{D\rho}{Dt} + \rho \nabla \cdot \mathbf{v} \right) d\Omega = 0 \quad (2.50)$$

where the variables stated are interpreted in spatial coordinates. As this Equation maintains for any sub-domain Ω , the mass conservation produces a successive *first-order partial differential*, also called the *continuity equation*,

$$\frac{D\rho}{Dt} + \rho \nabla \cdot \mathbf{v} = 0 \quad \text{or} \quad \dot{\rho} + \rho v_{i,i} = 0 \quad (2.51)$$

We can rewrite the continuity equation by incorporating the first term in Equation 2.51 and the material time derivative in Equation 2.22 to get,

$$\frac{\partial \rho}{\partial t} + (\rho v_i)_{,i} = 0 \quad (2.52)$$

Equation 2.52 is commonly well-known as the *conservative configuration* of the mass conservation equation. If we take the material to be incompressible,

then we can state that the density is constant and the material time derivative within the continuity equation vanishes.

$$\nabla \cdot \mathbf{v} = 0 \quad \text{or} \quad v_{i,i} = 0 \quad (2.53)$$

Equation 2.53 is known as the continuity equation utilized within this research where the fluid and/or gas is considered to be incompressible. We can attain an numerical equation for the density by assimilating time in to the mass conservation equation 2.49 to get

$$\rho(\bar{x}, t)J = \rho_0(\bar{x}) \quad (2.54)$$

This equation is also known as the Lagrangian definition for the mass conservation equation.

Conservation of Linear and Angular Momentum

The *conservation of linear momentum*, also known as *momentum conservation principle* describes that total ratio of change of its linear momentum equates to applying the entire force. Let us examine an arbitrary domain Ω with surface constraint Γ within the current arrangement governed to body forces $\rho \mathbf{b}$ and surface tractions \mathbf{t} . The total/entire force \mathbf{f} is determined by

$$\mathbf{f}(t) = \int_{\Omega} \rho \mathbf{b}(x, t) d\Omega + \int_{\Gamma} \mathbf{t}(x, t) d\Gamma \quad (2.55)$$

where \mathbf{b} is the force per unit mass. We can define the linear momentum by the product of the density ρ and the velocity \mathbf{v} over the stated domain

$$\mathbf{p}(t) = \int_{\Omega} \rho \mathbf{v}(x, t) d\Omega \quad (2.56)$$

By using Equation 2.56, we can portray the conservation of linear momentum as,

$$\frac{D}{Dt} \int_{\Omega} \rho \mathbf{v}(x, t) d\Omega = \int_{\Omega} \rho \mathbf{b}(x, t) d\Omega + \int_{\Gamma} \mathbf{t}(x, t) d\Gamma \quad (2.57)$$

By consolidating Equations 2.47, 2.51 and 2.57, we can obtain the rate of change of the linear momentum to be,

$$\frac{D}{Dt} \int_{\Omega} \rho \mathbf{v}(x, t) d\Omega = \int_{\Omega} \rho \frac{D\mathbf{v}(x, t)}{Dt} d\Omega \quad (2.58)$$

By utilizing Equation 2.49 and *Gauss' Divergence Theorem*, we can translate the boundary integral in Equation 2.57 to a domain integral, viz

$$\int_{\Gamma} \mathbf{t}(x, t) d\Gamma = \int_{\Omega} \nabla \cdot \boldsymbol{\sigma}(x, t) d\Omega \quad (2.59)$$

By incorporating Equations 2.58 and 2.59 into Equation 2.57, we get

$$\int_{\Omega} \left(\rho \frac{D\mathbf{v}}{Dt} - \rho \mathbf{b} - \nabla \cdot \boldsymbol{\sigma} \right) d\Omega = 0 \quad (2.60)$$

The above equation remains true for any arbitrary domain, therefore, one can specify the **momentum equation** to take the form

$$\rho \frac{D\mathbf{v}}{Dt} = \nabla \cdot \boldsymbol{\sigma} + \rho \mathbf{b} \quad \text{or} \quad \rho \frac{Dv_i}{Dt} = \frac{\partial \sigma_{ij}}{\partial x_j} + \rho b_i \quad (2.61)$$

The *momentum equation* can be described in the Lagrangian form where all the variables are represented in material coordinates, such as

$$\rho \frac{\partial \mathbf{v}}{\partial t} = \nabla \cdot \boldsymbol{\sigma} + \rho \mathbf{b} \quad \text{or} \quad \rho \frac{\partial v_i}{\partial t} = \frac{\partial \sigma_{ij}}{\partial x_j} + \rho b_i \quad (2.62)$$

It should be noted that Equation 2.61 is established in the current arrangement, the divergence variable is stated in spatial coordinates and accordingly $\boldsymbol{\sigma}(\bar{\mathbf{x}}, t)$ is represented by $\boldsymbol{\sigma}(\phi^{-1}(x, t))$, in order to evaluate the spatial gradient of the stress field.

The *conservation of angular momentum* is determined by taking the cross product of the current vector position \mathbf{x} by each term of the linear momentum Equation 2.57, giving

$$\frac{D}{Dt} \int_{\Omega} \mathbf{x} \times \rho \mathbf{v}(x, t) d\Omega = \int_{\Omega} \mathbf{x} \times \rho \mathbf{b}(x, t) d\Omega + \int_{\Gamma} \mathbf{x} \times \mathbf{t}(x, t) d\Gamma \quad (2.63)$$

This can be deduced to give the following expression

$$\boldsymbol{\sigma} = \boldsymbol{\sigma}^T \quad (2.64)$$

If we assume that the loads are applied slowly, the acceleration variable in Equation 2.61 can be ignored, implying that the inertial forces are negligible.

This assumption leads us to the following expression

$$\nabla \cdot \boldsymbol{\sigma} + \rho \mathbf{b} = 0 \quad \text{or} \quad \frac{\partial \sigma_{ij}}{\partial x_j} + \rho b_i = 0 \quad (2.65)$$

which is commonly recognised as the *equilibrium equation*. Any problems that

adopts the equilibrium equation are known as static problems.

The conservation of linear momentum could additionally be represented in the reference arrangement. Let us examine an arbitrary domain Ω_0 with the surface constraint Γ_0 governed by body forces $\rho_0 \mathbf{b}$ and surface tractions \mathbf{t}_0 , then we can state the total force \mathbf{f} as

$$\mathbf{f}(t) = \int_{\Omega_0} \rho_0 \mathbf{b}(\bar{\mathbf{x}}, t) d\Omega_0 + \int_{\Gamma_0} \mathbf{t}(\bar{\mathbf{x}}, t) d\Gamma_0 \quad (2.66)$$

We can describe the linear momentum by

$$\mathbf{p}(t) = \int_{\Omega_0} \rho \mathbf{v}(\bar{\mathbf{x}}, t) d\Omega_0 \quad (2.67)$$

Therefore, we can define the conservation of linear momentum as,

$$\frac{d}{dt} \int_{\Omega_0} \rho \mathbf{v}(\bar{\mathbf{x}}, t) d\Omega_0 = \int_{\Omega_0} \rho_0 \mathbf{b}(\bar{\mathbf{x}}, t) d\Omega_0 + \int_{\Gamma} \mathbf{t}(\bar{\mathbf{x}}, t) d\Gamma_0 \quad (2.68)$$

Using a similar approach to Equation 2.59; the boundary integral in Equation 2.68 can be translated to a domain integral by utilizing Equation 2.49 and *Gauss' Divergence Theorem* to get

$$\int_{\Gamma_0} \mathbf{t}_0(\bar{\mathbf{x}}, t) d\Gamma_0 = \int_{\Omega_0} \nabla_0 \cdot \mathbf{P}(\bar{\mathbf{x}}, t) d\Omega_0 \quad (2.69)$$

where $\nabla_0 \cdot (\bullet)$ is the divergence with regards to the material coordinates. The Lagrangian form of the momentum equation in the reference arrangement can be deduced by neglecting the derivation conditions which follows from Equation 2.68, viz.

$$\rho_0 \frac{\partial \mathbf{v}}{\partial t} = \nabla_0 \cdot \mathbf{P} + \rho_0 \mathbf{b} \quad \text{or} \quad \rho_0 \frac{\partial v_i}{\partial t} = \frac{\partial P_{ji}}{\partial X_j} + \rho_0 b_i \quad (2.70)$$

The Equation 2.70 is also known as the *Total Lagrangian Formulation* for non-linear solid finite elements. The reciprocal equilibrium equation for this characterization, viz.

$$\nabla_0 \cdot \mathbf{P} + \rho_0 \mathbf{b} = 0 \quad \text{or} \quad \frac{\partial P_{ji}}{\partial X_j} + \rho_0 b_i = 0 \quad (2.71)$$

As an after-effect of the conservation of angular momentum from Equations 2.63 and Equation 2.64, the *nominal stress tensor* deduces the following non-symmetric expression

$$\mathbf{F} \cdot \mathbf{P} = \mathbf{P}^T \cdot \mathbf{F}^T \quad (2.72)$$

The sum of demands enforced by angular momentum conservation are generally enforced directly on the constitutive equation. Applying Equation 2.45 into Equation 2.72, we can determine the Second Piola-Kirchhoff symmetric stress tensor as

$$\mathbf{S} = \mathbf{S}^T \quad (2.73)$$

Conservation of Energy

In general terms, the *conservation of energy* asseverates that the total energy of an isolated system can never change; it can be stated that the total energy is conserved over time.

The generic definition of 'kinetic energy' for any given material is stated as,

$$\epsilon_{KE} = \int_{\Omega} \frac{1}{2} \rho \mathbf{v} \cdot \mathbf{v} \, d\Omega \quad (2.74)$$

It should be noted that for continuum body \mathcal{B} , this is not the total energy. The other contributing factor to the total energy is the *internal energy*, ω_{IE} per unit mass. The internal energy per unit volume can be stated as,

$$\epsilon_{IE} = \int_{\Omega} \rho \omega_{IE} \, d\Omega \quad (2.75)$$

Hence, we can use the descriptions of the kinetic energy and the internal energy for a continuum body \mathcal{B} to represent the total energy as,

$$\epsilon_{TOT} = \epsilon_{IE} + \epsilon_{KE} \quad (2.76)$$

The *energy conservation principle* postulates that the power of total energy must equate the power of applied forces in addition to the power at which other energies enter into the domain. The other energies may take a variety of configurations but the highest significance is the energy on account of the heat sources and heat flux over the continuum body \mathcal{B} . The variety of energy forms may emerge from radiation, chemical changes, electromagnetic fields, etc. Within this research, we only account for therm-mechanical processes.

The power of the total energy can be represented as

$$\mathbf{P}_{TOT} = \mathbf{P}_{IE} + \mathbf{P}_{KE} = \frac{D}{Dt} \int_{\Omega} \rho \omega_{IE} \, d\Omega + \frac{D}{Dt} \int_{\Omega} \frac{1}{2} \rho \mathbf{v} \cdot \mathbf{v} \, d\Omega \quad (2.77)$$

The power of the applied forces can be stated as

$$\mathbf{P}_{EXT} = \int_{\Omega} \mathbf{v} \cdot \rho \mathbf{b} \, d\Omega + \int_{\Gamma} \mathbf{v} \cdot \mathbf{t} \, d\Gamma \quad (2.78)$$

The power provided by the heat sources \mathbf{s} and the heat flux \mathbf{q} is

$$\mathbf{P}_{HEAT} = \int_{\Omega} \rho \mathbf{s} \, d\Omega - \int_{\Gamma} \mathbf{n} \cdot \mathbf{q} \, d\Gamma \quad (2.79)$$

Therefore, the conservation of energy can be illustrated as

$$\mathbf{P}_{TOT} = \mathbf{P}_{EXT} + \mathbf{P}_{HEAT} \quad (2.80)$$

Equation 2.80 is called the *first law of thermodynamics*. By substituting the relevant variables into Equation 2.80 from the Equations 2.77, 2.78 and 2.79, we can derive the *Equation of Conservation of Energy* as

$$\begin{aligned} \frac{D}{Dt} \int_{\Omega} \rho \omega_{IE} \, d\Omega + \frac{D}{Dt} \int_{\Omega} \frac{1}{2} \rho \mathbf{v} \cdot \mathbf{v} \, d\Omega &= \int_{\Omega} \mathbf{v} \cdot \rho \mathbf{b} \, d\Omega \\ &+ \int_{\Gamma} \mathbf{v} \cdot \mathbf{t} \, d\Gamma + \int_{\Omega} \rho \mathbf{s} \, d\Omega - \int_{\Gamma} \mathbf{n} \cdot \mathbf{q} \, d\Gamma \end{aligned} \quad (2.81)$$

The integral of Equation 2.81 produces the subsequent Eulerian partial differential equation of energy conservation

$$\rho \frac{D\omega_{IE}}{Dt} = \boldsymbol{\sigma} : \mathbf{d} - \nabla \cdot \mathbf{q} + \rho \mathbf{s} \quad (2.82)$$

As we only deal with the mechanical component within this research, the above equation develops into a non-partial differential equation

$$\rho \frac{D\omega_{IE}}{Dt} = \boldsymbol{\sigma} : \mathbf{d} \quad (2.83)$$

As an after-effect of Equation 2.83, one can state that the Cauchy stress tensor $\boldsymbol{\sigma}$ alongside the rate of deformation tensor \mathbf{d} are *conjugate in power*. The Lagrangian description can additionally be used to represent the conservation of energy in the reference arrangement. We can illustrate the equivalent part of Equation 2.81 as

$$\begin{aligned} \frac{d}{dt} \int_{\Omega_0} \left(\rho_0 \omega_{IE} + \frac{1}{2} \rho_0 \mathbf{v} \cdot \mathbf{v} \right) d\Omega_0 &= \int_{\Omega_0} \mathbf{v} \cdot \rho_0 \mathbf{b} d\Omega_0 \\ &+ \int_{\Gamma_0} \mathbf{v} \cdot \mathbf{t}_0 d\Gamma_0 + \int_{\Omega_0} \rho_0 \mathbf{s} d\Omega_0 - \int_{\Gamma_0} \mathbf{n}_0 \cdot \mathbf{q} d\Gamma_0 \end{aligned} \quad (2.84)$$

This yields the following Lagrangian partial-differential equation of energy conservation

$$\rho_0 \dot{\omega}_{IE} = \mathbf{P} : \dot{\mathbf{F}}^T - \nabla_0 \cdot \mathbf{q} + \rho_0 \mathbf{s} \quad (2.85)$$

As stated previously, we only consider the mechanical element of this equation, therefore, the Lagrangian energy conservation becomes

$$\rho_0 \dot{\omega}_{IE} = \mathbf{P} : \dot{\mathbf{F}}^T \quad (2.86)$$

It can be demonstrated from Equation 2.86, that the nominal stress tensor and the material derivative of the deformation gradient are *conjugate in power*. By substituting Equation 2.45 into Equation 2.86, we can achieve the following energy conservation equation in regards to the Piola-Kirchhoff stress tensor

$$\rho_0 \dot{\omega}_{IE} = \mathbf{S} : \dot{\mathbf{E}} \quad (2.87)$$

which represents the second Piola-Kirchhoff stress tensor and the rate of the Green-lagrange strain tensor being *conjugate in power*.

2.1.6 Constitutive Equations

To accurately establish the mechanical behaviour of any material, we need to define the *constitutive equations* of the material. Generally, for a sole mechanical methodology, the constitutive equations of the material indicate the stress tensor dependency in regards to the kinematic factors, such as, the strain tensor.

Linear Elasticity It has been well documented that engineering materials like metal or concrete undergo minute alterations of shape when they are regulated by external forces. If these forces are removed, the material returns to its original shape. As the shape change of the material is minuscule, there is no disparity between the reference and current arrangement.

The behaviour of these materials can be successfully described by the *linear elasticity theory*. The infinitesimal strain tensor $\boldsymbol{\varepsilon}$ can be adopted to evaluate the strains and the Cauchy stress tensor $\boldsymbol{\sigma}$ is used to evaluate the stresses. We can represent the energy conservation equation in regards to the linear elasticity theory as

$$\rho_0 \dot{\omega}_{IE} = \boldsymbol{\sigma} : \dot{\boldsymbol{\varepsilon}} = \sigma_{ij} \dot{\varepsilon}_{ij} \quad (2.88)$$

where $\boldsymbol{\sigma}$ and $\dot{\boldsymbol{\varepsilon}}$ are conjugate in power. Traditionally, the internal energy per unit volume, $\rho_0\omega_{IE}$ is commonly symbolized as W_{IE} which is known as the *strain energy function*. In terms of a linear elastic material, the strain energy function relies on the components ε_{ij} solely and, is represented by the quadratic function of the form:

$$W_{IE} = \frac{1}{2}\mathcal{C}_{ijkl}\varepsilon_{ij}\varepsilon_{kl} \quad \text{or} \quad W_{IE} = \frac{1}{2}\boldsymbol{\varepsilon} : \boldsymbol{C} : \boldsymbol{\varepsilon} \quad (2.89)$$

where we denote \mathcal{C}_{ijkl} as the elastic constants. Elastic constants are completely symmetric and can be illustrated as

$$\mathcal{C}_{ijkl} = \mathcal{C}_{jikl} = \mathcal{C}_{klij} = \mathcal{C}_{ijlk} \quad (2.90)$$

From Equation 2.90, we can state that for isotropic materials, the properties/characteristics are the same in all directions. As W_{IE} only relies on ε_{ij} , the material derivative of Equation 2.89 can be stated as

$$\frac{\partial W_{IE}}{\partial t} = \frac{\partial W_{IE}}{\partial \varepsilon_{ij}} \frac{\partial \varepsilon_{ij}}{\partial t} = \frac{\partial W_{IE}}{\partial \varepsilon_{ij}} \dot{\varepsilon}_{ij} \quad (2.91)$$

where the material symmetry has been stated. Incorporating Equation 2.89 into Equation 2.88, yields

$$\sigma_{ij} = \frac{\partial W_{IE}}{\partial \varepsilon_{ij}} \quad (2.92)$$

Nevertheless, from Equation 2.89 and Equation 2.90, we can deduce

$$\frac{\partial W_{IE}}{\partial \varepsilon_{ij}} = \mathcal{C}_{ijkl} \varepsilon_{kl} \quad (2.93)$$

By incorporating Equation 2.93 into Equation 2.92, we get the following constitutive equation that correlates stresses and strains.

$$\sigma_{ij} = \mathcal{C}_{ijkl} \varepsilon_{kl} \quad \text{or} \quad \boldsymbol{\sigma} = \mathbf{C} : \boldsymbol{\varepsilon} \quad (2.94)$$

The constitutive equation completes the set of equations that define the mechanical behaviour of linear elastic materials. It can be stated that for an isotropic material, \mathcal{C}_{ijkl} can be illustrated as

$$\mathcal{C}_{ijkl} = \lambda \delta_{ij} \delta_{kl} + \mu (\delta_{ik} \delta_{jl} + \delta_{il} \delta_{jk}) \quad \text{or} \quad \mathbf{C} = \lambda \mathbf{I} \otimes \mathbf{I} + 2\mu \mathbb{I} \quad (2.95)$$

where λ and μ are the *Lamé constants*. \mathbf{I} is the second order identity tensor and \mathbb{I} is the fourth-order symmetric identity tensor represented by $\frac{1}{2}(\delta_{ik} \delta_{jl} + \delta_{il} \delta_{jk})$. It should be noted that only two constants (*Lamé constants*) remain of the initial eighty-one of the fourth-order tensor due to the constraints of material isotropy and stress symmetry on a material. The constitutive equation 2.94 can be written as

$$\sigma_{ij} = \lambda \varepsilon_{kk} \delta_{ij} + 2\mu \varepsilon_{ij} \quad \text{or} \quad \boldsymbol{\sigma} = \lambda \text{tr}(\boldsymbol{\varepsilon}) \mathbf{I} + 2\mu \boldsymbol{\varepsilon} \quad (2.96)$$

where $\text{tr}(\boldsymbol{\varepsilon})$ is the trace of $\boldsymbol{\varepsilon} = \varepsilon_{kk}$.

Non-linear Elasticity

Just like the linear elasticity theory accounting for small deformations, there exists a contradictory theory that accounts for materials involving petite strains and big deformations. These contradictory mechanical behavioural effects originate from big displacements and big rotations of the structure. The *Saint Venant-Kirchhoff* material can be used to represent the material characteristics which can be stated as an abstraction of the linear theory to big deformations conferring to the non-linear elasticity theory. The strain energy function for a non-linear elastic material is a simplified notation of Equation 2.90 and can be expressed as

$$W_{IE} = \frac{1}{2} \mathcal{C}_{ijkl} E_{ij} E_{kl} \quad \text{or} \quad W_{IE} = \frac{1}{2} \mathbf{E} : \mathbf{C} : \mathbf{E} \quad (2.97)$$

where the stress can be stated as

$$\mathcal{S}_{ij} = \frac{\partial W_{IE}}{\partial E_{ij}} \quad (2.98)$$

The equivalent part of Equation 2.94 in the non-linear theory gives

$$\mathcal{S}_{ij} = \mathcal{C}_{ijkl} E_{kl} \quad \text{or} \quad \mathcal{S} = \mathbf{C} : \mathbf{E} \quad (2.99)$$

where \mathcal{C}_{ijkl} is defined by Equation 2.95. Adopting these equations, we can rewrite the constitutive equation for non-linear elastic material as

$$\mathcal{S}_{ij} = \lambda E_{kk} \delta_{ij} \quad \text{or} \quad \mathcal{S} = \lambda \text{tr}(\mathbf{E}) \mathbf{I} + 2\mu \mathbf{E} \quad (2.100)$$

The Lamé constants λ and μ can also be represented in regards to other physical calculations such as

$$\mu = \frac{E}{2(1 + \nu)} \quad (2.101)$$

$$\lambda = \frac{\nu E}{(1 + \nu)(1 - 2\nu)} \quad (2.102)$$

$$\mathcal{K} = \lambda + \frac{2}{3}\mu \quad (2.103)$$

where E is the Young's modulus, ν is the Poisson's ratio and \mathcal{K} is the bulk modulus.

Newtonian Fluid

In this research, we will be investigating enclosed inflatable membranes with internal fluid cavities; therefore, it is essential to define the equations that can consolidate the material behaviour associated with this. An equation that can correlate linearly the stress tensor to the rate of strain tensor within a fluid is termed the constitutive equation for *Newtonian fluids*. Let us consider a static fluid with only normal components of the stress tensor on the surface constraint, hence the stress tensor for a fluid at rest is isotropic and can be stated as

$$\sigma_{ij} = -p\delta_{ij} \quad (2.104)$$

where p is the thermodynamic pressure associated with the density ρ and

temperature T . Additional components of stress originate from non-static (moving) fluids due to viscosity, giving

$$\sigma_{ij} = -p\delta_{ij} + \sigma_{ij}^{dev} \quad (2.105)$$

where the strain rate tensor is linearly associated with the deviatoric stress tensor σ_{ij}^{dev} via

$$\sigma_{ij}^{dev} = C_{ijkl}d_{kl} \quad (2.106)$$

Incorporating Equation 2.33 and Equation 2.96 into Equation 2.106 with Equation 2.105 yields

$$\sigma_{ij} = -p\delta_{ij} + \lambda d_{kk}\delta_{ij} + 2\mu d_{ij} \quad (2.107)$$

where $d_{kk} = \nabla \cdot \mathbf{v}$ and is defined as the volumetric strain rate. If the generic *Stoke's assumption* ($\lambda + \frac{2}{3}\mu = 0$) is integrated into Equation 2.107 to link λ and μ , the *constitutive equation for Newtonian fluids* can be written as

$$\sigma_{ij} = -\left(p + \frac{2}{3}\mu\nabla \cdot \mathbf{v}\right)\delta_{ij} + 2\mu d_{ij} \quad \text{or} \quad \boldsymbol{\sigma} = -\left(p + \frac{2}{3}\mu\nabla \cdot \mathbf{v}\right)\mathbf{I} + 2\mu\mathbf{d} \quad (2.108)$$

In terms of incompressible fluids, the continuity Equation 2.53 is integrated into the above Equation 2.108 giving rise to the following form

$$\sigma_{ij} = -p\delta_{ij} + 2\mu d_{ij} \quad \text{or} \quad \boldsymbol{\sigma} = -p\mathbf{I} + 2\mu\mathbf{d} \quad (2.109)$$

where p is denoted as the mechanical pressure for incompressible fluids.

2.2 Mechanics of Membrane Structures

In this section, we will give a brief overview about the model which is suitable to define the mechanical behaviour of inflatable membrane structures. In essence, a membrane is characterised as a member of the class of continua and therefore, the theory of continuum mechanics discussed in the previous section is inherently valid for membrane mechanics. Although, it should be noted that the governing equations for general continua stated previously have been notably conventionalized as a result of the assumptions made for membrane structures.

2.2.1 Membrane Theory

Fundamentally, a membrane can be considered as a thin shell with no stiffness in the flexure direction, therefore, a membrane subjected to compression can not showcase any resistance. Within this stated theory, only the in-plane stress resultants are incorporated. The deformation state of the membrane is stated by the position of points on the surface of the Euclidean space. A number of numerical solutions for membranes have been documented adopting a finite element method approach. Case study solutions for petite deformations can be researched in Zienkiewicz [15]. In regards to big deformation case study solutions, the proceedings from Simo [16] and Braun [17] may be of interest to the reader. A basic formulations for membranes established on Curvilinear coordinates is stated by Bonet [11] while Valdes [18] suggested a large displacement formulation of a triangular membrane element established

on Cartesian coordinates.

From a mechanical standpoint, a membrane can be classified as a thin walled structure with exceedingly low bending stiffness which predetermines the load carrying behaviour. This behaviour results in the membrane deforming considerably subjected to applied forces perpendicular to its mid-surface to another arrangement in which a balance between the applied forces and stresses developed within the tangential plane of the membrane mid-surface is held. Establishing on this characteristic, we can state the following assumptions:

- The membrane is exceptionally thin with an even thickness h across the surface during the deformation. Due to this, the *Poisson's effect* which associated the in-plane deformation and the thickness direction can be neglected. Therefore, shear strains relating the thickness direction disappear

$$E_{13} = E_{23} = 0$$

- The normal stresses in the tangential plane of the mid-surface are distributed evenly over the thickness
- The plane stress precondition is presumed on the mid-plane of the membrane where all stress components in regards to the thickness direction are ignored

$$\sigma_{i3} = \sigma_{3i} = 0$$

2.2.2 Membrane Wrinkling

It has been documented by Khoma [19] that when a membrane undergoes a compression in a sole principal direction and tension in the alternative principal direction, the membrane will buckle and, will generate a number of narrow wrinkles with crests and troughs relatively laterally to the tensile direction, which is apparent from figure 2.3. In this figure, we can see the square membrane subjected to tangential displacements away from the centre of the membrane at two opposite corners. The membrane is only fixed in the z-direction at these points of displacement while the remaining membrane is free moving. The reduction in the flexural stiffness of the membrane leads to the reduction of the critical buckling stress and the separation amidst the crests of the membrane. In conclusion, once the flexural stiffness disappears, so does the critical buckling stress and creating an absolute amount of wrinkles laterally along the tensile direction. Nevertheless, conventional theory can withstand compression without wrinkling, even though the flexural stiffness disappears. Hence, one key complication in modelling membranes is to accurately describe the wrinkling phenomena that is not accountable by the conventional membrane theory. A successful membrane theory which portrays the wrinkling effectively does not permit any negative stresses to appear in the model. As when the negative stress is about to materialize, the membrane would wrinkle.

The modelling of membranes undergoing wrinkling was initiated by Wagner [21]. Herbert Wagner attempted to describe the behaviour of thin metal webs and spars transmitting a shear load exceeding the initial buckling value. Since this publication, a number of authors such as Reissner [22] and Mansfield [23] have researched the linear analysis of wrinkles in materials.

To this day, a large number of documented and published results have been

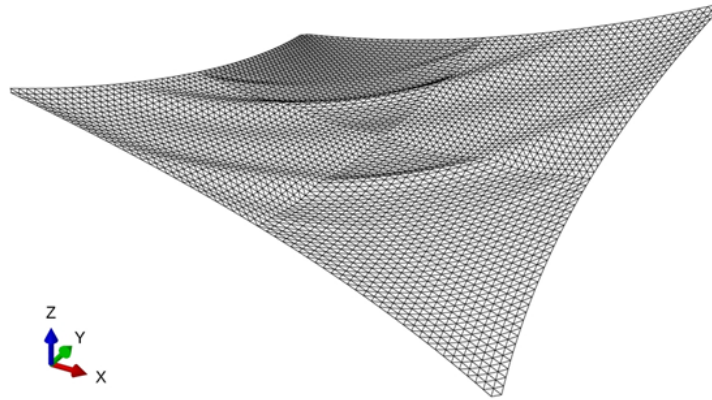


Figure 2.3: *An Example of Wrinkling within a Square Membrane subjected to Tangential Displacement at Opposite Corners [20]*

stated globally devoted to the research of wrinkling models investigated via different concepts. Some generic description of the basic concepts will be illustrated here to give the reader a broad understanding of the theory behind these models while concepts integrated to the research within this thesis will be given in the relevant subsequent chapters accordingly.

The first concept incorporates the modification of the constitutive relations of the membrane to replicate wrinkling on the surface. In the work presented by Contri [24] a no compression material model is used in a two step procedure to obtain the mean deformed position of the wrinkled surface. In a similar concept, Liu [25] suggests a penalty parameter altered material model with a fixed parameter, which revolves the constitutive equation to the direction of principal strains. After which the values of the second principal strains are castigated to zero and then the constitutive equation is revolved back to its initial arrangement. The model procedure suggested by Liu *Liu* was taken one step further by Rossi [26], by adding in one additional variable to keep the convergence properties of the material element.

A second concept proposition is established on transforming the deformation gradient tensor without altering the constitutive relation. A membrane model based on the wrinkling of membranes plane-stress theory was given by Wu [27]. In this model, the deformation gradient tensor was altered by adding an extra parameter. The value of this additional parameter was dependant on the limitation of the stress in the wrinkling direction equating to zero. This alteration of the deformation gradient selected on the basis that the principal Cauchy directions do not alter during the wrinkling process, which is only valid when the material is considered to be isotropic. Roddeman [28] created an alternative model to manage the anisotropy of the material by proposing the correct criterion to calculate the arrangement of the membrane at any point. This complex formulation led to explicit expressions for the nodal forces and the tangent stiffness matrix of the material. However, this work inspired Mutin [29] to simplify the *wrinkling theory of Roddeman* for curved membranes using a curvilinear coordinate system, which also used numerical calculations to determine the internal forces and the tangent stiffness matrix.

It should be noted that conventional finite element software packages do not normally support tension field models, resulting in inaccurate wrinkle modelling. In the present work, following a similar concept to Jarasjarungkiat [30] we will create and utilize our very own modified material model for isotropic and orthotropic membranes. The prime difference between the two models is how the algorithm computes the membrane dynamics during deformation. The model showcased by Jarasjarungkiat [30] takes into account the membrane within three separate states and only computes these states at start of the incremental step during analysis while our algorithm will run a step by step approach during each iteration of the incremental analysis. Our approach leads to a much more accurate model of membrane wrinkling and deformation when compared to previously documented integrated subroutines. This approach

will allow us to input the relevant material model criterion as a user-defined material subroutine to predict the material deformation dynamics accurately. A detailed study on this user-defined material subroutine will be presented in an consequent subsection.

2.2.3 Membrane Wrinkling Algorithm

In this section, we will discuss a developed algorithm based on the modified material model to depict wrinkling within the material. The principle behind the algorithm is to calculate the wrinkling phenomena which is not relatively predicted by conventional membrane theory even when the flexural stiffness disappears. It should be noted that this algorithm is not proposed for the time-history analysis, ergo, solely the final precise solution.

It is well known that a membrane must be in one of three states at any given point. In the *taut* state, the membrane is undergoing tension in all directions. In the *slack* state, the membrane is said to be in a relaxed state, no stretching in any direction. If the membrane is not within the taut or slack state, it is said to be in the *wrinkle* state, experiencing uni-axial tension. In the wrinkled or slack criterion, the 'actual' arrangement of the membrane is ambiguous and not defined. To overcome this, the wrinkled or slack area can be substituted with a mean smoothed pseudo-surface where the material points on the 'actual' wrinkled surface are blueprinted onto the pseudo-surface.

To forecast the 'actual' arrangement of the wrinkled membrane, a very close-knit finite element is essential to achieve a successful analysis, which occasionally requires an initial perturbation, see Tessler [31]. In the present work, the work carried out by Roddeman [32], will be incorporated detailing the wrinkling criterion established on principal stresses and principal strains. The

Stress and Strain	Wrinkling	Membrane
$S_{II} > 0$	No	Taut
$E_I > 0$ and $S_{II} \leq 0$	One axial	Wrinkled
$E_I \leq 0$	Two axial	Slack

Table 2.1: *Wrinkling criterion to define the different membrane states*

main purpose of this is to distinguish between the different membrane states, represented in table 2.1.

2.3 Time Integration Methods

It can be stated that the majority of dynamic problems within the field of mechanics cannot be computed analytically. In order to achieve a satisfactory solution, numerical time stepping methods for integration of differential equations must be utilized. We will make use of the following generic structural dynamic equilibrium equations, also known as the governing equations for the deployment simulation.

$$\mathbf{M}\ddot{\mathbf{d}} + \mathbf{C}\dot{\mathbf{d}} + \mathbf{F}_{int} = \mathbf{F}_{ext} \quad (2.110)$$

$$\mathbf{M}\ddot{\mathbf{d}} + \mathbf{C}\dot{\mathbf{d}} + \mathbf{K}\mathbf{d} = \mathbf{F}_{ext} \quad (2.111)$$

where \mathbf{M} is the mass matrix, \mathbf{C} is the damping matrix and \mathbf{K} is the stiffness matrix. \mathbf{F}_{int} and \mathbf{F}_{ext} are the internal and external loading vectors while \mathbf{d} , $\dot{\mathbf{d}}$, and $\ddot{\mathbf{d}}$ are known as the displacement, velocity and acceleration, accordingly. It should be noted that both these equations 2.110 and 2.111 represent the exter-

nal loads equating a combination of inertia forces, damping forces and internal stresses. In this section, we will investigate two well-known but essentially different methods, namely, implicit and explicit methods.

2.3.1 Explicit Time Integration Method

In an explicit analysis, the solution in each step relies solely upon the quantities achieved within the previous step. This implies that the displacements at $t_n + \Delta t$ are functions of the data at times t_t and $t_n - \Delta t$, where Δt is the time step and n is the time. If \mathbf{M} and \mathbf{C} are stated as diagonal matrices, each individual time step is computed very quickly as the solution of simultaneous equations is not needed. The explicit analysis is computing Equation 2.110 for each time step and the initial values are $\mathbf{d}^0 = 0$ and $\dot{\mathbf{d}}^0 = 0$ at time $t^0 = 0$ [33].

The algorithm yields:

- 1 If $n = 0$: calculate the acceleration at t^0 , the velocities at $t^{1/2}$ and the displacement at t^1 :

$$\ddot{\mathbf{d}}^0 = \mathbf{M}^{-1}(\mathbf{F}_{ext}^0 - \mathbf{F}_{int}^0)$$

$$\dot{\mathbf{d}}^{1/2} = \frac{1}{2}\Delta t \ddot{\mathbf{d}}^0$$

$$\mathbf{d}^1 = \mathbf{d}^0 + \Delta t \dot{\mathbf{d}}^{1/2}$$

- 2 If $n \neq 0$: calculate the velocity at $t^{n+1/2}$ and the displacement at t^{n+1}

$$\dot{\mathbf{d}}^{1/2} = \left(\frac{1}{\Delta t} \mathbf{M} + \frac{1}{2} \mathbf{C} \right)^{-1} \left[\left(\frac{1}{\Delta t} \mathbf{M} - \frac{1}{2} \mathbf{C} \right) \dot{\mathbf{d}}^{(n-1/2)} + \mathbf{F}_{ext}^n - \mathbf{F}_{int}^n \right]$$

$$\mathbf{d}^{(n+1)} = \mathbf{d}^n + \Delta t \dot{\mathbf{d}}^{(n+1/2)}$$

3 Not a prerequisite for calculating the displacements but the velocity and acceleration at t^n can be calculated as

$$\dot{\mathbf{d}}^n = \frac{1}{2}(\dot{\mathbf{d}}^{(n+1/2)} + \dot{\mathbf{d}}^{(n-1/2)})$$

$$\ddot{\mathbf{d}}^n = \frac{1}{\Delta t}(\dot{\mathbf{d}}^{(n+1/2)} - \dot{\mathbf{d}}^{(n-1/2)})$$

4 Increment the time $t^{(n+1)} = t^n + \Delta t$ and revisit to *step 2*.

It should be noted that the computer efficiency is increased by the capitalization of the diagonal mass and damping matrices which leads to the manageable matrix inversion $(\mathbf{M}/\Delta t + \mathbf{C}/2)^{-1}$. Another major contributing factor is the composition of the tangent stiffness matrix is not required, and the solution computes without any iterations. These benefits do not come without a drawback; the explicit analysis demands long computational times due to the incremental time steps essential to achieve stability. The central difference operator is provisionally stable, and the stability limit for undamped systems can be stated as

$$\Delta t_{stable} \leq \frac{2}{\omega_{max}} \quad (2.112)$$

The stable time increment can be described in regards to the highest eigenvalue in the model (ω_{max}), also known as the maximum angular frequency and the fraction of the critical damping (ξ) in the highest mode as

$$\Delta t_{stable} \leq \frac{2}{\omega_{max}}(\sqrt{1 + \xi^2} - \xi) \quad (2.113)$$

The stable time increment is the minimum time that a dilatational (i.e. pressure) wave takes to move across any element in the model. The dilatation consists of volume expansion and contraction. Therefore, we can express the dilatational wave speed as:

$$c_d = \sqrt{\frac{2\mathbf{E}(1 - \nu)}{\rho(1 + \nu)(1 - 2\nu)}} \quad (2.114)$$

where \mathbf{E} is the Young's modulus, ρ is the density and ν is the Poisson's ratio. In order for the solution to converge, it is essential that the time increments employed in the analysis are smaller than the stability limit of the central difference operator.

2.3.2 Implicit Time Integration Method

The implicit analysis computes the Equation 2.111 and the displacements, velocities and accelerations at time $t^n + \Delta t$ are determined by exploiting the data attained from times $t^n - \Delta t$, t^n and $t^n + \Delta t$. Contradictory to the explicit analysis, within the implicit method, an array of coupled equations must be solved concurrently. The implicit time integration algorithm taking advantage of the *Newmark General formula* can be stated as

$$\dot{\mathbf{d}}^{(n+1)} = \dot{\mathbf{d}}^n + (1 - \gamma)\Delta t \ddot{\mathbf{d}}^{(n+1)}$$

$$\mathbf{d}^{(n+1)} = \mathbf{d}^n + \Delta t \dot{\mathbf{d}} + \Delta t^2 \left(\frac{1}{2} - \beta \right) \ddot{\mathbf{d}}^n + \Delta t^2 \beta \ddot{\mathbf{d}}^{(n+1)}$$

The average acceleration method gives the following variables, $\gamma = 1/2$ and $\beta = 1/4$ in defining the accuracy and stability of the implicit time integration analysis. The algorithm gives the following:

- 1 Calculate the acceleration:

$$\ddot{\mathbf{d}}_t = \frac{1}{2} \left(\mathbf{F}_{ext}^n - \mathbf{C} \dot{\mathbf{d}}^n - \mathbf{K} \mathbf{d}^n \right)$$

- 2 Define the incremental time:

$$t^{(n+1)} = t^n + \Delta t^n$$

- 3 Express the displacements and velocities:

$$\dot{\mathbf{d}}_{\star}^{(n+1)} = \dot{\mathbf{d}}^n + (1 - \gamma) \Delta t \ddot{\mathbf{d}}^n$$

$$\mathbf{d}_{\star}^{(n+1)} = \mathbf{d}^n + \Delta t \dot{\mathbf{d}}^n + \left(\frac{1}{2} - \beta \right) \Delta t^2 \ddot{\mathbf{d}}^n$$

- 4 Calculate the acceleration:

$$\mathbf{S} = \mathbf{M} + \gamma \Delta t \mathbf{C} + \beta \Delta t^2 \mathbf{K}$$

$$\ddot{\mathbf{d}}^{(n+1)} = \mathbf{S}^{-1} \left(\mathbf{F}_{ext}^{(n+1)} - \mathbf{C} \dot{\mathbf{d}}_{\star}^{(n+1)} - \mathbf{K} \mathbf{d}_{\star}^{(n+1)} \right)$$

Explicit Analysis Method	Implicit Analysis Method
+ no stiffness matrix assembly	+ large time steps
+ no matrix inversion necessary	+ time steps include full iterations
+ simplification of contact interaction	
- very small time steps	- stiffness matrix assembly needed
- time steps scale with mass density	- matrix inversion needed

Table 2.2: *Advantages and Disadvantages for Explicit and Implicit Methods*

5 Regulate the displacements and velocities:

$$\dot{\mathbf{d}}_{(n+1)} = \dot{\mathbf{d}}_{\star}^{(n+1)} + \gamma \Delta t \ddot{\mathbf{d}}^{(n+1)}$$

$$\mathbf{d}^{(n+1)} = \mathbf{d}_{\star}^{(n+1)} + \beta \Delta t^2 \ddot{\mathbf{d}}^{(n+1)}$$

6 Calculate the residual forces

$$\mathbf{F}^{(n+1)} = \mathbf{F}_{ext}^{(n+1)} - \mathbf{M}\ddot{\mathbf{d}}^{(n+1)} - \mathbf{C}\dot{\mathbf{d}}^{(n+1)} - \mathbf{K}\mathbf{d}^{(n+1)}$$

7 If the solution does not converge, i.e. $\|\mathbf{F}^{(n+1)}\| > \text{tolerance}$, specify

$$\dot{\mathbf{d}}_{\star}^{(n+1)} \doteq \dot{\mathbf{d}}^{(n+1)}$$

$$\mathbf{d}_{\star}^{(n+1)} \doteq \mathbf{d}^{(n+1)}$$

and repeat *steps 4-6* until solution reaches convergence

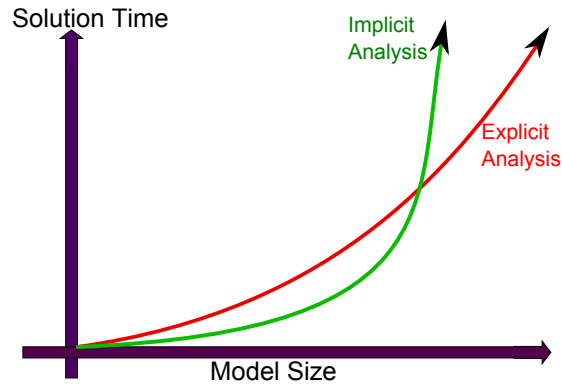


Figure 2.4: *An Example of Wrinkling within a Square Membrane*

2.3.3 Explicit versus Implicit Integration Methods

From the information stated in the preceding sections, it is apparent that there are major differences between the two methods in terms of modelling and computational time. A basic representation of this can be seen in figure 2.4 showcasing the differences of the analysis relative to the model size and computational time. A basic summary of advantages and disadvantages of both these methods can be seen in table 2.2. However, there are two further key advantages for selecting an explicit time integration method for the models investigated within this research, namely, wrinkling and contact phenomena.

ARCHIE-WeSt

In order to compensate for the simulation processing speed, we used the ARCHIE-WeSt High Performance Computer located on the premises of the University of Strathclyde. ARCHIE-WeSt is a regional supercomputer centre funded by EPSRC and dedicated to research excellence and wealth creation in the West of Scotland. Archie comprises almost 3500 cores for distributed parallel computing providing almost 38 Teraflops peak performance, eight 512GB

RAM large memory nodes, 8 GPU servers, 2 visualisation servers and 150TB of high performance LUSTRE storage. Due to these technical specifications, I was able to run parallel simulations to reach accurate results within my dynamic simulation modelling. It should be noted, that if there was no funding put aside for the use of Archie, it would have been very unlikely to utilize the explicit integration method due to the high computing power needed for simulation models to reach convergence.

Contact Modelling

The implicit procedure in Abaqus-Standard makes use of constraints to administer the contact conditions. This implies that the solver must iterate to comply with all contact conditions. There will be a decrease of the time increments if the contact conditions are not satisfied in an acceptable number of iterations. Three-dimensional models generally have a very large number of conceivable contact points, and transforming contact conditions can lead to exceptionally small time steps or convergence complications.

The explicit integration method efficiently solves extremely discontinuous events. In essence, contact is an extremely discontinuous form of non-linearity and it is possible to solve complicated, very general, three-dimensional contact problems with deformable bodies in Abaqus/Explicit. The explicit procedure provides two algorithms for modelling contact:

- 1 **General Contact** gives the user the possibility of representing contact between a large amount or all of the regions of the model with a single interaction. Interactions typically include all bodies in the model and Abaqus automatically defines the surface but the user can include/exclude surface pairs. The contact conditions are administered

by the Penalty method.

2 **Contact pairs** describe contact between two given surfaces. The user needs to be very careful when defining this type of contact as every possible contact pair interaction must be defined. Unfortunately, this type of contact has a large restriction on the types of surfaces involved. The contact constraints are governed by two separate methods within the Contact Pairs algorithm, namely, the Kinematic Compliance method and the Penalty method.

The time increment size is independent of the number of contact points and the intricacy of the contact conditions for the kinematic method. The penalty method can affect the size of the time increment of the model.

Local Instabilities

The nature of the drawing processes as previously stated induce compressive stresses within the material, which leads to wrinkling. Wrinkling alone can cause severe convergence complications in the implicit procedure. From the implicit algorithm, it can be stated that the implicit procedure is optimal for smooth non-linear response while wrinkling represents an abrupt buckling discontinuity within the non-linear response. This can lead to considerable decrease in the time increment size, forecasting convergence not being achieved in some cases.

Although wrinkling can cause a number of difficulties within the implicit procedure, it is relatively straightforward within the explicit procedure. Displacements, velocities and accelerations are calculated independently of the discontinuity severity. Inertia within the model prevents unchecked growth of the

instability through the time step. The explicit analysis however has one limitation: since the method calculates problems by propagating disturbances as waves (which travel from elements to their nearest neighbours in each time increment), it can be relatively slow for very simple stages, such as lateral loading of a 2-D membrane.

2.4 Originality of the Current Work

The majority of previous published work deals with the deformation of un/inflated membrane using numerical calculations with little focus on simulation modelling showcasing the deformations from a visual perspective. Even though stress-strain criterion within membranes has been documented extensively, taking into account deformation of rectangular and cylindrical membranes, to the authors knowledge, the process of re-inflation of a deformed cylindrical membrane structure and the adaptive membrane structure has not been simulated before. The originality of the current work lies within five principal points: each principal point stated will be discussed in detailed within the subsequent section:

- 1 A novel patent pending smart adaptive space structure to harness solar energy to be re-used as a potential source of green energy on the ground.
- 2 Design of the new cell structures for the adaptive smart cell to be shaped to the user specification after deployment.
- 3 The post-inflation of the deformed inflated membrane structure to restore it to its approximate initial configuration.
- 4 Simulation design of the membrane elements used within Abaqus using the fluid cavity inflation and internal layer method.

- 5 Abaqus simulation technique employed to meet convergence and run successfully.

However, in order to meet the parameters of the above points within our FEA simulation model, careful consideration has been given to the following:

- In regards to membrane deformation, an in-depth look is given into the interaction between the structural forces and membrane wrinkling.
- Modelling the geometric non-linearity behaviour of the membrane by integrating a user defined VUMAT subroutine to define the membrane material dynamics. It should be noted that previous research has been published for UMAT subroutines and the author only modified a previous UMAT by changing the calculation of the mixed wrinkling criterion at each incremental phase during the course of the Abaqus dynamic explicit analysis based on the Stein-Hedgepeth theory.
- Once the model characterizes the membrane using a mixed wrinkling criterion, an iterative scheme is utilized to calculate the wrinkling orientation angle and the stress distribution.
- A 3-Dimensional Finite Element model which integrates wrinkling and frictionless contact has been developed to simulate the adaptive smart cell and cylindrical membrane structure.

A computer model has been developed to accomplish exceptional performance in relation to accuracy, competency, computing hardware, software expense, complexity and the model convergence rate. The numerical algorithm is created to be malleable/flexible for a large variety of material models and has been showcased to work successfully for two very different models undergoing different inflation and deformation.

2.4.1 A novel patent pending smart adaptive space structure to harness solar energy to be re-used as a potential source of green energy on the ground

A comprehensive study has been presented where by solar energy can be harnessed in space and beamed to a ground station for re-use. An experimental apparatus was created using PET elastic membrane material to showcase the residual air inflation method however Kapton DuPoint is suggested for mission use for protection against UV radiation. The solar energy smart cell structure comprises of two specific structures: the solar panel assembly & transmission assembly and the deployable concentrator. The inflatable smart cells within the deployable concentrator are coated with a reflective material that can redirect and focus the sun's energy onto the stationary solar panel & assembly in space. The cells can be interchangeable, if one fails, it does not affect the whole structure and can be replaced with ease using robots. This implies that the structure is robust enough to meet mission requirements even under extreme scenarios of a meteorite shower puncturing some of the inflated cells. The cells can be inflated in two proposed methods, namely using a pressure tank in space to inflate each cell incrementally or inflating each cell using the residual inflation method which was utilized within this research.

2.4.2 Design of the new cell structures for the adaptive smart cell to be shaped to the user specification after deployment

As the deployable concentrator is bio-inspired, two inflatable cells are connected together via micro-pumps. The innovative micro-pumps are used to

allow air change between two neighbouring cells, therefore, changing the volume of the cells. A large horizontal level structure can be created by joining actuator elements. Changing the actuator and other connecting actuators locally on the structure will translate the global shape of the structure into any given shape. The proposed design concept is effortlessly adaptable and scalable to any dimensions as a result of the cellular technique of each cell employed.

2.4.3 The post-inflation of the deformed inflated membrane structure to restore it to its approximate initial configuration

Extensive research has been done into the deformation of a bent & buckled beam using numerical calculations and finite element simulations. However, to the author's knowledge, no research has been found on the post-inflation of a bent & buckled beam using FE simulation software. This research is vital for a detailed understanding of inflatable beams as these could be used as acting support booms for inflatable structures such as, solar sails. If the support boom of the solar sail has been deformed, restoring it back to its initial configuration will allow the mission to be carried out successfully or for the potential structure to be manoeuvred back to a relay point for repair or maintenance.

2.4.4 Simulation design of the membrane elements used within Abaqus using the fluid cavity inflation and internal layer method

Abaqus isn't the conventional software used for inflation simulations such as airbag deployment. With the integration of a custom programming scripting and exploiting the fluid cavity (**control volume*) method alongside the internal element layer (**skin*) method, Abaqus was executed successfully to attain accurate and robust results. By using the **skin* method, the internal elements of the structure are defined in order to prescribe conditions on dedicated nodes as opposed to the nodes occupying both inside and outside regions of the membrane structure. As the width of the membrane element is so small, a finite element software package usually prescribes the one node for both the inside and outside the membrane structure. This is fine as you can define two separate surface areas but a node must be defined to characterize the reference conditions of the gas during stability and inflation. In order to meet these requirements, a separate internal layer needs to be defined which conforms to the simple constraint of being one global structure and doesn't affect/deviate the outcome of the simulation result. By using the method, we were able to model an enclosed volume for gas inflation using the **control volume* method. The **control volume* method allows you to define gas expansion of tapped air administering the structure to a decreased pressure situation. The mass flow needed for the control volume method was deduced by utilizing simplistic ellipsoidal geometric and thermodynamic equations by postulating that the gas is an ideal gas. A custom triangular shaped mass flow attribute is created and utilized due to the essence of the residual air inflation method presumably starting slow, leading to an optimal maximum and eventually slowing down.

2.4.5 Abaqus simulation technique employed to meet convergence and run successfully

Finite Element Analysis provides engineering information about a structure/component which cannot be obtained by using traditional analysis methods. It is possible to generate a simulation of any design concept and to determine its real world behaviour under almost any imaginable environments, therefore allowing the concept to be refined prior to the creation of drawings.

Abaqus was used over conventional software packages due to the following benefits:

- The Abaqus coupled Eulerian Lagrangian technique provides the ability to model gas flow in the airbag and include the effects of surrounding air during deployment.
- Ability to easily enforce contact interactions between the Lagrangian bodies and the materials in the Eulerian mesh using the powerful and robust general contact algorithm.
- Extensive material library to model woven airbag fabrics and gas equations of state.
- GPU Acceleration of AMS and of the modal frequency response solver.
- Generation of cohesive elements through the Mesh function.

The Abaqus software suite delivers accurate, robust, high-performance solutions for challenging non-linear problems, large-scale linear dynamics applications, and routine design simulations. Its unmatched integration of implicit and explicit FEA capabilities enables you to use the results of one simulation

directly in a subsequent analysis to capture the effects of prior history, such as manufacturing processes on product performance. User programmable features, scripting and GUI customization features allow proven methods to be captured and deployed to your enterprise, enabling more design alternatives to be analysed in less time.

Chapter 3

Rectangular Membrane Model

In the era of light structures, thin membranes structures have gained vital roles in a multitude of Engineering disciplines from deep sea to space applications such as solar arrays, sun shields, inflatable antennas and radars. These pre-stressed membrane structures normally remain partially wrinkled in there operational arrangement. Mitigating and erasing the wrinkles on the membrane requires a biaxially tensile stress state, hence, considerably increasing the loads transmitted to the edges of the deployable structure that supports the membrane [34] [35].

These wrinkles can cause complications in solar sail manoeuvrability and also reduce the performance of solar reflectors and sun shields. In order for membranes to perform at optimum levels, the membrane must remain wrinkle free. To deal with such complications, wrinkling models based on kinematic or material modifications are preferred to costly computer simulations with very densely refined model meshes. The second part of this chapter focuses on the user-defined material subroutine to modify the stress-strain relationship of an element to erase all compressive stresses. This is justifiable as the relative

simulations focus on the 'global' stress and displacement field, and hence, the single wrinkle is neglected.

The modified material model approach incorporates a user-defined material subroutine to define the material behaviour dynamics. We will discuss the validity of using Abaqus as a finite element software for our membrane modelling simulations and thereafter investigate the benefits of using a material modified subroutine approach alongside Abaqus. The main objective of this chapter is to study the important components of wrinkling of thin membranes. It should be noted that several fundamental analyses were completed to tackle several issues associated with membrane simulation modelling, such as element type, mesh density, imperfection sensitivity, material model and stabilizing factor to function as a reference point for subsequent analyses. The wrinkle onset and wrinkle profiles of membranes undergoing loading and shearing are investigated on the conclusions of the pre-buckling eigenvalue analysis and post-buckling analysis respectively.

3.1 Literature Review of Rectangular Membrane Structures

In this section, we will give a comprehensive critical literature review of experimental and simulation models which have carried out similar research goals with numerous different procedures. In essence, we use a modified approach to the subsequent citations and a comparison has been executed within this section.

Satish Kumar [36] gave a comprehensive investigation of the formation and evolution of wrinkle patterns that are observed in stretched thin membranes.

The model investigated is set up under numerous displacement load conditions. As a pre-requisite condition for wrinkling, creation of compressive stresses in the transverse direction is deduced to be dependent on both the length-to-width aspect ratio and thickness of the thin membrane. The calculated shape and size of the wrinkle also depends on the applied tensile strain and shear strain.

A prime advantage of the study investigated by Satish Kumar [36] is that one can probe the simulation results in order to gain additional insights into the characteristics of wrinkles and their evolution under deviating thickness, number of elements, loads or boundary conditions on different shapes. Kumar gives a FEA simulation procedure to investigate the membrane wrinkling, which prognosticates with favourable accuracy and natural frequencies and mode shapes of wrinkled membrane structures. Kumar predicts that the out-of-plane pressure can be utilized to remove some wrinkles by overwhelming compression in the bulk of the membrane. However, this may be true, the key problem is to take into account the membrane dynamics on the formation of the initial wrinkles which lead to secondary wrinkles. This cannot be deduced by conventional tension field models but by integrating an Iterative Modified Properties (*IMP*) method as used within this study.

An alternative to the tension field theory model was initially created by Xinxiang [37]. The prime distinction between Kumar's method and the IMP method is that, in lieu of modifying the material properties iteratively, the utilizer pre-selects a soi-distant penalty tension field parameter to provide a modicum of stiffness in the direction transverse to the wrinkles. This avails to surmount the numerical singularities associated with vanishingly minute diagonal terms in the tangent stiffness matrix. [37] compounded the approach of their earlier paper with the semi-analytical firmness of the impending buckling model by

Lin and Mote [38]. The wrinkle wavelength and amplitude, by applying Lin and Mote's eigenvalue analysis to regulate the number of wrinkles. The wrinkle amplitude is then derived through an argument fundamentally comparatively equivalent to that put forward by Wong and Pellegrino [34] [39]. It is implicitly theorized that the number of wrinkles will not vary once the wrinkles have commenced to compose (which is inaccurate), and that the wrinkled region can be theorized to deport as a simply fortified rectangular plate. Xinxiang [37] has shown this approach to provide plausibly precise results for square membranes subjected to a concrete coalescence of tension and shear but the results lack consistency for different shapes of membranes and cannot be used as foundation theory for our research.

Several iterative schemes that utilize no-compression material models have been proposed. In their simplest form, these schemes begin by assuming that the behaviour of the membrane is linear elastic. Then, any compressive principal stresses are equated to zero and the associated stiffness matrix coefficients are also equated to zero. The principal stresses are recalculated at every iteration, to eschew history dependency in the results. Contri and Schrefler [24] set a sample quandary that many others have subsequently tackled. An analogous approach was carried out in this study as Kumar using the *NO COMPRESSION command within Abaqus but to no avail, poor convergence was observed within the results. Determinately, a user-defined membrane finite element that incorporates wrinkling within its material dynamics formulation has been designed and integrated as a VUMAT subroutine within ABAQUS.

The wrinkling of a uniformly stretched thin elastic plate administered to a pressure acting perpendicular to its surface is revisited by Coman [40]. This problem is solved under the presumption that the basic state can be adequately depicted by a suitable non-linear membrane analysis. The validity of this sim-

plification was presumed reasonable based on recent published work in which numerical simulations established that bending effects tend to be negligible for conventional load levels that induce the initial axi-symmetric deformation of the plane to bifurcate into an asymmetric mode. The effect of this presumed inconsequential alteration on the asymptotic depiction of the wrinkling instability is investigated by Coman [40] in its entirety and, an absolute quantitative assessment is made with earlier results in which the bending resistance of the axi-symmetric deformation mode was accounted for.

Coman studied the edge wrinkling of a uniformly stretched thin elastic plane subjected to a normal pressure acting on one of its faces. Coman [40] took advantage of the local nature of the instability, boundary-layer arguments have led to accurate asymptotic formulae for both the critical pressure and the reciprocal number of wrinkles in a clear interpretation of the problem. In order to achieve this result, Coman [40] neglected the bending stiffness in the pre-buckling stage which leaves the base state (non-linear) equations free of any boundary layers, and the entire asymptotic structure of the problem can be traced back to the three coupled displacement bifurcation. This approach however accurate for membrane plates, could not be utilized within ABAQUS or with membrane elements within ABAQUS. Upon running numerous simulations, convergence was not met and the initial conditions of negating the bending stiffness were proving detrimental to the formation of wrinkling within the displacement loading steps.

In contradiction to conventional methods, Mosler [41] examines every aspect of the physical problem, deriving from minimization of suitable energy functionals. A variational formulation of finite plasticity theory, which corresponds to a minimization problem for the constitutive updates, serves as the initiation point for the derivations. In consideration for the kinematics inferred by wrin-

kles and slacks, a relaxed version of the finite strain functional is theorized. In effect, the local increment stress-strain relations are derived via differentiation of the relaxed energy functional in correlation to the strains. Hence, the given formulation by Mosler [41] is completely analogous to that of hyper-elasticity with the sole exception that the aforementioned functional depends on history variables and, accordingly, it is path dependant. Once the wrinkling occurs, the resulting stress field can be calculated from the classical tension field theory, albeit, the tension field theory does not derive any information on wrinkle formation. Hence, an additional criterion is needed, which is commonly based on the principal strains, principal stresses or a combination of both. Clearly, since these loading conditions often introduced in ad-hoc manner, there is no guarantee that they comply well with tension field theory. As a deduction, the resulting boundary value problem is not continuous in general.

Alternatively, a comprehensively variational procedure convenient for the analysis of wrinkles and slacks in membranes was proposed in a series of papers by Pipkin [42], [43], and [44]. Pipkin examined the energy of a membrane under given assumptions and validated that the quasi-convexification of the Helmholtz energy delineates a relaxed energy functional whose derivatives generate the membrane stresses, i.e. the stresses expected by this relaxed potential fulfil the restrictions dictated by the tension field theory. The methodology introduced by Pipkin encompasses physically sound loading and unloading conditions; additional ad-hoc presumptions are not required. As an after-effect, the proceeding the boundary value is continuous (more precisely, sufficiently smooth), which makes it physically and mathematically sound and convenient for numerical implementations. Pipkin's idea was further elaborated by Mosler [41], in which a novel variational algorithmic formulation for wrinkling at finite strains were proposed. In accordance with Pipkin's original method, the unknown wrinkle distribution is calculated by minimizing the Helmholtz energy

of the membrane with the respect to the wrinkling parameters. The finite element model allows to employ arbitrary, fully three-dimensional hyper-elastic constitutive models directly. This methodology was taken one step further by adopting a fully variational approach by Mosler, i.e. the wrinkling parameters, together with the plasticity related variables, follow from relaxing an incrementally characterized potential. Therefore, the relaxed potential is formally identical to that of the standard hyper-elasticity. Clearly, such a variational method showcases numerous advantages in comparison to conventional strategies. For instance, it opens up the possibility of applying standard optimization algorithms to the numerical implementation. This is especially important for highly non-linear or singular problems such as wrinkling. On the other hand, minimization principles provide a suitable basis for posteriori error estimation and thus, for adaptive finite element formulations.

Within this study, the Mosler fully variational formulation to account for wrinkling in elastic membranes at finite strains is integrated alongside the Miller-Hedgepeth membrane model. The distinguishing aspect of the new methodology used is that every part of the problem is considered using an iterative scheme taking into account the material dynamics for wrinkling. The addition of ad-hoc loading conditions are not required, but they emanate naturally from the mathematically and physically sound variational principal itself. The VUMAT subroutine is discussed in detail in a later section.

3.2 Finite Element Analysis with Abaqus

Membrane wrinkling is a highly geometrically non-linear phenomenal, creating instability within the structure. To accurately simulate this type of phenomenal demands a non-linear solution method and an entirely dynamic, transient

analysis. The primary non-linear solution method within Abaqus is the full '*Newton-Raphson*' method. This method solves a sequence of non-linear equilibrium equations incrementally with increasing load or displacement. An alternative method for determining the post-buckling snap-through problems is the '*Arc-length*' method, commonly recognized as the '*modified Riks*' method. In this method, a sequence of equilibrium states is determined within the load-displacement space by the two parameters, nodal displacement and loading. Both these parameters are used incrementally to achieve equilibrium solutions, rather than solely controlling a single load or displacement increment as in the Newton-Raphson method. Wong [39] [45] documented unsuccessful attempts at the Riks method due to highly localized instability, concluding that monotonic displacement incrementation as a successful working option.

3.3 Analysis Procedure

A detailed flowchart is given in figure 3.1 stating the simulation procedure used by the finite element analysis software Abaqus.

3.3.1 Initial Conditions

In order to stabilize the membrane, a small uniform pre-stress is applied in the first stage of the analysis. It should be noted that the magnitude of the applied pre-stress should be sufficiently big to compensate the successive buckling mode analysis but, not too big to influence the first solution.

An edge displacement is prescribed to define the level of pre-stress required. After the initial pre-stress has been applied to the membrane, a static non-

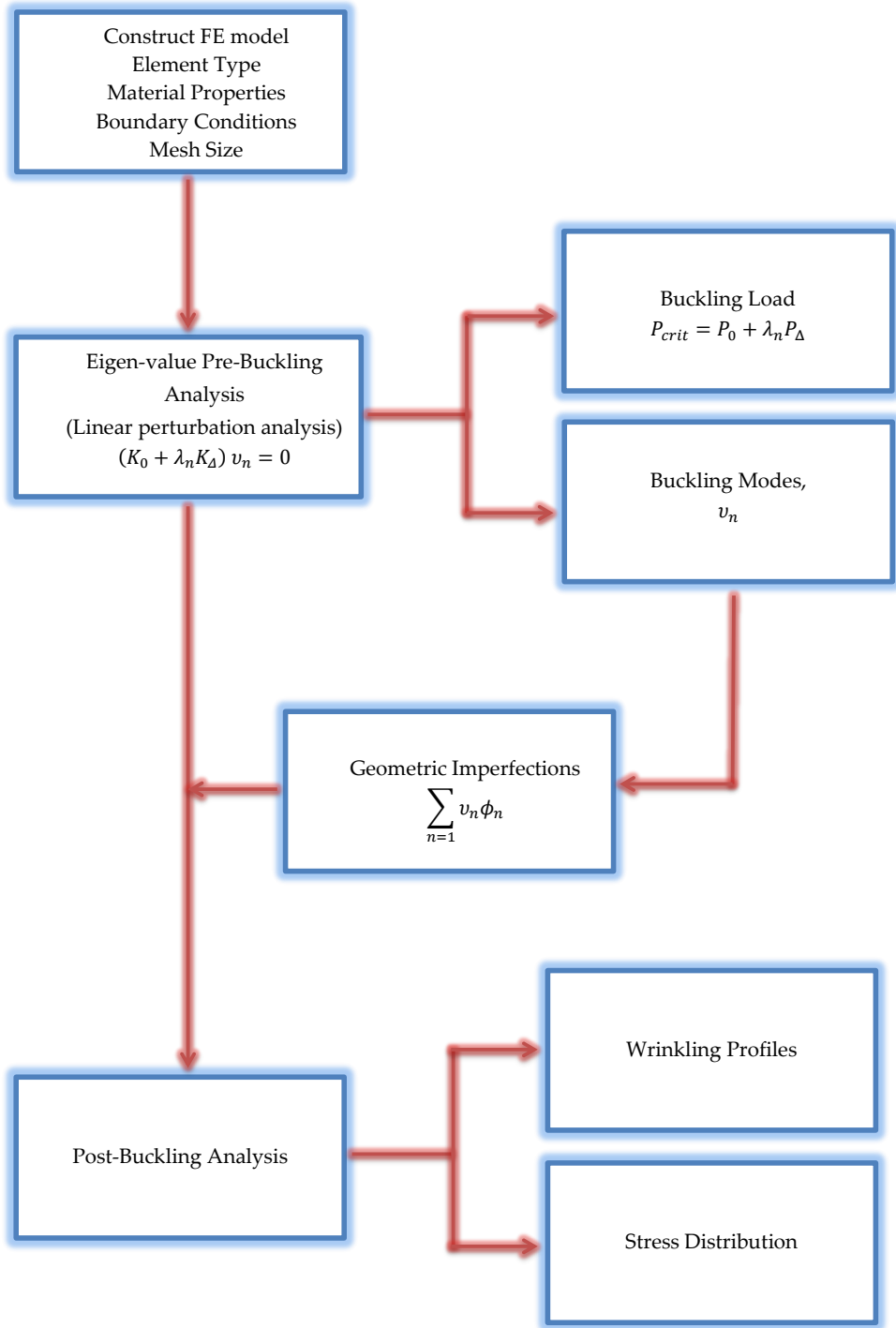


Figure 3.1: Flowchart depicting the Abaqus Wrinkling Analysis

linear geometric check is executed. This check assigns a small redistribution of the pre-stress state alongside the small in-plane displacement.

3.3.2 Pre-Buckling Eigenvalue Analysis

In the consequent stage of the analysis, the buckling mode-shapes of the pre-stressed membrane are computed. These calculated modes are used to seed petite imperfections that prompt the development of wrinkle formation in the successive non-linear analysis.

In order to achieve this, we use the *BUCKLE option within Abaqus to forecast the buckling load and the potential wrinkling modes of the membrane dependant on the boundary constraints and loading conditions. Rather than defining the load as a force here, it is instead defined as an edge displacement.

Generically, we expect the loads for the model stiffness matrix to become singular during an eigenvalue buckling analysis, viz.

$$K_{ij}v_i = 0$$

where K_{ij} is the tangent stiffness matrix when the loads are administered, v_i are the non-trivial displacement solutions, i and j are the degrees of freedom for the complete model. Abaqus uses two standard eigensolvers to derive the eigenvalues, namely *Subspace iteration* and *Lanczos method*.

Standard Eigensolvers

Before we can define the *Subspace Iteration* method or the *Lanczos method*, we need to understand the simplest iterative method available, the *Power method*.

Power Method is the basic iterative method. It takes a starting vector and lets the matrix operate on it until we get vectors that are parallel to the leading eigenvector. It converges when there is one unique eigenvalue of largest magnitude, but even in these favourable cases it is slower than other algorithms, such as the Lanczos method.

Subspace Iteration, also called Simultaneous Iteration lets the matrix operate on a set of vectors simultaneously, until the iterated vectors span the invariant subspace of the leading eigenvalues. It is the basis of several structural engineering software packages and has a simple implementation and theory of convergence to recommend it. It is, however, slower to converge than algorithms based on the Lanczos orthogonalization.

Lanczos method builds up an orthogonal basis of the Krylov sequence of vectors produced by repeated application of the matrix \mathbf{A} to a starting vector. In this orthogonal basis, the matrix operator is represented by a tridiagonal matrix \mathbf{T} , whose eigenvalues yield Ritz approximations to several of the eigenvalues of the original matrix \mathbf{A} . Its main advantage, compared to the power method, is that it yields approximations to several eigenvalues from one sequence of vectors and that these converge after much fewer matrix-vector multiplications. On the other hand, there are potential complications: even if a simple three-term recurrence is enough to give a mathematically orthogonal basis, rounding errors will destroy orthogonality as soon as the first eigenvalue

converges, and one has to apply some kind of re-orthogonalization. If one needs only eigenvalues, the Lanczos algorithm is economical in storage space.

For modelling relatively thin membranes, the eigenvalue buckling analysis is complex due to the applied initial pre-stress. An applied pre-stress that is too small can lead to two ramifications: the model fails to converge, or only negative eigenvalues are written in the eigenvalue buckling analysis. The negative eigenvalues express the membrane buckling if the loads were enforced in the reverse direction, e.g. the membrane is much more inclined to buckle when the tensile load is substituted by a compressive load. If a large enough pre-load is applied prior to the buckling analysis, these negative buckling modes can be averted. It should be noted that with the Lanczos solver, only positive eigenvalues can be attained by imposing a lower limit to the eigenvalue.

The model configuration after the initial step, during which the pre-load P^N is exercised to the membrane, is known as the base state of the buckling step. The buckling loads are determined comparative to the base state of the membrane structure. An incremental load (*'live'* load), Q_N is prescribed in the eigenvalue buckling step. The degree of this loading is insignificant as it will be scaled by the load multipliers, λ_n , established in the eigenvalue analysis:

$$(K_{ij}^0 + \lambda_n K_{ij}^\Delta) v_i^n = 0$$

where K_{ij}^0 is the stiffness matrix relative to the base state which incorporates the effects of any pre-loads, K_{ij}^Δ is the differential initial stress and loads stiffness matrix as a result of the incremental loading pattern, Q_N , λ_n are the eigenvalues, v_i^n are the buckling mode shapes (eigenvectors) and n indicates the buckling mode number.

The buckling loads can now be stated as,

$$P = P_N + \lambda_n Q_N$$

Typically, the minimum value of λ_n is of interest and the pre-load P_N and the perturbation load Q_N may be of a dissimilar nature. In the course of this research, they are both established as edge displacements in the longitudinal direction. It should be noted that the buckling mode shapes v_i are standardized vectors and do not depict the real deformation value at critical load. The buckling mode shapes are standardized to assure the maximum displacement component equates to 1.0. These attained buckling mode shapes can be regarded as a key component in the eigenvalue analysis, as they forecast the possible failure mode of the structure.

In an eigenvalue buckling prediction step, Abaqus initiates a static perturbation analysis to calculate the internal stress, $\Delta\sigma$ due to Q_N . This in turn creates the stiffness matrix K_{Δ}^{ij} relating to $\Delta\sigma$. The stiffness matrix K_0^{ij} relating to the base state geometry is created during the eigenvalue extraction part of the buckling step. The initial stress and load stiffness variables in relation to the pre-load, P_N , are incorporated and derived based on the base state geometry.

$P_N + \lambda_1 Q_N$ with λ_1 being the eigenvalue minimum, usually gives a good approximate for the critical buckling load other than structures with closely spaced eigenvalues, leading to complex numerics. An array of densely spaced eigenvalues demonstrate that the structure is imperfection sensitive. An eigenvalue buckling analysis does not yield a precise forecast of the buckling load for imperfection sensitive structures.

Normally a buckling analysis is carried out for 'hard' structures, it is not a necessity to incorporate the effects of geometric alterations in reaching equilibrium for the base state. However, it is concluded that for some membrane ranges, the pre-load has to be large enough in order to achieve positive eigenvalues. In these circumstances, the pre-load may prompt considerable geometric alteration within the base state. Therefore, we make use of the geometric non-linearity feature, *NLGEOM within Abaqus is incorporated for the base step and during the whole analysis in each simulation. The *NLGEOM option indicates that geometric non-linearity should be accounted for during the analysis step (stress analysis, fully coupled thermal-stress analysis, and coupled thermal-electrical-stress analysis only). Once the NLGEOM option has been switched on, it will be active during all subsequent steps in the analysis.

3.3.3 Post-Buckling Analysis

Once the buckling mode shapes have been determined, we interpolate a linear combination of chosen eigenmodes into the model as a geometric imperfection. The eigenvectors related to the lowest eigenvalues are of major importance within the analysis, and typically the seeded imperfections of a model are attained as a linear sequence of these chosen eigenvectors. The preference of the imperfection modes that are interpolated within the membrane model have to be established on the proposed final wrinkling pattern. Therefore, the selected eigenmodes must mirror the wrinkle pattern forecast.

After establishing relevant eigenmode shapes, we incorporate geometrical imperfections as out-of-plane deformations within the model using option *IMPERFECTION within Abaqus.

$$\delta z = \sum_i \phi_n v_n$$

where v_n is the n th eigenmode and ϕ_n is a scaling factor whose value is determined as a factor of the membrane thickness. Different values for the membrane thickness have been investigated to evaluate the sensitivity of a predicted response.

A geometric non-linear analysis (*NLGEOM) is executed using edge displacement incrementation employing the Newton-Raphson method. In order to overcome a model instability, a transient analysis is performed using the stabilize feature (*STABILIZE) within Abaqus. This feature automatically administers pseudo-inertia and pseudo-viscous forces at all nodes when an instability is identified, and replicates a potential dynamic response of the membrane as it snaps to achieve the first static equilibrium state after the snapping has developed. After which, rather than progressing with the quasi-static analysis, Abaqus systematically changes to a dynamic integration of the equations of motion for the model, hence lowering the possibility of numerical singularities.

3.3.4 Material Model

Hyper-elastic membrane materials like Kapton HN have very high flexibility in comparison to their compressibility. Simulink Abaqus software can provide a useful tool in determining the compressibility of elastomer's by implementing them into a hyper-elastic material model.

Within Abaqus software, hyper-elastic materials are represented in regards to the 'strain energy potential', $U(\epsilon)$, which is called the strain energy kept within the material per unit of the reference volume, as an operator of the deformation

at that point within the material. It can be stated that, there are a variety of strain energy potentials within Abaqus that are used to model isotropic materials: namely Arruda-Boyce form, the Marlow form, the polynomial and reduced polynomial forms, the Yeoh form, the Van der Walls form and the Ogden form.

Abaqus systematically establishes the optimal strain energy potential(s) based on the initial model conditions stated, calculates the relevant coefficients in the strain energy potential formula, and constructs the stress-strain curve(s) of the reciprocal hyper-elastic model. Due to the constraints and objectives of this work, we will not divulge into greater depth of the various strain energy potential forms but adopt the modified Mooney-Rivlin model as our standard model. This is the most efficient and typical form of the polynomial class, whose strain energy potential can be represented as

$$U = \sum_{i+j=1}^N C_{ij} (\bar{I}_1 - 3)^i (\bar{I}_2 - 3)^j + \sum_{i=1}^N \frac{1}{D_i} (J^{el} - 1)^{2i},$$

where N is the material component, C_{ij} and D_i are the temperature dependant components, \bar{I}_1 and \bar{I}_2 are the first and second deviatoric strain invariants, and J^{el} is the elastic volume ratio. The bulk and shear modulus is represented via,

$$\mu_0 = 2(C_{10} + C_{01}), \quad K_0 = \frac{2}{D_1}$$

It should be noted that when implementing the Mooney-Rivlin model within Abaqus, it is impossible to adopt the assumption that the material is completely incompressible as the Abaqus model has no algorithm to impose such a constraint at every material calculation point. Due to this complexity, the user must define some data on the incompressibility parameters to be used.

Commonly, general hyper-elastic material model simulations are vastly unstable when in comparison with linear elastic material models. All attempts to use the evaluated Mooney-Rivlin material model within the buckling analysis were unsuccessful and a linear elastic model was adopted with the material parameters stated in table 3.2 for all the numerical simulations within this model.

3.3.5 Element Selection

A key requirement in successfully modelling an accurate simulation model within Abaqus is the selection of the element type used to discretize the structure. There is an abundant supply of different elements within the Abaqus software which can be used in a wide range of scenarios, of which membrane elements and shell elements were recognized as potential nominees for modelling membrane structures within this study. In essence, membrane elements have fewer degrees-of-freedom when compared with shell elements but require significantly less memory and solution time when solving the relative model. While shell elements do give increased accuracy (e.g., if a few percent increase in maximum stress due to the inclusion of bending stresses is critical), the trade off with computer power needed was satisfactory and therefore shell elements were used for all material models presented.

The shell elements within Abaqus can be generically categorised into two types, conventional shell elements and continuum shell elements. Continuum shell elements discretize the complete three dimensional body, allowing only the displacement degree of freedom. However, conventional shell elements discretize a body by characterizing the geometry at a reference surface, allowing displacement and rotational degrees of freedom.

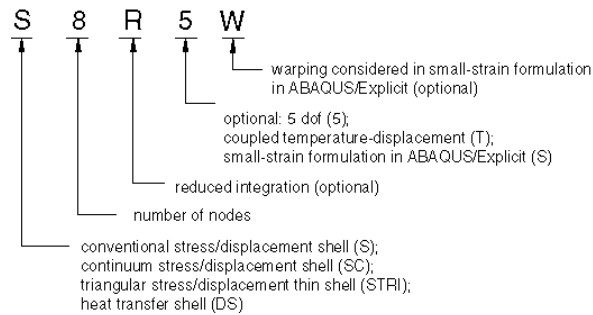


Figure 3.2: *Shell Element Name representation within Abaqus*

Conventional shell elements can be used in linear interpolation and include both finite-strain and small-strain elements. Element types such as S3, S3R, S4 and S4R elucidate finite membrane strains and forthwith large rotations within Abaqus and therefore are well suited for large-strain analysis. While element types such as S4R5, S8R, S8R5 and S9R5 are used for small membrane strains and forthwith large rotation problems. The small-strain shell elements within Abaqus cater to a computation efficient substitute to the finite-membrane strain elements for suitable utilization albeit solution accuracy may diminish as membrane strains increase. Complexities of shell structures experiencing large-scale buckling may implement either of the two types of element depending on the measure of in-plane stretching and compression on the membrane.

In figure 3.2, we can see the three dimensional shell element representation as given by Abaqus. For instance, S4R5 is a a 4-node, quadrilateral, stress/displacement shell element with reduced integration, small-strain formulation and an optional 5 degrees of freedom.

In the case of conventional shell elements within Abaqus, the Poisson's ratio must be defined in accordance with the shell section definition. This is to account for the modification of the shell thickness in finite-strain elements as a function of the membrane strain. It should be noted that if the Poisson's ratio is stated as zero within this section, the shell thickness for the membrane

will remain constant, hence, well suited for small-strain models. If the user was to simulate materials that incur large-strain applications, the Poisson ratio would need to be given in order to generate the incompressible response of the material during high-plastic or hyper-elastic deformation.

For all simulations within this study, the element S4R5 will be used as this element type gives a lower critical buckling strain and a lower tensile strain at maximum wrinkle amplitude when compared with other element types. This however is common knowledge as element types S4R5 and S8R5 are small-strain elements and may underestimate the membrane strain or overestimate the wrinkle amplitude at small strains. But the S4R5 produces fairly accurate results and has the biggest advantage of being computationally efficient.

3.3.6 Responsiveness to Stimuli

One of the drawbacks of finite element simulations are the complexities occurred when analysing post-buckling problems and Abaqus is no different. Within Abaqus, the post-buckling complication cannot be solved as a result of the discontinuous response (*bifurcation*) at the initiation of buckling. To overcome this complication, the problem in question must be transformed into a problem with continuous response, which can be achieved by injecting a geometric imperfection pattern within the ideal geometry in order to create some response in the buckling mode prior to the critical load is attained.

Imperfections within the Abaqus model are introduced via perturbations within the geometry. Generally, imperfections can be characterized within Abaqus in two forms: firstly, by the linear superimposition of buckling eigenmodes from the displacements of static analysis or secondly by literally designating the node number and imperfection constants. The normals are then computed

by generic algorithms dependant on the perturbed coordinates. It should be noted that on most cases, the former method is adopted since the precise and accurate shape of the model imperfection is usually unknown. The structural response in most structures relies upon the imperfections of the original model geometry, specifically in cases where the buckling modes merge post-buckling. By conforming the proportional values of the scaling factors of the individual buckling modes, the imperfection responsiveness to stimuli *sensitivity* can be calculated. The proportional values of the perturbation are commonly a few percent of the corresponding structural dimension, such as shell thickness.

In order to achieve accurate simulation results, a number of examinations should be carried out to examine the responsiveness to stimuli of the structure to imperfections. For each proportional value, a full wrinkling simulation was determined, with geometrical imperfections seeding to the immaculate mesh using the *IMPERFECTION command within Abaqus. It was noted that the maximum wrinkle amplitude and relating strain were not sensitive to the proportional values of the geometric imperfections. For small-scale imperfections, the deformation is minuscule below the critical load. From this point at the critical load, the response increases drastically, generating a expeditiously behaviour modification. Alternatively, a large imperfection contributes to the structural instability at the initial stage of deformation, and the corresponding post-buckling response will rise consistently prior to the critical load being achieved. In the latter case, the progression to the post-buckling behaviour will be easy to analyse and comparatively steady. Using previously documented experimental results, the Abaqus element guide and experimental Abaqus membrane simulations, an intermediate scale factor of 1% is selected for the membrane thickness for all subsequent wrinkling membrane models.

3.3.7 Stabilizing Factor

Problems exhibiting buckling are very unstable due to the non-linear geometrical dynamics of the structure. Abaqus automatically implements an algorithm for balancing unstable quasi-static problems through the integration of volume-proportional damping. It should be noted that this algorithm is generated by integrating automatic stabilization in any non-linear model.

A key assumption made during the simulation is that the structure is stable at the beginning of the step and that any instability is developed over the time-frame of the step. When the model is presumed to be in the steady state, viscous forces acting on the model and the viscous energy dissipated is very small. Therefore, the integration of the artificial damping has no effect on the model. The local velocities of the structure increase when the local region of the model becomes unstable, ergo, some of the strain energy is dissipated by the integrated damping. However, Abaqus can, if need be, decrease the time increment to allow the simulation to ensue without the unstable response producing a big displacement. Abaqus computes the damping factor established on the solution of the initial increment of a step. As stated previously, the initial increment of a step assumes the model is stable, hence, the damping factor is then calculated to such a degree that the deduced dissipated energy for the initial step is a little portion of the deduced strain energy. This portion is called the dissipated energy fraction and has a default value of 2.0×10^{-4} and can be an arbitrary value.

In order to reach an accurate and efficient solution, the dissipated energy fraction should be set to the lowest possible value to attain convergence. This value was adjusted progressively, relative to the convergence of the solution by using the *RESTART option within Abaqus. This method allows the user to

minimise the initial numerical damping value, and the corresponding deviation between the calculated equilibrium path and the actual path, and only raise the value when needed. It should be noted that the smaller the stabilizing factor, the longer the computation time needed to reach a solution. The smallest factor used for all subsequent simulations was 1×10^{-7} for the two finite element models discussed in the next section and relative computation time listed in table 3.1.

Stabilizing Factor	Computation Time (secs)	ω_{max}	Strain at ω_{max}
2×10^{-4} (default)	1924	0.2972	11.28%
1×10^{-6}	2738	0.3100	11.46%
1×10^{-7}	3452	0.3100	11.42%

Table 3.1: *Effect of the Stabilizing Factor on the Post-buckling Analysis solution*

3.3.8 Finite Element Models

In the following sections, we will investigate and discuss two separate finite element models experiencing axial loading and shear loading. The dimensions and material properties of the Kapton membrane used within all wrinkling analyses presented within this study is given in table 3.2.

The two models investigated initially deal with the stretching and shearing of a rectangular Kapton Du Point membrane with the specifications stated in table 3.2.

Parameters	Physical Model	SI Units
Length, L	0.5	metre(s)
Width, W	1.0	metre(s)
Thickness, d	0.005	metre(s)
Young's Modulus, E	5×10^6	Pascal(s)
Poisson's Ratio, ν	0.34 ^a	

Table 3.2: *Kapton Membrane parameters used within Abaqus*

3.4 Axial Loading on the Membrane Structure

It has been previously documented that wrinkling onset in relation to buckling strain (*critical*) is very difficult to measure. However, from experimentation conclusions, the membrane dimensions can also play a significant role in understanding the membrane structural instability in regards to in-plane tensile loading.

The quantitative effects of these attributes on our model must be understood to accurately predict deformation. A series of simulations were employed and executed for a variety of membrane dimensions in the pre-buckling analysis phase of the model. 114 dimensions with widths ranging from 20 mm to 150 mm and lengths from 50 mm to 250 mm were examined and compared with previously (*experimental*) documented results to perceive the accuracy of the model.

3.4.1 Simulation Methodology

This model was created in Abaqus software by using the initial conditions defined in the preceding section. Initially, the model was assigned an *ASYM-

METRIC boundary condition to the central location to fix the membrane in place prior to the displacement load acting on the membrane. This allowed the user to apply a uniform displacement load on the model without creating any static warp on the model. The displacement loads were applied using the *BOUNDARY CONDITION option and gave a linear amplitude to the acting displacement. This allowed a gradual load to be applied to the membrane structure and mitigated any sudden out-of-plane deformations. This gradual load also allowed the deformation to be monitored and the failure points to be identified.

3.4.2 Simulation Analysis

By interpolating the 114 data points listed from the 100 dimensions, a contour map displaying the relative critical buckling strain can be created as depicted in figure 3.3. The length and width of the membrane is represented by each coordinate of the data point illustrated on the contour map. Each contour line links the ranges with similar values of critical buckling strain. As stated previously, the 100 dimensions of rectangular membrane were subjected to axial loading under the same boundary and loading conditions. From the results for each membrane analysis, the membrane critical buckling strain were exported to a spreadsheet where Matlab was used to layer the relative results of each membrane. These layered membranes were then integrated/correlated together by linking nodes of similar critical buckling strain values to make the plot more appealing to the naked eye and to view a well documented analysis from a different perspective.

From the contour map, it can be clearly stated that wrinkles appear to occur more frequently in larger membranes when compared to smaller ones. From

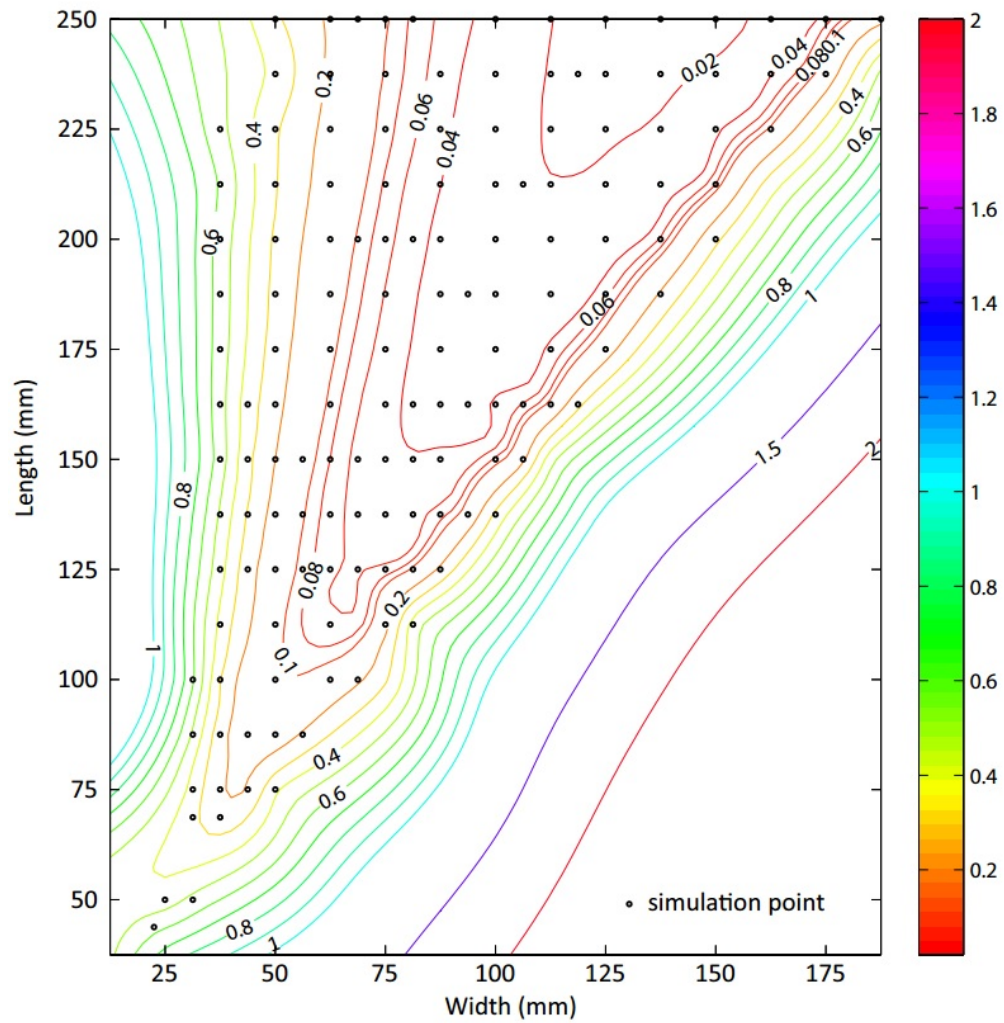


Figure 3.3: *Contour Map depicting the Buckling Strain (critical) for 0.1mm thickness membranes [46]*

the Abaqus simulations, it can be concluded that the lowest critical buckling strain of 1.5% occurs within the 250×140 mm membrane while the highest critical buckling strain of 62.5% occurs within the 100×30 mm membrane. Furthermore, it can be stated that wrinkling generally develops on membranes with intermediary aspect ratios in comparison with membranes with severe aspect ratios.

In order to obtain a comprehensive wrinkling analysis on the structure, two separate analysis approaches are combined: The Bifurcation Analysis and The Tension Field Theory. Both of these approaches have their own relative merit and a brief definition of each approach will be given.

The Bifurcation Analysis

The analysis of a system of ordinary differential equations (ODE's) under parameter variation. In this analysis, the membrane has a non-zero bending stiffness and is treated like a thin shell. Commonly, a geometrically non-linear finite element procedure is utilized with the use of shell elements for numerical analysis [47] [33].

By this approach, we can predict both the post buckling behaviour and the critical conditions for wrinkling. For comparatively straightforward scenarios, analytical techniques have also been postulated and suggested to attain proximate solutions.

The Tension Field Theory

Investigation of the formation of wrinkling in isotropic membranes being subjected to finite deformations. The first assumption we make here is that the

membrane has zero bending stiffness. The conceptualization of tension field theory was first proposed by Wagner in 1929 [21].

This was used to clarify the post buckling investigation of malleable shear panels in aeroplane manufacture. Due to the applied shear edge loading, the thin panel is severely affected by the post buckling range. During this phase, a load is spread fundamentally on one of primary axes of stress, while bending effects stay secondary. The panel warps to a wavy or irregular surface, the crests of the wrinkled waves coincides roughly with trajectories of the tensile stress [48].

Here Wagner created a tractable concept by completely ignoring bending stiffness and depicting the stress to be uni-axial. The next dilemma is to resolve the magnitude and direction of stress and thereby infer the overall load-deflection response of the buckled panel. This idea forms the basic foundation of subsequent investigations into wrinkling as a load transmission mechanism in membranes.

3.4.3 Wrinkling Analysis

The adoption of both analyses not only accurately predicts the critical buckling load (*eigenvalues*) but also the buckling modes (*eigenvectors*). In an wrinkling analysis, the thickness of the sheet becomes a very major factor. Practically, the two factors: the magnitude and the area of compressive stresses must be big enough to stimulate buckling. It can be stated that the outcomes from the eigenvalue (bifurcation) analysis, along with the corresponding eigenvalues and eigenmodes, relies drastically on the sensitivity of the width-to-thickness proportion of the Kapton membrane alongside the applied pre-stretch.

The following figures represent the initial symmetric wrinkling modes in relation to the smallest eigenvalues of the Kapton membrane with inherent variant aspect ratios.

These simulated wrinkling modes give greater insight on the possible deformations that can take place within membranes upon the critical buckling strain. One clear observation that can be made is the formation of the wrinkles, the wrinkles always form parallel to the direction of load. Generally, three primary wrinkles would form on the membrane within the initial mode except for membranes with acute aspect ratios whereby five primary wrinkles would be generated. From the simulated results, it was also concluded that the formation of the wrinkles differ with varying aspect ratio although they always form on the longitudinal medial level surface of the membrane for symmetric modes. This is postulated by the locational position of the eigenvectors with the greatest weighting. It was further concluded that membranes with the aspect ratio $L/W \leq 2.8$, wrinkles would commence from the central location of the membrane; where in fact membranes with an aspect ratio $L/W \geq 2.9$, wrinkling would commence from two separate locations equally spaced from the central point of the membrane. This separation distance from the central location increases proportionally with the increasing of the membrane aspect ratio.

Generally, the modes of membrane wrinkling are generated in pairs (symmetric and anti-symmetric). The smallest eigenvalue is given by the initial two modes, stating that the resultant simulation has an even chance in deforming into any mode past the critical buckling load.

It can be seen that with the aspect L/W ratio increases, the number of wrinkles decreases but the size of the wrinkle increases as showcased in figure 3.4. The amplitude of wrinkle increases with increasing load. The corresponding out-of-

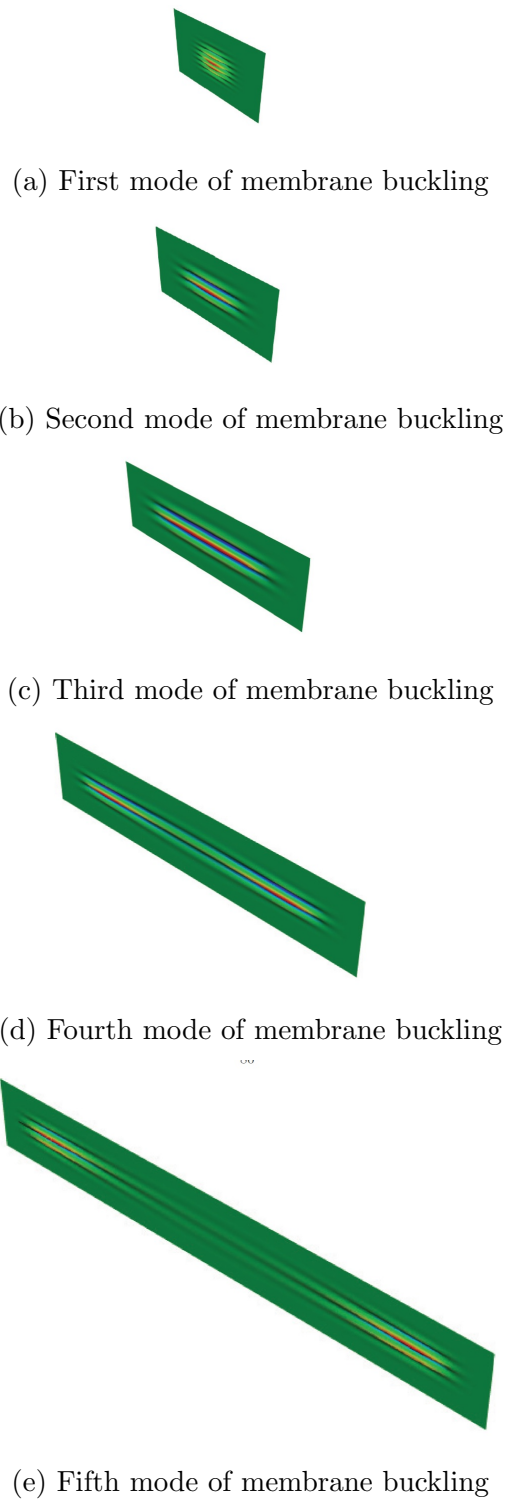


Figure 3.4: *Buckling analysis of the Kapton membrane under axial loading in five stages*

plane displacements are re-scaled to the same amplitude such that, when these sets of displacements are added together and then correlated at the mesh, the maximum imperfection height is equal to the membrane thickness.

3.4.4 Validation of the Axial Loading on the Membrane

In order to prove the validity of preceding model, a previously published model by Satish Kumar [36] is replicated using our computational framework within Abaqus finite element analysis software. The characteristics of the Kapton membrane material used within this validity simulation are stated in table 3.3. The dimensions of the Kapton membrane material are $1.5m \times 0.5m$ with a variational thickness of $2.5 \times 10^{-4}m$, $5.0 \times 10^{-4}m$ and $1.0 \times 10^{-4}m$

Mass Density	Young's Modulus	Poisson's Ratio	Element
1420 (kg/m^3)	$2.5 \times 10^9 (N/m^2)$	0.34	S4R

Table 3.3: *Material properties of the Kapton membrane used for the validation simulation within Abaqus FEA*

Using the same initial conditions, constraints and boundary conditions as stated in previous section, 3.4. An axial load is applied in the longitudinal direction of the membrane to act as the horizontal displacement. The axial load is defined as $\varepsilon = \frac{L}{L_0}$ where L is the stretched length of the membrane material and L_0 is the original membrane material length. The geometry of the membrane is defined as a single dimensionless ratio (α) between the length (L_0) and the width (W), giving the formulation, $\alpha = \frac{L_0}{W}$.

The eigenvalue increases with decreases in width-to-thickness (W/L) ratio increases as shown in figure 3.5. This result correlates perfectly with the axial loading simulation in the previous section as the dimensionless ratio (α) in-

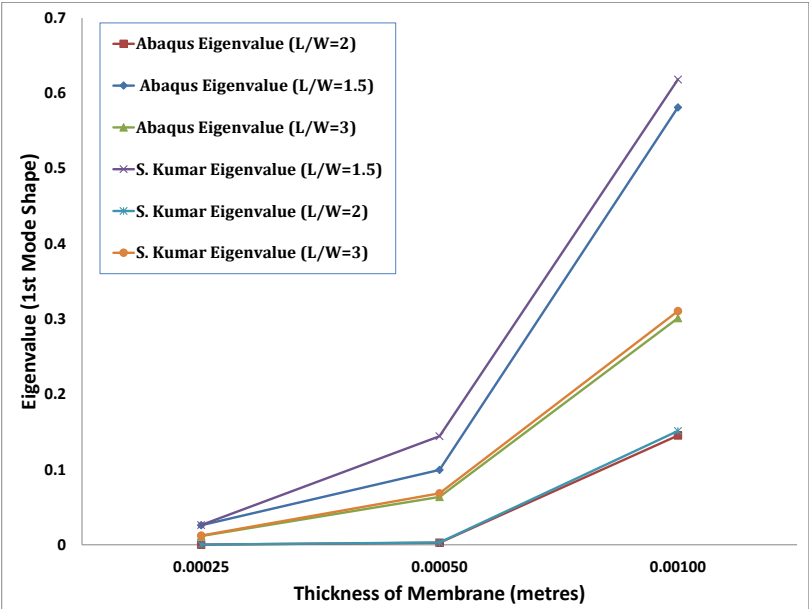


Figure 3.5: Comparison of eigenvalues with different thickness and aspect ratios for the Abaqus FEA simulation and previously documented results

creases, the number of wrinkles decreases but the relative size of the wrinkle increases as shown in figure 3.4. This is further verified by previous documented results, namely [39] and [42], which state that the amplitude of the wrinkle increases when the applied load is increased.

From figure 3.5, we can see the biggest disparity is seen within the $L/W = 1.5$ as 31% and this is concluded as an anomaly. The simulation was run successive times and the same results were achieved. A model was also run without the implementation of an IMP subroutine and even then, the highest disparity was measured as 29% for the $L/W = 1.5$ eigenvalue during axial loading. The contradictory statement is that the other two values have only a 1% and 3.7% difference which fit within the error margins of this work. Small percentage differences can be attributed to the integration of the IMP subroutine to define the membrane material dynamics to simulate wrinkling which has not been included in the work published by Satish Kumar [36].

3.5 Shear Loading on the Membrane Structure

There are a large amount of space missions whereby high accuracy and precision membrane structures of varied shapes and sizes are essential to the mission success. For example, sun shields for cold climate telescopes, inflatable reflector antennas, cosmic arrays & sails and space based radars. A few of the above stated membrane structures will be partially wrinkled during deployment and functional commission, which may cause substantial problems. For instance, wrinkles in the solar array, could cause insufficient heat extraction and wrinkling within solar sails could make them uncontrollable. However, it has been stated that small magnitude wrinkles could also produce benefiting effects i.e. a growth in the out-of-plane stiffness or the reverberation or the oscillation desensitization of the membrane.

In this section, we will present a numerical examination of a wrinkled membrane under shear loading. It should be noted that a number of experimental results and solutions have been published already but the primary aim of this simulation is to explore the dynamic accuracy and robustness of our membrane model created within Abaqus. The prime focus of this study will be to investigate the evolution of wrinkles on the surface of a Kapton membrane subjected to shear displacement.

3.5.1 Simulation Methodology

In order to stabilize the model before any loads are administered, a small uniform pre-stress was applied to the membrane at the start of the simulation. One must be careful at the amount of pre-stress applied to the structure

as it must be sufficient to govern the preceding buckling analysis but minuscule enough to not influence the derived solution. Once the pre-stress has been applied to the model, a static non-geometric non-linear equilibrium check (*STATIC, NLGEOM) is performed in order to permit the repositioning of the pre-stress phase, alongside the acute in-plane displacements.

Eigenvalue Buckling Analysis

After the initial conditions have been met, the next phase of the simulation is to perform an analysis to determine the buckling modes of the rectangular membrane. Once derived, these modes are utilized to seed acute imperfections which will cause the creation of wrinkles within the consequent non-linear geometric study.

In order to anticipate the relative modes of wrinkling of the membrane regulated by the boundary conditions and loads acting, an eigenvalue buckling analysis must be performed using the *BUCKLE command within Abaqus. It is critical to accurately compute the tangent stiffness matrix; the pair of the primary stresses and displacements from the preceding phase of the analysis, alongside the applied loads on the membrane. The corresponding eigenvalues and eigenvectors associated with the tangent stiffness matrix correlate to the potential wrinkling modes of the membrane, both in magnitude and shape.

Once the potential wrinkling modes have been derived, a linear sequence of chosen eigenmodes is integrated into the model as a geometric imperfection. The eigenvectors matching the smallest eigenvalues are of great interest as these eigenvalues are associated with the initial buckling load i.e. the formation of the initial wrinkle. But the primary objective of the study is to determine evolution of the initial wrinkle and the creation of subsequent wrin-

kles thereafter. Hence, the chosen imperfection modes which are integrated in our analysis is based on the accurate prediction of the final wrinkling pattern.

Once the suitable eigenmode shapes are selected, geometrical imperfections are applied via out-of-plane deformations within Abaqus using the *IMPERFECTION command.

$$\Delta z = \sum_i \omega_i \phi_i$$

where ω_i is the i^{th} eigenmode and ϕ_i is the the relative scale factor selected giving a magnitude as a fraction of the membrane thickness.

Post Wrinkling Analysis

Using the Newton-Raphson Method, a geometrical non-linear (*NGLEOM) analysis is executed governed by under edge displacement incrementation. In order to calculate the complete response of the structure, the Riks Method is utilized. The Riks Method is in theory the only accurate procedure since the equilibrium track of the membrane wrinkling has a number of unstable divisions, with each correlating to a bounded snap-through because of the generation of an additional wrinkle.

In simple cases linear eigenvalue analysis may be sufficient for design evaluation; but if there is concern about material non-linearity, geometric non-linearity prior to buckling, or unstable post-buckling response, a load-deflection (RIKS) analysis must be performed to investigate the problem further. The Riks method uses the load magnitude as an additional unknown; it solves simultaneously for loads and displacements. Therefore, another quantity must be used to measure the progress of the solution; Abaqus/Standard uses the

“Arc Length,” l , along the static equilibrium path in the load-displacement space. This approach provides solutions regardless of whether the response is stable or unstable. It was noticed that the model would fail if the displacement acting on the model is increased monotonically due to failure in the structural response. This failure led to all successive trials to utilize the arc-length resolution procedure in Abaqus (*RIKS) were unsuccessful, perhaps due to the wrinkling phenomena being a very bounded type of instability. Due to this failure, the only possibility of a successful simulation would be to use monotonic incremental displacement.

Stabilization was maintained in the model using the automatic *STABILIZE function within Abaqus. This function automatically interpolates pseudo-inertia and pseudo-viscous forces at every node when an instability is encountered. Once a instability is encountered, Abaqus stops using the quasi-static analysis and shifts to a dynamic integration for the equation of motion for the model, hence diminishing the possibility of generating numerical aberrations.

The viscous forces that are interpolated into the analysis model by the stabilize function are computed via the structural response within the initial step of the dissection phase, by presuming that the power exhausted to be a portion of the strain energy amid the initial phase. In order to attain excellent accuracy, it is recommended to set this variable to smallest value possible to reach convergence within the model.

3.5.2 Simulation Analysis

A rectangular Kapton membrane with similar dimensions to the Axial loading analysis was used, therefore 114 dimensions with widths ranging from 20 mm to 150 mm and lengths from 50 mm to 250 mm were used. The first step stabilized

the membrane model by administering a uniform pre-stress $\phi_y = 1.7N/mm^2$. This pre-stress was applied in the y-direction by manoeuvring the uppermost edge of membrane by $0.0005m$.

The consequent step in the process was to initiate an eigenvalue buckling analysis by applying a horizontal displacement at the upper edge of the membrane of a value of $3mm$. From initial analysis, it was concluded that eigenmodes correlating to eigenvalues lower than 0.2 relate to local deformation modes of the rectangular membrane. For this reason, the remaining analysis was carried out for eigenvalues above 0.2 and the Lanczos Solver within Abaqus is utilized to produce these eigenmodes.

To understand the membrane sensitivity against the amplitude of the established imperfections, a variety of synthesis of different eigenmodes and scaling factors were examined. For each set, a comprehensive wrinkling analysis was completed and the respective minimum ω_{min} and maximum ω_{max} out-of-plane displacements were calculated and can be seen in table 3.4.

Pre-Stress	ω_{max} (mm)	ω_{min} (mm)
0.025t	1.12	-1.49
0.050t	1.10	-1.48
0.075t	1.11	-1.49
0.100t	1.11	1.49
0.125t	1.09	-1.49
0.150t	1.11	1.50
0.200t	1.11	1.50
0.250t	1.14	-1.51

Table 3.4: *Effects of Imperfection Magnitudes*

From the computed values in table 3.4, we can see that the out-of-place dis-

placements are comparatively consistent even when the imperfection magnitude is reciprocated by a factor of 10.

From these computed results, it can be stated that the imperfection magnitude selected for the analysis is insignificant and a standard imperfection greater value than 0.2 were selected for this analysis, established by Abaqus and each multiplied by $\phi_i = 0.125t$. The variable that maintains and applies the damping factor to manage occurring instability within Abaqus was altered from the default value of 2×10^{-4} to 1×10^{-8} . This was altered using the *STABILIZE FACTOR = 1×10^{-8} to reduce the aberration between the simulated equilibrium way and the physical way.

3.5.3 Wrinkling Analysis

From the simulation results, it can be concluded that the general behaviour of the membrane is relatively linear, however a small softening can be seen at the origin of the membrane. This conforms to the generation of the initial series of wrinkles, therefore, indicating the end of the exclusive in-plane nature of the membrane. The introductory in-plane shear stiffness is $100N/mm$, which eventually lowers by one third. From figure 3.6, it can be seen that the direction of the major principal stress relates to the orientation of the wrinkles, which are formed about 45° and evenly across the centre of the membrane.

The post wrinkling behaviour of the membrane under shear loading showcases some very intriguing effects, if looked in detail. As the shear displacement is raised, the wrinkles also escalate in amplitude. Eventually becoming unstable and in turn creating additional wrinkles with small wavelengths. It is observed from the simulation results that there is a high density of wrinkles in the middle of the membrane, implying that new wrinkles are mostly created in this area.

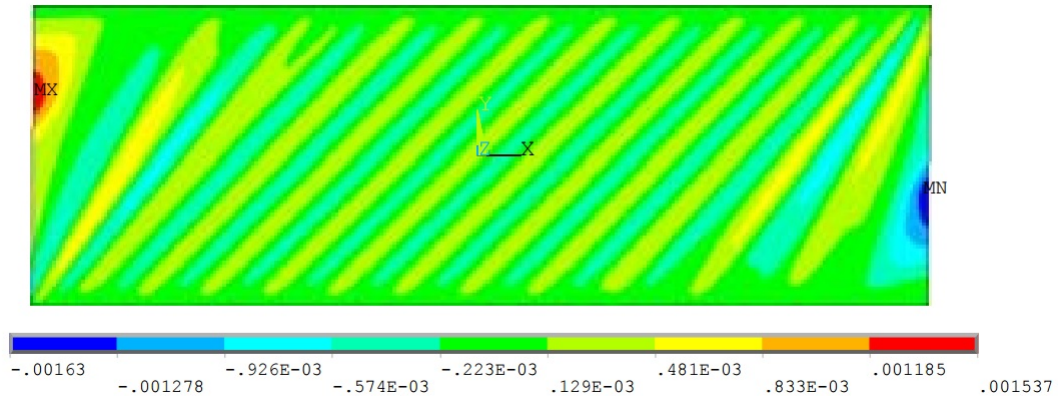


Figure 3.6: *Wrinkling of the membrane under shear loading*

The large wrinkles occur at the ends of the membrane, the end sides and do not move much across the membrane as they are restrained by the corner supports.

The transition from one shape of the wrinkle to the next is very rough and is caused by the local instability. In some of the simulations, it was concluded that the solution would not converge and the analysis had to be restarted with the damping intensity factor decreased to 1×10^{-7} . This allowed the computation to finish successfully however the damping factor had to be further increased for the subsequent step. In essence, changing the damping factor within the simulation has a similar effect of generating a varied amount of hysteresis within the model.

3.5.4 Validation of the Shear Loading on the Membrane

Once again, a model is created within Abaqus to prove its validity when compared with previous published and documented results. Similar membrane properties and characteristics are utilized within this shear validation model as stated in Section 3.4.4 with the sole difference of the applied load and boundary constraints on the Kapton membrane. The bottom section of the

S.No.	Thickness	Abaqus FEA Results		S. Kumar Results	
		No. of Wrinkles	Eigenvalue (1st)	No. of Wrinkles	Eigenvalue (1st)
1	0.01	14	0.30284	13	0.30289
2	0.02	13	0.30311	13	0.30314
3	0.03	13	0.30339	13	0.30342
4	0.04	12	0.30362	12	0.30371
5	0.05	12	0.30378	12	0.30402

Table 3.5: *Comparison of Eigenvalue and Number of Wrinkles when the pre-stressed of 0.005m is applied to the membrane Kapton material subjected to shear loading*

Kapton membrane is constrained using the *ASYMMETRIC boundary condition within Abaqus and a horizontal displacement of 0.03m is applied to the top of the membrane to initiate shearing in the x-direction only.

As the pre-tensioning is increased within the rectangular membrane, major wrinkles begin to form by propagating along straight lines between the loaded vertices. These also finely trace the regions of negative principal stresses, which show more clearly thin bands of compression on the free edges where wrinkles may be expected in practice. Number of wrinkles increases when element size decreases and eigenvalues vary with varying type of elements, number of elements within the mesh and thickness of the membrane as showcased in table 3.5 and the graphical representation in figure 3.7. Eigenvalue decreases by one tenth when the shear forces increase by ten times. This implies that the eigenvalue is inversely proportional to the shear force. At the end of the Abaqus simulation, the wrinkling pattern bears a clear similarity with previously documented results although the previous stated results do not showcase visually the secondary wrinkling formation between the primary wrinkles.

It is apparent from figure 3.7 that the model abides by the relativistic results expected from membrane shearing. The largest disparity between the results

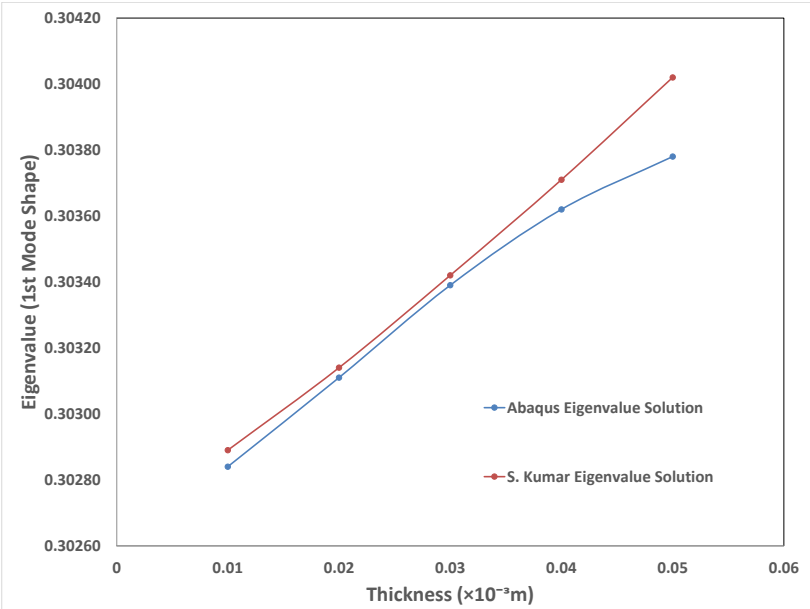


Figure 3.7: Comparison of eigenvalues with different thickness for the Abaqus FEA simulation solution, S. Kumar solution [36]

achieved from the Abaqus finite element simulation and Satish Kumar’s [36] published results are 0.08%. Even though this percentage difference is negligible, it can be attributed to the implementation of the wrinkling dynamic properties taken into account within this model while Satish Kumar did not implement a IMP subroutine to define the membrane material dynamics.

3.6 Discussions & Conclusions

In this chapter, we have defined the primary initial conditions used for all precedent and subsequent Abaqus simulations. These initial conditions are essential to create the fundamental governing equations that membrane structures abide to in physical reality. In order to understand the accuracy of our initial conditions, two separate simulations were designed, executed and com-

pared to previous documented work, namely published work by Satish Kumar [36]. This comparison allowed the accuracy of the rectangular Kapton membrane undergoing axial and shear loading.

The Finite Element analysis solutions deduced using continuum membrane elements within Abaqus and the variation in natural frequency is observed. In the simulation, we remove the initial imperfection from our model to eliminate the influence of the imperfections on the post-wrinkling characteristics by using the commands available within Abaqus and by applying an initial pre-stress. The relevant modes due to this initial pre-stress are found. The analysis of wrinkling problems of the wrinkle prediction of rectangular membranes under variation of thickness, element type, mesh density, length-to-width aspect ratio, tensile and shear loading has been studied.

The unconventional membrane theory was not adopted for this research due to the membrane theory underestimating the magnitude of the loading at impending wrinkling. Membrane theory predicts that the wrinkled regions are those under compression and also that an infinite number of wrinkle lines appear in the wrinkled regions. However, the wrinkles extend the length of the membrane and the shapes and sizes of the wrinkled regions are different from those of the regions under width compression. Therefore, the effects of the small flexural stiffness on the prediction of the critical non-linear component of the edge loading that causes wrinkling, on the number and the direction of the wrinkle lines, and on the sizes and shapes of the wrinkled regions are significant and cannot be neglected. Due to this, an iterative displacement approach is adopted within Abaqus FEA based on the Newton-Raphson method alongside a modified approach to the membrane theory is utilized to achieve successful results.

The FEA simulations presented within this chapter have been presented to

be accurate, reliable and capable of generating great quality results. Both simulations are accurate and the extended conclusions drawn lie within the governing equations used to simulate the deformation within the membrane.

Chapter 4

Smart Adaptive Structures

With energy becoming increasingly expensive and the current energy manufacture trends being limited and eco-hazardous, new solutions to sustain our current energy standards are needed. The modern trend in generating energy is using green processes to harvest natural environmental phenomena's and convert this into usable energy. For space based missions, the only natural and extensive natural source is the sun and, if there was a procedure to harvest the sun's rays and convert this into usable energy for space applications, the possibilities of use would be limitless. For these proposed solar power structures, massive structures are needed to harness sufficient energy for recycled use in other applications on ground or space. In the current climate, the only possibility of such a size of structure is a deployable inflatable structure that can be manipulated to fit into a payload volume of a space launcher available today. In this chapter, we will present a new concept and design of such a structure which has been biologically inspired and is able to increase its size and volume once deployed and is able to change its shape to any mission requirement needed.

This project has been carried out with Thomas Sinn, who is a PhD candidate from the Mechanical & Aerospace Department from the University of Strathclyde. Thomas has completed the LS-DYNA model of the deployment of the structure but his work has not been included within this research. A visual verification was carried out to test both models within Abaqus and LS-Dyna and they were considered satisfactory with difference of 4 % within the wrinkle formation, we believe this may be due to the inflation mechanisms being different in both simulation packages leading to varied stresses at different parts of the cell structure. The designed Abaqus model is used as a comparison with a physical experimental apparatus to showcase consistency, accuracy and robustness of the simulation.

An example of this type of structure would be the adaptive concentrator dish of the space based solar power station which will be manipulating the solar panels to have them perpendicularly facing against the incoming sun rays for efficient and effective energy gathering depending on the time of solar day. The respective multi-body was created to simulate the dynamic behaviour of the structure and relative perturbations acting on the structure using Abaqus and LS-Dyna.

4.1 Literature Review of Adaptive Smart Structures

Within this section, we will cover the modern published research within adaptive smart structures and the influences they may have had on the current research investigated within this Doctorate research. A critical examination is carried out, showcasing similarities, discrepancies, modifications and enhance-

ments of the current state of art techniques and procedures used to investigate the simulation of inflatable adaptive smart structures.

The study within this research has been derived from a number of previous research theories which led to a novel patented concept of smart adaptive structures. One aspect of the smart adaptive structure is the actuating pumps interconnected within the inflatable membrane cells in order to transfer pressure between each cell. The theory behind this intrinsic bio-inspired principle was utilized within this study as successfully implemented by Fleurent-Wilson [49]. Fleurent-Wilson proposed a bio-inspired application for an actuator which is derived from the ciliary muscle and choroidea controlling the curvature of the human ocular lens. The roles of the choroidea are akin to those of the curved aluminium plate and MFC's respectively, which govern the tension in the zonule fibers and the curvature of the lens (the membrane and its wrinkling, respectively).

The application of piezo-electric materials on curved plates have long been researched as actuator's [50] [51], an application for which there has been difficulty leveraging the large forces and small displacements available from piezo-electric materials [52] [53]. Fleurent-Wilson's contribution to the field is the actuated-MFC design and their application to control localized wrinkling of gossamer structures. The experiment is modelled, in part, after the symmetric corner tensile loaded membrane experiments by [39] [54]. The tension in the initially unwrinkled membrane was increased until visible wrinkling developed across the diagonal without the actuator. The actuator was adjusted to eliminate the target wrinkle for the initial non-actuator diagonal wrinkling tension. We have used a simple bio-inspired principle as the actuating control of membrane cells bending with the transfer of internal pressure between connected membrane cells.

One aspect of the studied problem is the bio-inspired concept; another is to simulate the inflation of the membrane accurately. The globally adopted uniform pressure approach can simulate the behaviour of a side curtain air-bag after its full deployment, but is incapable of deducing accurate inflation kinematics at the early stages of the analysis due to the large discrepancy of pressure and temperature from one end of the membrane air-bag to the other end. Consequently, a coupling Computational Fluid Dynamics (CFD) code with a Finite Element (FE) code, the Finite Point Method (FPM) is able to simulate the gas dynamics inside the air-bag, therefore, resulting in a much more robust and realistic inflation kinematics.

It should be noted however, that the conventional air-bag model was unable to predict neither the kinematics of the deployment or anything occurring during the inflation of the air-bag with the uniform pressure model. The restraint of this approach can be accounted for by the basic assumption that the algorithms used by this model do not account for the non-uniformity of the fluid dynamic variables, such as temperature, pressure etc.

In order to overcome this, Gai [55] proposed a concept to simulate the side curtain air-bag by utilizing the FPM approach and a comparison of computation results alongside test data results for both the flat airbag folded airbag showcased good correlation. The new model, named FPM is utilized to solve the compressible viscous and non-viscous flows. The density, velocity and pressure fields are deduced at specific points (Finite Points) established on interpolation over a cloud of neighbouring points. Due to the integration of the Lagrangian formulation, the points follow the streamlines of the fluid. The designed FPM fluid code by [55], has been integrated with a solid finite element code PAM-SAFE within her research. The pressure on the boundary points of the fluid is applied to the air-bag membrane elements and the membrane elements provide

the position and velocity of the boundary back to the fluid. A CFD air-bag model such as FPM can have its advantages over the uniform pressure model as a consequence of its capability to prognosticate what actually happens in the initial milliseconds of the inflation deployment. The FPM model is a great way to test-model a controlled air-bag deployment but lacks the density of the material dynamics to take into account the secondary wrinkles that form on the membrane during inflation. The FPM method doesn't account for any jet effects induced by the air-bag inflator, nor any phenomenon of gas propagating from one chamber to the next. One key component which is missing within this model is its inability to predict local phenomena such as, local pressure variation at a specific location of the air-bag.

Groenenboom [56] constructed a model for the commercially available code PAM-SAFE which takes into account the turbulent diffusion in a conical jet originating from the gas generator during inflation. Similar models can be found in other codes, such as Lupker [57] in Madymo and Hallquist [58] in LS-Dyna. Jetting models have been tested by Fredriksson [59] for OOP problems, where an air-bag inflates against the chest of a hybrid III dummy. Fredriksson showcases that the chest acceleration values for the dummy model tend to be too large when using the control volume model with jetting. His conclusions in regards to this problem is the inability for the prediction of redirection of gases when it hits an obstacle using the control volume model. Recently, a number of conference papers on coupled fluid-structure analysis have been presented. Mestreau [60] combines the PAM-CRASH and PAM-SAFE codes and use a re-meshing technique for the modelling of the fluid within the air-bag membrane. Therefore, the fluid mesh is kept inside the structure throughout the simulation.

It should be noted that neither of these papers offer any experimental verifica-

tion or comparison with previous documented results. The inequalities showcased within the PAM-SAFE and FPM models have been included within our inflation model utilizing the *FLUID CAVITY option within the finite element software ABAQUS and therefore, the research showcased here gives better results in terms of material dynamics and wrinkling. A clearer definition of the approach utilized within this study is given in the subsequent sections.

A similar approach was used by Marklund [61] by utilizing a multi-material arbitrary Lagrangian-Eulerian technique in the explicit finite element code LS-Dyna is used for the fluid and it is coupled to the structure using a penalty based fluid structure contact algorithm. The correlation between the test results and the multi-material ALE simulation are good except for a few discrepancies. There is a 26% error within the acceleration peaks and an 11% discrepancy between the time needed for full inflation between the experiment and simulated models. Possible reasons for these errors could be errors in inlet parameters, modelling of the surrounding environment being inadequate or even damping in the structure. Due to these intrinsic disparities, we did not model our structure within LS-Dyna and chose Abaqus as our favourable simulation software.

Diaby [62] proposed an innovative method in dealing with the numerical computation of buckles and wrinkles appearing in membrane structures by means of the total Lagrangian formulation, utilizing zero bending stiffness finite elements and a pre-stressed hyper-elastic constitutive law. The bifurcation analysis is carried out without presenting any imperfections in the structure. By incorporating a simple yet effective technique designed by Lam and Morley [63] in the solution procedure to deal with the possible complex roots when solving the arc-length method, making thus possible the treatment of wrinkles by bifurcation. This solution formulation correctly predicts the critical values

for wrinkles to appear as well as the wrinkled regions. The usual singularity of the stiffness matrix at the beginning process has been avoided by pre-loading the structure, either with an artificial internal pre-stress or a real load or displacement prescribed on the boundary. Although the wrinkles were correctly defined, analysis needs to be carried out on the amplitude, wavelength and number of wrinkles present. When utilizing this approach within our research, it was found that there existed a discrepancy between the experimental results and simulation results, primarily at the source of wrinkle formation. The proposed [62] methodology presented a much more ideal solution than expected from a realistic viewpoint and experimental testing. Barsotti [64] investigated the membrane as a von-Karman plate with negligible bending stiffness. Their relaxed energy concept solutions in a consistent linear-wrinkle elasticity theory, which allows recognizing the boundary between taut, slack and wrinkled areas. The tension field theory supports correct stress allocations and forecasts for wrinkled and slack regions, yet not wrinkle details such as amplitude, wavelength and number of wrinkles.

Wang [54] investigated the explicit time integration method incorporating the model of 'AIRBAG' within LS-Dyna to analyse the dynamic deformation of wrinkles with time, including the occurrence and the evolution. A solution for the numerical simulation of the wrinkles in the membrane structures is the development of the iterative modified properties (IMP) method based on the tension field theory. The IMP method, based on the membrane element, allowed the extent of the wrinkled region, the wrinkle angle, and the stress state within the membrane. One key disadvantage on the use of this method is that the stability of the algorithm is feeble. Using the IMP approach adopted by Wang cannot obtain the detailed out-of-plane wrinkles within the membrane structure. The detailed information about the individual wrinkles, including the wrinkle amplitudes and wavelength, can be predicted using the non-linear

buckling finite element method, based on thin shell element. The convergence of this procedure is enhanced by including artificial damping. Nevertheless, for this to be accurate, a highly mesh density needs to be implemented within the membrane structure to achieve analysis robustness. To overcome this problem, Wang [54] adopted the explicit time integration method integrating the model of 'AIRBAG' within Abaqus to analyse the dynamic deformation of wrinkles with time, including the occurrence and the evolution. The self-contact and damping in the 'AIRBAG' model is used to ensure the convergence, and the effect of the mesh density on the characteristic of wrinkles. It was observed that this methodology gave robust and good quality results, and numerical results can accurately simulate the physical experimental results. It was observed however, that there was no change in the mesh density on the model solution to produce satisfactory results. However, this model does not take into account the material dynamics at each analysis step iteration and this may be due to the computation power needed to integrate within the model. As our model was run on the High Performance Computing Archie-West, we are able to integrate the methodology utilized by Wang and take it one step further by integrating a modified VUMAT subroutine based on the IMP approach.

4.2 Introduction

From a number of published and documented sources, it is apparent that the current trend in energy consumption can not be maintained by energy generation sources on Earth used today, especially with developing countries becoming wealthier and reaching industry standardization and consuming more and more energy requiring higher energy demands. A simplistic ideology and complex solution would be to utilize the abundant supply of energy received from the Sun. One modern day approach would be to convert all ground based

to solar based power plants, the energy lost from atmospheric conditions could be decreased to the fractional cost of current day systems [65] [66].

For this to be a viable solution, the space structure in question must be larger than anything that has been launched into space till the current date. For this basic reason, the only possible solution to meet the payload restrictions would be to utilize deployable inflatable structures as they can be loaded into the payload at a portion of the deployed size. Another expensive solution to this problem would be to utilize an orbit assembly such as the assembly of the International Space Station. However, this proposed method requires a number of rocket launches to deliver the relevant payloads for assembly and goes beyond the financial scope of this proposed solution and will not be investigated any further. In the modern climate, deployable structures are used in an abundance of different space missions ranging from space habitats, booms, space buggies to reflectors, sun-shields to solar sails, to name a few.

In the past decade, considerable interest has been given to deployable structures for potential future solar power generation space missions within the larger corporations such as ESA, NASA, JAXA and a number of predominant academic universities and institutes. In the year 2012, NASA launched an ingenious program called NIAC (NASA's Innovative Advance Concepts) under the team lead of John C. Mankins to further the research into modular solar power plant designs, named the SPS-Alpha [67].

The system is created to collect the sun's energy by large-scale movable mirrors designed like a bee-hive type of structure onto solar panels which transmit the collected energy to a ground station via microwaves. A graphical representation of the SPS-Alpha structure can be seen in figure 4.1 for your consideration.

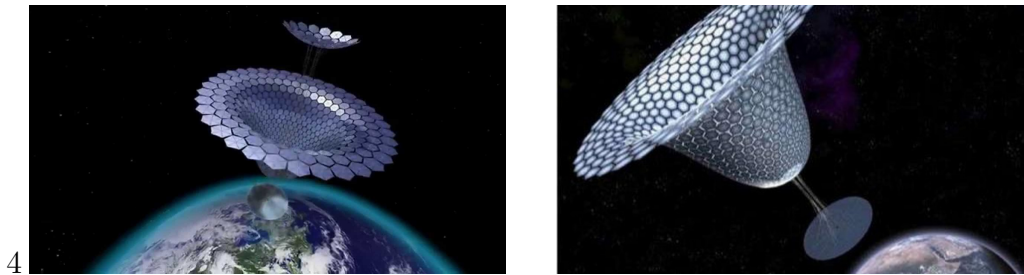


Figure 4.1: *Graphical Representation of the SPS-Alpha Structure*

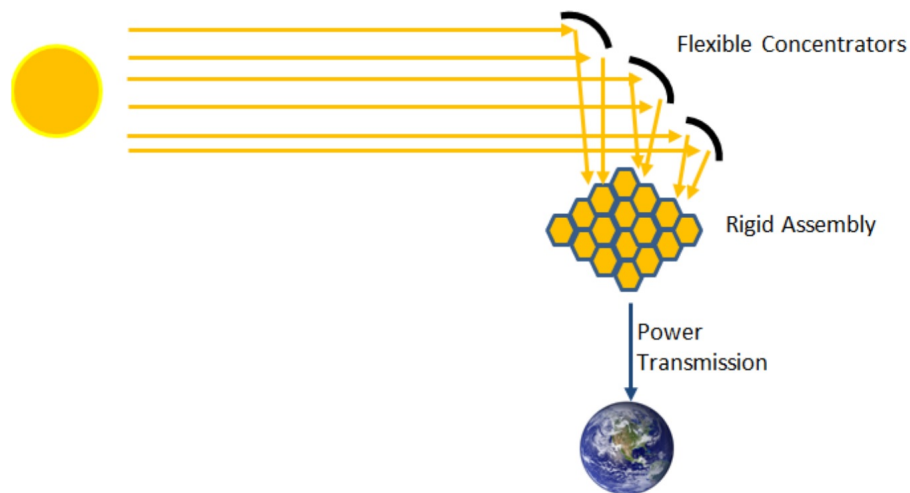


Figure 4.2: *Representation of the Space Segment in Operation*

4.3 System Design

The proposed design concept of the adaptive structure used to harness solar energy has two distinct segments. One of the segments is ground control which collects the transmitted energy and the space segment which is similar but not identical to the SPS-Alpha whereby, concentrators will be used to redirect and focus the solar energy onto the solar panels and this can be visualised on figure [4.2](#).

It should be noted that in order for safe operation of the space segment of the proposed design concept, since the energy collected needs to be transmitted to

the ground station in a control and collected manner. For this basic consideration, only the application of geostationary space platforms with a unique ground station location is possible.

4.3.1 Ground Segment

The location of the ground segment depends predominately on the energy usage, the corresponding population density at the chosen area and the position of the space segment in orbit. The recommended locations for possible ground location are Brazil or Columbia for the Americas continent, Indonesia for the continents of Asia and Australia and Kenya or Congo for the African continent. Care must be taken in selecting a ground location, taking into account the international politics and the effects of the national and local community at the chosen site.

4.3.2 Space Segment

As stated previously, the basic design and architecture for the proposed space segment is similar to that of NIAC's SPS-Alpha structure. The proposed design consists of two separate sections, the stiff solar panel & transmission assembly and the deployable concentrator that redirects and focuses the energy from the Sun onto the solar panel. It should be noted that the deployable concentrator is a novel approach with a patent pending via the University of Strathclyde Research and Knowledge Exchange Services and the Department of Mechanical and Aerospace Engineering. This patent will be filed with the Intellectual Property Office within the UK initially with the final scope of having an international and corporation classification.

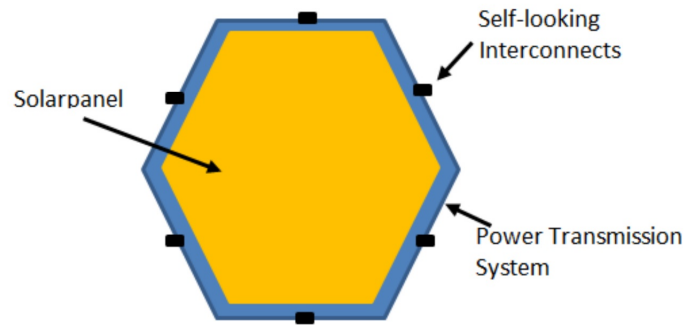


Figure 4.3: *Representation of the rigidized solar panel on top and the power transmission system at the bottom*

Solar Panel Assembly and Transmission Assembly

The solar panel and power transmission assembly is comprised of stiff hexagons with a radius of approximately 2.5 metres. This radius is chosen for easy transportation in the payload as several of the hexagonal shells could be stacked together, allowing the structure to be folded numerous times. A graphical visualization of the hexagonal shell can be seen in figure 4.3 and, showcase a high efficiency solar panel situated at the top and a power transmission system at the bottom pointing towards the ground segment. The energy will be transmitted to the ground segment via microwaves or lasers, however, these possibilities strongly depends on the legal schema and the safety issues associated with the use of these technologies for energy transmission.

The stiff shells are merged together after the deployment in space in a geostationary orbit. The shells can interlock with each other using the mechanical and electrical interconnects located on each of the six sides of the panel. The relative characteristics of each panel, such as health data and pressure is monitored and shared between panels. This allows up-to-date accurate information to be monitored with a validation method using neighbouring panels. It is proposed to employ controlled robots to assemble the relative panels into place

and act as maintenance robots for the complete life-cycle of the structure. For example, this may include damage due to space debris or micro-meteoroids.

Deployable Concentrator

For the deployable concentrator to work effectively and efficiently, the size of the concentrator has to be large enough to redirect and focus the sun's energy onto the stationary solar panels/power transmission assembly. The propose concept is an adaptable lightweight inflatable structure that can alter its shape and volume in space. The primary application of the proposed conceptual design is that several provinces, each with several individual cell structures will be integrated and assembled in space which will then become the basic framework for singular joined structure [68].

Each province consists of either a two dimensional flat surface or a three dimensional surface compromising of inflatable cells envisioning the cardinal pressure source. The interchangeable provinces and the cells are malleable i.e. the provinces and cells can be altered to any application from nano to macro scale. The high pressure used to inflate each individual cell is stored in a pressure tank and filled at the initial phase of the mission. Once deployed, the pressure is used to inflate each cell until the pressure tank is empty.

Each of the malleable cells or provinces used to compromise the solar power plane can be free-moving in a pre-defined distance to the solar panel/power transmission assembly or it could be anchored to a structure like the SPS-Alpha [67].

There are a number of ways to construct the various provinces once deployed in space to create the global structure. One possible solution is to deploy

a large number of provinces in one single space launch and inflate the cells with a predetermined pressure and cellular configuration. Once deployed, a space robot can construct the relative provinces into one global structure. The benefit of this method is that the construction robots have time to examine each cell and province before construction and therefore leads to a more robust and reliable global structure. If there is a failure in the global structure, the construction robots can easily replace any section or even alter the principal shape of the global structure.

4.4 Bio-Inspiration for the Structure

Over the millennia, evolution has led nature to safeguard its organisms in the harsh Earth environment. This key statement does not testify to the survival of the biggest or strongest organisms but to the survival of the organisms that are better at adapting in changing environments. In order to fully exploit this condition, it has become a common place for space systems to be bio-inspired [69].

One proposal for implementing this application is studying the execution of a plant or organism to an incurred catalyst, these experiences are called tropisms.

4.4.1 Heliotropism and Phototropism

Some flowers have the ability to trace the path of the Sun in the sky by using their leaves, or flower heads. This phenomena was discovered and documented in 1832 by the ancient Greeks and called Helio-tropism but the action was hypothesized to be passive [70].

Following a number of lab experiments in the 19th century, it was observed that some sort of growth processes in stems play an integral role within the phenomena and the phenomena was renamed in Photo-tropism in 1892. The rationale for the change in name was due to the number of lab experiments carried out on algae which demonstrated intense reliance to the luminosity and direction of light and not only sunlight.

The lab experimentation was inspired by the inherent motion of sunflower heads to follow the path of the Sun in the sky. In principle, the natural phenomena of Helio-tropism and Photo-tropism can be modelled in the lab without using the Sun as a light source.

4.4.2 The Principal

The biological cells which give the plant the capability to move are termed motor cells and they basically behave like hinges or joints. The motion of the plant is induced by the shrinking and inflammation of the contending cell sectors of the pulvinus (*motor organ*) [71].

The motor cells govern the density of the internal potassium ions and can change their internal turgor pressure and therefore alter the inherent shape. The aggregation of the potassium ions through the pathways in the plasma membrane facilitates the osmotic uptake of water into the cell, whereby expanding the volume and making the cell turgid. Additionally, the potassium pathways can also discharge potassium ions leading to water discharge and the shrinking of the cell. The alteration of the turgor pressure within the plant is a continuous slow process and can take from a few minutes upto hours. A faster example of this process is the carnivorous venus fly trap plant closing of its leaves to trap small insects. Once provoked, the motor cells in the leave



Figure 4.4: *Residual air inflated cell within a vacuum chamber*

joint line become candidly absorbent to potassium ions compelling the water to exit the cell, culminating to the prompt collapse of the cells and consequently closing of the leaf and trapping of in the insect.

With this simplistic operation, the flower has skill to perform relatively speedy motion of its head without the requirement of developing extra cells. Due to the absence of complication in this method, the action due to variation in pressure is ideal for the utilization in space based structures.

4.4.3 Residual Air Inflation

Residual air inflation is entirely a passive deployment mechanism which can be adopted and utilized in a variety of space applications. Conventional deployment mechanisms generally demand an intricate method or extensive auxiliary structures for successful deployment [72].

The principal behind the residual air inflation relies on small pockets of air,

trapped within a sealed membrane, expanding when the structure is exposed to vacuum. This expansion of trapped air then inflates the membrane.

The fundamental concept of the residual air inflation method is to exploit the increase in air when transitioning in a pressure variation from ambient sea level pressure to vacuum pressure. By encompassing the air within an elastic flexible membrane material, a super lightweight and compressible structure can be developed. If the cell with the trapped air is subjected to a vacuum environment, the inflation pressure of a few Pascals is sufficient enough to develop a semi-rigid structure. Figure 4.4 showcases two cells inflated using the change in pressure within a vacuum chamber at the Advanced Space Concepts Laboratory at the University of Strathclyde. This test proved the underlying theory of the cell inflation. Two separate thin layers of material were placed one on top of the other and, joined around the cell circumference.

4.4.4 Cell Design

The basic design objective was to integrate a very robust deployment system with the skill to change an organisms shape from nature. The concluding structure comprises of a considerable amount of cells which are rigidized using residual air inflation. Thin elastic membrane material is used to fabricate the cells. Further information will be given in the subsequent sections to investigate the fabrication process. A experimental laboratory test was designed and executed using Polyethylene Terephthalate (*PET*) as the elastic membrane material. This material is readily available in the market and generally used in rescue or space blankets. However, for an actual mission, it is advised to use Kapton DuPoint due to its protection against UV radiation. Heat was employed to glue the circumferences of the two cells at sea level pressure



Figure 4.5: *38 Cell array modelled in Abaqus simulation software*

and then vacuum conditions were administered to the membrane, resulting in rigidization and inflation.

To conform the inflatable cells to obey the basic laws of helio-tropism in regards to pressure change, two inflatable cells are connected together via a micro-pump. The micro-pumps sole purpose is to be the medium between neighbouring cells to allow air change between them and in turn, changing the volume of the cells. We can create a large horizontally level structure by joining actuator elements. Changing this actuator and other actuators locally on the structure can translate global shape of the structure into any given shape. A representation of a 19 actuator element array can be seen in figure 4.5. It can be seen in this figure, that there has been no actuation force applied and hence the presented membrane is flat.

As there is no single inflated cell, it mitigates the risk of a deflated cell within the global structure when compared with conventional inflatable structures. The global structural integrity and the adaptive nature of surrounding cells will ensure the array will maintain the desired shape even when one or several inflated cells deflate. This implies that a direct hit of a micro-meteoroid or space debris would not automatically cause structural failure of the complete global structure.

The entire design is effortlessly adaptable and scalable to any dimensions as a result of the cellular technique. For this study, we have used a cell with diameter of 14.5 cm. This diameter allows close packaging of cells into a $10 \times 10 \text{ cm}^2$ box.

4.4.5 Cell Fabrication

In order to establish a viable accurate and robust concept, relative fabrication techniques need to be investigated for the cells. Due to the widespread of applications and a variety of sizes, only a few cell types could be investigated due to time and money constraints.

The first fabrication concept investigated is to use flat circular Mylar sheets for the membrane material. These Mylar sheets are welded together along the circumference creating perfect ellipsoids once inflated. An array of Mylar cells was created with the dimensions $5 \times 2 \times 1$ (x, y, z direction) and can be visualised in figure 4.6. Mylar as a material is very easily available for fine sheets of acute thickness of micro metres and high plane stiffness. High stiffness is beneficial for inflatable structures as they provide a semi-rigid inflatable cell but detrimental for escalating the volume further once inflated. This is because of the large tensional stiffness of the membrane material, preserving consistent cell surface area. The fabrication techniques investigated for this study have been: heat welding the material, self-adhesive material and an additional adhesive layer.

The second fabrication concept investigated is to fabricate the cells with a hyper-elastic material, such as Latex or silicon rubber which in theory can increase its surface area with variation in internal pressure. The fundamentals of helio-tropism takes into account the relative volume variation of specific



Figure 4.6: *Prototype of the Myler array*

cells, whereby altering the global shape of the structure. In order to obtain these behavioural characteristics and attain a volume variation, the cell needs a membrane material which is very flexible and elastic so that acute differential pressure changes result in large increases in volume and also conclude that differential pressure resides within the inflated cell to self-deflate when susceptible to a vacuum environment. Albeit the requisite for elasticity and flexibility of the membrane cell is critical, it is also critical that the material chosen can be integrated with all other factors into the comprehensive architectural design of the cell. Therefore, the material capability used in the comprehensive fabrication process which permits for coherent assimilation of all factors into a single cell becomes a vital parameter for the design of the material. On this basis, a silicone based polymer material has been chosen as the membrane material.

4.5 Deployment Simulations

All simulations of the membrane deployment were modelled in Abaqus finite element software. Abaqus is not the conventional software used for airbag deployment analysis but using custom programming scripting code was written to model this phenomena.

The key benefits of using Abaqus to simulate this inflation is:

- 1 The Abaqus coupled Eulerian Lagrangian technique provides the ability to model gas flow in the airbag and include the effects of surrounding air during deployment
- 2 Ability to easily enforce contact interactions between the Lagrangian bodies and the materials in the Eulerian mesh using the powerful and robust general contact algorithm

- 3 Extensive material library to model woven airbag fabrics and gas equations of state

In order to model the enclosed inside surface area of the cell, the *CAVITY method is used to define the enclosed surface area. The *CONTROL VOLUME method is used to model the cell inflation. In order to use this method, a pre-defined mass flow rate into the enclosed structure has to be stated. The inflation is progressed by the gas expansion of the trapped air administering the structure to a decreased pressure situation. The residual air approach has no mass in-flow within the system but, it has to be predefined in the simulation in order to use the *CAVITY method within Abaqus. By integrating the control volume method and employing it to the complete structure, a complementary inflation attribute compared to the residual air method can be attained, on the basis that the complete volume increases without a stated initial point. The mass flow needed for the control volume method was deduced by utilizing simplistic ellipsoidal geometrics and thermodynamic equations by postulating that the gas is an ideal gas.

By assuming the modelled sphere is ideal, the computed volume of one inflated sphere is 1596cm^3 . The simulations showcased that if a flat shaped sphere of diameter 14.5 cm is used, after inflation, an ellipsoid of approximate volume of 500cm^3 is formed. Assuming the desired inflation volume of the cell in space to be 500cm^3 and assuming the pressure variation between the inside structure and vacuum environment of 100 pascals, the trapped gas mass deduced is in the order of 595×10^{-9} kg.

A custom triangular shaped mass flow attribute is chosen over the rectangular advancement due to the essence of the residual air inflation approach which will presumably start slow, lead to an optimal maximum and eventually slow down. The adopted triangular mass in-flow is given in figure 4.7.

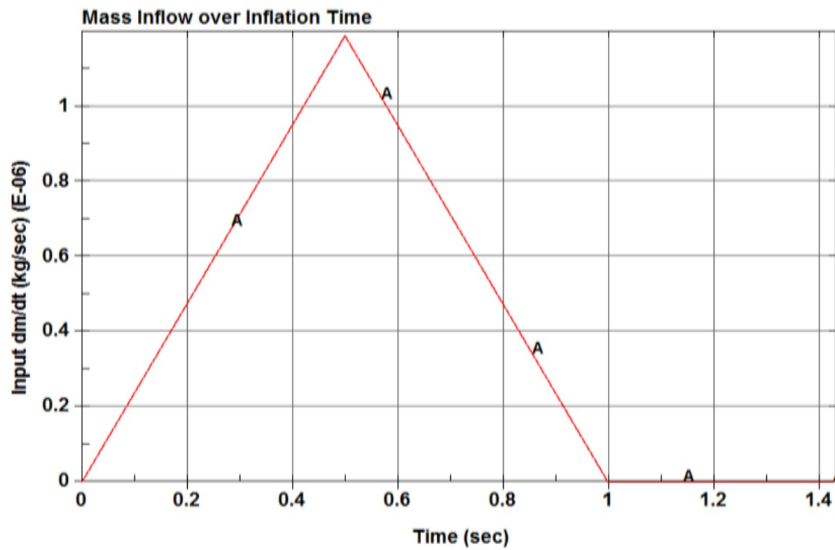


Figure 4.7: *Adopted triangular mass inflow for the control volume approach*

From the Abaqus simulations, it is apparent that the full inflated volume is accomplished at a portion of the inflation time, while the pressure expansion demands the entire inflation time. The pressure expansion is by cause of the prescribed triangular mass in-flow, it has to be confirmed if the actual pressure functions in a similar manner throughout the bench test.

4.5.1 Smart Adaptive Single Cell Simulation

Initially, a single cell was modelled in Abaqus. Two individual circular membrane sheets with a radius of 7.25 centimetre were placed above one another with a 1 millimetre gap in between as shown in figure 4.8. The side elements of the circumference were joined together using the *CONTACT CONTROLS to provide the enclosed volume required for inflation. The *CONTACT CONTROLS commands allows the user to provide additional optional solution controls for models involving contact between bodies. These are essential when contact incurs between two complex geometrical bodies and numerous contact

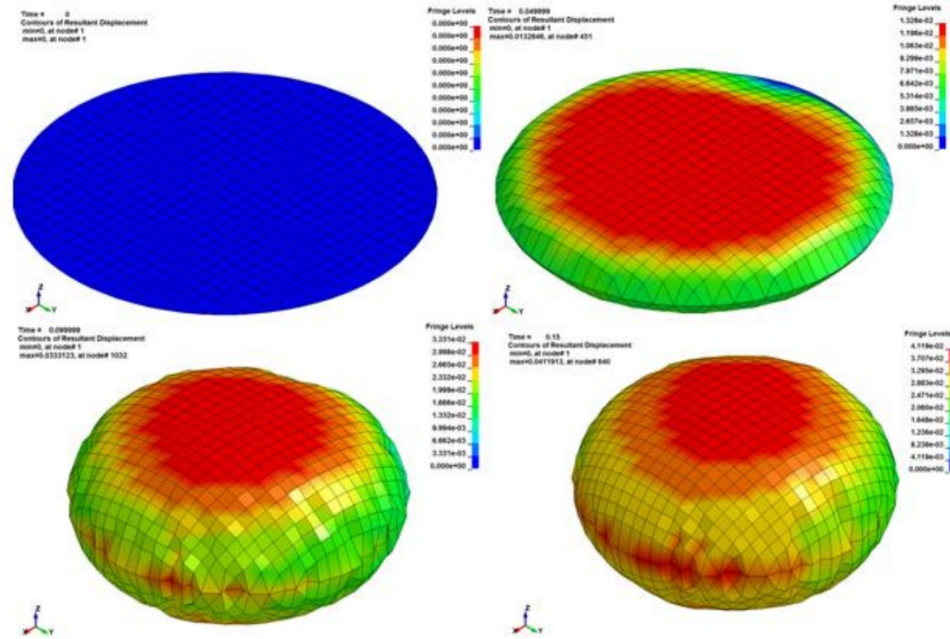


Figure 4.8: *Simulation of the inflation of a single cell in Abaqus*

interfaces. The simulation time for inflation was chosen to be one second.

We used the equations derived by Mladenov, an non-inflated radius of the 7.25cm circular sheet leads to an inflated diameter of 10.80cm. Using the stated calculations, it can be stated that the thickness of the inflated ellipsoidal membrane will be approximately 6.50 cm [73].

The single cell Abaqus inflation acts as a validation method for the residual air inflation concept and the practical vacuum tests carried out at the University of Strathclyde. Due to the size constraints of the vacuum chamber and only a small number of cells fitting the chamber at any one time, therefore, a number of simulations had to run consecutively for multiple cells. It should also be noted that with any ground testing or vacuum chamber experiments, all bodies are subject to approximately 1g gravity and should be taken into consideration for all analysis. This can be a severe external factor within low pressure and low stiffness structures and needs to be corrected for in order to obtain accurate

and reliable results. In order to correct for this, a secondary experiment of a sounding rocket, Rexus13 is suggested and was carried out in spring 2014.

REXUS13 Experiment

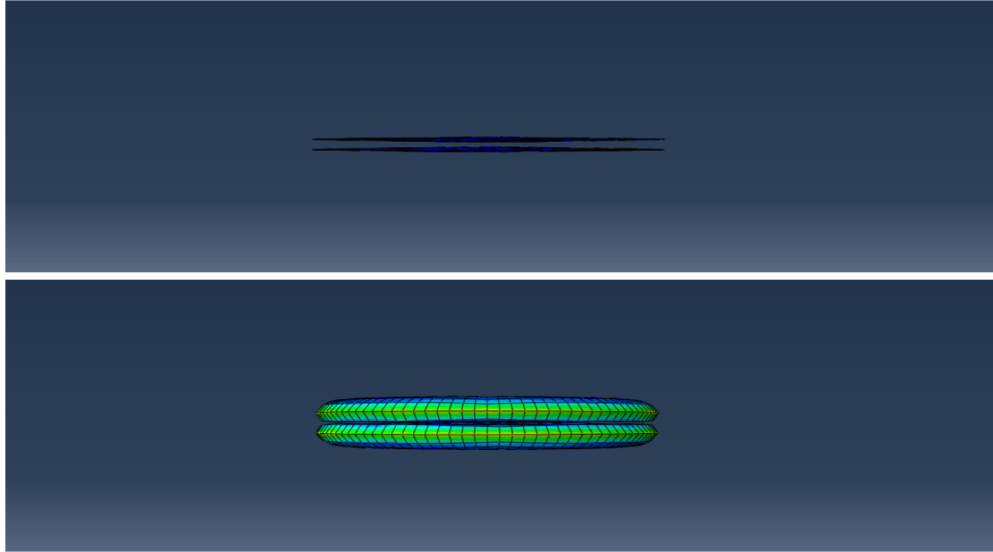
The experiment StrathSat-R was launched on-board the sounding rocket REXUS13 from the Swedish Space Port ESRANGE. The REXUS (Rocket Experiments for University Students) has been running for a number of years and is funded and managed by the German Aerospace Centre (DLR), European Space Association (ESA) and the Swedish National Space Board (SNSB). The mission programme is designed to discharge two cube satellites at an altitude of approximately 85 to 100km. Once the cube satellites have been discharged, the payloads will separate into inflatable structures using the residual air inflation method. One of the cube satellites and the one which infers to this study will deploy a 35 smart cell adaptive inflatable structure with two integrated actuators cells. This experiment was designed and contrived to verify and validate the residual air method and the mechanical modification of the biological inspired shape altering notion. Attached high resolution cameras and inertial motion units will record the deployment stages and dynamic behaviour of the actuation during deployment. The recorded information will be correlated to ground based simulations and experiments for comparison and error calculation.

4.5.2 Double Smart Adaptive Cell Simulation

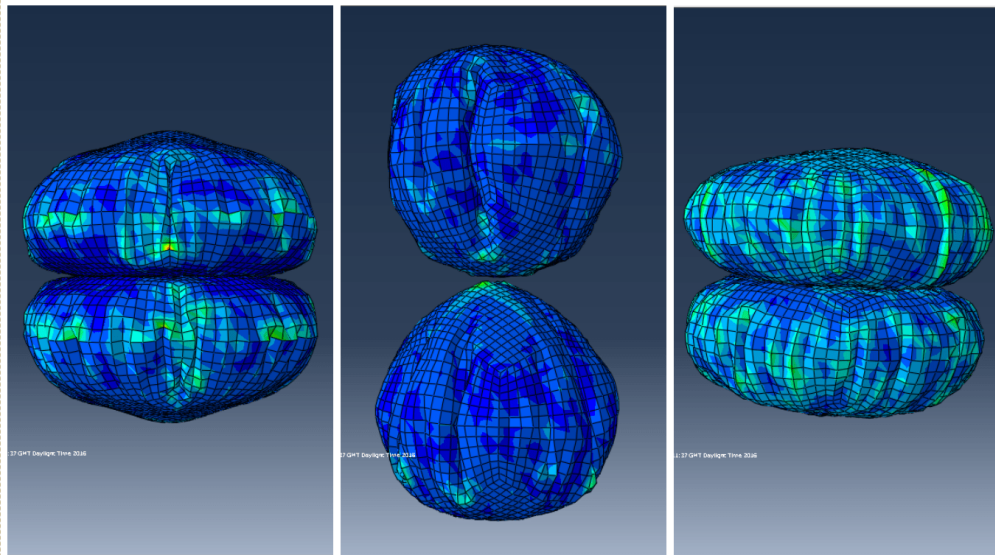
In order to ascertain a visual verification of the residual air inflation method of the double cell inflation, an Abaqus finite element simulation model is created. This model takes into account the specifications stated within the single cell

section with the only disparity being two cells are modelled in inflation as a connected structure. From the final sub-figure 4.9c, a relative clean comparison can be made with the experimental vacuum cell inflation in figure 4.4. Both figures showcase the structural wrinkling with the residual air inflated cell representing larger wrinkling with structural deformation perpendicular to the seams. This may be due to the cells being man handled after inflation within the vacuum chamber to the work desk or, due to inherent pressure & heat loss during the transfer from vacuum conditions to atmospheric conditions. It should also be noted that the contact between two spherical flat cells has been chosen to be ideal i.e. perfect bonding around the circumference of the cell. This implies that ideal loads are exhibited at each point on the bonded cell surface, leading to uniform stress and strain during inflation. Albeit, this may not be the case for the residual air inflation method, as seen from the figure 4.4, the bonding width is larger in certain areas of the cell surface when compared with other points, implying that a uniform even bond has not been applied.

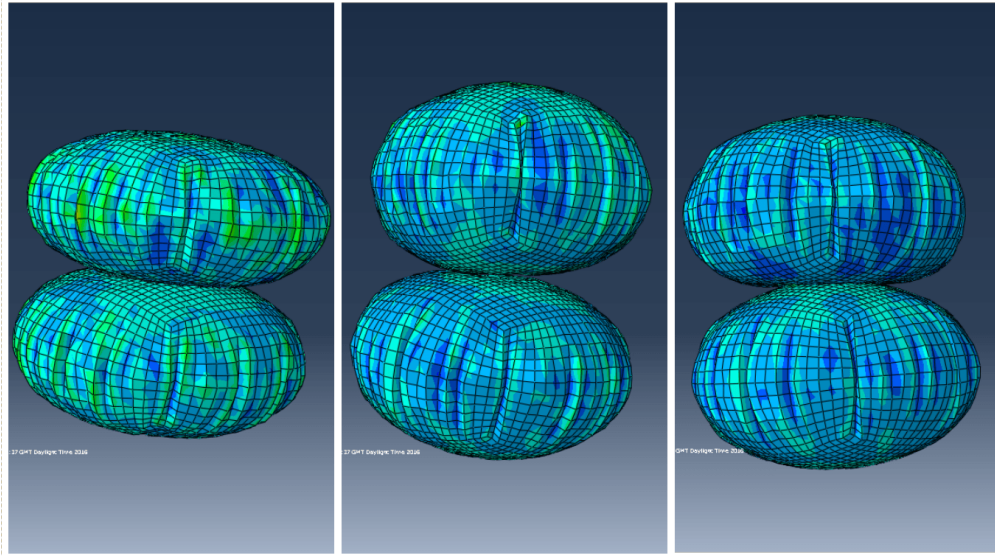
From figure 4.9, we can also see perturbations of the membrane within the double cell structure during inflation. As the cell is inflated, the gasses within the cell fluid cavity are moving and constantly attempting to reach equilibrium while at the same time increasing in mass for the initial 0.70 seconds. Within the Abaqus simulation model, this is illustrated as a bobbing motion of the cells along the incident normal of inflation i.e. the y-axis. from 0.70 seconds to 1.0 seconds, the gas inflation stops and a time is prescribed to the simulation to allow the gas mixture within the fluid cavity to reach a steady state of equilibrium.



(a) Showcases initial configuration of the double cells at 0.00 and 0.05 seconds of simulation



(b) Configuration of cells at 0.10, 0.20 and 0.30 seconds into the simulation analysis



(c) Final configuration of the inflated cells at 0.50, 0.70 and 1.0 seconds

Figure 4.9: Abaqus inflation of the multi-smart cell structure to be used as visual comparison with experimental results

4.5.3 Adaptive Smart Cell Array Simulation

Within Abaqus, a 5×2 adaptive smart cell array is simulated as represented in figure 4.10. This simulation was conducted to portray similar relativistic conditions as the experimental prototype inflation of the Mylar array as given in figure 4.6. As with the precedent section, this cell array model was only simulated to give base state for visual comparison against the experimental results and to convey some validation between the experimental apparatus and simulated solution.

The simulated cell array showcases similar wrinkling across the membrane surface of the inflated cell as the experimental mylar array. The volumetric size of cells from the experimental and simulated array are of similar magnitude with a discrepancy of only $0.2mm$ in the vertical radius and $0.4mm$ in the horizontal radius. This proves from visual inspection alone, the experimental

array inflated within vacuum conditions complies with theoretical principles adopted as given by the Abaqus finite element simulation.

Perturbations as showcased in the double cell simulated model can also be seen in the cell array model within Abaqus and this is due to the fluid cavity inflator gases reaching equilibrium. The cell array stops inflating at 0.7 seconds and 0.3 seconds are needed for the cell structures to reach equilibrium. It should also be noted that each cell within the array has a slight disparity between the inflation and final configuration i.e. wrinkling of the membrane surface the equilibrium path adopted. This is a critical consideration when modelling as it proves inevitably not one path is chosen by Abaqus during inflation with a gas mixture and every time the simulation is run, a difference of the inflation path can be seen while the final configuration is relativistically similar each time the simulation is completed.

A clear discrepancy which can be seen visually is the *5mm* gaps between the cells upon inflation. Extensive simulations were carried out to mitigate this gap but there were three key problems associated while modelling:

- 1 The gaps do not exist upon the initial configuration of the model within Abaqus before the commencement of inflation. Once the cells inflate, a decrease in diameter size is observed as the cells are stretched during inflation within the *y*-direction i.e. direction of principal gas inflation pressure.
- 2 One approach would be to constrain the edges of each cell with its neighbouring cell, as carried out within the experimental mylar array as represented in 4.6. The problem with simulating this in Abaqus is the inherent non-linearity present in the membrane material dynamics which would lead to self-penetration of the membrane surface upon inflation and the

resulting model would fail to converge due to negative eigenvalues.

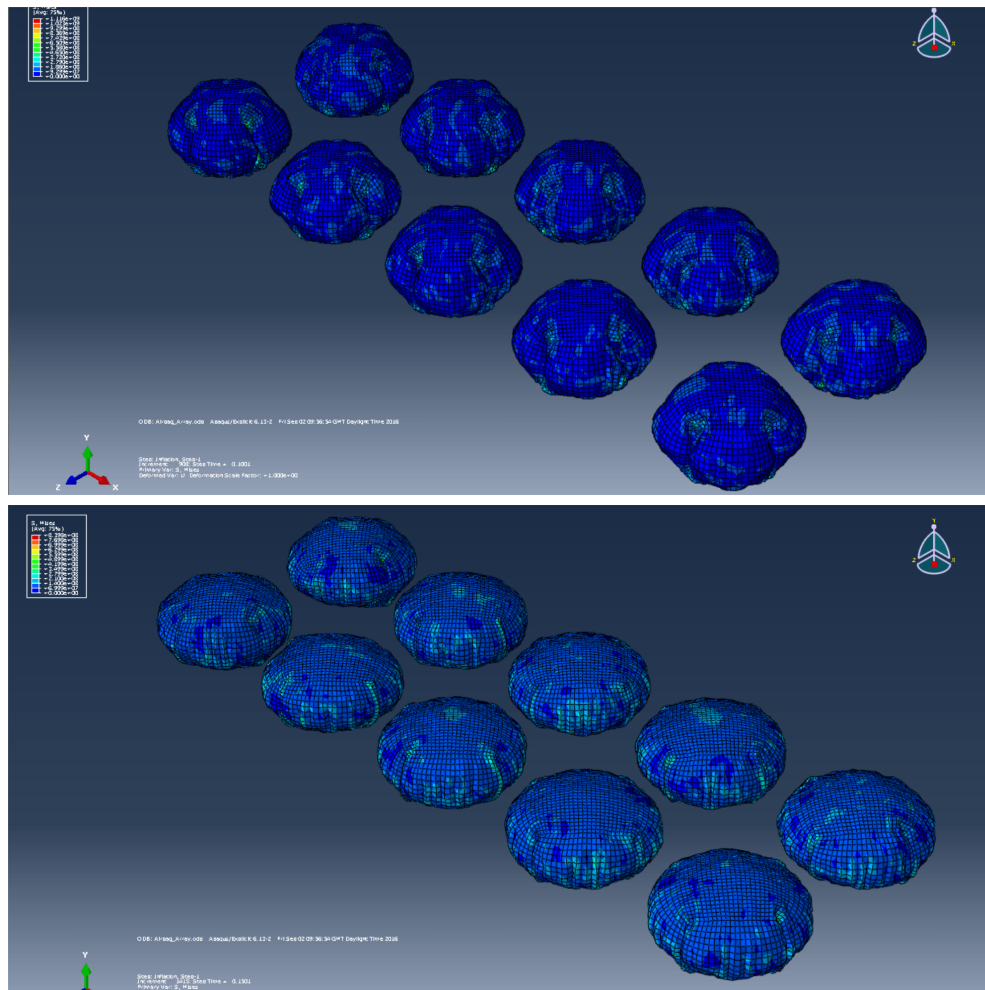
- 3 A secondary approach would be to overlap the cells within the initial configuration to alleviate the gap size upon inflation. If this concept was adopted, the model would be different from the comparison model and the base reasons for carrying out this simulation would be nullified.

Therefore, a simplistic visual inspection can be carried out of the experimental cell array and the Abaqus simulated cell array with clear focus on solely the membrane cell shape and size. While further investigation is needed to account for a much more robust and accurate model to showcase an exact verification. With the current computer needed and scope of the current work within this Doctorate, further research on this simulation has not been carried out but future work is proposed to use a different finite element simulation software to recreate the multiple adaptive smart cell array.

4.5.4 Multiple Cell Inflation from Packed Environment

A simulation of the inflation of a cluster of 18 cell elements comprising of two rows was modelled initially for a deployment analysis. For the starting configuration of this simulation i.e. before inflation, we assumed the cells to be flat in the axial plane of the 1U satellite deployment box, as shown in figure 4.11. Inflation time was chosen to be one second as before and all previously described initial conditions were assumed.

It can be seen from the inflation process, the membrane is constrained with the deployment box using the *BOUNDARY CONDITION, ENCASTRE command within Abaqus. This fixes all degrees of freedom at the selected region i.e. deployment box. The deployment box is an entirely fixed structure and



(b) Configuration of cell array at 0.10 and 0.15 seconds into the simulation analysis

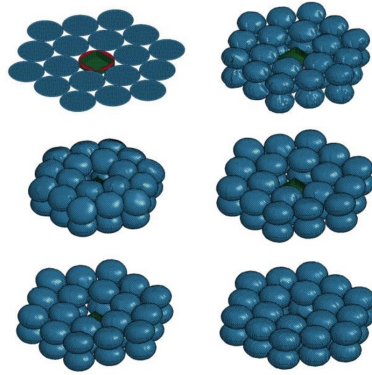


Figure 4.11: *Inflation of a flat packed array of adaptive membrane*

can therefore be considered a rigid body. Figure 4.11 illustrates the inflation from initial configuration to final configuration of the membrane inflation in six consecutive frames. The first five frames displayed have intervals of 0.1 seconds while the final frame showcases the configuration stabilization after three seconds of inflation commencement. The final frame was selected to represent the inflated membrane structure being completely stabilized i.e. without any oscillation as shown in figure 4.12.

Cell inflation from deployment box

For the secondary Abaqus simulation, we modelled a 19 cell array membrane being inflated from a deployment box, which relatively sits at the central point of the structure as shown in figure 4.13. Rigid constraints were used as the initial boundary conditions to compress the membrane within the deployment box before the inflation process.

An overview of the Abaqus simulation can be seen in the six frames displayed in figure 4.13. As stated previously in the first Abaqus simulation modelled, the first five frames have an interval spacing of 0.1 seconds while the sixth frame

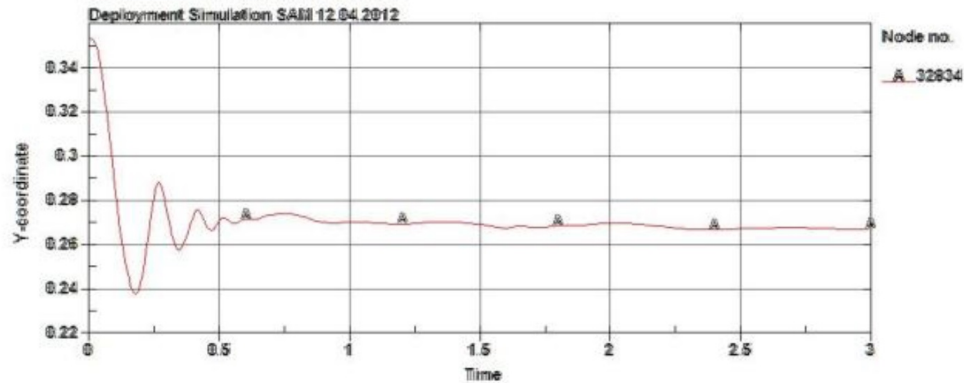


Figure 4.12: *Cell radius monitored during the inflation process from initial to final state*

is captured after three seconds have passed and no oscillation is detected of the membrane surface. It can be stated that the inflated membrane within the sixth frame is of the same shape and size configuration as depicted in the sixth frame in figure 4.11.

Within the first second of inflation, four constraints restrain the membrane from the sides acting as a rigid wall and one constraint is applied to the top, in order to compress the structure within the deployment box. Inflation of the membrane initiates after one second of the simulation and lasts for one second to reach final inflated configuration. From the Abaqus simulation, it can be seen that the initial radius of the membrane is 35 cm and decreases to 27.5 cm after inflation, which is the same radius as the deployment simulation from the first state described above. It can also be stated that the inherent shape and configuration of the final inflated structure is the same despite the packaging method.

Once the inflation is finished, the differential pressure does not change but one can apply leakage to specific cells or the complete array. Conventionally, this leakage could occur due to micrometeorite impacts, impurities in fabrication,

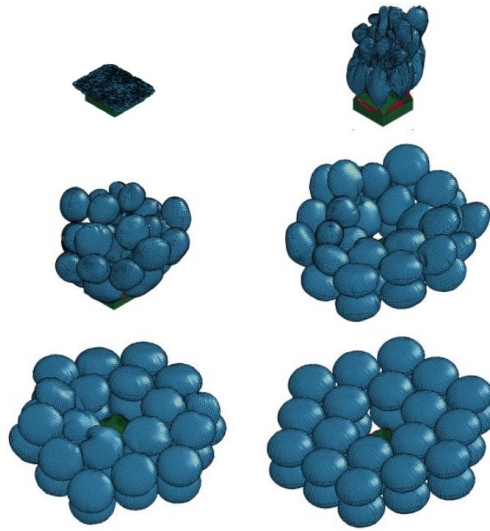


Figure 4.13: *Inflation of a membrane array (blue) from a deployment box (green)*

material deterioration, or innate leakage due to the inflatable structure being in space.

4.6 Method of Shape Adaption

The relative shape changing process of the inflatable membrane was modelled in Abaqus with a validation model created in LS-Dyna software as well. The process involved altering the air pressure between two neighbouring inflated cells. Due to the programming constraints in Abaqus and LS-Dyna for simulating accurate shape control of the membrane structure, a decision was made to create a multi-body code in Matlab and integrate it with the solution. Within this code, the cell is modelled as a point mass within the centre of the inflating cell. The connectors between these masses are posed as springs which can dynamically exhibit tension, compression and bending loads. Consequently, each point mass has three degrees of freedom (two in translation

and one in rotational). At present time, the structure is simulated in a two dimensional framework but plans are in place to expand the structure to be modelled in the three dimensional case soon. One aspect which is missing in the two dimensional case is to model the torsional stiffness within the springs but this will be incorporated within the three dimensional case. The complex problem of modelling the micro-pumps for the change of pressure between two neighbouring cells is very problematic in a three dimensional finite element software. This is primarily due to the model being unable to converge with a rigid structure bonded to two membrane cells which are drastically deforming subjected to internal inflation in a acute interval of time. Currently, all hopes of having the model converge with the computing power available have been non-successful, future work has been planned to incorporate our model on the Archie-West high performance computer to achieve a solution for overcoming the cost of computing time needed for a small incremental analysis.

A simplified diagrammatic of the designed multi-body can be seen in figure [4.14](#). In the course of actuation within the middle cells, air is translated from the bottom to the top cell producing a volume change within the cells. As showcased in the schematic, the top middle cell applies a force to the neighbouring cells while the two neighbouring bottom cells apply a force to the bottom middle cell. With this change in volume and concurrently the change in pressure will bend the global structure at that region of pressure change. By interpolating a control algorithm within the simulation model, the structural shape can be changed into a desired shape and therefore enhancing the shape changing process. This is of great importance when modelling the structure in a three dimensional case or a structure with a high number of elements as the required shape change can not be characterized intuitively.

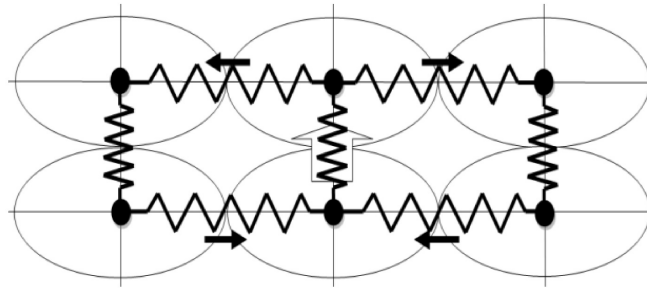


Figure 4.14: *Designed simplified schematic of the multi-body model*

4.7 Potential Applications

The designed smart structure alongside the finite element analysis and simulation code has a variety of potential applications due to scalability from the micro atom size robotic assembling structures to a couple of hundred metre long inflatable structures.

The structure concept has a number of applications such as solar sail substructure which can be rigidized during deployment and inflation. This flat rigidized structure gives a flat area for the solar particles to power the spacecraft for propulsion. Additionally, the flat rigidized sail can have its shape changed subject to solar wind and, therefore, making the spacecraft steerable with just the solar sail and, no need for additional thrusters.

An application for terrestrial rovers can also be proposed whereby the smart membrane structure could be continuously actuated to move the structure like a snake over terrain or swim in the water. As the actuation within the membrane occurs by inflating and deflating the structure, the rover can fit through small openings when compared to conventional rovers. Other proposed applications for this concept could be for disaster relief, for example, for finding survivors within collapsed buildings after an earthquake.

4.8 Discussions & Conclusions

The conceptual design of a solar based power station satellite is established on a geostationary based platform with a ground station where the energy can be transmitted for storage and distribution for use. The space part is comprised of a stiff structure made up of hexagonal cells which have solar panels on the top and power transmitters at the bottom. These hexagonal cells are connected to neighbouring cells via micro-pumps enabling pressure transfer between the cells to change the global shape of the structure.

An alternative approach for large space structures is given by using self-inflating adaptive membranes. With the passive residual air inflation method and the biologically inspired automation, a simple smart inflatable structure is constructed. Abaqus simulations were created of single cell and multiple cells and validated with experimental vacuum tests. Two separate inflation simulations were designed: one for the structure to be flat and the second for the structure to deploy from a deployment box and both simulations were compared for the final configuration of the inflated structure. This comparison illustrated that the desired configuration can be achieved regardless of the packaging shape. The deployment was further investigated by comparing the simulations to a REXUS experiment which launched in Spring 2014.

Abaqus simulations for the double cell and cell array structure were modelled to showcase visual validation between the experimental vacuum chamber results. The solutions achieved from Abaqus showcased validity on the size and shape of the final configuration, further verifying our previous statement. A disparity can be seen in the multiple cell array and this has been addressed in the previous sections and is sought to be due to the limitations of the Abaqus software and computer power when tackling problems with dense non-linearity

due to membrane wrinkling.

A customized design code was written to model the dynamic structure accurately within the inflation simulations. The code incorporated each inflated cell as a point mass which experiences bending, tension and torsion springs in-between them. The executed simulations illustrated that the structure can alter its focal point and orientation depending on the location of the sun in relation to the structure to ensure sufficient energy is redirected towards the solar power assembly. Particularly, decreasing the storage volume by folding up the deflated structure within the deployment box and the robust deployment of the concentrator should increase the cost and risk of launching a large structure into space.

Chapter 5

Inflated Beam Model

Inflatable booms are the support beams for 90% inflatable space structures. These booms act as load bearing pillars, which may act as structural members of trusses or the support structures of the membrane structure. The structural performance can be derived in numerous ways, including particular bending stiffness and buckled strength, or via combined performance index.

This chapter is divided into two primary sections, the bending and buckling of the inflated Kapton membrane beam and the post-inflation of the beam after deformation to restore the beam to its approximate starting configuration. The inflatable beam is modelled in the finite element software package Abaqus using membrane elements. To understand the membrane dynamics during deformation when wrinkling, the numerical subroutine based on the Miller-Hedgepeth membrane theory is created, utilizing a user-defined VU-MAT subroutine. In order to understand the behaviour of the non-linear inflated membrane, bending of a range of beams with different lengths and radii is investigated. And secondly, using the same software, the beam is re-inflated after the deformation has occurred and a range of pressures required to bring

the beam to its initial configuration is examined.

5.1 Literature Review of Inflatable Beam Models

Within this section, a brief literature review will be given of documented journal papers which have a direct influence on our methodology. Variations or modifications of previously documented work will be given, giving a clear understanding of the benefits and enhancements of our adopted simulation model to the inflatable membrane model subjected to deformation loads.

Leonard [74] and Comer & Levy [75] investigated the inflatable cylindrical cantilevered beams by the Euler beam theory. Within their research, the cross-section of the inflated beam is presumed unaltered during the deformation and the non-linear wrinkle behaviour of the fabric was reputed for by the presumption of the compressive stress in the fabric not being pertinent. Based on this theory, the wrinkle moment $M_w = \pi R^3 p / 2$ and the collapse moment $M_c = \pi R^3 p$ were calculated respectively. Within these equations, R is denoted as the radius of the cylindrical beam and p is the inflation pressure. Main [76] further researched inflatable cylindrical cantilevered beams with the application of the biaxial stress state in the beam fabric due to the consolidation of pressurization and structural loads. Main debated that the wrinkle of the fabric was due to the compressive strain rather than the stress and therefore, deduced lower wrinkling and collapse moments such as $M_w = \pi R^3 p (1 - 2\nu/2)$ and $M_c = \pi R^3 p (1 - 2\nu)$, where ν is the Poisson's ratio of the fabric. It should be noted that the above stated references do not account for the effects of the internal pressure and shear deformation of the fabric, Wielgosz and Thomas

[77] modelled the inflatable cylindrical beams by considering the pressure as a follower force and using the Timoshenko's beam theory to account for the shear deformations of the fabric. Therefore, an inflatable beam element was created and utilized for the analysis of simply supported inflatable cylindrical beam subjected to a central load. The numerical results calculated agree with the experimental data reasonably. However, their element does not include the wrinkling effects as they have carried out the analysis on a membrane element instead of a shell element. On a publication, Davids [78] refined an inflatable beam element by considering the internal pressure through the volume change and local fabric wrinkle utilizing Stein and Hedgepeth [79] taut and wrinkled criterion. The numerical results agreed very well with the experimental results of three-point bending test. Unfortunately, no comparison between these inflatable beam elements and the experiments of the cantilevered inflated cylindrical beams are available in the documented literature.

Zhu [80] investigates experimentally the bending of inflatable cylindrical cantilevered beams made of modern fabric materials. Using a dimensionless form of the load vs deflection, Zhu was able to characterize and generalize the bending behaviour of the inflatable cylindrical cantilevered beams of different sizes, materials, and inflation pressures in a unified way for easy application. It should be noted that within Zhu's experimental approach, the initial wrinkle is hardly noticeable and the transition from non-wrinkle to wrinkle is mainly given by the slope alteration of the load-deflection curve. Compared with the experimental data, the strain-based wrinkle moment provides a lower bound prediction while the stress-based wrinkle moment gives an upper bound prediction. In the post-wrinkle stage, the adopted Euler-beam theory using a non-linear moment-curvature model gives an upper bound estimation of load-deflection relationship while the finite element analysis established on membrane theory gives lower bound estimation. This discrepancy, of the measured

collapse moment and the theoretical prediction is approximately 42% and can be stated as primarily due to the beam-type method assuming the cross-section of the beam undeformed in bending while the finite element method approach has no restriction. Zhu stated that the actual collapse moment is very hard to deduce in experiments due to the inflatable beam becoming unstable near the collapse stage.

Wrinkling, developing from compressive stresses, often occurs for inflated membrane structures, and can be seen associated to geometric effects. The wrinkles evolve in the membrane in the direction orthogonal to the negative principal stress. This breaks the convexity condition of the strain energy density function of the membrane as stated by Pipkin [42] and Steigmann [48], therefore, the standard strain energy function cannot be used in the wrinkled areas.

In a research study on wrinkling, Pipkin [42] introduces the use of a relaxed strain energy function to examine wrinkling of an isotropic membrane, with wrinkling idealized as continuously distributed over membrane surface to maintain the strain compatibility. This research showcased that when a relaxed energy function is replacing the standard strain energy functions, tension field theory appears as an integral part of the membrane theory, and automatically satisfies several conditions such as convexity and Legendre-Hadamard conditions. In subsequent papers, Pipkin [43] [44] has demonstrated minimum energy and minimum complementary energy theorems with a relaxed strain energy density function for small and large deformation of membranes.

Patil [81] considers a hyper-elastic cylindrical membrane with non-uniform thickness pressurized by internal gas or fluid. When pre-stretched and inflated, the wrinkles are generated in a certain portion of the membrane depending on the loading medium and boundary conditions. The wrinkling is established through a criterion based on kinematic conditions acquired from

non-negativity of Cauchy principal stresses. The equilibrium solution of a wrinkled membrane is acquired by a particularized combination of standard and relaxed strain energy functions. The governing equations are discretized by a finite difference approach and a Newton-Raphson procedure is utilized to derive the solution. An interesting relationship between stretch induced, softening/stiffening with the wrinkling phenomenon has been identified. The effects of pre-stretch, inflating medium, thickness variations and boundary conditions on the wrinkling patterns are clearly delineated. No limit point or snap through behaviour was detected by Patil for the researched membranes with non-uniform thickness in the considered angles of pressures. One prime disadvantage of Patil's approach is not knowing the final shape of the membrane after wrinkling as detailed structure of wrinkles within a membrane is governed by its bending stiffness [82]. As this is neglected by Patil's incorporated membrane theory, the wrinkled surface is represented by plane surfaces through the definition of the relaxed strain energy function. It can be stated from Patil's research that for a more general usage, advanced simulations must be developed to consider a priori unknown principal stretch orientations, for instance through the eigen-solutions to the local strain tensor. These advanced simulations required to enhance Patil's work has been provided herewith in our research by using the finite element software Abaqusm with an integrated VUMAT subroutine.

Chan-Guo [83] proposed a new model to accurately deduce the wrinkling and collapse loads of a membrane inflated beam. Chan-Guo considers the pressure effects and utilizes a modified factor to achieve this accurate solution via modifying the pressure-related structural parameters established on elastic small strain considerations, and the modified factor is determined by our test data. A critical concern in regards to wrinkling and collapse loads of inflated beams is whether the material is regarded as an actual membrane, or as a very thin

shell, and therefore, there are two subsequent models for inflated beams. For the membrane model, the wrinkles will occur when the axial and compression reaches zero, in essence, the wrinkles will cancel out the compressive stress in the membrane. In the membrane model, both the critical wrinkling and the collapse moments are independent of the material properties, and therefore related to the cross-sectional size and inflated pressure only. In the thin shell model, the wrinkles will occur when the compressive stress reaches a critical value.

Compared to previous documented results, Chang-Guo's [83] test data gives a better correlation with the test results than the existing models in predicting the wrinkling and collapse loads of inflated beams with a discrepancy of up to 4.18%. This discrepancy is stated due to the modified parameter value which was obtained from experimental results and therefore, Chang-Guo stated that further bending tests were needed to derive a much more accurate modified factor. One key problem with Chang-Guo's method is that this modified parameter relies on a number of experimental tests in order to gain a precise modified factor and this brings a number of risk factors within the apparatus, such as using the same atmospheric conditions while testing, using the same variables and attributes for each experimental test, etc. Using previous documented experimental test results and comparing that to our derived finite element simulation model would have some discrepancy of 1.4% but was much lower than what was experienced by Chang-Guo. This lower observed discrepancy may be due to using vacuum conditions within our simulation and is discussed subsequently in this Chapter. Due to the financial limitations of this thesis, we were unable to carry out experimental test results and therefore adopted a theoretical approach within the analysis, comparing our values with previous documented results for validation.

5.2 Introduction

Inflatable beams and booms are utilized in a wide range of space applications due to their compressed storage, lightweight and easy packaging. Although it should be noted that a membrane element has approximately zero bending stiffness and, therefore, the wrinkles are easy to form during manufacturing, packaging and compression of these thin structures. Wrinkles are generally caused by surface irregularities and minimizing the load bearing capacity of precision space membrane design. These errors can impede the mechanical efficiency, hence, a large amount of study has been conducted on membrane wrinkling of membrane structures.

A number of researchers and scientists have created wrinkling analyses of inflated and non-inflated membrane structures. One of the preliminary studies was the tension field theory, in this theory it was postulated that the investigated membrane has no bending stiffness and no compressive stress is transmitted. With these conditions, the antecedent wrinkling is considered as an in-plane complication. Hence, within this theory, only the wrinkled areas and the wrinkling orientation is attained. Mansfield [84] [23] created a world renowned tension field theory and executed a comprehensive analysis of the load transmission of a wrinkled membrane. Pipkin [42] investigated the relative relaxed energy density for isotropic flexible membrane. This was the first documented solution to integrate the wrinkling theory with the iterative material properties model (IMP) created by Hedgepeth [85] and Miller [86]. This method was primarily based on the inspection of the membrane element presumed to be wrinkled, the geometric strain incurred perpendicular to the wrinkling direction caused by the materials out-of-plane deformation can be created by incorporating a changeable Poisson's ratio for the element.

As stated by Satish Kumar [36], wrinkling theory was the Iterative Materials Properties model (IMP) is predicted on the observation that if during a simulation a membrane element is deemed to be wrinkled, the geometric strain in the direction perpendicular to the direction of the wrinkles, due to out-of-plane deformation of the material, can be modelled by introducing a variable efficacious Poisson's ratio for the element. By administering an iterative material properties approach, Adler [87] incorporated this approach as a user-defined material (VUMAT) subroutine within the ABAQUS finite element software. Yang [88] created and modified the analysis procedure of the wrinkling of membrane structures alongside a customized constitutive relationship model. In this study, an integrated subroutine is established based on the methodology set out by Adler [87] and Yang [88], in which the Newton-Raphson method and updated Lagrangian formulation are utilized. With the suggested design, an inflated cylinder is subjected to bending & buckling and re-inflated to restore it to its initial configuration.

In physical scenarios, the wrinkling phenomena is due to the bifurcation and is dramatically affected by acute bending stiffness's; Wong-Wesle [89] recommended a different non-linear geometric analysis method for wrinkling phenomena established on the bifurcation theory. The prime advantage of the bifurcation theory over the traditional tension field theory is that the comprehensive wrinkling behaviour such as the number and amplitude of wrinkles can be deduced, while this information cannot be obtained in the tension field theory. Wong and Pellegrino [34] [39] [45], gave an exhaustive practical lab investigation of the progression and shape of reversible wrinkles. They suggested a generalized interpretive method to conclude the pattern, location, direction, amplitude and wavelength of wrinkles in thin membranes. Using this methodology as the foundation, non-linear geometric finite element membrane models were used to depict the growth and commencement of the wrinkles. The non-

linear finite element solutions were researched by using the simple Newton iteration with the flexible load incrementation for mapping out the load deflection response of the inflated beam. To determine the relativistic effects of the geometric non-linearities and the inflation pressure on the stability behaviour of the inflatable beam, a supported beam was studied within the finite element package Abaqus.

Within this research, the approach to govern the wrinkling progression and deformation arrangement with the simplistic process of secondary inflation to compensate for the deformation is theoretically investigated. To understand the non-linear behaviour of the inflatable cylindrical membrane due to wrinkling, the object is simulated in the finite element software Abaqus with an integrated VUMAT subroutine. The VUMAT subroutine for membrane wrinkling is established on the Miler-Hedgepeth membrane theory. The membrane material used is DuPoint Kapton with the same material properties as stated in the previous chapters. To identify the relative non-linear behaviours of the inflatable cylinder, number of simulations are carried out at different cylindrical radii and initial inflation pressures. Secondary inflation of the membrane cylinder will allow the structure to return to its approximate initial configuration to mitigate the structural performance deterioration incurred from membrane deformation.

5.3 Deformation of the Inflated Cylinder

In this section, we will evaluate the methodology used to model the inflated cylinder subjected to displacement loading. This inflated cylinder bends & buckles and the relative load-deflection is measured with and without the wrinkling subroutine, various material thickness's, elastic moduli and inter-

nal pressures. The wrinkling subroutine is explained in detail, showcasing the underpinning theory used and the benefits of using this approach compared to conventional methods.

5.3.1 Simulation Method

The *DYNAMIC, EXPLICIT analysis method was used to model the deformation in the cylinder. This method has been created to resolve exceedingly discontinuous, fast dynamic complications with ease. The method has an integrated powerful and reliable contact algorithm which inhibits additional degrees of freedom to the model. The complete cylindrical membrane was modelled in Abaqus and the end caps and cylinder body were created using three separate parts. These parts were assembled together using the *CONTACT CONTROLS function and this allowed the user to set the type of contact needed between different surfaces touching together. In order to apply accurate loading to the cap and edge of the cylinder body, the *RIGID BODY function was used. This function allows the user to select one node or element and applies the same load to any other selected area of the model. Therefore, for this study, we selected the middle node of the cap and using the sub-function *TIE, we connected this node to the edge of the circumference of the cylinder. This was done for both caps with their respective cylinder ends.

To model the inflation within the cylinder, the *SKIN method was used to define the inside surface of the enclosed cylindrical beam. This allowed only this surface to be isolated from the rest of the cylinder. Using the *FLUID CAVITY method as stated in the previous chapter, the inside of the cylinder surface was given a prescribed surface pressure. In order to prescribe a new pressure, an initial pressure of magnitude 6000 Pascals, must be given to the

inside surface using `*INITIAL CONDITIONS` function. This has two benefits, firstly, the cylinder is assigned a prescribed pressure in order to activate the fluid cavity method and secondly, the cylinder is made from an elastic membrane and it stops the cylinder from self-collapsing while having an acute enough temperature and pressure to not affect the final results. The relative behaviours for the inside gases must be prescribed within the coding and the properties defined by Abaqus within the user manual were used. These properties were used in an air-bag example and have been verified from experimental results. The gases used within the inflation were air, carbon dioxide, nitrogen, helium, nitrogen oxide and argon. Expansion parameters for each gas over a given time-scale were stated. Using the `*FLUID CAVITY ACTIVATION` function, the inflation of the cylinder was commenced. The amount of total pressure could be altered and the corresponding fractal of gases used were lowered or increased automatically. An amplitude was assigned to the load and inflation to give a smooth change in configuration to stop failure within the simulation and, allow the solution to converge. The bottom cap of the cylinder was fixed using the `*BOUNDARY CONDITION, ENCASTRE` function and, there were no degrees of freedom given to this region. The cylinder was inflated to an initial stable configuration and a load was applied to the cylinder using the `*DSLOAD` function, this allows a prescribed displacement to be given to any region of the cylinder.

5.3.2 Simulation Model

In simulating the inflated cylinder utilizing finite element method, the membrane element is generally employed due to the vast behavioural similarities to thin film structures. It has been stated that a membrane element has no bending rigidity and is stated as a surface element which relays solely in-plane

Parameter Name	Value of Parameter
Diameter of Beam	0.2m
Length of Beam	1.0m
Thickness of Beam	30 μ m
Young's Modulus	3.0 GPa
Poisson's Ratio	0.34

Table 5.1: *Membrane properties and geometric dimensions of the Kapton beam membrane*

forces. This inherent attribute makes it near impossible for membranes to showcase three dimensional wrinkling patterns or out-of-plane deformations but it does allow the computations of stress and strain in the membrane surface. The inflatable beam is numerically simulated by using M3D4 membrane elements with an initial resulting pre-stress, this is in essence, the initial internal pressure of the beam to stop the beam from collapsing on itself. The relative properties of the DuPoint Kapton membrane used and geometric dimensions of the beam can be seen in table 5.1.

Wrinkling VUMAT subroutine

Structural wrinkling of an inflatable structure can have detrimental effects on the performance, manoeuvrability and stability. Therefore, the wrinkling phenomena must be taken into account during the analysis phase to effectively account for non-linear behaviours of inflatable structures. Even though this prediction is a necessity for accurate modelling of amplitude and deformed area, it is still considered a very difficult and tedious process. Therefore, alongside the integration of a finite element subroutine, the simulation of the wrinkled region and the global dynamic response of the membrane structure

can be successfully modelled. To model the wrinkling deformation, a numerical algorithm established on the Miller-Hedgepeth membrane theory is created utilizing the user-defined material VUMAT subroutine inscribed in FORTRAN. The wrinkled area and directional magnitude, customized stress and strain of the structure can all be computed with the written algorithm. The *IMP Iterative Modified Properties* approach integrated in the VUMAT subroutine is a recurrent stiffness-adjustment operation to prognosticate the membrane condition such as taut, wrinkled or slack. The relative condition of the membrane is generally resolved with definitive standards established on principal stress or strain. The modern day prevailing standard of combined stress-strain criterion [90] are stated as:

$$\sigma_2 > 0 : \textit{taut} \tag{5.1}$$

$$\varepsilon_1 > 0 \textit{ and } \sigma_2 \leq 0 : \textit{wrinkled} \tag{5.2}$$

$$\varepsilon_1 \leq 0 : \textit{slack} \tag{5.3}$$

where σ_1 is known as the principal maximum stress, σ_2 is known as the principal minimum stress, and ε_1 is known as the principal maximum strain.

After the condition of membrane is postulated by the stated standards, the stiffness of each element must be adjusted as stated [90]:

$$K_{taut} = \frac{E}{1-\nu^2} \begin{vmatrix} 1 & \nu & 0 \\ \nu & 1 & 0 \\ 0 & 0 & \frac{1-\nu}{2} \end{vmatrix} \quad (5.4)$$

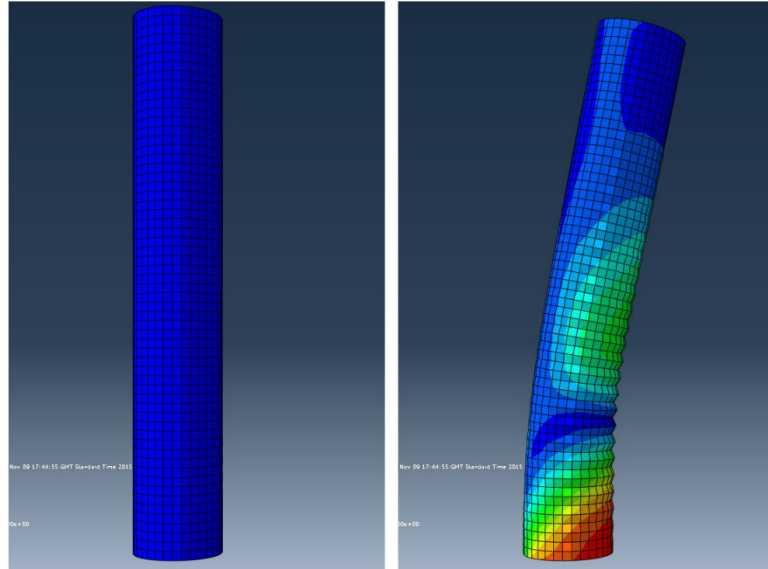
$$K_{winkled} = \frac{E}{4} \begin{vmatrix} 2(1+P) & 0 & Q \\ 0 & 2(1+P) & Q \\ Q & Q & 1 \end{vmatrix} \quad (5.5)$$

$$K_{slack} = \begin{vmatrix} 0 & 0 & 0 \\ 0 & 0 & 0 \\ 0 & 0 & 0 \end{vmatrix} \quad (5.6)$$

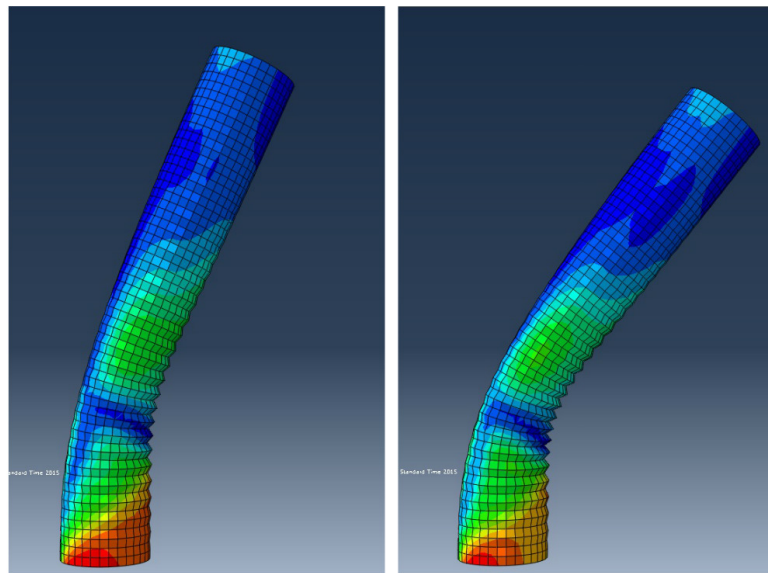
where $P = \cos(\alpha)$, $Q = \sin(\alpha)$, and α is the principal stress angle.

5.3.3 Simulation Analysis

An incremental step by step process of the deformed cylinder can be seen in figure 5.1, the increments were in 0.05 second intervals and the simulation can be summarized in 0.20 seconds from start to finish. The bending stiffness of the beam can be used to deduce the structural performance of the inflated structure. To account for bending stiffness, only the beam deflection versus the beam loading is needed. After extensively investigating the wrinkled region of the membrane from the output data file, it was concluded that progression of wrinkles degrades the structural performance of the inflatable membrane beam. Specifically, the deflection dramatically escalates subjected to an acute load once wrinkled regions are produced. There are numerous variables that can influence the behaviour of the simulated inflatable membrane beam, such as the membrane material, material properties, internal pressure, thickness



(a) Showcases initial configuration of cylinder and configuration at 0.05 seconds of simulation



(b) Configuration of cylinder at 0.10 and 0.15 seconds into the simulation

Figure 5.2: *Graphical representation of the buckling of the membrane model with and without the wrinkling subroutine*

Figure 5.3: *Correlation of the elastic modulus of the membrane model versus the beam deflection at a given displacement load*

Figure 5.4: *Impact of the membrane material thickness in regards to the beam deflection under the same given load*

5.3. As the modulus of the material escalates, the beam structure becomes inflexible in the course of linear deformation. The relative thickness of the membrane material i.e. Kapton DuPoint also assists in the beam stiffness, just like material modulus presented in figure 5.4. The dominant factor in the beams behavioural response and load carrying capacity is the internal pressure. Figure 5.5 displays the amount of load the inflated beam can withstand while its internal pressure is altered. While the linear deformation slope showcased in the figure is acutely raised, the maximum load, which can be sustained by the inflated beam is decidedly elevated.

The results obtained from Abaqus finite element software were further processed into a dimensionless load-deflection form and are showcased in figure 5.6. As a validation for comparison, the load-deflection relationship of the

Figure 5.5: *Depiction of the deflection load versus an altered internal pressure until membrane failure*

Euler beam theory is showcased in figure 5.6 together with the Abaqus FEA solution, and results derived by Comer & Levy [75], Yoo [91] [92] and Zhu [80] as given on the figure. This clearly depicts the dimensionless correlation between published work, showcasing the accuracy of our derived model.

This dimensionless data clearly demonstrates that this dimensionless load-deflection relationship can be approximated into a best fit single curve. Compared with the Euler theory, the deflection is linearly dependant on the external load and agrees very well with the Euler theory upto a value of 0.2. Beyond that value, the load-deflection relationship becomes non-linear due to the onset of wrinkling of the beam membrane until the external load reaches the theoretical collapse moment of the beam theory. In this post wrinkle phase, the solution based on the Euler beam theory with non-linear moment-curvature model gives an upper bound of the load capacity of the partially wrinkled inflatable membrane. This is primarily because the Comer & Levy's non-linear moment-curvature model neglected the cross-section ovalization of the wrinkled beam.

Figure 5.6: *Comparison of FEM dimensionless load-deflection relationships between current study and previous documented results [75] [80] [83] [91] [92]*

The comparisons also show that the Abaqus finite element method solution predicts a lower bound of load capacity in the post-wrinkle stage of the inflatable beam in comparison with the theoretical solution of Comer & Levy. This may be because the membrane finite element solution accounts for the cross-section ovalization effect of the inflatable beam, which is neglected by the Euler beam theory.

The initial wrinkle can be seen in the Abaqus finite element solution while is hardly noticeable in previous documented results stated and the transition from the non-wrinkle to wrinkle state occurs gradually. The critical point of wrinkle is deduced by monitoring the slope change of the load-deflection curve or by visual inspection of the Abaqus simulation.

5.4 Post-Inflation for Wrinkling Control

In this section, we investigate the pressure force needed to bring the deformed inflated beam back to its approximate initial upright configuration by applying an additional internal inflation pressure to the beam. It should be noted that with this secondary inflation, the beam returns to its upright configuration but is further deformed as the beam is enlarged and the membrane is stretched. This secondary deformation increases the strain at the edges and brings the material close to its rupture biting point. Although the beam reaches rupture point, it can still act as a vital support boom to the inflatable space structure until maintenance has been arranged for repair or replacement.

5.4.1 Simulation Method

As with the previous cylinder simulation, this simulation phase was also modelled in Abaqus and the final stage of the deformed cylinder from *Section 3* was used as the starting stage for this simulation. All initial model parameters were kept constant. Secondary inflation was added to the cylinder by increasing the various gas pressures within the *FLUID CAVITY option and applying a secondary *FLUID INFLATOR ACTIVATION command. It should be noted that the deformation phase and the post-inflation phase of the cylinder were modelled in two separate Abaqus simulations. This was due to the constraint in Abaqus of solely applying one *FLUID CAVITY option within any given simulation. This is due to a number of reasons for our model, primarily, for every fluid cavity an associated cavity reference node must be stated. Alongside the fluid cavity name, the reference node is used to identify the fluid cavity. The fluid cavity may be referenced by fluid exchange and inflator definitions. These reference nodes should not be connected to any

elements within the model. During the deformation of the inflated cylinder, the membrane undergoes a complex deformation, this deformation changes the position of the reference cavity node drastically. Due to this, we are unable to use the same cavity reference node and another cavity reference node must be selected concurrently, creating a new model simulation for simplicity.

The *FLUID INFLATOR ACTIVATION option is used to activate the fluid inflator definitions. The fluid inflator definitions can be used for:

- 1 Inflating a fluid cavity to simulate actual inflators used for air-bag supplemental restraint systems.
- 2 Inflating a fluid cavity with an ideal gas mixture different from that present in the fluid cavity.

This option is used to increase the underlying pressure within the cylinder. This pressure overcomes the deformation force and the cylinder starts to return to its approximate initial configuration i.e. approximate horizontal configuration.

5.4.2 Simulation Model

As used in the 'deformation of an inflated cylinder' section, we will use the same membrane element attributes for this model. The inflated beam is modelled by using M3D4 membrane elements with an initial resulting pre-stress and undergoing wrinkling deflection. The wrinkling deflection of the final configuration of an pre-stressed inflated beam under acute loading i.e. final configuration of the beam from the previous section's simulation FEA model.

The relative properties of the DuPoint Kapton membrane used and geometric dimensions of the beam can be seen in table 5.1.

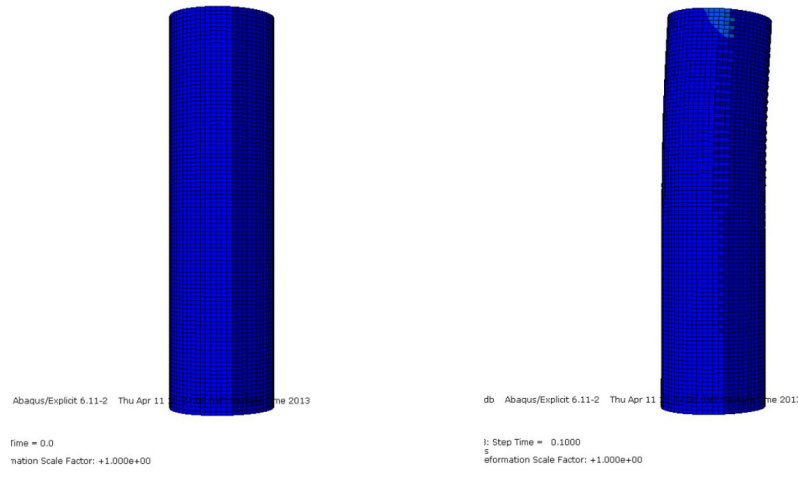
The full graphical illustration depicting the progression of the inflated cylinder from initial configuration to each phase of progression in 0.05 second intervals is shown.

5.4.3 Simulation Analysis

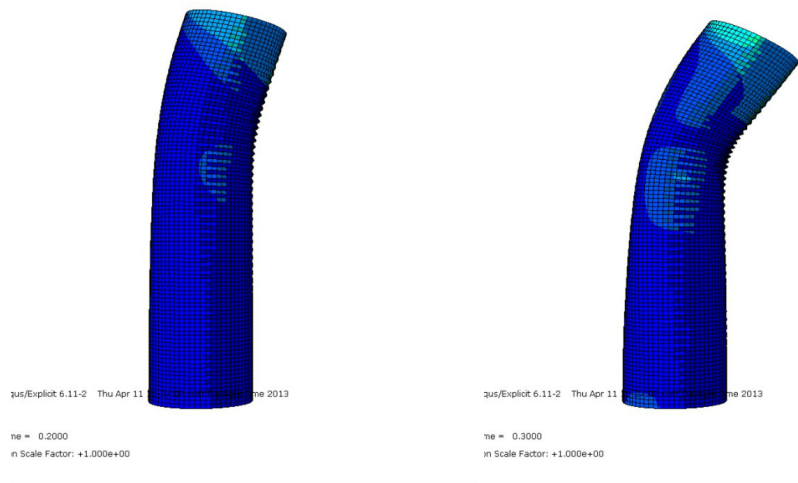
As stated previously, the bending stiffness can be used to calculate the beam configuration and the structural performance of the inflated structure. Using the beam deflection, beam loading and post-inflation pressure, we can calculate the bending stiffness and the membranes deflection configuration. It can be concluded from the output data file that the wrinkled region is mitigated as the membrane beam is post-inflated. This is due to the beams deflection being mitigated, resulting in the decreasing of wrinkles and enhancing the structural performance of the beam.

It should be noted that the due to the increase in pressure, the membrane is pushed to its limits and becomes fragile at the seams of the enclosed caps. This can be due to less flexure in this region when compared with the rest of the membrane. Therefore, the deflection is effectively diminished once the acute load is compensated for by the post-inflation pressure. As stated previously, the amount of inflation pressure needed to restore the deflected beam depends not only on the internal pressure, but also on the membrane material, material properties, internal pressure, thickness and the wrinkling formation.

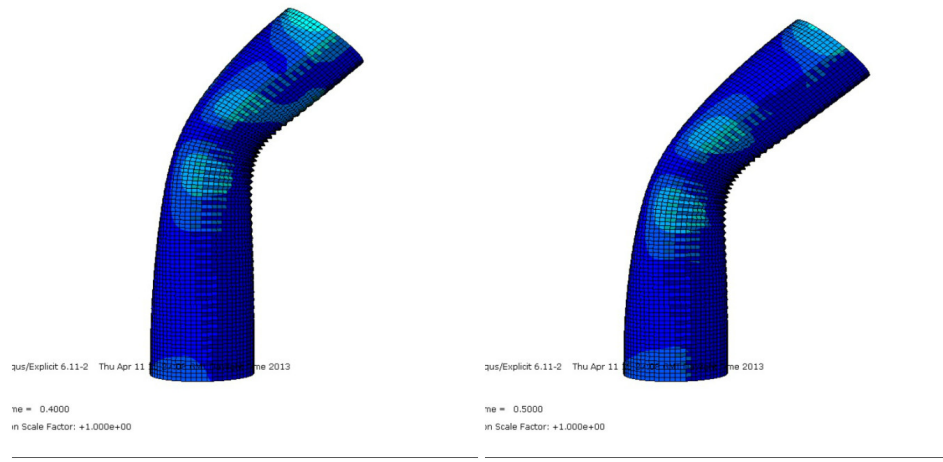
In this section, we discuss the above stated variables in relation to the response of the inflated deflected beam when subjected to post-inflation pressure of a



(a) *The bending and buckling of the cylinder from initial configuration to 0.05 seconds into analysis*



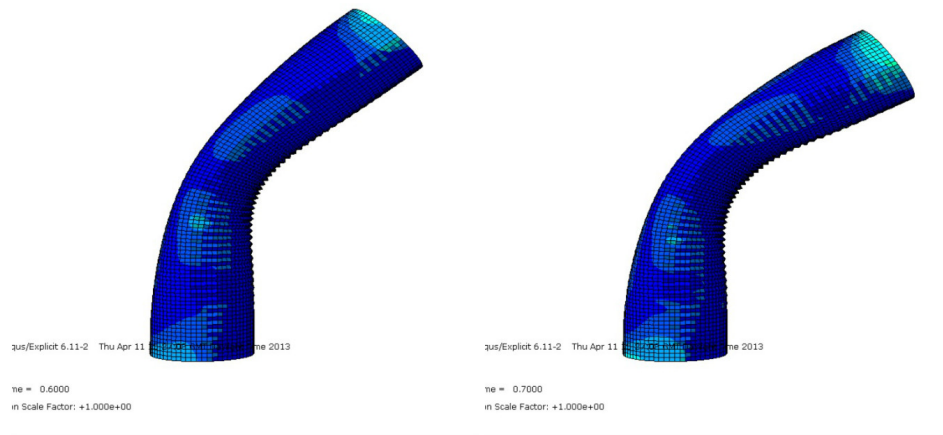
(b) *The configuration of the cylinder at 0.10 and 0.15 seconds of the bending and buckling analysis*



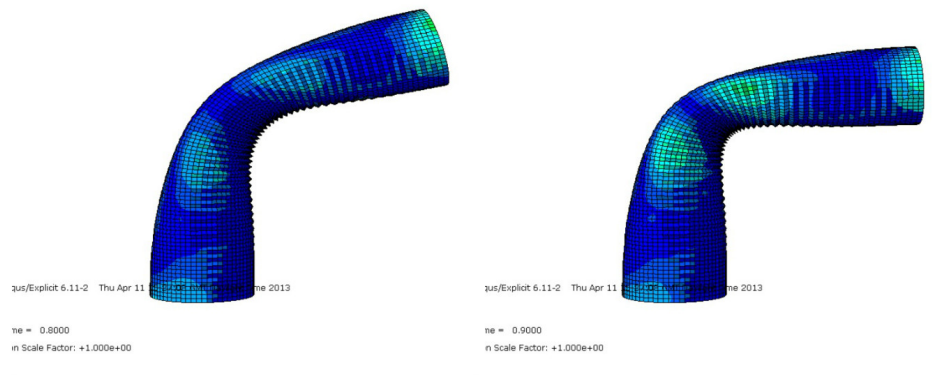
(c) *The configuration of the cylinder at 0.20 and 0.25 seconds of the bending and buckling analysis*

Figure 5.7: *Representation of the six phases at 0.05 second increments within the bending and buckling analysis*

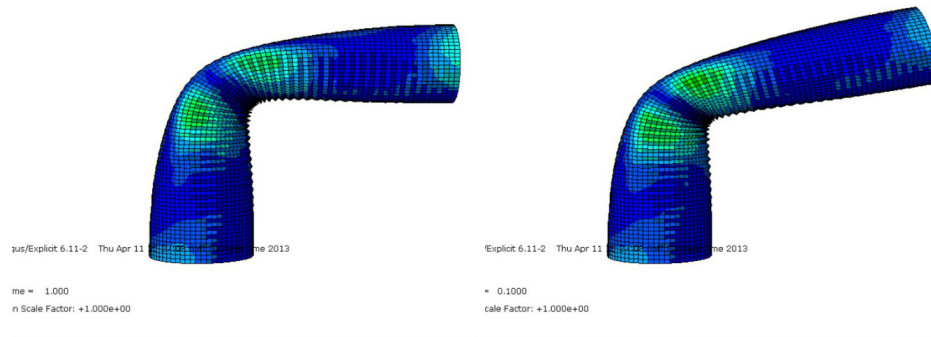
given amount. From the graphical depiction represented in figure 5.9, it can be shown that the inflated membrane reaches localized instability during the post-inflation phase. This is due to the post-inflation pressure overcoming the bending & buckling load and, the resulting pressure creates an instability at the unconstrained end of the cylinder. This instability is slowly dispersed, leading the inflated cylinder to reach an equilibrium balanced configuration. From figure 5.11, we can see the relative magnitude of the instability within the post-inflated membrane cylinder. This scale of magnitude is repeated in every simulation of varied cylindrical attributes, implying this spring-back of the unconstrained region of the cylinder is inevitable. It was noticed that with lower pressures of post-inflation led to smaller magnitudes of spring-back and the corresponding instability value. This could lead to a negligible instability which can be ignored by this study, and bearing that this study is only concerned with the cylinder overcoming the bending & buckling load and



(a) *The configuration of the cylinder at 0.30 and 0.35 seconds of the bending and buckling analysis*

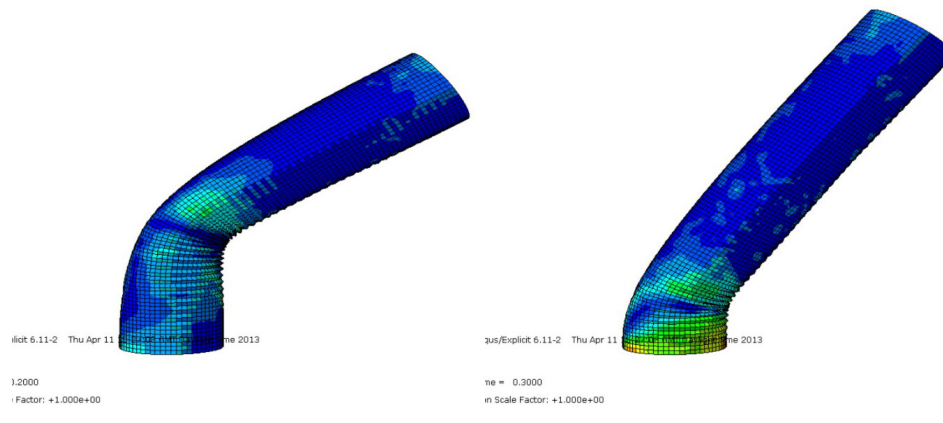


(b) *The configuration of the cylinder at 0.40 and 0.45 seconds of the bending and buckling analysis*

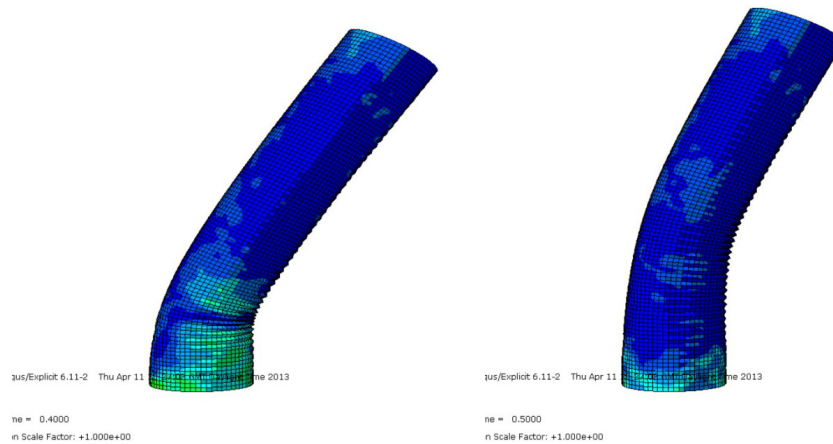


(c) The configuration of the cylinder at 0.50 of the bending and buckling phase while at 0.55 seconds, the analysis shifts into the post-inflation phase

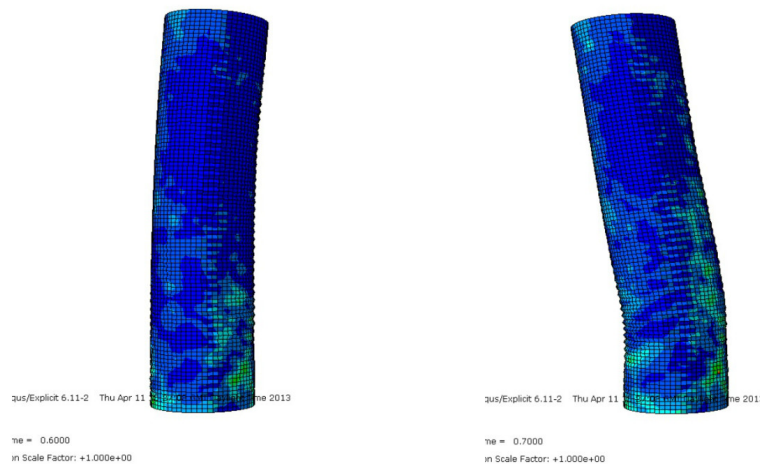
Figure 5.8: Representation of the final phases of the bending and buckling analysis while the last frame depicts the start of the post-inflation phase



(a) The configuration of the cylinder at 0.60 and 0.65 seconds of the post-inflation analysis phase

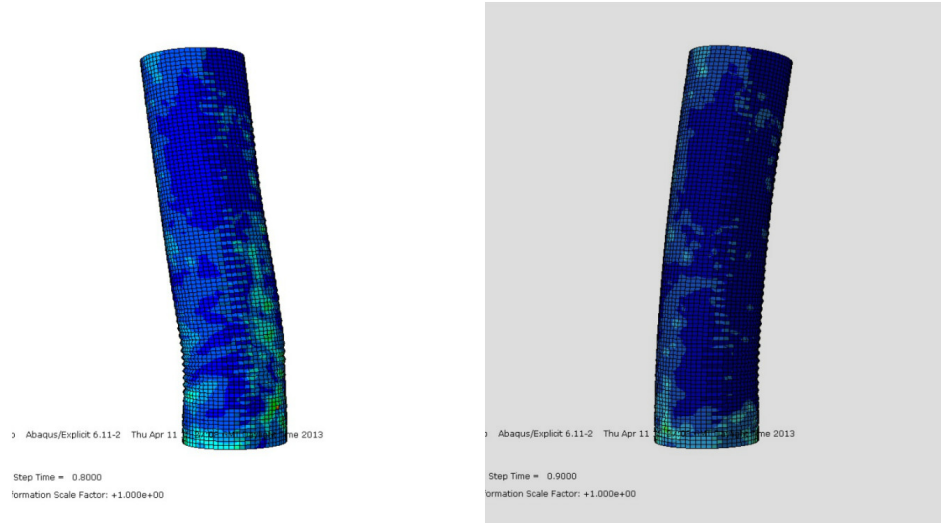


(b) *The configuration of the cylinder at 0.70 and 0.75 seconds of the post-inflation analysis phase*

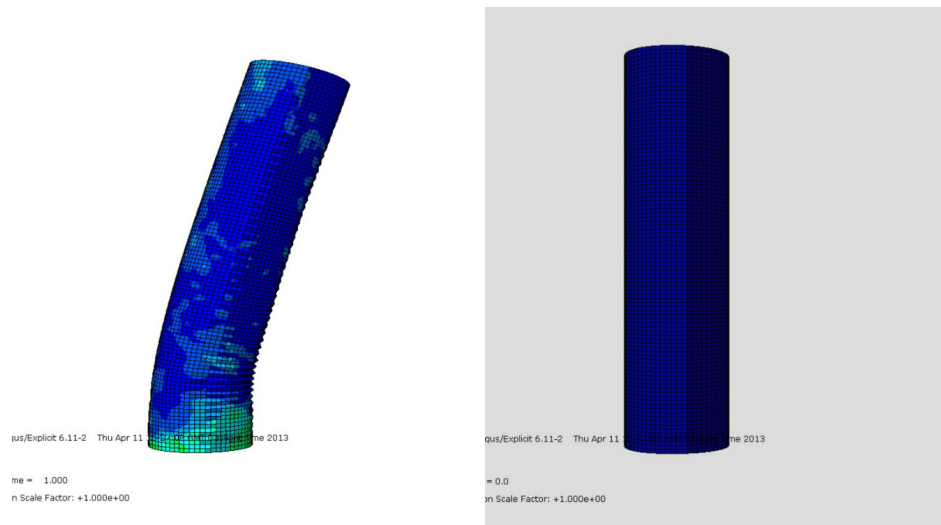


(c) *The configuration of the cylinder at 0.80 and 0.85 seconds of the post-inflation analysis phase where the cylinder overshoots the initial configuration and bends on the opposite side of loading*

Figure 5.9: *Illustration of the post-inflation phase of the inflated cylinder subjected to bending and buckling. The final frame also depicts the over compensation of loading*



(a) *Depiction of the third & second last (0.90 seconds & 0.95 seconds) stages of the analysis. Here, the instability of the cylinder is apparent with it weaving like a pendulum circumscribed to atmospheric frictional resistance*



(b) *Representation of the final two phases at 1.00 and 1.05 second interval. The remaining instability within the cylinder reaches critical point dispersion, resulting in an equilibrium balanced configuration*

Figure 5.10: *Illustration of the post-inflation phase of the inflated cylinder subjected to bending and buckling. The final frame also depicts the over compensation of loading and the dispersion of the instability forces on the inflated cylinder*

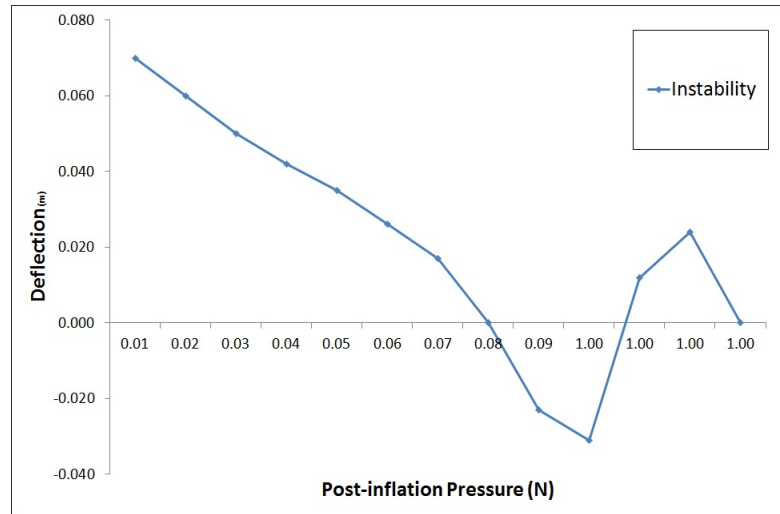


Figure 5.11: *Displaying the magnitude of the cylindrical instability within the post-inflation analysis*

returning to its approximate initial configuration.

From figure 5.12, the modulus of the material increases as the inflation pressure within the membrane cylinder increases. This can be contributed to the beam becoming increasingly stiff and rigid as the membrane reaches rupture point and, the bending & buckling force is overcome. As the membrane cylinder has no more flexure, the overcompensation of the post-inflation pressure leads to the instability within the membrane. Another variable which is intrinsically linked to the membranes young's modulus is membrane thickness. As the modulus of the material increases and the membrane is post-inflated to rupture point, the membrane is also stretched, leading to a decrease in thickness of the membrane and a larger radius of the cylindrical caps. Another depiction of how the membrane thickness affects the post-inflation pressure of the membrane can be seen in figure 5.13. Figure 5.13 represents the decreasing magnitude of membrane thickness with increasing post-inflation pressure on the membrane cylinder. Therefore, once the deflection is overcome, the material thickness is decreased with the stretching of the membrane material.

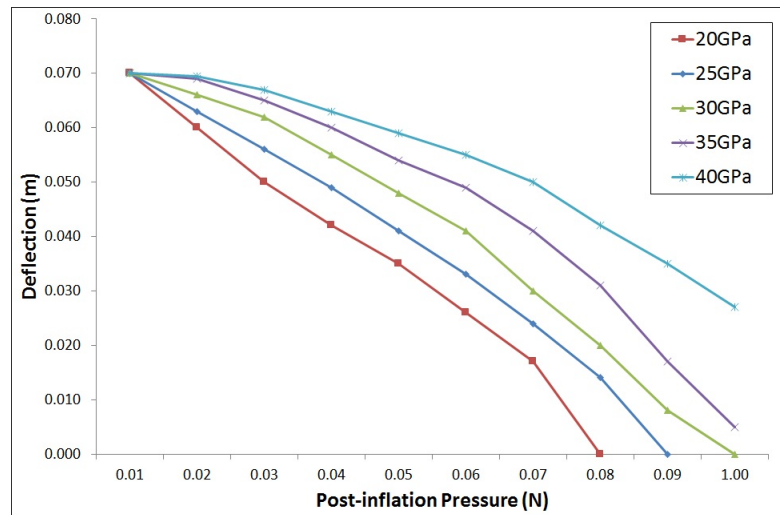


Figure 5.12: *Depiction of how the beams Young's Modulus effects the rate of post-inflation of the bent and buckled cylinder*

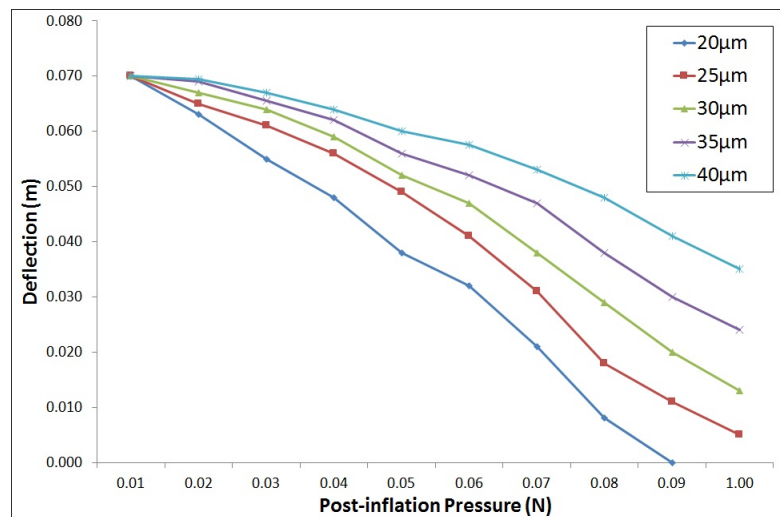


Figure 5.13: *Graph showing the correlation with varied membrane thickness against post-inflation pressure and deflection*

5.5 Potential Applications

This Abaqus model with the incorporated subroutine can be used to model any membrane or shell structure subjected to any type of internal or external forces. This tested approach could be used to simulate and model future applications of inflatable space structures, such as inflatable booms & reflectors, solar sails etc., to understand the stresses and strains that may act on the structure when being launched or deployed. This simple model could be used as a secondary test during the design and analysis phase before initial conceptual prototype design.

This model is not limited to space applications but can also be used in a variety of other applications. Such as being used to model inflatable habitats for living, storage or instrumentation protection from the external environment on Earth or any other planet. Currently this model has been used by Ben Board from the Isle of Wight to invent a life-saving inflatable tube that can be inflated to rescue people drowning at sea. This inflatable tube, named CentiFloat, designed by the Unique Group is designed to be deployed from a rescue ship to sea via inflation. It is fitted with grab handles for people to grip on and be towed to safety. This CentiFloat is presented in figure 5.14. Future proposals of inflatable membrane structures are to be used as a space habitat for the colonization of the Moon. This can be used for astronauts to practice living, working and completing science experiments before taking longer and riskier trips to Mars. The Moon is a natural first step in space exploration as it is nearby and the closest floating body in outer space.



Figure 5.14: *Image of the CentiFloat being used by the Migrant Offshore Aid Station (image courtesy of the Huffington Post)*

5.6 Discussions & Conclusions

In this chapter, a novel approach has been provided in modelling via Abaqus simulation, the inflation, bending, buckling and post-inflation of a cylindrical membrane structure throughout the entire phase transition of each configuration. We have discussed briefly, a summary of research carried out in this subject and any theories or methodologies that are incorporated in our study.

Each simulation is broken into three separate parts: simulation method, simulation model and simulation analysis. The simulation method describes the Abaqus methodology and the steps taken to achieve a successful working finite element model within Abaqus. The simulation model describes the theory behind the model, the model properties and any characteristics associated with the membrane model. Finally, the simulation analysis describes the results and conclusions derived from the analysis. All relevant information is illustrated by graphical representation. A modified VUMAT subroutine was incorporated

within both models, so that the simulation could successfully model the intricate membrane wrinkling behaviour during deformation. The comparison with and without this VUMAT subroutine is depicted and the necessity of incorporating this can be seen.

A brief description has been given where this model can be used and implemented for potential applications. A real life example of where it has been used, out-with the context of this PhD research has been showcased. I believe this is only a portion of examples where this model can be integrated, and this can however be used in much wider applications such as biomedical engineering. Currently, The Department of Biomedical Engineering at the University of Strathclyde is researching on using inflatable membrane tubes as potential grafts for arteries and veins within the human anatomy.

Chapter 6

Thesis Conclusions

This research study presented herewith for the degree of Doctorate of Philosophy has investigated new innovative wrinkling models for membrane materials, taking into account model competency, accuracy, simulation expenditure and the rate of convergence. These deduced wrinkling models can be modified to be applied to a wide range of scenarios allowing for detailed visual inspection in it's entirety. The relativistic pressure effects have been considered within our study by assimilating additional stiffness terms within the constitutive equations which are caused either by the variation of the membrane surface normals, altering cavity pressure or the deformation of the membrane. To account the membrane material dynamics and contact issues for inflatable membranes undergoing large deformation, a user-defined material VUMAT subroutine has been integrated alongside the Abaqus finite element simulation software. This integration results in an accurate, reliable and stable formula which gives much more realistic solutions when compared to the conventional treatment of membrane material and contact problems.

6.1 Research Overview

In previous years there has been little study using simulation software for the conceptualization of inflatable membrane space structures with most of the documented literature focusing on theoretical numerical calculations. This research advanced the prior understanding of wrinkling within inflated membranes by using complex structures subjected to deformation loads.

A comprehensive computational framework for the numerical analysis of the interaction between acting forces on the membrane and the membrane structure dynamics is given. In regards to membrane deformations, the correlation amid the membrane wrinkling and structural forces has been investigated, resulting in a dynamic wrinkling problem which has been modelled by using a finite element software program Abaqus.

Using the Abaqus FEA simulation, key consideration was given in modelling the geometric non-linearity behaviour of the membrane. By utilizing the existing continuum mechanics expression for the virtual internal work in curvilinear coordinates, a modified formulation has been derived to showcase the transition phase of the deformation of the membrane structure from initial analysis to final equilibrium path.

A critical feature of the new formulation is the addition of the pre-stressed forces on the membrane structure. The novel approach developed, established on the alteration of the material stiffness matrix to integrate the effects of wrinkling and deformation, can be utilized to calculate the behaviour of the membrane within a finite element simulation. In the wrinkling model, the state of the membrane element *taut*, *wrinkled* or *slack* is characterized by a mixed wrinkle criterion at each incremental analysis step. Once the membrane element has been identified as wrinkled, the iterative scheme looks for the

wrinkled orientation angle and the precise stress distribution, including only uni-axial tension in the wrinkle direction, is then deduced.

The wrinkling model has been verified and validated by contrasting the simulated conclusions with documented results for the instance of a time-independent membrane subjected to deformation loads. Utilizing the time integration method, a time-dependant pseudo-elastic stiffness matrix was represented and therefore, rather than calculating the convolution integral all through the Abaqus simulation, the behaviour of the membrane structure is derived by the superposition of a series of incremental steps in basic finite element software.

A three-dimensional FEM which integrates the wrinkling and friction-less contact has been developed to simulate the membrane models. The loading of the inflated structures is given by a non-uniform differential inflation pressure with a continual gradient adjacent to height. The resultant solution integrates a user defined subroutine to account for elastic wrinkling deformation that administers a combined stress-strain criterion. Frictionless contact has been prescribed within the model to prohibit the penetration of the membrane structure through itself.

The simulated models created accomplish the purpose of exceptional sub-grid performance in relation to accuracy, competency, computing hardware and software expense, complexity and successful convergence rate. The numerical algorithm has been created in general context and can be adopted for a large variety of material models.

6.2 Research Conclusions

Within the given research, three models were given in three chapters, namely the rectangular membrane model, smart adaptive structure model and the inflatable beam model. We will discuss the derived conclusions from each model in this section while speak about the originality of the research within a subsequent section:

6.2.1 Rectangular Membrane Model

The first studied model within this research was the rectangular membrane model whereby the primary initial conditions and governing equations were established to base all subsequent research on. These base equations are critical to create the fundamental governing equations that membrane structures abide to in physical reality. In order to understand the accuracy of our initial conditions, two separate simulations were designed, executed and compared to previous documented work. This comparison allowed the accuracy of the rectangular Kapton membrane undergoing axial and shear loading to be given.

The Finite Element analysis solutions deduced using continuum membrane elements within Abaqus and the variation in natural frequency is observed. In the simulation, we remove the initial imperfection from our model to eliminate the influence of the imperfections on the post-wrinkling characteristics by using the commands available within Abaqus and by applying an initial pre-stress. The relevant modes due to this initial pre-stress are found. The analysis of wrinkling problems of the wrinkle prediction of rectangular membranes under variation of thickness, element type, mesh density, length-to-width aspect ratio, tensile and shear loading has been studied.

Loading	Highest %	Lowest %
Axial	29.0	1.01
Shear	0.08	0.01

Table 6.1: Table representing the highest and lowest eigenvalue (*1st mode*) percentile differences between the derived Abaqus results and results published by Satish Kumar [36]

The unconventional membrane theory was not adopted for this research due to the membrane theory underestimating the magnitude of the loading at impending wrinkling. Membrane theory predicts that the wrinkled regions are those under compression and also that an infinite number of wrinkle lines appear in the wrinkled regions. However, the wrinkles extend the length of the membrane and the shapes and sizes of the wrinkled regions are different from those of the regions under width compression. Therefore, the effects of the small flexural stiffness on the prediction of the critical non-linear component of the edge loading that causes wrinkling, on the number and the direction of the wrinkle lines, and on the sizes and shapes of the wrinkled regions are significant and cannot be neglected. Due to this, an iterative displacement approach is adopted within Abaqus FEA based on the Newton-Raphson method alongside a modified approach to the membrane theory is utilized to achieve successful results.

In order to validate the Abaqus axial and shear loading Kapton membrane simulation model by replicating the model published and documented by Satish Kumar [36]. The lowest and highest percentile disparity between the Abaqus simulation results derived and results published by Satish Kumar are stated in table 6.1.

Only one value given in table 6.1 falls out with the accepted tolerances of

this research. Successive simulation models were run to mitigate any input errors but this difference could not be explained and was attributed to an anomaly. The remaining disparity values can be accounted for the integration of the iterative membrane properties (*IMP*) subroutine to predict the membrane dynamics within the Abaqus simulation. The IMP subroutine leads to the mixed wrinkling criterion being calculated incrementally at each phase of the simulation process as opposed to a set value assigned at the start of the simulation.

6.2.2 Smart Adaptive Structure Model

The conceptual design of a solar based power station satellite is established on a geostationary based platform with a ground station where the energy can be transmitted for storage and distribution for use. The space part is comprised of a stiff structure made up of hexagonal cells which have solar panels on the top and power transmitters at the bottom. These hexagonal cells are connected to neighbouring cells via micro-pumps enabling pressure transfer between the cells to change the global shape of the structure.

An alternative approach for large space structures is given by using self inflating adaptive membranes. With the passive residual air inflation method and the biologically inspired automation, a simple smart inflatable structure is constructed. Abaqus simulations were created of single cell and multiple cells and validated with experimental vacuum tests. Two separate inflation simulations were designed: one for the structure to be flat and the second for the structure to deploy from a deployment box and both simulations were compared for the final configuration of the inflated structure. This comparison illustrated that the desired configuration can be achieved regardless of the packaging shape.

The deployment was further investigated by comparing the simulations to a REXUS experiment which launched in Spring 2014.

Abaqus simulations for the double cell and cell array structure were modelled to showcase visual validation between the experimental vacuum chamber results conducted. The solutions achieved from Abaqus demonstrated validity on the size and shape of the final cell configuration, further verifying our previous statement. A disparity can be seen in the multiple cell array and this has been concluded to be due to the limitations of the Abaqus software and computer power when tackling problems with dense non-linearity due to membrane wrinkling.

A customized design code was written to model the dynamic structure accurately within the inflation simulations. The code incorporated each inflated cell as a point mass which experiences bending, tension and torsion springs between them. The executed simulations illustrated that the structure can alter its focal point and orientation depending on the location of the sun in relation to the structure to ensure sufficient energy is redirected towards the solar power assembly. particularly, decreasing the storage volume by folding up the deflated structure within the deployment box and the robust deployment of the concentrator should increase the cost and risk of launching a large structure into space.

6.2.3 Inflated Beam Model

The inflatable beam model is comprised of two key simulations: the bending & buckling of the inflated beam and the post-inflation of the bent & buckled beam. Abaqus software was used to simulate the inflatable beam during each configuration utilizing the integration of a modified VUMAT subroutine.

To understand the membrane dynamics during deformation when wrinkling, the numerical subroutine based on the Miller-Hedgepeth membrane theory is created. In order to comprehend the behaviour of the non-linear inflated membrane, bending of a range of beams with different lengths and radii is investigated. And secondly, the beam is re-inflated after the deformation to bring the beam back to its initial configuration. This study allows the wrinkling progression and deformation arrangement within the inflated cylinder to be examined. To identify the relative non-linear behaviours of the inflatable cylinder, number of simulations are carried out at different cylindrical radii, internal pressure, elastic modulus, material thickness and displacement loading. To validate the Abaqus simulation model with previous documented literature, a dimensionless formulation has been created and a relativistic comparison has been made to showcase good agreement with current work.

From the deformation simulation of the inflated cylinder, it was concluded that the progression of wrinkles degrades the structural performance of the beam. Specifically, the deflection dramatically escalates when subjected to an acute load once wrinkling occurs on the membrane surface. As the modulus of the material increases, the beam structure becomes inflexible in the course of linear deformation. The membrane thickness also assists in the beam stiffness which acts similarly to the elastic modulus of the membrane. The dominant factor for the beams behavioural response observed within the simulations is the internal pressure. These derived solutions are deduced into a dimensionless form which is compared to previously documented and published results to showcase the validity of the presented model. The dimensionless data showcases in clarity that the dimensionless load-deflection relationship can be approximated into a best fit single curve. Compared with the Euler beam theory, the deflection is linearly dependant on the external load and correlates well with the Euler theory until the value of 0.2. Albeit beyond this value, the load-deflection

relationship becomes non-linear due to onset of wrinkling until the applied load reaches the theoretical collapse moment of the beam theory.

From the post-inflation for wrinkling control of the deflected beam, it can be stated that the membrane wrinkled region is mitigated as the beam is post-inflated. This is due to the beams deflection being mitigated, resulting in the decreasing of wrinkles and enhancing the structural performance of the beam. It should be taken into account that as the beam is post-inflated, the membrane is pushed to its rupture breaking point at the end caps and enclosed seams due to less flexure within this region when compared to rest of the membrane.

6.3 Originality of Research

The research carried out during this Doctorate has led to several original pieces of work which has enhanced the knowledge within this field significantly. The work given in this section will present the main points of the work conducted.

- 1 A novel patent pending smart adaptive space structure to harness solar energy to be re-used as a potential source of green energy on the ground. The solar energy smart cell structure constitutes two structural parts: the solar & transmission assembly and a deployable concentrator. The deployable concentrator is created of inflatable smart cells coated with a reflective material to redirect and focus the Sun's energy onto the geostationary space solar panel & transmission assembly.
- 2 Design of the new cell structures for the adaptive smart cell to be shaped to the user specification after deployment. The deployable concentrator comprises of numerous inflated cells which are interconnected by micro-pumps. The micro-pumps allow air change between two neighbouring

cells, therefore, changing the volume between these neighbouring cells. Changing the connecting actuators locally will translate the global shape of the structure into any given shape.

- 3 A simulation model depicting the post-inflation of a deformed inflated membrane beam structure to restore it to its initial configuration. This research is vital for understanding the limitations of post-inflation of a deformed beam as this approach could be used for restoring support booms after the onset of bending and buckling.
- 4 Utilizing Abaqus for the simulation design of membrane elements using the fluid cavity inflation method and the internal layer method. Abaqus is not the conventional approach for inflation simulations. However, with the integration of a custom programming scripting and exploiting the fluid cavity (**control volume*) method alongside the internal element layer (**skin*), Abaqus was used successfully to attain accurate and robust results.

6.4 Relevance of the Abaqus Simulations

This thesis is robustly based on methodological and modelling of membrane structures using Abaqus finite element analysis software. With using modelling software as the basis of this research, the question arises, how and to what extent, the methods given here can be used in the real world of engineering.

It has been documented previously that an engineer only needs a minimum of three points to model a structure.

- 1 Information on the surrounding environment.

- 2 Information on the correlation amidst the environment and the forces acting on the structure.
- 3 Information on the structural behaviour resulting from the acting forces.

The software created within this thesis encompasses bullet point 2, although, constraints arise from the dynamic behaviour of the membrane. The strength of the simulation lies in the integration bullet point 3, as the correlation between the structure and environment can be modelled explicitly, and the effect of the structural behaviour can be integrated. The surrounding environment, as stated in bullet point 1, can also be implemented within the model using initial conditions and pre-programmed material characteristics. This proves the importance and relevance of the Abaqus simulation.

6.5 Discussion and Outlook

The software introduced within this research is an important tool for any experienced engineer, to design an inflatable membrane structure subjected to any internal or external forces. Within the constraints of the model, any structural integrity, deformation or configuration can be analysed, completely taking into consideration the interaction. Hence, the modelling methodology demonstrated is an encouraging addition to and the improvement of existing methods of analytical, sub-analytical, or experimental procedures in membrane modelling.

The flexibility of the software environment can be improved within Abaqus to include atmospheric or weather conditions, which have already been done in open-source solvers such as OpenFOAM. All post-processing for the simulations were carried out in Matlab by exporting relative results, it would make

visualization easier and less chance of human error, if this was available within Abaqus.

This research has led to two conference papers and two journal paper submissions. These models comply with relative theories leading to accurate simulated results of structures subjected to various internal and external forces.

Delete '

Appendix A

Appendix One

Input files for the programs for a rectangular Kapton membrane subjected axial loading and shear loading.

A.1 Axial Loading Input File

*Heading

Stretching the aluminium foil using a symmetric boundary condition on one edge

** Job name: Kapton Axial Loading Model name: Model-1

** Generated by: Abaqus/CAE 6.13-2

*Preprint, echo=NO, model=NO, history=NO, contact=NO

**

** PARTS

**

*Part, name="Kapton Sheet"

```
*End Part
**
**
** ASSEMBLY
**
*Assembly, name=Assembly
**
*Instance, name="Kapton Sheet-1", part="Kapton Sheet"
*Node
1, 0., 0., 0.
2, 0.5, 0., 0.
3, 1., 0., 0.
4, 1.5, 0., 0.
5, 2., 0., 0.
6, 2.5, 0., 0.
***
**
*
**
***
1269, 19., 15., 0.
1270, 19.5, 15., 0.
1271, 20., 15., 0.
*Element, type=M3D4R
1, 1, 2, 43, 42
2, 2, 3, 44, 43
3, 3, 4, 45, 44
***
**
```

```
*
**
***
1198, 1227, 1228, 1269, 1268
1199, 1228, 1229, 1270, 1269
1200, 1229, 1230, 1271, 1270
*Nset, nset=Complete, generate
1, 1271, 1
*Elset, elset=Complete, generate
1, 1200, 1
** Section: Shell Membrane
*Membrane Section, elset=Complete, material=Kapton
5e-05,
*End Instance
**
*Nset, nset="Displaced Edge", instance="Kapton Sheet-1", generate
41, 1271, 41
*Elset, elset="Displaced Edge", instance="Kapton Sheet-1", generate
40, 1200, 40
*Nset, nset="Fixed Edge", instance="Kapton Sheet-1", generate
1, 1231, 41
*Elset, elset="Fixed Edge", instance="Kapton Sheet-1", generate
1, 1161, 40
*Nset, nset=Set-9, instance="Kapton Sheet-1", generate
1, 1231, 41
*Elset, elset=Set-9, instance="Kapton Sheet-1", generate
1, 1161, 40
*Nset, nset=PickedSet16, internal, instance="Kapton Sheet-1", generate
1, 1231, 41
```

```
*Elset, elset=PickedSet16, internal, instance="Kapton Sheet-1", generate
1, 1161, 40
*Elset, elset=Surf-1-E2, internal, instance="Kapton Sheet-1", generate
40, 1200, 40
*Surface, type=ELEMENT, name=Surf-1
Surf-1-E2, E2
*End Assembly
*Amplitude, name="Equally Spaced", definition=EQUALLY SPACED, fixed
interval=1.
0., 1.
**
** MATERIALS
**
** A polyimide film of DuPoint Kapton
*Material, name=Kapton
*Density
1420.,
*Elastic
2.5e+09, 0.34
*Plastic
1.45e+08, 0.
1.52e+08, 0.0608
**
** BOUNDARY CONDITIONS
**
** Name: Fixed Edge Type: Symmetry/Antisymmetry/Encastre
*Boundary
Set-9, ENCASTRE
**
```

```
** STEP: Displacement
**
*Step, name=Displacement, nlgeom=YES
Displacing RHS of membrane
*Dynamic, Explicit
, 1.
*Bulk Viscosity
0.06, 1.2
**
** BOUNDARY CONDITIONS
**
** Name: Displacement Type: Displacement/Rotation
*Boundary, amplitude="Equally Spaced"
"Displaced Edge", 1, 1, 1.75
"Displaced Edge", 6, 6
**
** OUTPUT REQUESTS
**
*Restart, write, number interval=1, time marks=NO
**
** FIELD OUTPUT: F-Output-1
**
*Output, field, variable=PRESELECT
**
** HISTORY OUTPUT: H-Output-1
**
*Output, history, variable=PRESELECT
*End Step
```

A.2 Shear Loading Input File

```
*Heading
** Job name: Shear Model name: ShearModel
** Generated by: Abaqus/CAE 6.13-2
*Preprint, echo=NO, model=NO, history=NO, contact=NO
**
** PARTS
**
*Part, name=ShearModel
*End Part
**
**
** ASSEMBLY
**
*Assembly, name=Assembly
**
*Instance, name=ShearModel-1, part=ShearModel
*Node
1, 0.200000003, 0.100000001, 0.
2, 0.165000007, 0.100000001, 0.
3, 0.129999995, 0.100000001, 0.
***
**
*
**
***
75, -0.0799999982, -0.100000001, 0.
76, -0.115000002, -0.100000001, 0.
```

```
77, -0.150000006, -0.100000001, 0.
*Element, type=M3D4R
1, 1, 2, 13, 12
2, 2, 3, 14, 13
3, 3, 4, 15, 14
***
**
*
**
***
58, 63, 64, 75, 74
59, 64, 65, 76, 75
60, 65, 66, 77, 76
*Nset, nset=Complete, generate
1, 77, 1
*Elset, elset=Complete, generate
1, 60, 1
** Section: ShellMembrane
*Membrane Section, elset=Complete, material=Kapton
5e-05,
*End Instance
**
*Nset, nset=Fixed, instance=ShearModel-1, generate
67, 77, 1
*Elset, elset=Fixed, instance=ShearModel-1, generate
51, 60, 1
*Nset, nset="Lower Left Node", instance=ShearModel-1
77,
*Elset, elset=Mid, instance=ShearModel-1, generate
```

```
11, 50, 1
*Nset, nset="Middle Node", instance=ShearModel-1
39,
*Nset, nset=Shear, instance=ShearModel-1, generate
1, 11, 1
*Elset, elset=Shear, instance=ShearModel-1, generate
1, 10, 1
*Nset, nset="Upper Right Node", instance=ShearModel-1
1,
*Elset, elset=Bottom-SNEG, internal, instance=ShearModel-1, generate
1, 60, 1
*Surface, type=ELEMENT, name=Bottom
Bottom-SNEG, SNEG
*Elset, elset=Mid, internal, instance=ShearModel-1, generate
11, 50, 1
*Surface, type=ELEMENT, name=Mid
Mid,
*Elset, elset=Top-SPOS, internal, instance=ShearModel-1, generate
1, 60, 1
*Surface, type=ELEMENT, name=Top
Top-SPOS, SPOS
*End Assembly
*Amplitude, name=Smooth, definition=SMOOTH STEP
0., 0., 0.5, 0.5, 1., 1.
**
** MATERIALS
**
*Material, name=Kapton
*Density
```

```
1420.,
*Elastic
1.42e+09, 0.34
**
** INTERACTION PROPERTIES
**
*Surface Interaction, name=IntProp-1
**
** BOUNDARY CONDITIONS
**
** Name: Fixed Type: Symmetry/Antisymmetry/Encastre
*Boundary
Fixed, PINNED
**
** STEP: ShearLoad
**
*Step, name=ShearLoad, nlgeom=YES
*Dynamic, Explicit
, 1.
*Bulk Viscosity
0.06, 1.2
**
** BOUNDARY CONDITIONS
**
** Name: ShearLoading Type: Displacement/Rotation
*Boundary, amplitude=Smooth
Shear, 1, 1, 0.1
Shear, 2, 2
**
```

```
** INTERACTIONS
**
** Interaction: General-Contact
*Contact, op=NEW
*Contact Inclusions, ALL EXTERIOR
*Contact Property Assignment
, , IntProp-1
**
** OUTPUT REQUESTS
**
**Restart, write, number interval=1, time marks=NO
**
** FIELD OUTPUT: F-Output-1
**
*Output, field
*Node Output
A, RF, U, V
*Element Output, directions=YES
E, EVF, LE, PE, PEEQ, PEEQVAVG, PEVAVG, S, SVAVG
*Contact Output
CSTRESS,
**
** HISTORY OUTPUT: H-Output-1
**
*Output, history, variable=PRESELECT
*End Step
```

Appendix B

Appendix Two

Input execution files for the adaptive structures program. The first program is for the single cell Abaqus program and the second for the multi-cell LS-Dyna program.

B.1 Single Smart Cell Abaqus Input File

```
*Heading
** Job name: Airbag Model name: Airbag
** Generated by: Abaqus/CAE 6.13-2
*Preprint, echo=NO, model=NO, history=NO, contact=NO
**
** PARTS
**
*Part, name=PART-1
*Node
```

```
1, 320., 0., 0.
2, 319.3685, 0., -20.0936565
3, 317.476532, 0., -40.1080055
***
**
*
**
***
3850, 0.0145595493, -0.0001682695, -0.000832545164
3851, 0.0155301858, -0.000112179667, -0.000888048147
3852, 0.0165008232, -5.60898334e-05, -0.000943551189
*Element, type=M3D4R
1, 129, 130, 113, 112
2, 130, 131, 114, 113
3, 131, 132, 115, 114
***
**
*
**
***
2776, 19.9969769, -4.83975649, 20.2555809
2777, 9.99697685, -4.83975649, 30.2555809
2778, 19.9969769, -4.83975649, 30.2555809
*Element, type=M3D4
1, 239, 242, 244, 238
2, 238, 244, 245, 237
3, 237, 245, 232, 233
***
**
```

```
*
**
***
2648, 2620, 2652, 2650, 2621
2649, 2637, 2636, 2646, 2652
2650, 2652, 2646, 2645, 2650
*Elset, elset=CHAMBER, generate
1, 2650, 1
** Section: Section-1-CHAMBER
*Membrane Section, elset=CHAMBER, material=FABRIC
0.35,
*End Part
**
**
** ASSEMBLY
**
*Assembly, name=Assembly
**
*Instance, name=PART-1-1, part=PART-1
*End Instance
**
*Nset, nset=CHAMBER, instance=PART-1-1
1, 2714
*Nset, nset=Fixed, instance=PART-1-1
2163,
*Nset, nset=Fixed-Bot, instance=PART-1-1
2655,
*Nset, nset=Plate, instance=PART-1-1
2086, 2087, 2090, 2091, 2101, 2102, 2194, 2195, 2196, 2197, 2254, 2255, 2260,
```

2261, 2262, 2263

2374, 2375, 2452, 2453, 2460, 2461, 2462, 2463, 2566, 2567, 2568, 2575, 2576,
2578, 2579, 2580

2654, 2655, 2657, 2702

*Elset, elset=-CHAMBER-SURFACE, internal, instance=PART-1-1

1,

*Elset, elset=-CONTACT-AIRBAGTOPLATE, internal, instance=PART-1-1

1, 1325

*Elset, elset=-CONTACT-PLATETOAIRBAG, internal, instance=PART-1-1

1,

*Elset, elset=-SURFACE-BOT, internal, instance=PART-1-1

1, 1326, 2650

*Elset, elset=-SURFACE-TOP, internal, instance=PART-1-1

1, 1325

*Elset, elset=-CHAMBER-SURFACE-, internal, instance=PART-1-1, gener-
ate

1, 2650, 1

*Surface, type=ELEMENT, name=CHAMBER-SURFACE

-CHAMBER-SURFACE-,

*Elset, elset=-CHAMBER-SURFACE-1-SNEG, internal, instance=PART-1-

1, generate

1, 2650, 1

*Surface, type=ELEMENT, name=CHAMBER-SURFACE-1

-CHAMBER-SURFACE-1-SNEG, SNEG

*Elset, elset=-CHAMBER-EXT-SKIN-SURF-SNEG, internal, instance=PART-

1-1, generate

1, 2650, 1

*Surface, type=ELEMENT, name=CHAMBER-EXT-SKIN-SURF

-CHAMBER-EXT-SKIN-SURF-SNEG, SNEG

```
*Elset, elset=-SURFACE-BOT-SNEG, internal, instance=PART-1-1
1, 1326, 2650
*Surface, type=ELEMENT, name=SURFACE-BOT
-SURFACE-BOT-SNEG, SNEG
*Elset, elset=-SURFACE-TOP-SNEG, internal, instance=PART-1-1
1, 1325
*Surface, type=ELEMENT, name=SURFACE-TOP
-SURFACE-TOP-SNEG, SNEG
*End Assembly
*Amplitude, name=AMP-DAMPING-1-VBF
0., 0., 0.25, 0.5, 0.5, 0.75, 0.75, 1. 1., 1.
*Amplitude, name=AMP-DAMPING-2-VBF
0., 0., 0.0009999999, 0., 0.001, 100., 0.009999999, 100. 0.01, 0.
*Amplitude, name=RAMPSTRESS, time=TOTAL TIME, definition=SMOOTH
STEP
0., 0., 0.0025, 1., 1., 1.
*Filter, name=FILTER-1000HZ, type=BUTTERWORTH
1000.
**
** MATERIALS
**
** _____ M A T E R I A L D A T A _____
** _
*Material, name=FABRIC
*Damping, beta=1e-06
*Density
1.42,
*Elastic
2.5e+09, 0.34
```

```
**  
** INTERACTION PROPERTIES  
**  
*Fluid Behavior, name=AIR  
*Molecular Weight  
2.897e-05  
*Capacity, type=POLYNOMIAL  
28110., 1.967, 0.004802, 0., 0.  
*Fluid Behavior, name=AR  
*Molecular Weight  
3.995e-05  
*Capacity, type=POLYNOMIAL  
20785.,0.,0.,0.,0.  
*Fluid Behavior, name=CO2  
*Molecular Weight  
4.401e-05  
*Capacity, type=POLYNOMIAL  
25999., 43.5, -0.0148, 0., 0.  
*Surface Interaction, name=DEFAULT  
*Surface Interaction, name=GENERAL-CONTACT  
*Friction  
0.,  
*Fluid Behavior, name=H2O  
*Molecular Weight  
1.802e-05  
*Capacity, type=POLYNOMIAL  
32200., 1.9, 0.0106, 0., 0.  
*Fluid Behavior, name=HE  
*Molecular Weight
```

```
4.003e-06
*Capacity, type=POLYNOMIAL
20785.,0.,0.,0.,0.
*Fluid Behavior, name=N2
*Molecular Weight
2.801e-05
*Capacity, type=POLYNOMIAL
27296., 5.23, 0., 0., 0.
*Fluid Behavior, name=N2O
*Molecular Weight
4.401e-05
*Capacity, type=POLYNOMIAL
25188., 52.1, -0.02, 0., 0.
*Fluid Behavior, name=O2
*Molecular Weight
3.2e-05
*Capacity, type=POLYNOMIAL
25723., 12.98, -0.00386, 0., 0.
**
** PHYSICAL CONSTANTS
**
*Physical Constants, absolute zero=0., universal gas=8314.41
**
** BOUNDARY CONDITIONS
**
** Name: Disp-BC-1 Type: Symmetry/Antisymmetry/Encastre
*Boundary
Plate, ENCASTRE
** _____
```

```
**
** STEP: Inflation
**
*Step, name=Inflation, nlgeom=YES
Step-1
*Dynamic, Explicit, element by element, scale factor=0.8
, 0.5001
*Bulk Viscosity
0.06, 1.2
** Mass Scaling: Semi-Automatic
** Whole Model
*Variable Mass Scaling, dt=1e-06, type=below min, frequency=10
**
** LOADS
**
** Name: Load-1 Type: Pressure
*Dload, amplitude=AMP-DAMPING-1-VBF
CHAMBER-SURFACE-1, P, 500000.
**
** OUTPUT REQUESTS
**
*Restart, write, number interval=2, time marks=NO
**
** FIELD OUTPUT: F-Output-1
**
*Output, field
*Node Output
A, AR, AT, RF, U, UR, UT, V
VR, VT
```

```
*Element Output, directions=YES
EFABRIC, ERV, LE, MISESMAX, NE, PEEQ, PEEQMAX, PEQC, S, SFAB-
RIC
*Contact Output
CFORCE, CSTRESS, CTHICK
**
** HISTORY OUTPUT: H-Output-1
**
*Output, history
*Energy Output
ALLAE, ALLCD, ALLCW, ALLDC, ALLDMD, ALLFD, ALLIE, ALLKE,
ALLMW, ALLPD, ALLPW, ALLSE, ALLVD, ALLWK,
ETOTAL
*End Step
```

B.2 Double Smart Cell Abaqus Input File

```
*Heading ** Job name: Double-Airbag Model name: Double-Airbag
** Generated by: Abaqus/CAE 6.13-2
*Preprint, echo=NO, model=NO, history=NO, contact=NO
**
** PARTS
**
*Part, name=PART-1
*Node
1, 320., 0., 0.
2, 319.3685, 0., -20.0936565
3, 317.476532, 0., -40.1080055
```

```
***
**
*
**
***
2776, 19.9969769, -4.83975649, 20.2555809
2777, 9.99697685, -4.83975649, 30.2555809
2778, 19.9969769, -4.83975649, 30.2555809
*Element, type=M3D4
1, 239, 242, 244, 238
2, 238, 244, 245, 237
3, 237, 245, 232, 233
***
**
*
**
***
2648, 2620, 2652, 2650, 2621
2649, 2637, 2636, 2646, 2652
2650, 2652, 2646, 2645, 2650
*Elset, elset=CHAMBER, generate
1, 2650, 1
** Section: Section-1-CHAMBER
*Membrane Section, elset=CHAMBER, material=FABRIC
0.35,
*End Part
**
*Part, name=PART-2
*Node
```

```
1, 320., 0., 0.
2, 319.3685, 0., -20.0936565
3, 317.476532, 0., -40.1080055
***
**
*
**
***
2776, 19.9969769, -4.83975649, 20.2555809
2777, 9.99697685, -4.83975649, 30.2555809
2778, 19.9969769, -4.83975649, 30.2555809
*Element, type=M3D4
1, 239, 242, 244, 238
2, 238, 244, 245, 237
3, 237, 245, 232, 233
***
**
*
**
***
*Elset, elset=CHAMBER, generate
1, 2650, 1
** Section: Section-1-CHAMBER
*Membrane Section, elset=CHAMBER, material=FABRIC
0.35,
*End Part
**
**
** ASSEMBLY
```

```
**
*Assembly, name=Assembly
**
*Instance, name=PART-1-1, part=PART-1
0., -1., 0.
*End Instance
**
*Instance, name=PART-2-1, part=PART-2
-9.36057660671164e-14, -19.5, -4.79600788710216e-14
-9.36057660671164e-14, -19.5, -4.79600788710216e-14, 0.729024887084867, -
19.5,
0.684487223625135, 180.
*End Instance
**
*Nset, nset=CHAMBER, instance=PART-1-1
1, 2714
*Nset, nset=CHAMBER-PART2, instance=PART-2-1
1, 2714
*Nset, nset=Fixed, instance=PART-1-1
2163,
*Nset, nset=Fixed-PART2, instance=PART-2-1
2163,
*Nset, nset=Fixed-Bot, instance=PART-1-1
2655,
*Nset, nset=Fixed-Bot-PART2, instance=PART-2-1
2655,
*Nset, nset=Plate, instance=PART-1-1
2086, 2087, 2090, 2091, 2101, 2102, 2194, 2195, 2196, 2197, 2254, 2255, 2260,
2261, 2262, 2263
```

2374, 2375, 2452, 2453, 2460, 2461, 2462, 2463, 2566, 2567, 2568, 2575, 2576,
2578, 2579, 2580

2654, 2655, 2657, 2702

*Nset, nset=Plate-PART2, instance=PART-2-1

2260, 2262, 2568, 2575, 2655, 2664, 2672, 2674, 2682, 2698, 2700, 2702, 2706,
2708, 2710, 2712

2714, 2716, 2717, 2719, 2724, 2727, 2729, 2731, 2736, 2740, 2741, 2743, 2745,
2747, 2756, 2757

2760, 2766, 2775, 2778

*Elset, elset=-CHAMBER-SURFACE, internal, instance=PART-1-1

1,

*Elset, elset=-CONTACT-AIRBAGTOPLATE, internal, instance=PART-1-1

1, 1325

*Elset, elset=-CONTACT-PLATETOAIRBAG, internal, instance=PART-1-1

1,

*Elset, elset=-SURFACE-BOT, internal, instance=PART-1-1

1, 1326, 2650

*Elset, elset=-SURFACE-TOP, internal, instance=PART-1-1

1, 1325

*Elset, elset=-CHAMBER-SURFACE-, internal, instance=PART-1-1, gener-
ate

1, 2650, 1

*Surface, type=ELEMENT, name=CHAMBER-SURFACE

-CHAMBER-SURFACE-,

*Elset, elset=-CHAMBER-SURFACE-1-SNEG, internal, instance=PART-1-

1, generate

1, 2650, 1

*Surface, type=ELEMENT, name=CHAMBER-SURFACE-1

-CHAMBER-SURFACE-1-SNEG, SNEG

```
*Elset, elset=-CHAMBER-SURFACE-1-PART2-SNEG, internal, instance=PART-
2-1, generate
1, 2650, 1
*Surface, type=ELEMENT, name=CHAMBER-SURFACE-1-PART2
-CHAMBER-SURFACE-1-PART2-SNEG, SNEG
*Elset, elset=-CHAMBER-SURFACE-PART2-SPOS, internal, instance=PART-
2-1, generate
1, 2650, 1
*Surface, type=ELEMENT, name=CHAMBER-SURFACE-PART2
-CHAMBER-SURFACE-PART2-SPOS, SPOS
*Elset, elset=-CHAMBER-EXT-SKIN-SURF-SNEG, internal, instance=PART-
1-1, generate
1, 2650, 1
*Surface, type=ELEMENT, name=CHAMBER-EXT-SKIN-SURF
-CHAMBER-EXT-SKIN-SURF-SNEG, SNEG
*Elset, elset=-SURFACE-BOT-SNEG, internal, instance=PART-1-1
1, 1326, 2650
*Surface, type=ELEMENT, name=SURFACE-BOT
-SURFACE-BOT-SNEG, SNEG
*Elset, elset=-SURFACE-BOT-PART2-SNEG, internal, instance=PART-2-1
1350, 2648
*Surface, type=ELEMENT, name=SURFACE-BOT-PART2
-SURFACE-BOT-PART2-SNEG, SNEG
*Elset, elset=-SURFACE-TOP-SNEG, internal, instance=PART-1-1
1, 1325
*Surface, type=ELEMENT, name=SURFACE-TOP
-SURFACE-TOP-SNEG, SNEG
*Elset, elset=-SURFACE-TOP-PART2-SPOS, internal, instance=PART-2-1
25,
```

```
*Elset, elset=-SURFACE-TOP-PART2-SNEG, internal, instance=PART-2-1
2130,
*Surface, type=ELEMENT, name=SURFACE-TOP-PART2
-SURFACE-TOP-PART2-SPOS, SPOS
-SURFACE-TOP-PART2-SNEG, SNEG
*End Assembly
*Amplitude, name=AMP-DAMPING-1-VBF
0., 0., 0.2, 0.5, 0.4, 0.75,
0.6, 1. 0.8, 1., 1., 1.
*Amplitude, name=AMP-DAMPING-2-VBF
0., 0., 0.0009999999, 0., 0.001, 100.,
0.0099999999, 100. 0.01, 0.
*Amplitude, name=RAMPSTRESS, time=TOTAL TIME, definition=SMOOTH
STEP
0., 0., 0.0025, 1., 1., 1.
*Filter, name=FILTER-1000HZ, type=BUTTERWORTH
1000.
**
** MATERIALS
**
** _____ M A T E R I A L D A T A _____
** _
*Material, name=FABRIC
*Damping, beta=1e-06
*Density
1.42,
*Elastic
2.5e+09, 0.34
**
```

```
** INTERACTION PROPERTIES
**
*Fluid Behavior, name=AIR
*Molecular Weight
2.897e-05
*Capacity, type=POLYNOMIAL
28110., 1.967, 0.004802, 0., 0.
*Fluid Behavior, name=AR
*Molecular Weight
3.995e-05
*Capacity, type=POLYNOMIAL
20785.,0.,0.,0.,0.
*Fluid Behavior, name=CO2
*Molecular Weight
4.401e-05
*Capacity, type=POLYNOMIAL
25999., 43.5, -0.0148, 0., 0.
*Surface Interaction, name=DEFAULT
*Surface Interaction, name=GENERAL-CONTACT
*Friction
0.,
*Fluid Behavior, name=H2O
*Molecular Weight
1.802e-05
*Capacity, type=POLYNOMIAL
32200., 1.9, 0.0106, 0., 0.
*Fluid Behavior, name=HE
*Molecular Weight
4.003e-06
```

```
*Capacity, type=POLYNOMIAL
20785.,0.,0.,0.,0.
*Fluid Behavior, name=N2
*Molecular Weight
2.801e-05
*Capacity, type=POLYNOMIAL
27296., 5.23, 0., 0., 0.
*Fluid Behavior, name=N2O
*Molecular Weight
4.401e-05
*Capacity, type=POLYNOMIAL
25188., 52.1, -0.02, 0., 0.
*Fluid Behavior, name=O2
*Molecular Weight
3.2e-05
*Capacity, type=POLYNOMIAL
25723., 12.98, -0.00386, 0., 0.
**
** PHYSICAL CONSTANTS
**
*Physical Constants, absolute zero=0., universal gas=8314.41
**
** BOUNDARY CONDITIONS
**
** Name: Disp-BC-1 Type: Symmetry/Antisymmetry/Encastre
*Boundary
Plate, PINNED
** Name: Plate-PART2 Type: Symmetry/Antisymmetry/Encastre
*Boundary
```

```
Plate-PART2, PINNED
** _____
**
** STEP: Inflation
**
*Step, name=Inflation, nlgeom=YES
Step-1
*Dynamic, Explicit, element by element, scale factor=0.8
, 1.
*Bulk Viscosity
0.06, 1.2
** Mass Scaling: Semi-Automatic
** Whole Model
*Variable Mass Scaling, dt=1e-06, type=below min, frequency=10
**
** LOADS
**
** Name: Load-1 Type: Pressure
*Dload, amplitude=AMP-DAMPING-1-VBF
CHAMBER-SURFACE-1, P, 305000.
** Name: Load-2 Type: Pressure
*Dload, amplitude=AMP-DAMPING-1-VBF
CHAMBER-SURFACE-1-PART2, P, 305000.
**
** INTERACTIONS
**
** Interaction: Int-2
*Contact, op=NEW
*Contact Inclusions, ALL EXTERIOR
```

```
*Contact Property Assignment
, , GENERAL-CONTACT
CHAMBER-SURFACE-1 , CHAMBER-SURFACE-1-PART2 , GENERAL-
CONTACT
**
** OUTPUT REQUESTS
**
*Restart, write, number interval=2, time marks=NO
**
** FIELD OUTPUT: F-Output-1
**
*Output, field
*Node Output
A, AR, AT, RF, U, UR, UT, V
VR, VT
*Element Output, directions=YES
EFABRIC, ENER, ERV, LE, MFL, MISESMAX, NE, PEEQ, PEEQMAX,
PEQC, RD, S, SFABRIC, STH
*Contact Output
CFORCE, CSTRESS, CTHICK
**
** HISTORY OUTPUT: H-Output-1
**
*Output, history
*Energy Output
ALLAE, ALLCD, ALLCW, ALLDC, ALLDMD, ALLFD, ALLIE, ALLKE,
ALLMW, ALLPD, ALLPW, ALLSE, ALLVD, ALLWK,
ETOTAL
*End Step
```

B.3 Smart Cell Array Input File within Abaqus

```
*Heading
** Job name: Airbag-Array Model name: Airbag-Array
** Generated by: Abaqus/CAE 6.13-2
*Preprint, echo=NO, model=NO, history=NO, contact=NO
**
** PARTS
**
*Part, name=PART-1
*Node
1, 320., 0., 0.
2, 319.3685, 0., -20.0936565
3, 317.476532, 0., -40.1080055
***
**
*
**
***
2776, 19.9969769, -4.83975649, 20.2555809
2777, 9.99697685, -4.83975649, 30.2555809
2778, 19.9969769, -4.83975649, 30.2555809
*Element, type=M3D4
1, 239, 242, 244, 238
2, 238, 244, 245, 237
3, 237, 245, 232, 233
***
**
*
```

```
**  
***  
2648, 2620, 2652, 2650, 2621  
2649, 2637, 2636, 2646, 2652  
2650, 2652, 2646, 2645, 2650  
*Elset, elset=CHAMBER, generate  
1, 2650, 1  
** Section: Section-1-CHAMBER  
*Membrane Section, elset=CHAMBER, material=FABRIC  
0.35,  
*End Part  
**  
**  
** ASSEMBLY  
**  
*Assembly, name=Assembly  
**  
*Instance, name=PART-1-1, part=PART-1  
*End Instance  
**  
*Instance, name=PART-1-2, part=PART-1  
640., 0., 0.  
*End Instance  
**  
*Instance, name=PART-1-3, part=PART-1  
1280., 0., 0.  
*End Instance  
**  
*Instance, name=PART-1-4, part=PART-1
```

```
1920., 0., 0.
*End Instance
**
*Instance, name=PART-1-5, part=PART-1
2560., 0., 0.
*End Instance
**
*Instance, name=PART-1-6, part=PART-1
-0.0345600000000559, 0., -640.
*End Instance
**
*Instance, name=PART-1-7, part=PART-1
639.96544, 0., -640.
*End Instance
**
*Instance, name=PART-1-8, part=PART-1
1279.96544, 0., -640.
*End Instance
**
*Instance, name=PART-1-9, part=PART-1
1919.96544, 0., -640.
*End Instance
**
*Instance, name=PART-1-10, part=PART-1
2559.96544, 0., -640.
*End Instance
**
*Nset, nset=CHAMBER, instance=PART-1-1
1, 2714
```

```
*Nset, nset=CHAMBER-PART2, instance=PART-1-2
1, 2453
*Nset, nset=CHAMBER-PART3, instance=PART-1-3
1, 2453
*Nset, nset=CHAMBER-PART4, instance=PART-1-4
1, 2453
*Nset, nset=CHAMBER-PART5, instance=PART-1-5
1, 2453
*Nset, nset=CHAMBER-PART6, instance=PART-1-6
1, 2453
*Nset, nset=CHAMBER-PART7, instance=PART-1-7
1, 2453
*Nset, nset=CHAMBER-PART8, instance=PART-1-8
1, 2453
*Nset, nset=CHAMBER-PART9, instance=PART-1-9
1, 2453
*Nset, nset=CHAMBER-PART10, instance=PART-1-10
1, 2453
*Nset, nset=Fixed, instance=PART-1-1
2163,
*Nset, nset=Fixed-PART2, instance=PART-1-2
2163,
*Nset, nset=Fixed-PART3, instance=PART-1-3
2163,
*Nset, nset=Fixed-PART4, instance=PART-1-4
2163,
*Nset, nset=Fixed-PART5, instance=PART-1-5
2163,
*Nset, nset=Fixed-PART6, instance=PART-1-6
```

```
2163,  
*Nset, nset=Fixed-PART7, instance=PART-1-7  
2163,  
*Nset, nset=Fixed-PART8, instance=PART-1-8  
2163,  
*Nset, nset=Fixed-PART9, instance=PART-1-9  
2163,  
*Nset, nset=Fixed-PART10, instance=PART-1-10  
2163,  
*Nset, nset=Fixed-Bot, instance=PART-1-1  
2655,  
*Nset, nset=Fixed-Bot-PART2, instance=PART-1-2  
2655,  
*Nset, nset=Fixed-Bot-PART3, instance=PART-1-3  
2655,  
*Nset, nset=Fixed-Bot-PART4, instance=PART-1-4  
2655,  
*Nset, nset=Fixed-Bot-PART5, instance=PART-1-5  
2655,  
*Nset, nset=Fixed-Bot-PART6, instance=PART-1-6  
2655,  
*Nset, nset=Fixed-Bot-PART7, instance=PART-1-7  
2655,  
*Nset, nset=Fixed-Bot-PART8, instance=PART-1-8  
2655,  
*Nset, nset=Fixed-Bot-PART9, instance=PART-1-9  
2655,  
*Nset, nset=Fixed-Bot-PART10, instance=PART-1-10  
2655,
```

```
*Nset, nset=Plate, instance=PART-1-1
2086, 2087, 2090, 2091, 2101, 2102, 2194, 2195, 2196, 2197, 2254, 2255, 2260,
2261, 2262, 2263
2374, 2375, 2452, 2453, 2460, 2461, 2462, 2463, 2566, 2567, 2568, 2575, 2576,
2578, 2579, 2580
2654, 2655, 2657, 2702

*Nset, nset=Plate-PART2, instance=PART-1-2
2086, 2087, 2090, 2091, 2102, 2103, 2188, 2189, 2194, 2195, 2196, 2197, 2251,
2252, 2253, 2254
2255, 2260, 2261, 2262, 2263, 2375, 2460, 2461, 2462, 2463, 2566, 2567, 2575,
2576, 2578, 2654
2657, 2702, 2734, 2775

*Nset, nset=Plate-PART3, instance=PART-1-3
2086, 2087, 2090, 2091, 2101, 2102, 2194, 2195, 2196, 2197, 2254, 2255, 2260,
2261, 2262, 2263
2374, 2375, 2452, 2453, 2460, 2461, 2462, 2463, 2566, 2567, 2568, 2575, 2576,
2578, 2579, 2580
2654, 2655, 2702, 2716

*Nset, nset=Plate-PART4, instance=PART-1-4
2086, 2087, 2090, 2091, 2101, 2102, 2194, 2195, 2196, 2197, 2254, 2255, 2260,
2261, 2262, 2263
2374, 2375, 2452, 2453, 2460, 2461, 2462, 2463, 2566, 2567, 2568, 2575, 2576,
2578, 2579, 2580
2654, 2655, 2657, 2702

*Nset, nset=Plate-PART5, instance=PART-1-5
2086, 2087, 2090, 2091, 2101, 2102, 2194, 2195, 2196, 2197, 2254, 2255, 2260,
2261, 2262, 2263
2374, 2375, 2452, 2453, 2460, 2461, 2462, 2463, 2566, 2567, 2568, 2575, 2576,
2578, 2579, 2580
```

2654, 2655, 2657, 2702

*Nset, nset=Plate-PART6, instance=PART-1-6

2086, 2087, 2090, 2091, 2101, 2102, 2194, 2195, 2196, 2197, 2254, 2255, 2260,
2261, 2262, 2263

2374, 2375, 2452, 2453, 2460, 2461, 2462, 2463, 2566, 2567, 2568, 2575, 2576,
2578, 2579, 2580

2654, 2655, 2702, 2716

*Nset, nset=Plate-PART7, instance=PART-1-7

2086, 2087, 2090, 2091, 2101, 2102, 2194, 2195, 2196, 2197, 2254, 2255, 2260,
2261, 2262, 2263

2374, 2375, 2452, 2453, 2460, 2461, 2462, 2463, 2566, 2567, 2568, 2575, 2576,
2578, 2579, 2580

2654, 2655, 2657, 2702

*Nset, nset=Plate-PART8, instance=PART-1-8

2086, 2087, 2090, 2091, 2101, 2102, 2194, 2195, 2196, 2197, 2254, 2255, 2260,
2261, 2262, 2263

2374, 2375, 2452, 2453, 2460, 2461, 2462, 2463, 2566, 2567, 2568, 2575, 2576,
2578, 2579, 2580

2654, 2655, 2657, 2702

*Nset, nset=Plate-PART9, instance=PART-1-9

2086, 2087, 2090, 2091, 2101, 2102, 2194, 2195, 2196, 2197, 2254, 2255, 2260,
2261, 2262, 2263

2374, 2375, 2452, 2453, 2460, 2461, 2462, 2463, 2566, 2567, 2568, 2575, 2576,
2578, 2579, 2580

2654, 2655, 2657, 2702

*Nset, nset=Plate-PART10, instance=PART-1-10

2086, 2087, 2090, 2091, 2101, 2102, 2194, 2195, 2196, 2197, 2254, 2255, 2260,
2261, 2262, 2263

2374, 2375, 2452, 2453, 2460, 2461, 2462, 2463, 2566, 2567, 2568, 2575, 2576,

2578, 2579, 2580

2654, 2655, 2657, 2702

*Elset, elset=-CHAMBER-SURFACE, internal, instance=PART-1-1

1,

*Elset, elset=-CONTACT-AIRBAGTOPLATE, internal, instance=PART-1-1

1, 1325

*Elset, elset=-CONTACT-PLATETOAIRBAG, internal, instance=PART-1-1

1,

*Elset, elset=-SURFACE-BOT, internal, instance=PART-1-1

1, 1326, 2650

*Elset, elset=-SURFACE-TOP, internal, instance=PART-1-1

1, 1325

*Elset, elset=-CHAMBER-SURFACE-, internal, instance=PART-1-1, generate

1, 2650, 1

*Surface, type=ELEMENT, name=CHAMBER-SURFACE

-CHAMBER-SURFACE-,

*Elset, elset=-CHAMBER-SURFACE-1-SNEG, internal, instance=PART-1-

1, generate

1, 2650, 1

*Surface, type=ELEMENT, name=CHAMBER-SURFACE-1

-CHAMBER-SURFACE-1-SNEG, SNEG

*Elset, elset=-CHAMBER-SURFACE-1-PART2-SNEG, internal, instance=PART-

1-2, generate

1, 2650, 1

*Surface, type=ELEMENT, name=CHAMBER-SURFACE-1-PART2

-CHAMBER-SURFACE-1-PART2-SNEG, SNEG

*Elset, elset=-CHAMBER-SURFACE-1-PART3-SNEG, internal, instance=PART-

1-3, generate

1, 2650, 1

*Surface, type=ELEMENT, name=CHAMBER-SURFACE-1-PART3
-CHAMBER-SURFACE-1-PART3-SNEG, SNEG

*Elset, elset=-CHAMBER-SURFACE-1-PART4-SNEG, internal, instance=PART-
1-4, generate

1, 2650, 1

*Surface, type=ELEMENT, name=CHAMBER-SURFACE-1-PART4
-CHAMBER-SURFACE-1-PART4-SNEG, SNEG

*Elset, elset=-CHAMBER-SURFACE-1-PART5-SNEG, internal, instance=PART-
1-5, generate

1, 2650, 1

*Surface, type=ELEMENT, name=CHAMBER-SURFACE-1-PART5
-CHAMBER-SURFACE-1-PART5-SNEG, SNEG

*Elset, elset=-CHAMBER-SURFACE-1-PART6-SNEG, internal, instance=PART-
1-6, generate

1, 2650, 1

*Surface, type=ELEMENT, name=CHAMBER-SURFACE-1-PART6
-CHAMBER-SURFACE-1-PART6-SNEG, SNEG

*Elset, elset=-CHAMBER-SURFACE-1-PART7-SNEG, internal, instance=PART-
1-7, generate

1, 2650, 1

*Surface, type=ELEMENT, name=CHAMBER-SURFACE-1-PART7
-CHAMBER-SURFACE-1-PART7-SNEG, SNEG

*Elset, elset=-CHAMBER-SURFACE-1-PART8-SNEG, internal, instance=PART-
1-8, generate

1, 2650, 1

*Surface, type=ELEMENT, name=CHAMBER-SURFACE-1-PART8
-CHAMBER-SURFACE-1-PART8-SNEG, SNEG

*Elset, elset=-CHAMBER-SURFACE-1-PART9-SNEG, internal, instance=PART-

1-9, generate

1, 2650, 1

*Surface, type=ELEMENT, name=CHAMBER-SURFACE-1-PART9

-CHAMBER-SURFACE-1-PART9-SNEG, SNEG

*Elset, elset=-CHAMBER-SURFACE-1-PART10-SNEG, internal, instance=PART-

1-10, generate

1, 2650, 1

*Surface, type=ELEMENT, name=CHAMBER-SURFACE-1-PART10

-CHAMBER-SURFACE-1-PART10-SNEG, SNEG

*Elset, elset=-CHAMBER-SURFACE-PART2-SPOS, internal, instance=PART-

1-2, generate

1, 2650, 1

*Surface, type=ELEMENT, name=CHAMBER-SURFACE-PART2

-CHAMBER-SURFACE-PART2-SPOS, SPOS

*Elset, elset=-CHAMBER-SURFACE-PART3-SPOS, internal, instance=PART-

1-3, generate

1, 2650, 1

*Surface, type=ELEMENT, name=CHAMBER-SURFACE-PART3

-CHAMBER-SURFACE-PART3-SPOS, SPOS

*Elset, elset=-CHAMBER-SURFACE-PART4-SPOS, internal, instance=PART-

1-4, generate

1, 2650, 1

*Surface, type=ELEMENT, name=CHAMBER-SURFACE-PART4

-CHAMBER-SURFACE-PART4-SPOS, SPOS

*Elset, elset=-CHAMBER-SURFACE-PART5-SPOS, internal, instance=PART-

1-5, generate

1, 2650, 1

*Surface, type=ELEMENT, name=CHAMBER-SURFACE-PART5

-CHAMBER-SURFACE-PART5-SPOS, SPOS

```
*Elset, elset=-CHAMBER-SURFACE-PART6-SPOS, internal, instance=PART-
1-6, generate
1, 2650, 1
*Surface, type=ELEMENT, name=CHAMBER-SURFACE-PART6
-CHAMBER-SURFACE-PART6-SPOS, SPOS
*Elset, elset=-CHAMBER-SURFACE-PART7-SPOS, internal, instance=PART-
1-7, generate
1, 2650, 1
*Surface, type=ELEMENT, name=CHAMBER-SURFACE-PART7
-CHAMBER-SURFACE-PART7-SPOS, SPOS
*Elset, elset=-CHAMBER-SURFACE-PART8-SPOS, internal, instance=PART-
1-8, generate
1, 2650, 1
*Surface, type=ELEMENT, name=CHAMBER-SURFACE-PART8
-CHAMBER-SURFACE-PART8-SPOS, SPOS
*Elset, elset=-CHAMBER-SURFACE-PART9-SPOS, internal, instance=PART-
1-9, generate
1, 2650, 1
*Surface, type=ELEMENT, name=CHAMBER-SURFACE-PART9
-CHAMBER-SURFACE-PART9-SPOS, SPOS
*Elset, elset=-CHAMBER-SURFACE-PART10-SPOS, internal, instance=PART-
1-10, generate
1, 2650, 1
*Surface, type=ELEMENT, name=CHAMBER-SURFACE-PART10
-CHAMBER-SURFACE-PART10-SPOS, SPOS
*Elset, elset=-CHAMBER-EXT-SKIN-SURF-SNEG, internal, instance=PART-
1-1, generate
1, 2650, 1
*Surface, type=ELEMENT, name=CHAMBER-EXT-SKIN-SURF
```

```
-CHAMBER-EXT-SKIN-SURF-SNEG, SNEG
*Elset, elset=-SURFACE-BOT-SNEG, internal, instance=PART-1-1
1, 1326, 2650
*Surface, type=ELEMENT, name=SURFACE-BOT
-SURFACE-BOT-SNEG, SNEG
*Elset, elset=-SURFACE-TOP-SNEG, internal, instance=PART-1-1
1, 1325
*Surface, type=ELEMENT, name=SURFACE-TOP
-SURFACE-TOP-SNEG, SNEG
*End Assembly
*Amplitude, name=AMP-DAMPING-1-VBF
0., 0., 0.25, 0.5, 0.5, 0.75,
0.75, 1. 1., 1.
*Amplitude, name=AMP-DAMPING-2-VBF
0., 0., 0.0009999999, 0., 0.001, 100.,
0.0099999999, 100. 0.01, 0.
*Amplitude, name=RAMPSTRESS, time=TOTAL TIME, definition=SMOOTH
STEP
0., 0., 0.0025, 1.,
1., 1.
*Filter, name=FILTER-1000HZ, type=BUTTERWORTH
1000.
**
** MATERIALS
**
** _____ M A T E R I A L D A T A _____
** _
*Material, name=FABRIC
*Damping, beta=1e-06
```

```
*Density
1.42,
*Elastic
2.5e+09, 0.34
**
** INTERACTION PROPERTIES
**
*Fluid Behavior, name=AIR
*Molecular Weight
2.897e-05
*Capacity, type=POLYNOMIAL
28110., 1.967, 0.004802, 0., 0.
*Fluid Behavior, name=AR
*Molecular Weight
3.995e-05
*Capacity, type=POLYNOMIAL
20785.,0.,0.,0.,0.
*Fluid Behavior, name=CO2
*Molecular Weight
4.401e-05
*Capacity, type=POLYNOMIAL
25999., 43.5, -0.0148, 0., 0.
*Surface Interaction, name=DEFAULT
*Surface Interaction, name=GENERAL-CONTACT
*Friction
0.,
*Fluid Behavior, name=H2O
*Molecular Weight
1.802e-05
```

```
*Capacity, type=POLYNOMIAL
32200., 1.9, 0.0106, 0., 0.
*Fluid Behavior, name=HE
*Molecular Weight
4.003e-06
*Capacity, type=POLYNOMIAL
20785.,0.,0.,0.,0.
*Fluid Behavior, name=N2
*Molecular Weight
2.801e-05
*Capacity, type=POLYNOMIAL
27296., 5.23, 0., 0., 0.
*Fluid Behavior, name=N2O
*Molecular Weight
4.401e-05
*Capacity, type=POLYNOMIAL
25188., 52.1, -0.02, 0., 0.
*Fluid Behavior, name=O2
*Molecular Weight
3.2e-05
*Capacity, type=POLYNOMIAL
25723., 12.98, -0.00386, 0., 0.
**
** PHYSICAL CONSTANTS
**
*Physical Constants, absolute zero=0., universal gas=8314.41
**
** BOUNDARY CONDITIONS
**
```

```
** Name: Disp-BC-1 Type: Symmetry/Antisymmetry/Encastre
*Boundary
Plate, ENCASTRE
** Name: Disp-BC-2 Type: Symmetry/Antisymmetry/Encastre
*Boundary
Plate-PART2, ENCASTRE
** Name: Disp-BC-3 Type: Symmetry/Antisymmetry/Encastre
*Boundary
Plate-PART3, ENCASTRE
** Name: Disp-BC-4 Type: Symmetry/Antisymmetry/Encastre
*Boundary
Plate-PART4, ENCASTRE
** Name: Disp-BC-5 Type: Symmetry/Antisymmetry/Encastre
*Boundary
Plate-PART5, ENCASTRE
** Name: Disp-BC-6 Type: Symmetry/Antisymmetry/Encastre
*Boundary
Plate-PART6, ENCASTRE
** Name: Disp-BC-7 Type: Symmetry/Antisymmetry/Encastre
*Boundary
Plate-PART7, ENCASTRE
** Name: Disp-BC-8 Type: Symmetry/Antisymmetry/Encastre
*Boundary
Plate-PART8, ENCASTRE
** Name: Disp-BC-9 Type: Symmetry/Antisymmetry/Encastre
*Boundary
Plate-PART9, ENCASTRE
** Name: Disp-BC-10 Type: Symmetry/Antisymmetry/Encastre
*Boundary
```

```
Plate-PART10, ENCASTRE
** _____
**
** STEP: Inflation
**
*Step, name=Inflation, nlgeom=YES
Step-1
*Dynamic, Explicit, element by element, scale factor=0.8
, 0.5001
*Bulk Viscosity
0.06, 1.2
** Mass Scaling: Semi-Automatic
** Whole Model
*Variable Mass Scaling, dt=1e-06, type=below min, frequency=10
**
** LOADS
**
** Name: Load-1 Type: Pressure
*Dload, amplitude=AMP-DAMPING-1-VBF
CHAMBER-SURFACE-1, P, 500000.
** Name: Load-2 Type: Pressure
*Dload, amplitude=AMP-DAMPING-1-VBF
CHAMBER-SURFACE-1-PART2, P, 500000.
** Name: Load-3 Type: Pressure
*Dload, amplitude=AMP-DAMPING-1-VBF
CHAMBER-SURFACE-1-PART3, P, 500000.
** Name: Load-4 Type: Pressure
*Dload, amplitude=AMP-DAMPING-1-VBF
CHAMBER-SURFACE-1-PART4, P, 500000.
```

```
** Name: Load-5 Type: Pressure
*Dload, amplitude=AMP-DAMPING-1-VBF
CHAMBER-SURFACE-1-PART5, P, 500000.
** Name: Load-6 Type: Pressure
*Dload, amplitude=AMP-DAMPING-1-VBF
CHAMBER-SURFACE-1-PART6, P, 500000.
** Name: Load-7 Type: Pressure
*Dload, amplitude=AMP-DAMPING-1-VBF
CHAMBER-SURFACE-1-PART7, P, 500000.
** Name: Load-8 Type: Pressure
*Dload, amplitude=AMP-DAMPING-1-VBF
CHAMBER-SURFACE-1-PART8, P, 500000.
** Name: Load-9 Type: Pressure
*Dload, amplitude=AMP-DAMPING-1-VBF
CHAMBER-SURFACE-1-PART9, P, 500000.
** Name: Load-10 Type: Pressure
*Dload, amplitude=AMP-DAMPING-1-VBF
CHAMBER-SURFACE-1-PART10, P, 500000.
**
** INTERACTIONS
**
** Interaction: Cell1 - Cell2
*Contact Pair, interaction=GENERAL-CONTACT, mechanical constraint=KINEMATIC,
cpset="Cell1 - Cell2"
CHAMBER-SURFACE, CHAMBER-SURFACE-PART2
** Interaction: Cell1 - Cell6
*Contact Pair, interaction=GENERAL-CONTACT, mechanical constraint=KINEMATIC,
cpset="Cell1 - Cell6"
CHAMBER-SURFACE, CHAMBER-SURFACE-PART6
```

```
** Interaction: Cell2 - Cell 7
*Contact Pair, interaction=GENERAL-CONTACT, mechanical constraint=KINEMATIC,
cpset="Cell2 - Cell 7"
CHAMBER-SURFACE-PART2, CHAMBER-SURFACE-PART7
** Interaction: Cell2 - Cell3
*Contact Pair, interaction=GENERAL-CONTACT, mechanical constraint=KINEMATIC,
cpset="Cell2 - Cell3"
CHAMBER-SURFACE-PART2, CHAMBER-SURFACE-PART3
** Interaction: Cell3 - Cell4
*Contact Pair, interaction=GENERAL-CONTACT, mechanical constraint=KINEMATIC,
cpset="Cell3 - Cell4"
CHAMBER-SURFACE-PART3, CHAMBER-SURFACE-PART4
** Interaction: Cell3 - Cell8
*Contact Pair, interaction=GENERAL-CONTACT, mechanical constraint=KINEMATIC,
cpset="Cell3 - Cell8"
CHAMBER-SURFACE-PART3, CHAMBER-SURFACE-PART8
** Interaction: Cell4 - Cell5
*Contact Pair, interaction=GENERAL-CONTACT, mechanical constraint=KINEMATIC,
cpset="Cell4 - Cell5"
CHAMBER-SURFACE-PART4, CHAMBER-SURFACE-PART5
** Interaction: Cell4 - Cell9
*Contact Pair, interaction=GENERAL-CONTACT, mechanical constraint=KINEMATIC,
cpset="Cell4 - Cell9"
CHAMBER-SURFACE-PART4, CHAMBER-SURFACE-PART9
** Interaction: Cell5 - Cell10
*Contact Pair, interaction=GENERAL-CONTACT, mechanical constraint=KINEMATIC,
cpset="Cell5 - Cell10"
CHAMBER-SURFACE-PART5, CHAMBER-SURFACE-PART10
** Interaction: Cell6 - Cell7
```

```
*Contact Pair, interaction=GENERAL-CONTACT, mechanical constraint=KINEMATIC,
cpset="Cell6 - Cell7"
CHAMBER-SURFACE-PART6, CHAMBER-SURFACE-PART7
** Interaction: Cell7 - Cell8
*Contact Pair, interaction=GENERAL-CONTACT, mechanical constraint=KINEMATIC,
cpset="Cell7 - Cell8"
CHAMBER-SURFACE-PART7, CHAMBER-SURFACE-PART8
** Interaction: Cell8 - Cell9
*Contact Pair, interaction=GENERAL-CONTACT, mechanical constraint=KINEMATIC,
cpset="Cell8 - Cell9"
CHAMBER-SURFACE-PART8, CHAMBER-SURFACE-PART9
** Interaction: Cell9 - Cell10
*Contact Pair, interaction=GENERAL-CONTACT, mechanical constraint=KINEMATIC,
cpset="Cell9 - Cell10"
CHAMBER-SURFACE-PART9, CHAMBER-SURFACE-PART10
**
** OUTPUT REQUESTS
**
*Restart, write, number interval=2, time marks=NO
**
** FIELD OUTPUT: F-Output-1
**
*Output, field
*Node Output
A, AR, AT, RF, U, UR, UT, V
VR, VT
*Element Output, directions=YES
EFABRIC, ERV, LE, MISESMAX, NE, PEEQ, PEEQMAX, PEQC, S, SFAB-
RIC
```

*Contact Output

CFORCE, CSTRESS, CTHICK

**

** HISTORY OUTPUT: H-Output-1

**

*Output, history

*Energy Output

ALLAE, ALLCD, ALLCW, ALLDC, ALLDMD, ALLFD, ALLIE, ALLKE,

ALLMW, ALLPD, ALLPW, ALLSE, ALLVD, ALLWK,

ETOTAL

*End Step

Appendix C

Appendix Three

Abaqus input files for the following:

1. Bending and buckling of the inflated cylinder without the Fluid Activation Method
2. Bending and buckling of the inflated cylinder with the Fluid Activation Method
3. Modified UMAT Fortran subroutine
4. post-inflation of the bent and buckled cylinder with the UMAT subroutine

C.1 Bending and buckling of the inflated cylinder without the Fluid Activation Method

```
*Heading
** Job name: BeamVumat Model name: Beam Bending Model
** Generated by: Abaqus/CAE 6.13-2
*Preprint, echo=NO, model=NO, history=NO, contact=NO
**
** PARTS
**
*Part, name=Complete
*End Part
**
**
** ASSEMBLY
**
*Assembly, name=Assembly
**
*Instance, name=Complete, part=Complete
*Node
1, 0.0599999987, 0., 0.
2, 0.0599999987, 0., 0.649999976
3, 0.0575695783, 0.0169039536, 0.
***
**
*
**
***
```

946, 0.0575695783, 0.0169039536, 0.598684192

947, 0.0575695783, 0.0169039536, 0.615789473

948, 0.0575695783, 0.0169039536, 0.632894754

*Element, type=M3D4R

1, 46, 47, 49, 48

2, 47, 1, 23, 49

3, 48, 49, 51, 50

**

*

**

130, 90, 129, 131

131, 90, 131, 133

132, 90, 133, 91

*Nset, nset=Beam

1, 2, 3, 4, 5, 6, 7, 8, 9, 10, 11, 12, 13, 14, 15, 16

17, 18, 19, 20, 21, 22, 23, 24, 25, 26, 27, 28, 29, 30, 31, 32

33, 34, 35, 36, 37, 38, 39, 40, 41, 42, 43, 44, 135, 136, 137, 138

**

*

**

907, 908, 909, 910, 911, 912, 913, 914, 915, 916, 917, 918, 919, 920, 921, 922

923, 924, 925, 926, 927, 928, 929, 930, 931, 932, 933, 934, 935, 936, 937, 938

939, 940, 941, 942, 943, 944, 945, 946, 947, 948

*Elset, elset=Beam, generate

133, 968, 1

```
*Nset, nset=CapOne
2, 24, 25, 26, 27, 28, 29, 30, 31, 32, 33, 34, 35, 36, 37, 38
39, 40, 41, 42, 43, 44, 90, 91, 92, 93, 94, 95, 96, 97, 98, 99
100, 101, 102, 103, 104, 105, 106, 107, 108, 109, 110, 111, 112, 113, 114, 115
116, 117, 118, 119, 120, 121, 122, 123, 124, 125, 126, 127, 128, 129, 130, 131
132, 133, 134
*Elset, elset=CapOne, generate
67, 132, 1
*Nset, nset=CapTwo
1, 3, 4, 5, 6, 7, 8, 9, 10, 11, 12, 13, 14, 15, 16, 17
18, 19, 20, 21, 22, 23, 45, 46, 47, 48, 49, 50, 51, 52, 53, 54
55, 56, 57, 58, 59, 60, 61, 62, 63, 64, 65, 66, 67, 68, 69, 70
71, 72, 73, 74, 75, 76, 77, 78, 79, 80, 81, 82, 83, 84, 85, 86
87, 88, 89
*Elset, elset=CapTwo, generate
1, 66, 1
*Nset, nset=Complete, generate
1, 948, 1
*Elset, elset=Complete, generate
1, 968, 1
** Section: ShellMembrane
*Membrane Section, elset=Complete, material="Kapton HN"
5e-05,
*End Instance
**
*Node
1, 0., -3.67394048e-18, 0.6499999976
*Node
2, 0., 3.67394048e-18, 0.
```

*Nset, nset=CavityNode, instance=Complete
45,

*Nset, nset=Fixed, instance=Complete
1, 3, 4, 5, 6, 7, 8, 9, 10, 11, 12, 13, 14, 15, 16, 17
18, 19, 20, 21, 22, 23

*Nset, nset=FixedBase, instance=Complete
1, 3, 4, 5, 6, 7, 8, 9, 10, 11, 12, 13, 14, 15, 16, 17
18, 19, 20, 21, 22, 23, 45, 46, 47, 48, 49, 50, 51, 52, 53, 54
55, 56, 57, 58, 59, 60, 61, 62, 63, 64, 65, 66, 67, 68, 69, 70
71, 72, 73, 74, 75, 76, 77, 78, 79, 80, 81, 82, 83, 84, 85, 86
87, 88, 89

*Elset, elset=FixedBase, instance=Complete, generate
1, 66, 1

*Nset, nset=RF
1,

*Nset, nset=TopCircum, instance=Complete
2, 24, 25, 26, 27, 28, 29, 30, 31, 32, 33, 34, 35, 36, 37, 38
39, 40, 41, 42, 43, 44

*Elset, elset=TopCircum, instance=Complete
68, 70, 72, 74, 76, 78, 80, 82, 84, 86, 88, 90, 92, 94, 96, 98
100, 102, 104, 106, 108, 110, 170, 208, 246, 284, 322, 360, 398, 436, 474, 512
550, 588, 626, 664, 702, 740, 778, 816, 854, 892, 930, 968

*Elset, elset=-Complete-, internal, instance=Complete, generate
1, 968, 1

*Surface, type=ELEMENT, name=Complete
-Complete-,

*Elset, elset=-Inside-SNEG, internal, instance=Complete, generate
1, 968, 1

*Surface, type=ELEMENT, name=Inside

```
-Inside-SNEG, SNEG
** Constraint: Constraint-1
*Rigid Body, ref node=RF, tie nset=TopCircum, position=CENTER OF MASS
*End Assembly
*Amplitude, name=Amp-1, definition=SMOOTH STEP
0., 0., 0.1, 0.1, 0.5, 0.5, 1., 1.
**
** MATERIALS
**
*Material, name="Kapton HN"
*Density
1420.,
*Elastic
1.42e+09, 0.34
**
** INTERACTION PROPERTIES
**
*Surface Interaction, name=ContactProp
**
** BOUNDARY CONDITIONS
**
** Name: Fixed Type: Symmetry/Antisymmetry/Encastre
*Boundary
Fixed, ENCASTRE
**
** INTERACTIONS
**
** Interaction: GeneralContact
*Contact, op=NEW
```

```
*Contact Inclusions, ALL EXTERIOR
*Contact Property Assignment
, , ContactProp
**
** STEP: Step-1
**
*Step, name=Step-1, nlgeom=YES
*Dynamic, Explicit
, 1.
*Bulk Viscosity
0.06, 1.2
**
** BOUNDARY CONDITIONS
**
** Name: BC-1 Type: Displacement/Rotation
*Boundary, amplitude=Amp-1
RF, 4, 4, 1.5787
**
** OUTPUT REQUESTS
**
*Restart, write, number interval=1, time marks=NO
**
** FIELD OUTPUT: F-Output-1
**
*Output, field, variable=PRESELECT
**
** HISTORY OUTPUT: H-Output-1
**
*Output, history, variable=PRESELECT
```

*End Step

C.2 Bending and buckling of the inflated cylinder with the Fluid Activation Method

*Heading

** Job name: CylinBuck Model

** Generated by: Abaqus/CAE 6.11-2

*Preprint, echo=NO, model=NO, history=NO, contact=NO

**

** PARTS

**

*Part, name=Complete

*Node

1, 0.129903123, -0.0433883741, 0.

2, 0.134670913, -0.0521435216, 0.

3, 0.140286759, -0.0603804402, 0.

**

*

**

7497, 0.319503069, 0.00995678455, 0.970000029

7498, 0.319503069, 0.00995678455, 0.980000019

7499, 0.319503069, 0.00995678455, 0.99000001

*Element, type=M4D4

1, 128, 129, 138, 137

2, 129, 130, 139, 138

3, 130, 131, 140, 139

**

*

**

7558, 1359, 1360, 7498, 7497

7559, 1360, 1361, 7499, 7498

7560, 1361, 112, 114, 7499

*Element, type=M3R3

568, 127, 128, 137

569, 127, 137, 146

570, 127, 146, 155

**

*

**

1258, 695, 1236, 1245

1259, 695, 1245, 1254

1260, 695, 1254, 696

**

*Node

8000, 220.E-03, 0., 0.5

*NSET, Nset=CavityNode

8000

**

*Elset, elset=-PickedSet2, internal, generate

```
1, 7560, 1
*Elset, elset=-PickedSet5, internal, generate
1, 7560, 1
*Elset, elset=-Inside-SPOS, internal, generate
1, 7560, 1
*Surface, type=ELEMENT, name=Inside
-Inside-SPOS, SPOS
** Section: Shell Homogeneous
*Shell Section, elset=-PickedSet2, material=Kapton HN
5e-05, 5
*End Part
**
**
** ASSEMBLY
**
*Assembly, name=Assembly
**
*Instance, name=Complete, part=Complete
-0.22, 0., 0.
**
** FLUID INFORMATION
**
*FLUID CAVITY, name=Cavity, Ambient Pressure=1.013250e05, REFNODE=CavityNode,
Ambient
Temperature=2.950000e02, SURFACE=Inside, MINIMUM VOLUME=INITIAL
VOLUME, BEHAVIOR=AIR, ADIABATIC
**
** GAS SPECIES DATA
```

```
**  
  
** FLUID CAVITY BEHAVIOUR DEFINITIONS  
  
**  
  
** GAS SPECIES: 'Air'  
  
**  
  
*Fluid behavior, Name=Air  
  
**  
  
*MOLECULAR WEIGHT  
  
0.0289  
  
**  
  
*CAPACITY, TYPE=POLYNOMIAL  
  
28.110, 1.967e-3, -1.966e-9, 0.0  
  
**  
  
** GAS SPECIES: 'O2'  
  
**  
  
*Fluid behavior, Name=O2  
  
**  
  
*Capacity, Type=POLYNOMIAL  
  
2.572300e+04, 1.298000e+01, -3.860000e-03, 0.000000e+00, 0.000000e+00  
  
**  
  
*Molecular weight  
  
3.200000e-05,  
  
**  
  
** GAS SPECIES: 'CO2'  
  
**  
  
*Fluid behavior, Name=CO2  
  
**  
  
*Capacity, Type=POLYNOMIAL  
  
2.599900e+04, 4.350000e+01, -1.480000e-02, 0.000000e+00, 0.000000e+00
```

```
**  
  
*Molecular weight  
4.401000e-05,  
**  
** GAS SPECIES: 'N2'  
**  
*Fluid behavior, Name=N2  
**  
*Capacity, Type=POLYNOMIAL 2.729600e+04, 5.230000e+00, 0.000000e+00,  
0.000000e+00, 0.000000e+00  
**  
*Molecular weight  
2.801000e-05,  
**  
** GAS SPECIES: 'HE'  
**  
*Fluid behavior, Name=HE  
**  
*Capacity, Type=POLYNOMIAL  
2.078500e+04, 0.000000e+00, 0.000000e+00, 0.000000e+00, 0.000000e+00  
**  
*Molecular weight  
4.003000e-06,  
**  
** GAS SPECIES: 'N2O'  
**  
*Fluid behavior, Name=N2O  
**  
*Capacity, Type=POLYNOMIAL
```

2.518800e+04, 5.210000e+01, -2.000000e-02, 0.000000e+00, 0.000000e+00

**

*Molecular weight

4.401000e-05,

**

** GAS SPECIES: 'AR'

**

*Fluid behavior, Name=AR

**

*Capacity, Type=POLYNOMIAL

2.078500e+04, 0.000000e+00, 0.000000e+00, 0.000000e+00, 0.000000e+00

**

*Molecular weight

3.995000e-05,

**

**

*FLUID INFLATOR, NAME=CavityInflation, PROPERTY=CavityInflationProperty

CavityNode

*

**

*FLUID INFLATOR PROPERTY, Name=CavityInflationProperty, TYPE=TEMPERATURE

AND MASS

**

0.000000e+00, 0.000000e+00, 0.000000e+00

1.000000e-04, 0.000000e+00, 0.000000e+00

2.000000e-04, 0.000000e+00, 0.000000e+00

**

*

**

3.990000e-02, 1.665000e+02, 1.875000e-05

4.000000e-02, 1.665000e+02, 1.875000e-14

1.000000e+00, 1.665000e+02, 0.000000e+00

**

**

*FLUID INFLATOR MIXTURE, Number species=6, Type=MOLAR FRAC-
TION

O2, CO2, AR, N2, HE, N2O

**

0.000000e+00, 1.000000e+00, 0.000000e+00, 0.000000e+00, 0.000000e+00, 0.000000e+00,
0.000000e+00

1.000000e-04, 1.000000e+00, 0.000000e+00, 0.000000e+00, 0.000000e+00, 0.000000e+00,
0.000000e+00

2.000000e-04, 1.000000e+00, 0.000000e+00, 0.000000e+00, 0.000000e+00, 0.000000e+00,
0.000000e+00

**

*

**

3.980000e-02, 2.400000e-02, 7.800000e-02, 6.284000e-01, 4.820000e-02, 8.980000e-
02, 1.316000e-01

3.990000e-02, 2.400000e-02, 7.810000e-02, 6.283000e-01, 4.820000e-02, 8.980000e-
02, 1.316000e-01

1.000000e+00, 2.400000e-02, 7.810000e-02, 6.283000e-01, 4.820000e-02, 8.980000e-
02, 1.316000e-01

**

```
*End Instance
**

*Node
1, 0., 0., 1.
*Nset, nset=-PickedSet37, internal
1,
*Nset, nset=-PickedSet39, internal
1,
*Node
8000, 220.E-03, 0., 0.5
*NSET, Nset=CavityNode, instance=Complete
8000
*Nset, nset=-PickedSet36, internal, instance=Complete
1, 2, 3, 4, 9, 10, 11, 15, 16, 19, 20, 21, 25, 26, 27, 28
33, 34, 35, 39, 40, 41, 45, 46, 47, 51, 52, 53, 57, 58, 59, 63
64, 65, 69, 70, 71, 75, 76, 77, 81, 82, 83, 84, 89, 90, 91, 92
***
**
*
**
***
1224, 1225, 1226, 1227, 1228, 1229, 1230, 1231, 1232, 1233, 1234, 1235, 1236,
1237, 1238, 1239
1240, 1241, 1242, 1243, 1244, 1245, 1246, 1247, 1248, 1249, 1250, 1251, 1252,
1253, 1254, 1255
1256, 1257, 1258, 1259, 1260, 1261, 1262
*Nset, nset=RF, instance=Complete
127,
*Nset, nset=-PickedSet40, internal, instance=Complete
```

5, 6, 7, 8, 12, 13, 14, 17, 18, 22, 23, 24, 29, 30, 31, 32
36, 37, 38, 42, 43, 44, 48, 49, 50, 54, 55, 56, 60, 61, 62, 66
67, 68, 72, 73, 74, 78, 79, 80, 85, 86, 87, 88, 93, 94, 95, 96
100, 101, 102, 106, 107, 108, 112, 113, 114, 118, 119, 120, 124, 125, 126
*Nset, nset=-PickedSet43, internal, instance=Complete
8000,
*Elset, elset=-PickedSurf41-SPOS, internal, instance=Complete, generate
1261, 7560, 1
*Surface, type=ELEMENT, name=-PickedSurf41, internal
-PickedSurf41-SPOS, SPOS
*Elset, elset=-PickedSurf42-SPOS, internal, instance=Complete, generate
1261, 7560, 1
*Surface, type=ELEMENT, name=-PickedSurf42, internal
-PickedSurf42-SPOS, SPOS
**
**
** Constraint: Rigid *Rigid Body, ref node=-PickedSet39, tie nset=-PickedSet40
*End Assembly
**
*PHYSICAL CONSTANTS, UNIVERSAL GAS CONSTANT=8.31434, AB-
SOLUTE ZERO=-293.15
**
**
*Amplitude, name=Pressure, Definition=SMOOTH STEP
0.0, 0.0
0.25, 25.0
0.5,50.0
0.75,100.0
1, 200.0

```
**  
  
*Amplitude, name=AMP-INFLATOR, Definition=SMOOTH STEP  
0.0, 0.0, 0.25, 25.0, 0.5, 50.0, 1, 100.0  
**  
  
*Amplitude, name=Smooth Step, Definition=SMOOTH STEP  
0., 0., 0.1, 0.5, 0.2, 1.0  
**  
  
**  
  
** MATERIALS  
**  
  
** A du point Kapton HN membrane  
*Material, name="Kapton HN"  
*Density  
1420.,  
*Elastic  
1.42e+09, 0.34  
**  
  
**  
  
** INITIAL FLUID CONDITIONS  
**  
  
*INITIAL CONDITIONS, TYPE=FLUID PRESSURE  
Complete.CavityNode, 0.0  
*INITIAL CONDITIONS, TYPE=TEMPERATURE  
Complete.CavityNode, 2.95e+02  
**  
  
**  
  
** BOUNDARY CONDITIONS  
**  
  
** Name: BC-3 Type: Displacement/Rotation
```

```
*Boundary
-PickedSet43, 3, 3
** Name: Fixed Base Type: Symmetry/Antisymmetry/Encastre
*Boundary
-PickedSet36, ENCASTRE
**
**
** STEP: Bending
**
*Step, name=Bending
*Dynamic, Explicit
, 1.
*Bulk Viscosity
0.06, 1.2
**
** BOUNDARY CONDITIONS
**
** Name: Bending Type: Displacement/Rotation
*Boundary, amplitude=Smooth Step
-PickedSet37, 5, 5, 1.57078
**
**
** FLUID INFLATION
**
*FLUID INFLATOR ACTIVATION, Inflation time amplitude=AMP-INFLATOR
Complete.CavityInflation
*Boundary, amplitude=Pressure
CavityNode, 8, 8, 100.
**
```

```
**  
**  
** OUTPUT REQUESTS  
**  
*Restart, write, number interval=1, time marks=NO  
**  
** FIELD OUTPUT: F-Output-1  
**  
*Output, field, variable=PRESELECT  
**  
** HISTORY OUTPUT: H-Output-1  
**  
*Output, history, variable=PRESELECT  
*End Step
```

C.3 UMAT Fortran subroutine

```
*USER SUBROUTINES  
subroutine vumat(  
C Read only (unmodifiable)variables -  
1 nblock, ndir, nshr, nstatev, nfieldv, nprops, lanneal,  
2 stepTime, totalTime, dt, cmname, coordMp, charLength,  
3 props, density, strainInc, relSpinInc,  
4 tempOld, stretchOld, defgradOld, fieldOld,  
5 stressOld, stateOld, enerInternOld, enerInelasOld,  
6 tempNew, stretchNew, defgradNew, fieldNew,  
C Write only (modifiable) variables -  
7 stressNew, stateNew, enerInternNew, enerInelasNew )
```

```

C
include 'vaba-param.inc'
C
dimension props(nprops), density(nblock), coordMp(nblock,*),
1 charLength(nblock), strainInc(nblock,ndir+nshr),
2 relSpinInc(nblock,nshr), tempOld(nblock),
3 stretchOld(nblock,ndir+nshr),
4 defgradOld(nblock,ndir+nshr+nshr),
5 fieldOld(nblock,nfieldv), stressOld(nblock,ndir+nshr),
6 stateOld(nblock,nstatev), enerInternOld(nblock),
7 enerInelasOld(nblock), tempNew(nblock),
8 stretchNew(nblock,ndir+nshr),
8 defgradNew(nblock,ndir+nshr+nshr),
9 fieldNew(nblock,nfieldv),
1 stressNew(nblock,ndir+nshr), stateNew(nblock,nstatev),
2 enerInternNew(nblock), enerInelasNew(nblock)
C
character*80 cmname
real DDSDDE(nblock,ndir+nshr,ndir+nshr)
real PSIG(nblock,ndir),PEPS(nblock,ndir)
real E,NU

Integer i,j,k,times,IFLAG,STATE,SWITCH
C
C open(1,file='C:',status='replace') C MATERIAL PROPERTIES FOR ISOTROPIC
MEMBRANE
IF (nprops .EQ. 3) THEN
E=PROPS(1)
NU=PROPS(2)

```

```

SWITCH=PROPS(3)
C MATERIAL PROPERTIES FOR TENDON
ELSE IF (nprops .EQ. 2) THEN
E=PROPS(1)
SWITCH=PROPS(2)
END IF

do 100 i=1,nblock
C
IF (ndir .EQ. 1) THEN
do j=1,nstatev-1
stateNew(i,j)=stateOld(i,j)+strainInc(i,j)
end do
stateNew(i,4)=stateNew(i,4)+strainInc(i,4)
stateNew(i,nstatev)=stateOld(i,nstatev)+1
times=stateNew(i,nstatev)

C Write (6,'(A,I,A,I)'),'i=',i,'times=',times

C WRITE (6,'(/A,E10.3E3,2X,A,E10.3E3,2X,A,E10.3E3,2X,A,E10.3E3)'),
C 'stateO11=',stateOld(i,1),'stateO22=',stateOld(i,2),'stateO33=',
C stateOld(i,3),'stateO12=',stateOld(i,4)

C WRITE (6,'(/A,E10.3E3,2X,A,E10.3E3,2X,A,E10.3E3,2X,A,E10.3E3)'),
C 'strainInc11=',strainInc(i,1),'strainInc22=',strainInc(i,2),
C 'strainInc=',strainInc(i,3),'stateO12=',strainInc(i,4)

C WRITE (6,'(/A,E10.3E3,2X,A,E10.3E3,2X,A,E10.3E3,2X,A,E10.3E3)'),
C 'state11=',stateNew(i,1),'state22=',stateNew(i,2),'state33=',

```

```
C stateNew(i,3),state12=,stateNew(i,4)

C CALCULATE CURRENT STRESS VALUES
C stressNew(i,1)=E*stateNew(i,1)
stressNew(i,1)=E*stateNew(i,1)

IF (times .GT. SWITCH) THEN
if (stateNew(i,1)i=0) then
stressNew(i,1)=0
endif
endif

ELSEIF (ndir .EQ. 3) THEN
do j=1,nstatev-1
stateNew(i,j)=stateOld(i,j)+strainInc(i,j)
end do
stateNew(i,4)=stateNew(i,4)+strainInc(i,4)
stateNew(i,nstatev)=stateOld(i,nstatev)+1
times=stateNew(i,nstatev)

C Write (6,'(A,I,A,I)'),i=i,i,times=,times

C WRITE (6,'(/A,E10.3E3,2X,A,E10.3E3,2X,A,E10.3E3,2X,A,E10.3E3)'),
C 'stateO11=',stateOld(i,1),'stateO22=',stateOld(i,2),'stateO33=',
C stateOld(i,3),'stateO12=',stateOld(i,4)

C WRITE (6,'(/A,E10.3E3,2X,A,E10.3E3,2X,A,E10.3E3,2X,A,E10.3E3)'),
C 'strainInc11=',strainInc(i,1),'strainInc22=',strainInc(i,2),
C 'strainInc=',strainInc(i,3),'stateO12=',strainInc(i,4)
```

```
C WRITE (6, '(/A,E10.3E3,2X,A,E10.3E3,2X,A,E10.3E3,2X,A,E10.3E3)'),  
C 'state11=',stateNew(i,1),'state22=',stateNew(i,2),'state33=',  
C stateNew(i,3),'state12=',stateNew(i,4)
```

```
C FORM INITIAL STIFFNESS MATRIX
```

```
do j=1,ndir+nshr  
do k=1,ndir+nshr  
DDSDDE(i,j,k)=0  
end do  
end do
```

```
C FORM TAUT STIFFNESS MATRIX
```

```
DDSDDE(i,1,1)=E/(1.0-NU*NU)  
DDSDDE(i,1,2)=E*NU/(1.0-NU*NU)  
DDSDDE(i,2,1)=DDSDDE(i,1,2)  
DDSDDE(i,2,2)=DDSDDE(i,1,1)  
DDSDDE(i,4,4)=E/(2.0*(1.0+NU))
```

```
C CALCULATE CURRENT STRESS VALUES
```

```
stressNew(i,1)=DDSDDE(i,1,1)*stateNew(i,1)+DDSDDE(i,1,2)  
*stateNew(i,2)+DDSDDE(i,1,3)*stateNew(i,3)+DDSDDE(i,1,4)  
*stateNew(i,4)  
  
stressNew(i,2)=DDSDDE(i,2,1)*stateNew(i,1)+DDSDDE(i,2,2)  
*stateNew(i,2)+DDSDDE(i,2,3)*stateNew(i,3)+DDSDDE(i,2,4)
```

```

*stateNew(i,4)

stressNew(i,3)=DDSDDE(i,3,1)*stateNew(i,1)+DDSDDE(i,3,2)
*stateNew(i,2)+DDSDDE(i,3,3)*stateNew(i,3)+DDSDDE(i,3,4)
*stateNew(i,4)

stressNew(i,4)=DDSDDE(i,4,1)*stateNew(i,1)+DDSDDE(i,4,2)
*stateNew(i,2)+DDSDDE(i,4,3)*stateNew(i,3)+DDSDDE(i,4,4)
*stateNew(i,4)

C WRITE (6,'(/A,E10.3E3,2X,A,E10.3E3,2X,A,E10.3E3,2X,A,E10.3E3)'),
C 'stress11=',stressNew(i,1),'stress22=',stressNew(i,2),'stress33=',
C stressNew(i,3),'stress12=',stressNew(i,4)

C CALCULATE PRINCIPAL STRESS
PSIG(i,1)=(stressNew(i,1)+stressNew(i,2))/2+sqrt(stressNew(i,4)
*stressNew(i,4)+(stressNew(i,1)-stressNew(i,2))
*(stressNew(i,1)-stressNew(i,2))/4)

PSIG(i,2)=(stressNew(i,1)+stressNew(i,2))/2-sqrt(stressNew(i,4)
*stressNew(i,4)+(stressNew(i,1)-stressNew(i,2))
*(stressNew(i,1)-stressNew(i,2))/4)

PSIG(i,3)=0

C WRITE (6,'(/A,E10.3E3,2X,A,E10.3E3,2X,A,E10.3E3,2X)'),
C 'PSIG(i,1)=' ,PSIG(i,1) , 'PSIG(i,2)=' ,PSIG(i,2) , 'PSIG(i,3)=' ,

```

```
C PSIG(i,3)
```

```
C CALCULATE PRINCIPAL STRAIN
```

```
PEPS(i,1)=(stateNew(i,1)+stateNew(i,2))/2+sqrt(stateNew(i,4)  
*stateNew(i,4)/4+(stateNew(i,1)-stateNew(i,2))  
*(stateNew(i,1)-stateNew(i,2))/4)
```

```
PEPS(i,2)=(stateNew(i,1)+stateNew(i,2))/2-sqrt(stateNew(i,4)  
*stateNew(i,4)/4+(stateNew(i,1)-stateNew(i,2))  
*(stateNew(i,1)-stateNew(i,2))/4)
```

```
PEPS(i,3)=0
```

```
IFLAG=0
```

```
STATE=1
```

```
C insert
```

```
C DETERMINE WHEN FIRST ITERATION STARTS (ZEROTH ITERA-  
TION WHEN NO STRAIN)
```

```
j=1
```

```
DO WHILE ((IFLAG.EQ.0).AND.(j.LE.ndir+nshr))
```

```
IF (stateNew(i,j).NE.0.0) IFLAG=1
```

```
j=j+1
```

```
END DO
```

```
C SKIP STATE TESTS FOR ZEROTH ITERATION
```

```
IF (IFLAG.EQ.1) THEN
```

```
IF (times.GT. SWITCH) THEN

C DETERMINE ELEMENT STATE (TAUT, SLACK, OR WRINKLED)
IF (PSIG(i,2).GT.0.0) THEN
C SET STRESS VALUES TO CURRENT VALUES (TAUT)
STATE=1
ELSE

IF (PEPS(i,1).GT.0.0) THEN

C FORM WRINKLED STIFFNESS MATRIX
Q=(stateNew(i,4))/(PEPS(i,1)-PEPS(i,2))
P=(stateNew(i,1)-stateNew(i,2))/(PEPS(i,1)-PEPS(i,2))
DO j=1,ndir+nshr
DO k=1,ndir+nshr
DDSDDE(i,j,k)=0.0
END DO
END DO
DDSDDE(i,1,1)=E*(1.0+P)/2.0
DDSDDE(i,1,4)=Q*E/4.0
DDSDDE(i,2,2)=E*(1.0-P)/2.0
DDSDDE(i,2,4)=DDSDDE(i,1,4)
DDSDDE(i,4,1)=DDSDDE(i,1,4)
DDSDDE(i,4,2)=DDSDDE(i,2,4)
DDSDDE(i,4,4)=E/4.0
STATE=0
ELSE

C FORM SLACK STIFFNESS MATRIX
```

```
DO j=1,ndir+nshr
DO k=1,ndir+nshr
DDSDDE(i,j,k)=0.0
END DO
END DO
STATE=-1
END IF
END IF
END IF
END IF
```

C RECALCULATE CURRENT STRESS VALUES

```
stressNew(i,1)=DDSDDE(i,1,1)*stateNew(i,1)+DDSDDE(i,1,2)
*stateNew(i,2)+DDSDDE(i,1,3)*stateNew(i,3)+DDSDDE(i,1,4)
*stateNew(i,4)
```

```
stressNew(i,2)=DDSDDE(i,2,1)*stateNew(i,1)+DDSDDE(i,2,2)
*stateNew(i,2)+DDSDDE(i,2,3)*stateNew(i,3)+DDSDDE(i,2,4)
*stateNew(i,4)
```

```
stressNew(i,3)=DDSDDE(i,3,1)*stateNew(i,1)+DDSDDE(i,3,2)
*stateNew(i,2)+DDSDDE(i,3,3)*stateNew(i,3)+DDSDDE(i,3,4)
*stateNew(i,4)
```

```
stressNew(i,4)=DDSDDE(i,4,1)*stateNew(i,1)+DDSDDE(i,4,2)
*stateNew(i,2)+DDSDDE(i,4,3)*stateNew(i,3)+DDSDDE(i,4,4)
*stateNew(i,4)
```

C RECALCULATE PRINCIPAL STRESS

```
PSIG(i,1)=(stressNew(i,1)+stressNew(i,2))/2+sqrt(stressNew(i,4)
*stressNew(i,4)+(stressNew(i,1)-stressNew(i,2))
*(stressNew(i,1)-stressNew(i,2))/4)
```

```
PSIG(i,2)=(stressNew(i,1)+stressNew(i,2))/2-sqrt(stressNew(i,4)
*stressNew(i,4)+(stressNew(i,1)-stressNew(i,2))
*(stressNew(i,1)-stressNew(i,2))/4)
```

```
PSIG(i,3)=0
```

```
C Insert
```

```
C WRITE (6,'(/A,E15.3E3,A,F8.2)'),'E=',E,'NU=',NU
```

```
C write (6,'(/A,I)'),'State=',state
```

```
C WRITE (1,'(/A,I,A,I)'),'NDIR=',NDIR,'NSHR=',NSHR
```

```
C WRITE (6,'(/A,E10.3E3,2X,A,E10.3E3,2X,A,E10.3E3,2X,A,E10.3E3)'),
```

```
C 'stress11=',stressNew(i,1),'stress22=',stressNew(i,2),'stress33=',
```

```
C stressNew(i,3),'stress12=',stressNew(i,4)
```

```
C write(6,'(//)')
```

```
END IF
```

```
100 continue
```

```
C
```

```
C close(1)
```

```
return
```

```
end
```

```
subroutine vload (  
  C Read only (unmodifiable)variables -  
  nblock, ndim, stepTime, totalTime,  
  2amplitude, curCoords, velocity, dirCos, jltyp, sname,  
  C Write only (modifiable) variable -  
  3value )  
  C  
  include 'vaba-param.inc'  
  C  
  dimension curCoords(nblock,ndim), velocity(nblock,ndim),  
  1 dirCos(nblock,ndim,ndim), value(nblock)  
  character*80 sname  
  C  
  
  do 100 km = 1, nblock  
  
  value(km)=(10.+0*curCoords(km,1))*amplitude  
  
  100 continue  
  C write (6,'(/A,I,/A,I)', 'stepTime=',stepTime,'totalTime',totalTime  
  
  return  
end
```

C.4 Post-inflation of the bent and buckled cylinder with the UMAT subroutine

```
*Heading
** Job name: Job-1 Model name: 06-Beam-0-65
** Generated by: Abaqus/CAE 6.11-2
*Preprint, echo=NO, model=NO, history=NO, contact=NO
**
** PARTS
**
*PART, NAME=Complete
*Node
1, 0.337500006, 0., 0.649999976
2, 0.337500006, 0., 0.
3, 0.335683852, 0.0149572287, 0.649999976
***
**
*
**
***
1300, 0.290170968, -0.00373930717, 0.649999976
1301, 0.305341929, -0.00747861434, 0.649999976
1302, 0.320512891, -0.011217922, 0.649999976
*Element, type=M3D4R
1, 2, 53, 95, 28
2, 53, 54, 96, 95
3, 54, 55, 97, 96
***
```

```
**  
*  
**  
***  
1298, 1300, 1301, 1226, 1225  
1299, 1301, 1302, 1227, 1226  
1300, 1302, 27, 1, 1227  
*Element, type=M3D3  
1197, 1145, 1146, 1149  
1198, 1145, 1149, 1152  
1199, 1145, 1152, 1155  
***  
**  
*  
**  
***  
1324, 1224, 1294, 1297  
1325, 1224, 1297, 1300  
1326, 1224, 1300, 1225  
*Nset, nset=-PickedSet2-3, internal  
1, 3, 4, 5, 6, 7, 8, 9, 10, 11, 12, 13, 14, 15, 16, 17  
18, 19, 20, 21, 22, 23, 24, 25, 26, 27, 1224, 1225, 1226, 1227, 1228, 1229  
1230, 1231, 1232, 1233, 1234, 1235, 1236, 1237, 1238, 1239, 1240, 1241, 1242,  
1243, 1244, 1245  
1246, 1247, 1248, 1249, 1250, 1251, 1252, 1253, 1254, 1255, 1256, 1257, 1258,  
1259, 1260, 1261  
1262, 1263, 1264, 1265, 1266, 1267, 1268, 1269, 1270, 1271, 1272, 1273, 1274,  
1275, 1276, 1277  
1278, 1279, 1280, 1281, 1282, 1283, 1284, 1285, 1286, 1287, 1288, 1289, 1290,
```

1291, 1292, 1293

1294, 1295, 1296, 1297, 1298, 1299, 1300, 1301, 1302

*Elset, elset=-PickedSet2-3, internal, generate

1223, 1326, 1

*Nset, nset=-PickedSet3-4, internal

1, 3, 4, 5, 6, 7, 8, 9, 10, 11, 12, 13, 14, 15, 16, 17

18, 19, 20, 21, 22, 23, 24, 25, 26, 27, 1224, 1225, 1226, 1227, 1228, 1229

1230, 1231, 1232, 1233, 1234, 1235, 1236, 1237, 1238, 1239, 1240, 1241, 1242,
1243, 1244, 1245

1246, 1247, 1248, 1249, 1250, 1251, 1252, 1253, 1254, 1255, 1256, 1257, 1258,
1259, 1260, 1261

1262, 1263, 1264, 1265, 1266, 1267, 1268, 1269, 1270, 1271, 1272, 1273, 1274,
1275, 1276, 1277

1278, 1279, 1280, 1281, 1282, 1283, 1284, 1285, 1286, 1287, 1288, 1289, 1290,
1291, 1292, 1293

1294, 1295, 1296, 1297, 1298, 1299, 1300, 1301, 1302

*Elset, elset=-PickedSet3-4, internal, generate

1223, 1326, 1

*Nset, nset=-PickedSet2-4, internal

2, 28, 29, 30, 31, 32, 33, 34, 35, 36, 37, 38, 39, 40, 41, 42

43, 44, 45, 46, 47, 48, 49, 50, 51, 52, 1145, 1146, 1147, 1148, 1149, 1150

1151, 1152, 1153, 1154, 1155, 1156, 1157, 1158, 1159, 1160, 1161, 1162, 1163,
1164, 1165, 1166

1167, 1168, 1169, 1170, 1171, 1172, 1173, 1174, 1175, 1176, 1177, 1178, 1179,
1180, 1181, 1182

1183, 1184, 1185, 1186, 1187, 1188, 1189, 1190, 1191, 1192, 1193, 1194, 1195,
1196, 1197, 1198

1199, 1200, 1201, 1202, 1203, 1204, 1205, 1206, 1207, 1208, 1209, 1210, 1211,
1212, 1213, 1214

1215, 1216, 1217, 1218, 1219, 1220, 1221, 1222, 1223

*Elset, elset=-PickedSet2-4, internal, generate

1119, 1222, 1

*Nset, nset=-PickedSet3-5, internal

2, 28, 29, 30, 31, 32, 33, 34, 35, 36, 37, 38, 39, 40, 41, 42

43, 44, 45, 46, 47, 48, 49, 50, 51, 52, 1145, 1146, 1147, 1148, 1149, 1150

1151, 1152, 1153, 1154, 1155, 1156, 1157, 1158, 1159, 1160, 1161, 1162, 1163,

1164, 1165, 1166

1167, 1168, 1169, 1170, 1171, 1172, 1173, 1174, 1175, 1176, 1177, 1178, 1179,

1180, 1181, 1182

1183, 1184, 1185, 1186, 1187, 1188, 1189, 1190, 1191, 1192, 1193, 1194, 1195,

1196, 1197, 1198

1199, 1200, 1201, 1202, 1203, 1204, 1205, 1206, 1207, 1208, 1209, 1210, 1211,

1212, 1213, 1214

1215, 1216, 1217, 1218, 1219, 1220, 1221, 1222, 1223

*Elset, elset=-PickedSet3-5, internal, generate

1119, 1222, 1

*Nset, nset=-PickedSet2-2, internal, generate

1, 1144, 1

*Elset, elset=-PickedSet2-2, internal, generate

1, 1118, 1

*Nset, nset=-PickedSet3-3, internal, generate

1, 1144, 1

*Elset, elset=-PickedSet3-3, internal, generate

1, 1118, 1

*Elset, elset=-Inside-SNEG, internal, generate

1, 1326, 1

*Node

8000, 0.275000006, 3.82702141e-18, 0.325

```
*Nset, Nset=CavityNode
8000
*Surface, type=ELEMENT, name=Inside
-Inside-SNEG, SNEG
**
**
** SHELL SECTION
**
** Section: Shell Membrane
*MEMBRANE SECTION, elset=-PickedSet2-2, material="Kapton HN"
5e-05,
** Section: Shell Membrane
*MEMBRANE SECTION, elset=-PickedSet2-4, material="Kapton HN"
5e-05,
** Section: Shell Membrane
*MEMBRANE SECTION, elset=-PickedSet2-3, material="Kapton HN"
5e-05,
**
**
*END PART
**
** ASSEMBLY
**
*Assembly, name=Assembly
**
*Instance, name=Complete, part=Complete
-0.22, 0., 0.
**
**
```

```
** FLUID INFORMATION
**
*FLUID CAVITY, Name=Cavity, Ambient Pressure=1.013250e05, REFNODE=CavityNode, Ambient
Temperature=2.950000e02, Surface=Inside, MINIMUM VOLUME=INITIAL
VOLUME, BEHAVIOR=AIR, ADIABATIC

**
**
** GAS SPECIES DATA
**
** FLUID CAVITY BEHAVIOUR DEFINITIONS
**
** GAS SPECIES: 'Air'
**
*FLUID BEHAVIOR, Name=Air
**
*MOLECULAR WEIGHT
0.0289
**
*CAPACITY, TYPE=POLYNOMIAL
28.110, 1.967e-3, -1.966e-9, 0.0
**
** GAS SPECIES: 'O2'
**
*FLUID BEHAVIOR, Name=O2
**
*CAPACITY, Type=POLYNOMIAL
2.572300e+04, 1.298000e+01, -3.860000e-03, 0.000000e+00, 0.000000e+00
```

```
**  
  
*MOLECULAR WEIGHT  
3.200000e-05,  
**  
** GAS SPECIES: 'CO2'  
**  
*FLUID BEHAVIOR, Name=CO2  
**  
*CAPACITY, Type=POLYNOMIAL  
2.599900e+04, 4.350000e+01, -1.480000e-02, 0.000000e+00, 0.000000e+00  
**  
*MOLECULAR WEIGHT  
4.401000e-05,  
**  
** GAS SPECIES: 'N2'  
**  
*FLUID BEHAVIOR, Name=N2  
**  
*CAPACITY, Type=POLYNOMIAL  
2.729600e+04, 5.230000e+00, 0.000000e+00, 0.000000e+00, 0.000000e+00  
**  
*MOLECULAR WEIGHT  
2.801000e-05,  
**  
** GAS SPECIES: 'HE'  
**  
*FLUID BEHAVIOR, Name=HE  
**  
*CAPACITY, Type=POLYNOMIAL
```

2.078500e+04, 0.000000e+00, 0.000000e+00, 0.000000e+00, 0.000000e+00

**

*MOLECULAR WEIGHT

4.003000e-06,

**

** GAS SPECIES: 'N2O'

**

*FLUID BEHAVIOR, Name=N2O

**

*CAPACITY, Type=POLYNOMIAL

2.518800e+04, 5.210000e+01, -2.000000e-02, 0.000000e+00, 0.000000e+00

**

*MOLECULAR WEIGHT

4.401000e-05,

**

** GAS SPECIES: 'AR'

**

*FLUID BEHAVIOR, Name=AR

**

*CAPACITY, Type=POLYNOMIAL

2.078500e+04, 0.000000e+00, 0.000000e+00, 0.000000e+00, 0.000000e+00

**

*MOLECULAR WEIGHT

3.995000e-05,

**

**

*FLUID INFLATOR, Name=CavityInflation, PROPERTY=CavityInflationProperty

CavityNode

**

```
**
*FLUID INFLATOR PROPERTY, Name=CavityInflationProperty, TYPE=TEMPERATURE
AND MASS
**
0.000000e+00, 0.000000e+00, 0.000000e+00
1.000000e-04, 0.000000e+00, 0.000000e+00
2.000000e-04, 0.000000e+00, 0.000000e+00
***
**
*
**
***
3.990000e-02, 1.665000e+02, 1.875000e-05
4.000000e-02, 1.665000e+02, 1.875000e-14
1.000000e+00, 1.665000e+02, 0.000000e+00
**
**
*FLUID INFLATOR MIXTURE, Number species=6, Type=MOLAR FRAC-
TION
O2, CO2, AR, N2, HE, N2O
**
0.000000e+00, 1.000000e+00, 0.000000e+00, 0.000000e+00, 0.000000e+00, 0.000000e+00,
0.000000e+00
1.000000e-04, 1.000000e+00, 0.000000e+00, 0.000000e+00, 0.000000e+00, 0.000000e+00,
0.000000e+00
2.000000e-04, 1.000000e+00, 0.000000e+00, 0.000000e+00, 0.000000e+00, 0.000000e+00,
0.000000e+00
3.980000e-02, 2.400000e-02, 7.800000e-02, 6.284000e-01, 4.820000e-02, 8.980000e-
02, 1.316000e-01
```

```
3.990000e-02, 2.400000e-02, 7.810000e-02, 6.283000e-01, 4.820000e-02, 8.980000e-
02, 1.316000e-01
1.000000e+00, 2.400000e-02, 7.810000e-02, 6.283000e-01, 4.820000e-02, 8.980000e-
02, 1.316000e-01
**
*End Instance
**
*Node
1, 0.275000006, 3.82702141e-18, 0.649999976
*Node
8000, 0.275000006, 3.82702141e-18, 0.325
*Nset, nset=CavityNode, instance=complete
8000
*Nset, nset=Fixed, instance=Complete
2, 28, 29, 30, 31, 32, 33, 34, 35, 36, 37, 38, 39, 40, 41, 42
43, 44, 45, 46, 47, 48, 49, 50, 51, 52, 1145, 1146, 1147, 1148, 1149, 1150
1151, 1152, 1153, 1154, 1155, 1156, 1157, 1158, 1159, 1160, 1161, 1162, 1163,
1164, 1165, 1166
1167, 1168, 1169, 1170, 1171, 1172, 1173, 1174, 1175, 1176, 1177, 1178, 1179,
1180, 1181, 1182
1183, 1184, 1185, 1186, 1187, 1188, 1189, 1190, 1191, 1192, 1193, 1194, 1195,
1196, 1197, 1198
1199, 1200, 1201, 1202, 1203, 1204, 1205, 1206, 1207, 1208, 1209, 1210, 1211,
1212, 1213, 1214
1215, 1216, 1217, 1218, 1219, 1220, 1221, 1222, 1223
*Elset, elset=Fixed, instance=Complete, generate
1119, 1222, 1
*Nset, nset="Top Circum", instance=Complete
1, 3, 4, 5, 6, 7, 8, 9, 10, 11, 12, 13, 14, 15, 16, 17
```

18, 19, 20, 21, 22, 23, 24, 25, 26, 27

*Elset, elset="Top Circum", instance=Complete

43, 86, 129, 172, 215, 258, 301, 344, 387, 430, 473, 516, 559, 602, 645, 688

731, 774, 817, 860, 903, 946, 989, 1032, 1075, 1118, 1225, 1228, 1231, 1234, 1237, 1240

1243, 1246, 1249, 1252, 1255, 1258, 1261, 1264, 1267, 1270, 1273, 1276, 1279, 1282, 1285, 1288

1291, 1294, 1297, 1300

*Nset, nset=RF, internal

1,

*Nset, nset=-PickedSet28, internal, instance=Complete

1, 3, 4, 5, 6, 7, 8, 9, 10, 11, 12, 13, 14, 15, 16, 17

18, 19, 20, 21, 22, 23, 24, 25, 26, 27

*Elset, elset=-PickedSet28, internal, instance=Complete

43, 86, 129, 172, 215, 258, 301, 344, 387, 430, 473, 516, 559, 602, 645, 688

731, 774, 817, 860, 903, 946, 989, 1032, 1075, 1118, 1225, 1228, 1231, 1234, 1237, 1240

1243, 1246, 1249, 1252, 1255, 1258, 1261, 1264, 1267, 1270, 1273, 1276, 1279, 1282, 1285, 1288

1291, 1294, 1297, 1300

*Elset, elset=-Inside-SNEG, internal, instance=Complete, generate

1, 1326, 1

*Surface, type=ELEMENT, name=Inside

-Inside-SNEG, SNEG

**

**

** CONSTRAINTS

**

** Constraint: Constraint-1

*RIGID BODY, ref node=RF, tie nset=-PickedSet28, position=CENTER OF MASS

*End Assembly

**

*PHYSICAL CONSTANTS, UNIVERSAL GAS CONSTANT=8.31434, ABSOLUTE ZERO=-293.15

**

**

** AMPLITUDES

**

*AMPLITUDE, name=Pressure, Definition=SMOOTH STEP

0.0, 0.0

0.25, 25.0

0.5,50.0

0.75,100.0

1, 200.0

**

*AMPLITUDE, name=Amp-Inflator, Definition=SMOOTH STEP

0.0, 0.0, 0.25, 25.0, 0.5, 50.0, 1, 100.0

**

*AMPLITUDE, name=Smooth-Step, Definition=SMOOTH STEP

0., 0., 0.1, 0.5, 0.2, 1.0

**

**

** MATERIALS

**

*MATERIAL, name="Kapton HN"

*DENSITY

```
1420.,
*ELASTIC
1.42e+09, 0.34
**
**
** INITIAL FLUID CONDITIONS
**
*INITIAL CONDITIONS, TYPE=FLUID PRESSURE
Complete.CavityNode, 0.0
*INITIAL CONDITIONS, TYPE=TEMPERATURE
Complete.CavityNode, 2.95e+02
**
**
** BOUNDARY CONDITIONS
**
** Name: Fixed Base Type: Symmetry/Antisymmetry/Encastre
*BOUNDARY
FIXED, ENCASTRE
**
**
** STEP: INITIAL INFLATION
**
*STEP, name="Initial Inflation"
The pressurization of the beam
*DYNAMIC, Explicit
, 1.
*BULK VISCOSITY
0.06, 1.2
**
```

```
** LOADS
**
** Name: Initial Pressure Type: Pressure
*DSLOAD
Inside, P, 0.1
**
** OUTPUT REQUESTS
**
*RESTART, write, number interval=1, time marks=NO
**
** FIELD OUTPUT: F-Output-1
**
*OUTPUT, field, time interval=1e-100
*NODE Output
A, RF, U, UR, UT, V
*ELEMENT Output, directions=YES
LE, P, PE, S
*CONTACT Output
CSTRESS,
**
** HISTORY OUTPUT: H-Output-1
**
*OUTPUT, history, variable=PRESELECT
*END STEP
**
**
** STEP: BENDING
**
*STEP, name=Bending
```

```
*DYNAMIC, Explicit
, 1.
*BULK VISCOSITY
0.06, 1.2
**
** BOUNDARY CONDITIONS
**
** Name: Constraint: Fixed End
*BOUNDARY, OP=MOD
Fixed, ENCASTRE
**
**
** Name: Initial Pressure Type: Pressure
*DSLOAD
Inside, P, 0.1
**
** Name: Bending Type: Displacement/Rotation
*BOUNDARY, amplitude=Smooth-Step
RF, 5, 5, 1.57078
**
**
** OUTPUT REQUESTS
**
*RESTART, write, number interval=1, time marks=NO
**
** FIELD OUTPUT: F-Output-1
**
*OUTPUT, field, time interval=1e-100
*NODE Output
```

```
A, RF, U, UR, UT, V
*ELEMENT Output, directions=YES
LE, P, PE, S
*CONTACT Output
CSTRESS,
**
** HISTORY OUTPUT: H-Output-1
**
*OUTPUT, history, variable=PRESELECT
*END STEP
**
**
** STEP: POST INFLATION
**
*STEP, name=Inflation
*DYNAMIC, Explicit
, 1.
*BULK VISCOSITY
0.06, 1.2
**
**
** BOUNDARY CONDITIONS MODIFIED
**
** Name: Constraint: Fixed End
*BOUNDARY, OP=NEW
Fixed, ENCASTRE
**
** ** Name: Bending Type: Displacement/Rotation
** *BOUNDARY, OP=NEW, Amplitude=Smooth-Step
```

```
** RF, 5, 5, 0
**
** Name: Initial Pressure Type: Pressure
*DSLOAD
Inside, P, 0.1
**
** FLUID INFLATION
**
*FLUID INFLATOR ACTIVATION, Inflation time amplitude=Amp-Inflator
Complete.CavityInflation
*BOUNDARY, OP=NEW, amplitude=Pressure
CavityNode, 8, 8, 10.
**
** OUTPUT REQUESTS
**
*RESTART, write, number interval=1, time marks=NO
**
** FIELD OUTPUT: F-Output-1
**
*OUTPUT, field, time interval=1e-100
*NODE Output
A, RF, U, UR, UT, V
*ELEMENT Output, directions=YES
LE, P, PE, S
*CONTACT Output
CSTRESS,
**
** HISTORY OUTPUT: H-Output-1
**
```

```
*OUTPUT, history, variable=PRESELECT  
*END STEP
```

Bibliography

- [1] S. Games. Tents - architecture of the nomads - faegre,t. *Riba Journal-Royal Institute of British Architects*, 86(8):360–360, 1979.
- [2] S. Armijos. The history of fabric structures. <https://armijos.wordpress.com/2010/03/22/fabric-architecturefabric-structures-history-101/>, 2, 2000.
- [3] A. Pagitz, Y. Xu, and S. Pellegrino. Stability of lobed balloons. *Next Generation of Scientific Balloon Missions*, 37(11):2059–2069, 2006.
- [4] M. A. Shampo and R. A. Kyle. Jacques-alexandre-cesar charles. *JAMA : the journal of the American Medical Association*, 251(19):2547, 1984.
- [5] A. Theuerkauf, M. Gerding, and F. J. Luebken. Litos - a new balloon-borne instrument for fine-scale turbulence soundings in the stratosphere. *Atmospheric Measurement Techniques*, 4(1):55–66, 2011.
- [6] Markus Pagitz. The future of scientific ballooning. *Philosophical Transactions of the Royal Society a-Mathematical Physical and Engineering Sciences*, 365(1861):3003–3017, 2007.
- [7] V. P. Dawson. Race to the stratosphere - manned scientific ballooning in america. *Technology and Culture*, 32(3):633–634, 1991.

-
- [8] Gregory Kennedy. The two explorer stratosphere balloon flights. *Website: <http://stratocat.com.ar/artics/explorer-e.htm>*, 2011.
- [9] Nichole M. Lareau, Larissa S. Fenn, Cody R. Goodwin, Brian O. Bachmann, and John A. McLean. Exploring conformation space for natural product discovery. *Abstracts of Papers of the American Chemical Society*, 241, 2011.
- [10] Brigitte Weitbrecht Ohillip Drew. *Frei Otto: Form und Konstruktion*. Verlag gerd hatje, Stuttgart, Germany, german edition, 1976.
- [11] J. Bonet, R. D. Wood, J. Mahaney, and P. Heywood. Finite element analysis of air supported membrane structures. *Computer Methods in Applied Mechanics and Engineering*, 190(5-7):579–595, 2000.
- [12] R. Poprawe. *B Addenda: Continuum Mechanics*, pages 455–477. VDI-Buch. Springer, New York, 2005.
- [13] V. Kompis. Introduction to nonlinear continuum mechanics. *Selected Topics in Boundary Integral Formulations for Solids and Fluids*, 2(433):1–9, 2002.
- [14] A. Ibrahimbegovic. Nonlinear solid mechanics. *Nonlinear Solid Mechanics: Theoretical Formulations and Finite Element Solution Methods*, 160:1–574, 2009.
- [15] O. C. Zienkiewicz, R. L. Taylor, and P. Nithiarasu. *The Finite Element Method for Fluid Dynamics Sixth edition Preface*, pages XI–XII. Elsevier Science Bv, Amsterdam, 2005.
- [16] J. C. Simo and D. D. Fox. On a stress resultant geometrically exact shell model: formulation and optimal parameterization. *Computer Methods in Applied Mechanics and Engineering*, 72(3):267–304, 1989.

- [17] M. Braun, M. Bischoff, and E. Ramm. Nonlinear shell formulations for complete 3-dimensional constitutive laws including composites and laminates. *Computational Mechanics*, 15(1):1–18, 1994.
- [18] J. G. Valdes, J. Miquel, and E. Onate. Nonlinear finite element analysis of orthotropic and prestressed membrane structures. *Finite Elements in Analysis and Design*, 45(6-7):395–405, 2009.
- [19] I. Y. Khoma. Nonlinear equations of the generalized theory of elastic shells. *Soviet Applied Mechanics*, 20(1):39–45, 1984.
- [20] D.X. Zhang W.J. Chen, L. Zhang. Research and development of bi-axial tension tester and experiments on the mechanical properties of envelop fabrics. In Proceedings of the International Conference on Textile Composites Structures and Inflatable, editors, *Structural Membranes*, 1996.
- [21] Herbert Wagner. Flat sheet metal girders with very thin metal web, 1931.
- [22] E. Reissner. The effect of transverse shear deformation on the bending of elastic plates. *Journal of Applied Mechanics-Transactions of the Asme*, 12(2):A69–A77, 1945.
- [23] Eh Mansfield. Load transfer via a wrinkled membrane. *Proceedings of the Royal Society of London Series a Mathematical and Physical Sciences*, 11(1525):269–, 1970.
- [24] P. Contri and B. A. Schrefler. A geometrically nonlinear finite element analysis of wrinkled membrane surfaces by a no compression material model. *Communications in Applied Numerical Methods*, 4(1):5–15, 1988.
- [25] X. Liu, C. H. Jenkins, and W. Schur. Large deflection analysis of pneumatic envelopes using a penalty parameter modified material model. *Finite Elements in Analysis and Design*, 37(3):233–251, 2001.

-
- [26] R. Rossi, M. Lazzari, R. Vitaliani, and E. Onate. Simulation of light-weight membrane structures by wrinkling model. *International Journal for Numerical Methods in Engineering*, 62(15):2127–2153, 2005.
- [27] C. H. Wu and T. R. Canfield. Wrinkling in finite plane stress theory. *Quarterly of Applied Mathematics*, 39(2):179–199, 1981.
- [28] D. G. Roddeman, J. Drukker, C. W. J. Oomens, and J. D. Janssen. The wrinkling of thin membranes: 1. theory. *Journal of Applied Mechanics-Transactions of the Asme*, 54(4):884–887, 1987.
- [29] F. Muttin. A finite element for wrinkled curved elastic membranes, and its application to sails. *Communications in Numerical Methods in Engineering*, 12(11):775–785, 1996.
- [30] A. Jarasjarungkiat, R. Wuechner, and K. U. Bletzinger. A wrinkling model based on material modification for isotropic and orthotropic membranes. *Computer Methods in Applied Mechanics and Engineering*, 197(6-8):773–788, 2008.
- [31] A. Tessler, D. W. Sleight, and J. T. Wang. Effective modeling and non-linear shell analysis of thin membranes exhibiting structural wrinkling. *Journal of Spacecraft and Rockets*, 42(2):287–298, 2005.
- [32] D. G. Roddeman, J. Drukker, C. W. J. Oomens, and J. D. Janssen. The wrinkling of thin membranes: 2. numerical analysis. *Journal of Applied Mechanics-Transactions of the Asme*, 54(4):888–892, 1987.
- [33] K. Willam. Computational methods for transient analysis. *Computer Methods in Applied Mechanics and Engineering*, 46(3):351–353, 1984.
- [34] Y. Wesley Wong and Sergio Pellegrino. Wrinkled membranes part 1: Experiments. *Journal of Mechanics of Materials and Structures*, 1(1):3–25, 2006.

- [35] H. Assilzadeh, J. K. Levy, X. Wang, Y. Gao, and Z. N. Zhong. Geosensing systems engineering for ocean security and sustainable coastal zone management. *Journal of Systems Science and Systems Engineering*, 19(1):22–35, 2010.
- [36] Satish Kumar and S.H. Upadhyay. Wrinkling simulation of membrane structures under tensile and shear loading. *Columbia International Publishing, Journal of Vibration Analysis, Measurement, and Control*, 3(1):17–33, 2015.
- [37] W. Schur Xinxiang Liu, Christopher Jenkins. Fine scale analysis of wrinkled membranes. *International Journal of Computational Engineering Science*, 1(2):1142–1148, December 2000 2000.
- [38] C. Lin and C. Mote. The wrinkling of rectangular webs under non-linearly distributed edge loading. *Journal of Applied Mechanics*, 63(3):655–659, 1996.
- [39] Y. Wesley Wong and Sergio Pellegrino. Wrinkled membranes part 2: Analytical models. *Journal of Mechanics of Materials and Structures*, 1(1):27–61, 2006.
- [40] C. D. Coman and A. P. Bassom. On the nonlinear membrane approximation and edge-wrinkling. *International Journal of Solids and Structures*, 82:85–94, 2016.
- [41] J. Mosler and F. Cirak. A variational formulation for finite deformation wrinkling analysis of inelastic membranes. *Computer Methods in Applied Mechanics and Engineering*, 198(27-29):2087–2098, 2009.
- [42] A.C. Pipkin. The relaxed energy density for isotropic elastic membranes. *IMA Journal of Applied Mathematics*, 20(No.12):1761–1763, 1986.

-
- [43] A.C. Pipkin. Convexity conditions for strain-dependent energy functions for membranes. *Archive for Rational Mechanics and Analysis*, 121(4):361–376, 1993.
- [44] A.C. Pipkin. Relaxed energy densities for large deformations of membranes. *IMA Journal of Applied Mechanics*, 52(3):297–308, 1994.
- [45] Y. Wesley Wong and Sergio Pellegrino. Wrinkled membranes part 3: Numerical simulations. *Journal of Mechanics of Materials and Structures*, 1(1):63–95, 2006.
- [46] James M. Gere and Stephen P. Timoshenko. *Mechanics of Materials*. Brooks/Cole; 6th Revised edition edition, Pacific Grove, California, US, 2003.
- [47] N. Friedl, F. G. Rammerstorfer, and F. D. Fischer. Buckling of stretched strips. *Computers and Structures*, 78(1-3):185–190, 2000.
- [48] D. J. Steigmann. Tension field theory. *Proceedings of the Royal Society of London Series a-Mathematical Physical and Engineering Sciences*, 429(1876):141–173, 1990.
- [49] Eric Fleurent-Wilson, Mohammed Ibrahim, Armaghan Salehian, and Asme. *A GEOMETRICALLY BIO-INSPIRED MFC ACTUATOR FOR WRINKLE CONTROL OF KAPTON MEMBRANES*. Proceedings of the Asme Conference on Smart Materials, Adaptive Structures and Intelligent Systems, Vol 2. 2012.
- [50] A. J. Moskalik and D. Brei. Force-deflection behavior of piezoelectric c-block actuator arrays. *Smart Materials and Structures*, 8(5):531–543, 1999.

- [51] M. W. Hyer and A. B. Jilani. Predicting the axisymmetric manufacturing deformations of disk-style benders. *Journal of Intelligent Material Systems and Structures*, 11(5):370–381, 2000.
- [52] C. E. Seeley, A. Chattopadhyay, and D. Brei. Development of a polymeric piezoelectric c-block actuator using hybrid optimization technique. *Aiaa Journal*, 34(1):123–128, 1996.
- [53] P. Duran-Martin, A. Vazquez, and D. D. N. Setter. Production and characterization of rainbow piezoelectric actuators. advantages from other traditional devices. *Boletin De La Sociedad Espanola De Ceramica Y Vidrio*, 38(6):662–666, 1999.
- [54] C. Wang, X. Du, and Z. Wan. Numerical simulation of wrinkles in space inflatable membrane structures. *Journal of Spacecraft and Rockets*, 43(5):1146–1149, 2006.
- [55] E. Gai and H. Zhang. Finite point method: a new approach to model the inflation of side curtain airbags. *International Journal of Crashworthiness*, 10(5):445–450, 2005.
- [56] P. Groenenboom. A diffusive gas jet model in pam-safe for airbag inflation. *SAE International Technical paper 930238*, 1(1), 1993.
- [57] H.A. Lupker. Gas jet model for airbag inflators. *SAE International Technical Paper 930645*, 1(1), 1993.
- [58] J.O. Hallquist. *LS-DYNA Theoretical Manual*, volume 4. 1991-2006 Livermore Software Technology Corporation, 7374 las Positas Road, Livermore, California, 94551, 2006.
- [59] L.A. Fredriksson. *PhD Thesis - A finite element data base for occupant substitutes*. Thesis, Department of Mechanical Engineering, 1996.

- [60] E. Mestreau. Airbag simulation using fluid/structure coupling. *34th Aerospace Sciences Meeting and Exhibit*, page 8, 1996.
- [61] P. O. Marklund and L. Nilsson. Simulation of airbag inflation processes using a coupled fluid structure approach. *Computational Mechanics*, 29(4-5):289–297, 2002.
- [62] A. Diaby, A. Le Van, and C. Wielgosz. Buckling and wrinkling of pre-stressed membranes. *Finite Elements in Analysis and Design*, 42(11):992–1001, 2006.
- [63] W. F. Lam and C. T. Morley. Arc-length method for passing limit points in structural calculation. *Journal of Structural Engineering-Asce*, 118(1):169–185, 1992.
- [64] R. Barsotti, S. S. Ligaro, and G. F. Royer-Carfagni. The web bridge. *International Journal of Solids and Structures*, 38(48-49):8831–8850, 2001.
- [65] Rick Docksai. Space solar power: The first international assessment of space solar power: Opportunities, issues and potential pathways forward. *Futurist*, 46(3):56–56, 2012. 0.
- [66] John C. Mankins. The first international assessment of space solar power: opportunities, issues, ad potential pathways forward, 2011.
- [67] John Mankins. Sps-alpha: The first practical solar power satellite via arbitrarily large phased array, 2011.
- [68] Thomas Hilbich Thomas Sinn. Inflatable shape changing colonies assembling versatile smart space structures, 2014.
- [69] C. Pandolfi R.Vidoni, T.Mimmo. Mimicking the thigmotropic behavior of climbing plants to design a tactile based grasping device for the space

- environment. Report, Faculty of Science and technology, Free University of Bolzano, 2013.
- [70] C. W. Whippo and R. P. Hangarter. Phototropism: Bending towards enlightenment. *Plant Cell*, 18(5):1110–1119, 2006. 65.
- [71] N. Moran, G. Ehrenstein, K. Iwasa, C. Mischke, C. Bare, and R. L. Satter. Potassium channels in motor cells of samanea-saman - a patch clamp study. *Plant Physiology*, 88(3):643–648, 1988. 82.
- [72] Goekhan Kiper and Eres Soylemez. Deployable space structures. *Rast 2009: Proceedings of the 4th International Conference on Recent Advances in Space Technologies*, pages 131–138, 2009.
- [73] M. Mladenov. New geometrical applications of the elliptic integrals: the mylar balloon. In *Geometrical methods in physics*, volume 11, pages 55–65. Journal of Nonlinear Math, 2000.
- [74] Robert W. Leonard, George W. Brooks, and Harvey G. Jr. McComb. Structural considerations of inflatable re-entry vehicles. *NASA; Washington, DC United States*, 19980228194(1):24, 1960.
- [75] RL COMER and S LEVY. Deflections of an inflated circular cylindrical cantilever beam. *Aiaa Journal*, 1(7):1652–1655, 1963.
- [76] JA Main, RA Carlin, E Garcia, SW Peterson, and AM Strauss. Dynamic analysis of space based inflated beam structures. *Journal of the Acoustical Society of America*, 97(2):1035–1045, 1995.
- [77] JC Thomas and C Wielgosz. Deflections of highly inflated fabric tubes. *Thin-Walled Structures*, 42(7):1049–1066, 2004.

- [78] William G. Davids, Hui Zhang, Adam W. Turner, and Michael Peterson. Beam finite-element analysis of pressurized fabric tubes. *Journal of Structural Engineering-Asce*, 133(7):990–998, 2007.
- [79] J.M. Hedgepeth M. Stein. Analysis of partly wrinkled membranes, 1961.
- [80] Z.H. Zhu, R.K. Seth, and B.M. Quine. Experimental investigation of inflatable cylindrical cantilevered beams. *International Journal of Space Science and Engineering*, 1(1):15, 2013.
- [81] Amit Patil, Arne Nordmark, and Anders Eriksson. Wrinkling of cylindrical membranes with non-uniform thickness. *European Journal of Mechanics a-Solids*, 54:1–10, 2015.
- [82] A Le van and C Wielgosz. Bending and buckling of inflatable beams: Some new theoretical results (vol 43, pg 1166, 2005). *Thin-Walled Structures*, 44(7):822–823, 2006.
- [83] Chang-Guo Wang, Hui-Feng Tan, Xing-Wen Du, and Xiao-Dong He. A new model for wrinkling and collapse analysis of membrane inflated beam. *Acta Mechanica Sinica*, 26(4):617–623, 2010.
- [84] E.H. Mansfield. Tension field theory. *Proceeding of the 12th International Congress of Applied Mechanics, Stanford University*, 12(1):305–320, 1969.
- [85] J.M. Hedgepeth R.K. Miller. An algorithm for finite element analysis of partly wrinkled membranes. *AIAA Journal*, 20(12):1761–1763, 1982.
- [86] R. K. Miller, J. M. Hedgepeth, V. I. Weingarten, P. Das, and S. Kahyai. Finite element analysis of partly wrinkled membranes. *Computers and Structures*, 20(1-3):631–639, 1985.
- [87] A. L. Adler, M. M. Mikulas, J. M. Hedgepeth, Aiaa, and Aiaa Aiaa. Static and dynamic analysis of partially wrinkled membrane structures.

Collection of the 41st Aiaa/Asme/Asce/Ahs/Asc Structures, Structural Dynamics, and Materials Conference and Exhibit, Vol 4, pages 158–171, 2000.

- [88] QingShan Yang, Feng Tan, and XiaoFeng Wang. Loading and wrinkling analysis of membrane structures. *Science China-Technological Sciences*, 54(10):2597–2604, 2011.
- [89] Y. Wesley Wong and Sergio Pellegrino. Wrinkled membranes. *Journal of Mechanics of Materials and Structures*, 1(1):8–25, 2009.
- [90] S. W. Kang and S. Im. Finite element analysis of dynamic response of wrinkling membranes. *Computer Methods in Applied Mechanics and Engineering*, 173(1-2):227–240, 1999.
- [91] S. L. Veldman and Cajr Vermerren. Inflatable structures in aerospace engineering - an overview. *European Conference on Spacecraft Structures, Materials and Mechanical Testing, Proceedings*, 468:93–98, 2001.
- [92] E. J. Yoo, J. H. Roh, and J. H. Han. Wrinkling control of inflatable booms using shape memory alloy wires. *Smart Materials and Structures*, 16(2):340–348, 2007.